QUASI-TWO-DIMENSIONAL KOLMOGOROV FLOW: BIFURCATIONS AND EXACT COHERENT STRUCTURES

A Thesis
Presented to
The Academic Faculty

by

Balachandra Suri

In Partial Fulfillment
of the Requirements for the Degree
Doctor of Philosophy in the
School of Physics

Georgia Institute of Technology
August 2017

QUASI-TWO-DIMENSIONAL KOLMOGOROV FLOW: BIFURCATIONS AND EXACT COHERENT STRUCTURES

Approved by:

Professor Michael F. Schatz, Advisor
School of Physics
Georgia Institute of Technology

Professor Kurt Wiesenfeld
School of Physics
Georgia Institute of Technology

Professor Roman O. Grigoriev
School of Physics
Georgia Institute of Technology

Professor Mark Paul
Department of Mechanical Engineering
Virginia Polytechnic Institute and State University

Professor Predrag Cvitanović
School of Physics
Georgia Institute of Technology

Date Approved: 27 June 2017

To

The Almighty, My Parents, Family, and Best Friends

Acknowledgments

There are several people who have directly or indirectly helped me finish my PhD, and thanking them for their support is personally very important. First and foremost, I am deeply indebted to my adviser Prof. Michael Schatz, who contributed immensely to my academic as well as personal development during my PhD. Research in SchatzLab was enjoyable, which I attribute largely to Mike's positivity and optimism. I am grateful to Mike for providing valuable scientific advice, for giving me the freedom to pursue new ideas, and for words of wisdom whenever I felt lost. Also, I thank Mike for the numerous opportunities he provided to me to interact with the scientific community, at conferences as well as at the hands-on schools. I am indebted to Prof. Roman Grigoriev who co-advised me during my PhD. Discussions with Roman helped me immensely to improve my ability to relate theory with experiment, for which I am very grateful to him. Roman is a wonderful teacher and I was fortunate to have him as my instructor for several graduate classes. Lastly, besides being wonderful supervisors, both Mike and Roman are genuinely caring human beings, which makes working with them a true honor.

I am grateful to Jeff Tithof for being a very close friend and a wonderful collaborator during all these years in graduate school. Very few graduate students I have met are as diligent and persevering as Jeff. I am grateful to Daniel Borrero for being a great mentor and a very close friend who helped me immensely in getting familiar with experiments during my early years in SchatzLab. I would like to thank Roman's graduate students Radford Mitchell, Ravi Kumar Pallantla, and Chris Marcotte for useful discussions on the theoretical aspects of the ECS problem. In particular, I am grateful to Radford for implementing the original version of the Newton-Krylov solver, without which I would have spent an extra year in graduate school. I thank Adam

Perkins for patiently and clearly replying to my emails seeking help for troubleshooting the Rayleigh-Bénard convection experiment. Finally, I thank my friends Chris Crowley, Logan Kageorge, Grace Chambers, and Brett Tregoning for not only making SchatzLab a fun place to work, but also for proofreading my thesis and helping me fix *italics* (and parenthesis) abuse.

Being a member of the Homology-group, which includes researchers from diverse backgrounds, was a unique experience. I would like to thank Prof. Mark Paul for providing insights into pattern formation during our group meetings, as well as for accepting to serve as a member on my thesis committee. I thank Prof. Konstantin Mischaikow for making abstract ideas from persistent homology accessible to non-mathematicians like me, which was invaluable. I thank Mu Xu, Rachel Levanger, Miro kramár, and Jacek Cyranka for sharing their technical know-how with us, be it regarding computing Lyapunov vectors or applying Persistent Homology to analyze flow patterns.

It thank Prof. Kurt Wiesenfeld for his encouragement, as well as for being one of the best teachers I ever had. I am thankful to Prof. Predrag Cvitanović for encouraging our scientific efforts, as well as for authoring some of my favorite scientific material. I thank both Kurt and Predrag for accepting to serve on my thesis committee. I thank Prof. Brian Storey for introducing me to computer simulations at the hands-on school in China. Finally, I thank my CFD teacher Prof. Alexander Alexeev, who guided me to useful scientific material on several occasions which helped me improve my coding skills.

There are several people beyond the Georgia Tech (GT) community who played a crucial role in my reaching the current stage of scientific pursuit. First and foremost, I am forever grateful to my parents Kumaraswamy and Vedavathi, and my brother Baladitya, for their love as well as for being unconditionally supportive of my endeavors. My mother is one of the most hard-working persons I have ever known. Her

courage in the face of adversity is both inspiring and humbling. My father is very kindhearted and I inherit from him the love for nature and music, which I hold very dear. As a kid, my conversations with him shaped my ability to reason. My brother has been a guiding force since childhood; I chose physics as my undergraduate major and nonlinear dynamics as my research area following his footsteps. I thank Divya Jain, my sister-in-law, for her support and encouragement during rough times. Lastly, I am thankful my late uncle Mani for being so loving and affectionate.

I thank my teachers Radhakrishna Mantripragada, Vadlamani Shyam, and James Devadas for their encouragement and support during my high-school days. I am deeply indebted to Chandu Kakaji, my spiritual guru, who gave me hope and strength to overcome adversity. I am very grateful to my cousin Srikanth Suri for providing tremendous support whenever I passed through rough times. A phone call to Kakaji or Srikanth gave me the belief that everything will be fine and helped me to get back to work. Since the time I left home for Kharagpur in 2004, my uncles and aunts, my cousins, our family friends, as well as the doctors back home have supported my family on numerous occasions. This gave me a sense of assurance and peace, which helped me to continue my studies uninterruptedly. I am deeply indebted to all of them.

I am grateful to Chitti Babu and Sita Bammidimarri for their affection as well as for their support as my local guardians in Atlanta during the first three years of my PhD. I am very thankful to Subbu and Sujatha Bhagavathi, who have treated me as a member of their family and have been very supportive. Lastly, I am greatly indebted to Danae Evans and Frank Pickens, without whose support I would not have finished my PhD.

Friends have played a very crucial role in my life since my high-school days and I take this opportunity to thank them. I thank Vamsi B.V.S and Swaroop Damaraju

who have been dear friends for nearly 20 years now, and have always been my well-wishers. I am grateful to my friend Varun Narasimhachar for offering wise advice at several crucial junctures, and for being extremely supportive all along. I thank my dear friends Srikanth Burra, Ravi Kumar Nadiminti, Raghuram Nadiminti, and Anirudh Nellutla for being unconditionally affectionate and making my stay at IIT-KGP memorable. I thank Somindu and Subhasri for encouraging me to pursue my interests. Lastly, I thank Abhishek Iyer, Srikanth Chitti, Sistla Teja, Mukul Singhee, Asha Parekh, and Anshuman Vinit who have all contributed in different ways to my academic pursuit.

I will cherish my stay in Atlanta not just for my experiences at GT, but also for meeting wonderful people. To begin, I am grateful to Ranjini Vaidyanathan for being a dear friend and one of the most affectionate persons I ever met. Diligent and wise, Ranjini was always one of the first persons I sought advice from whenever I was in a dilemma. I also thank Ranjini, as well as our friend Hagop, for the numerous coffee-shop study sessions that helped me finish drafting journal articles as well as my thesis. I thank Shreekrishna (SK), who was one of my first contacts at GT and soon became one of my dearest friends. Together, SK and I shared memorable moments listening to western classical concerts at the Atlanta Symphony Orchestra, specially Dvořák's symphonies 7,8 and 9. Nagesh Adiga and Deepthi Adiga have been great friends who have been extremely supportive all along. The badminton sessions at GT with SK and the Adigas, as well as the thanksgiving vacations spent in San Jose, are some of the happiest memories from the USA stay. I thank the amazing Bhanu Teertha Sama for being a dear and caring friend, and also for teaching me how to drive a car. I thank Sandeep and Sravani for being great friends; they were so incredibly welcoming that we turned their home into our "SFA headquarters" for weekend hangouts. I am deeply indebted to Krishna Chaitanya and Suvarchala for their tremendous support during the last two years of my PhD, and for hosting me

for over a month at a crucial juncture. I am very thankful to Swetha Rathan and Anita Rajamani for their friendship, advice, and support. I thank Poorna Roy for being a close friend and a source of inspiration. I thank Christina Carrol, one of most genuinely affectionate persons I met in the USA, for being a dear friend. I thank Ravi Kovvali and family for their affection and support. I am very thankful to A.C.R Lakshman, Aditya Konduri, and SK for being my (online) CFD gurus and helping sort coding issues during my PhD. Lastly, I thank my roommates, the members of "SFA", and my friends in "Atlanta-folks" for the fun times as well as for being helpful on various occasions.

Before concluding, I would like to thank four special people who played a crucial role in teaching me how to survive through times which I perceive as tough. I am forever indebted to Madhav K.S.V and Mithun T.M, who were great mentors and have been best friends since 2005. I am grateful to my cousin Subhadra for making me realize that giving up will not take one closer to goals which are dear and of great personal value. Finally, I am deeply thankful to Rafael Nadal for being an inspiration since 2007. His commitment to continuing to fight regardless of the result is inspiring and humbling. Rafa winning "La Decima" during the same week as my thesis defense is truly memorable.

TABLE OF CONTENTS

LIST OF TABLES

LIST OF FIGURES

SUMMARY

Fluid turbulence is nearly ubiquitous in natural and human-made systems. However, despite systematic research for over hundred years, scientists are yet to develop efficient ways to forecast and control the evolution of turbulent flows. The research presented in this thesis tests and extends recent ideas aimed at developing a simplified description of turbulent evolution. The underlying methodology includes computing *unstable, nonchaotic* solutions, called "Exact Coherent Structures" (ECS), of the Navier-Stokes equation which describes the evolution of fluid flows. While ECS exist in the same parametric regime where one observes turbulence, being unstable, they are observed only fleetingly during turbulent evolution. However, unlike turbulence, they display less complicated spatiotemporal features and are more tractable to analysis. Consequently, ECS may serve as building blocks in developing a simplified description of turbulent evolution, ultimately leading to its efficient forecasting and even control.

A vast majority of previous studies have focused on exploring the role of ECS in three-dimensional (3D) flows (e.g., flow in a pipe) which are experimentally and computationally challenging. Consequently, the dynamical role of ECS in turbulent evolution has not been unambiguously demonstrated. To address this shortcoming, the research presented in this thesis explores ECS in turbulence generated in an electromagnetically driven, shallow electrolyte layer. When the electromagnetic forcing is horizontal the flow in response is nearly horizontal as well, i.e., quasi-two-dimensional (Q2D), and can be quantified using strictly two-dimensional (2D) velocity field measurements. This Q2D flow in the experiment is modeled theoretically using

a strictly 2D equation, which is numerically discretized on a domain with dimensions and boundary conditions identical to those in the experiment in the horizontal directions. That the flow in both experiment and simulations can be treated as 2D helps circumventing the difficulties associated with studying 3D flows.

At low driving, the Q2D flow in the experiment displays simple spatiotemporal features. However, as the driving is increased, the flow transitions through a sequence of steady states before eventually becoming turbulent. The 2D model is validated by demonstrating quantitative agreement between its numerical simulation and the experiment, by comparing flow fields as well as the sequence of bifurcations in pre-turbulent regimes. Analyzing the dynamics in the weakly turbulent regime for signatures of ECS, it is identified that dramatic slowing-down in the evolution of the flow is related to turbulent trajectories in the state space visiting the neighborhoods of unstable equilibrium solutions. Several such equilibria, closely approached by trajectories in both the experiment and the simulation, are computed by iteratively refining turbulent flow fields at instants of slow evolution. The dynamical role of ECS is validated by showing that the geometry of state space around an equilirbium is shaped by its unstable manifold, which guides the evolution of nearby turbulent trajectories. Consequently, it is demonstrated that the evolution of turbulent trajectories in the neighborhood of an unstable equilibrium can be forecast by constructing its unstable manifold. In summary, the research presented in this thesis offers the first unambiguous evidence for the dynamical role of ECS in turbulence as well as the first ECS-based forecasting of turbulent evolution.

CHAPTER I

INTRODUCTION

Fluid flows are nearly ubiquitous. Water flowing in rivers and oceans, air currents circulating in the atmosphere, blood flowing through the arteries and veins of the human body, and oil pumping across countries through giant pipelines are all examples of flows that are of great relevance to humankind. Given their near ubiquity one may think that scientists, by now, should know "everything" about fluid flows. After all, human-kind has solved fluid problems since the times of Archimedes (2^{nd} century BC). In reality, however, the scientific community is still trying to develop effective ways to measure, quantify, forecast, and control the evolution of fluid flows in a vast majority of natural and human-made systems.

1.1 The Turbulence Problem

The level of difficulty in analyzing a certain flow depends on its complexity, which serves to broadly classify flows into two categories: "Laminar" flows which are smooth and regular, like the glassy stream of water flowing out of a faucet which is opened only slightly, and "Turbulent" flows which are irregular and sinuous [1], like the violent gush observed when the faucet is opened all the way. Viscosity (internal friction) in fluids causes dissipation of energy, which tends make the flow slow and consequently laminar. To overcome this friction and keep the fluid in motion, one requires driving (energy input). Since dissipation and energy input have opposite effects on the flow speed, their relative strength determines whether the flow remains laminar or turbulent. Most flows of practical importance are turbulent and, unfortunately, very difficult to study from both theoretical and experimental standpoints.

The Navier-Stokes equation, which is Newton's second law formulated for a continuous fluid medium, describes the evolution of both laminar and turbulent fluid[1] flows:

$$\frac{d\mathbf{V}}{dt} = \partial_t \mathbf{V} + \mathbf{V} \cdot \nabla \mathbf{V} = -\nabla p + \frac{1}{Re} \nabla^2 \mathbf{V} + \mathbf{F}_{ext}. \tag{1.1}$$

Here $\mathbf{V}(x, y, z, t)$ is an incompressible field ($\nabla \cdot \mathbf{V} = 0$) which quantifies the velocity at each point (x, y, z) in the volume of the fluid and at every instant t in time. p is proportional to the pressure and $\mathbf{F}_{ext}$ is an external force (e.g. gravity) acting on the fluid, both of which are usually employed as driving parameters to change the flow speed. The above equation is presented in a non-dimensional form, which implies that the variables $\mathbf{V}$, p and $\mathbf{F}_{ext}$ are all rescaled appropriately to have comparable magnitudes. The parameter Re, called the *Reynolds number* [1], quantifies the relative strengths of driving and dissipation:

$$Re = \frac{UL}{\nu}, \tag{1.2}$$

where U is the characteristic speed of the flow, L is its characteristic spatial dimension (like the thickness of a stream), and ν is the coefficient of (kinematic) viscosity which controls dissipation. A large Re indicates the diminishing relative strength of dissipation, modeled by the term $1/Re\, \nabla^2 \mathbf{V}$, which makes the flow more susceptible to becoming turbulent.

The Navier-Stokes is a *deterministic* partial differential equation, i.e., given an initial velocity field $\mathbf{V}(x, y, z, t = 0)$ and a set of boundary conditions for $\mathbf{V}$, one should be able to compute the spatiotemporal evolution of turbulence for all future times. However *nonlinearity*, which enters equation (1.1) through the term $\mathbf{V} \cdot \nabla \mathbf{V}$, poses serious limitations to practically accomplishing such computation. Nonlinearity restricts computing an analytical solution (simple formula) that can describe a flow

[1]Equation (1.1) describes the evolution of Newtonian-fluids, where the local viscous stress is linearly proportional to the local strain. Fluids such as water, silicone-oil, air are Newtonian under normal conditions, while ketchup, mayonnaise, etc., are non-Newtonian.

in experiments, even in the laminar or weakly turbulent regimes. Moreover, for sufficiently high Re where the viscous effects are weak it generates chaotic dynamics, which implies that two flow fields which differ only by an infinitesimal (tiny) amount at the initial time evolve in an exponentially (rapidly) diverging manner. Since one always incurs some error in measuring the exact velocity field quantifying a flow in real world situations, the governing equation can be used to predict turbulent evolution accurately for only a limited time into the future. This is the primary reason behind why weather predictions go wrong so often. The limitation on forecasting due to exponential divergence is so fundamental that numerical simulations starting from exactly the same initial velocity field, but performed on computers which differ in processors and compilers, will ultimately yield very different flow states after a long time due to rounding off errors.

The problem of computing turbulent evolution, while inherently hard due to chaotic behavior, is made even harder owing to the *high-dimensionality* of the governing equation. Typically, a reasonable description of a turbulent flow requires measuring (in experiments) or specifying (in simulations) the velocity field at 10^5 or more spatial locations on a grid. Consequently, computing the evolution governed by Navier-Stokes equation effectively transforms to simultaneously solving 10^5 coupled (ordinary differential) equations, which is computationally very expensive. Furthermore, the range of spatial scales in a turbulent flow, and consequently the number of grid points required to resolve them, scales as a power law of the Reynolds number, e.g., $Re^{9/4}$ [2]. Consequently, direct numerical simulations (DNS) of the Navier-Stokes equation become rapidly intractable as Re increases, rendering forecasting and control of turbulence using DNS practically impossible.

Historically, these limitations have forced researchers to model turbulence as a purely statistical phenomenon. The problem of studying spatiotemporal evolution

was, instead, replaced with characterizing statistical measures like mean flow profiles, velocity correlations, and energy spectra, which were largely explored using phenomenological approaches [2–6]. While the statistical studies provided a means to quantify turbulence, developing a simplified description of turbulent evolution, as well as relating the statistical picture to the governing equation (1.1), remained unaddressed by the vast majority of researchers.

The research presented in this thesis tests and extends recent ideas aimed at developing a simplified, deterministic description of turbulent evolution at moderate Reynolds numbers. The underlying methodology is to identify special unstable solutions (flow fields) of Navier-Stokes equation called "Exact Coherent Structures" (ECS)[2]*, which exist in the same parametric (Reynolds number) regime where one observes turbulence. ECS are special in the sense that, unlike turbulence, they display less complicated spatial and temporal features. However, being unstable, they are observed only fleetingly during turbulent evolution. Recent theoretical studies [7–12] have attempted to employ ECS to retrieve statistical measures of turbulent flows, which are otherwise available only from DNS performed for very long times. The research presented herein serves to complement such studies by exploring the possibility of employing ECS to build an efficient framework to forecast and even control turbulent evolution.*

1.2 Turbulence as a Dynamical System

With the statistical description of turbulence gaining widespread acceptance in the first half of 20th century, only a handful of studies had aimed to relate turbulent behavior to the stability of solutions to the governing equations [13–16]. The most popular among these studies are due Eberhard Hopf [13] and Lev Landau [14], who construed that aperiodic temporal dynamics, like those observed in turbulence, could

[2]ECS in this thesis is used to abbreviate both the singular and plural forms, exact coherent structure as well as exact coherent structures.

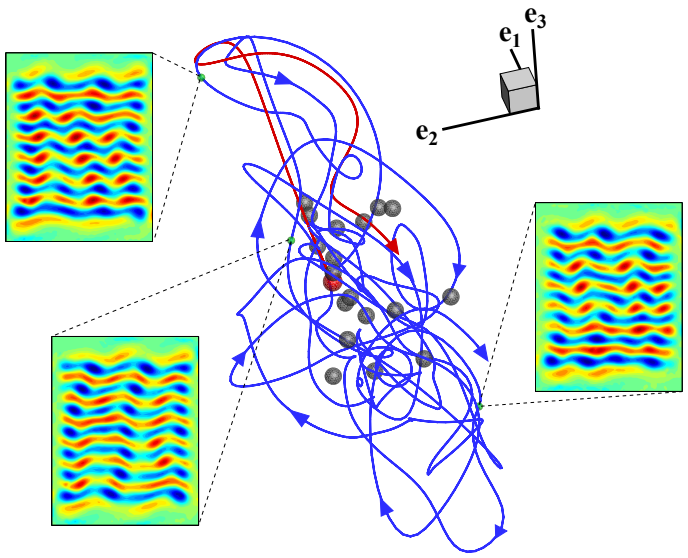

Figure 1.1: Turbulent evolution as a trajectory in a high-dimensional state-space. The flow field in the physical space is represented as a point (green sphere) in the state-space. The evolution of turbulent flow corresponds to a complicated trajectory (blue curve) in the state-space. The spheres (red and gray) indicate unstable solutions in the state space, called Exact Coherent Structures. The above is a 3D projection of the full state-space.

result from an infinite sequence of bifurcations (transitions) of flow states as Re is increased. The sequence would be characterized by the appearance of incommensurate[3] temporal frequencies leading to "quasi-periodic attractors" for the asymptotic ($t \to \infty$) dynamics. While this picture was never validated, even in later experiments, the approach in itself was a marked deviation from the existing statistical one.

Specifically, Hopf in his 1948 article titled "A Mathematical Example Displaying Features of Turbulence" [13] made several interesting conjectures on the nature of turbulent dynamics, using the state-space description of turbulence. In this picture, the flow field at an instant is represented as a point a high-dimensional state space, as depicted in Fig. 1.1. The coordinates of a point in the state space can be defined,

[3]While Hopf did not specifically mention the incommensurate part, since the frequency spectrum of turbulence is broad, it is safe to conclude that some of the frequencies that emerge are incommensurate.

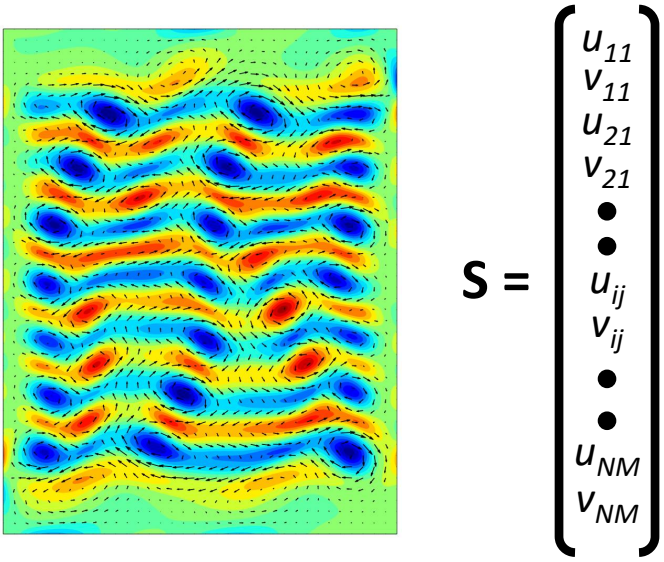

Figure 1.2: An example of constructing state space coordinates using measurements of a velocity field in physical space. In the image of a flow on the left the arrows indicate local flow velocity $\mathbf{V}_{ij} = u_{ij}\,\hat{\mathbf{x}} + v_{ij}\,\hat{\mathbf{y}}$ sampled on a grid of dimensions $N \times M$. Each grid location is identified using a pair of indices i, j.

for example, using the velocity field measured on a grid in the physical space, recast into a single vector as shown in Fig. 1.2. The evolution of the turbulent flow in the physical space corresponds to the state-space point tracing a sinuous (blue) trajectory as shown in Fig. 1.1. The asymptotic evolution of the turbulent trajectory, Hopf conjectured, takes place on a certain "inertial manifold" whose dimensionality is finite, since viscosity ensures smoothness of velocity fields and eliminates arbitrarily large velocities in the flow. Furthermore, he conjectured that the dimensionality of the manifold should increase as Re increases, capturing the increasing complexity of turbulence. The purpose of this geometrical picture, it was stated, is to compute invariant probability distributions associated with the state space flow, which will facilitate retrieving the temporal average of a quantity using a weighted state space average.

It was not until late 1960s that the deterministic description of turbulence received renewed attention, due to serendipitous discovery of "deterministic chaos" in

low-dimensional systems. Edward Lorenz, in numerical simulations of a toy-model[4] of the atmosphere with just three coupled nonlinear ordinary differential equations, found that the asymptotic dynamics can be aperiodic, much like in turbulence[5]. This discovery sparked widespread interest in chaotic dynamics of mechanical (see [17, 18] for several examples), electronic [19], chemical [20, 21], as well as biological [22] systems. Around the same time as chaos theory was being developed, using ideas from the theory of ordinary differential equations that describe low-dimensional dynamical systems [23, 24], Ruelle and Takens in their 1971 article "On the Nature of Turbulence" [25] argued, much like Hopf, that the asymptotic dynamics of turbulence occur on a "strange attractor" of finite dimensionality. An attractor can be described as the region of state space over which the asymptotic dynamics are confined to for a specific set of initial conditions and parameter values. Chaotic attractors are called strange to describe their complicated fractal structure, which results from exponential divergence of nearby trajectories (stretching) and subsequent coalescence (folding)[6] (cf. Fig. 1.1). Furthermore, Ruelle and Takens suggested that turbulence can result from a finite sequence of bifurcations [25, 26] (e.g., steady $\rightarrow$ periodic $\rightarrow$ aperiodic $\rightarrow$ turbulence), as opposed to the infinite one proposed by Hopf and Landau.

The Ruelle-Takens view of turbulence, unlike the Landau-Hopf view, found immediate experimental validation in experiments by Swinney and Gollub [27], who identified a sharp transition to aperiodic behavior in experimental studies of Taylor-Couette flow – fluid confined between two independently rotating coaxial cylinders.

[4]The Lorenz system was, in fact, derived using a three-mode Gelarkin truncation of the Navier-Stokes and heat equations, which together describe convection in a thin layer of fluid heated from below and cooled from above.

[5]The Lorenz equations are $\dot{x}_1 = \sigma(x_2 - x_1)$, $\dot{x}_2 = x_1(r - x_3) - x_2$, $\dot{x}_3 = x_1 x_2 - b x_3$, where the triad $\mathbf{s} = [x_1(t), x_2(t), x_3(t)]$ is the state-space coordinate of the system at an instant. The evolution of the chaotic trajectory can similarly be visualized in state-space, as in Fig. 1.1.

[6]The usual analogy is the kneading of pizza dough. Two points on the dough are often separated apart when the dough is stretched. Then, when the dough is folded back, they end up at places different from where they originated, but also with a new separation between them. At any given instant during the kneading process, the dough occupies a finite size, but with a very complex multi-layered structure.

A similar sharp transition was also observed in Rayleigh-Bénard convection experiments by Ahlers and co-workers [28], in which a thin layer of fluid confined between two parallel surfaces was heated from below and cooled from above. Experimental validation of the relatively small dimensionality of the strange attractor over which the asymptotic dynamics take place was provided by Brandstäter *et al.* [29], once again in Taylor-Couette experiments. In all the above studies, however, the exact state of the system (cf. Fig. 1.2) was not measured; either velocity time series at a single location in the flow or energy input into the system were used to quantify temporal dynamics, consequently not relating spatial features with temporal dynamics[7] [30].

The general consensus at the end of the 1980s, after two decades of experimental and numerical studies of fluid flows, is the following [30]: turbulence in general can be considered to have a finite dimensionality (which can be large depending on Re). For systems in spatially confined geometries like Taylor-Couette and Rayleigh-Bènard convection experiments, it was relatively straightforward to estimate the dimensionality of the attractor since single point or variable measurements were representative of the dynamics of the entire system. However, for systems with larger spatial extent or driven far from equilibrium (moderate or high Re), spatial scales over which dynamics stay correlated become small, and it was found that the techniques to quantify the dynamics were lacking [30–34]. Even with the hypothesis of finite dimensionality, the choice of a finite set of basis functions that would capture the features of turbulence – its evolution as well as its statistics – on the inertial manifold with reasonable accuracy was not known [35]. The limitations of experimental techniques in quantitatively measuring flow fields, and lack of computational resources to perform DNS of the governing equations were additional limiting factors in quantifying turbulence

[7] A short, but clear, summary of the problem of characterizing chaotic dynamics in large systems is provided in the book "Dynamical Systems Approach To Turbulence".

using ideas from low-dimensional deterministic chaos. A lucid account of chaos, its relation to fluid turbulence, and limitations in connecting the two phenomena (as perceived by the end of 1980s) can be found in articles by Narasimha [36] and Gollub [37].

1.3 Order in Chaos and Turbulence

While turbulence and low-dimensional chaos are complicated, there exists an enormous volume of research that shows the presence of underlying order in both. Consider a dynamical system whose evolution is represented as

$$\dot{\mathbf{s}} = \mathbf{E}(\mathbf{s}), \tag{1.3}$$

where $\mathbf{s} = [s_1, s_2, \cdots, s_N]$ is the state of the system and $\mathbf{E}$ is the set of rules which govern the evolution of each component s_k of $\mathbf{s}$, i.e.,

$$\dot{s}_k = E_k(\mathbf{s}). \tag{1.4}$$

For a turbulent flow E_k can be the discretized version of Navier-Stokes equation that governs evolution of the velocity components u_{ij} or v_{ij} at each grid location, which is denoted using an index k for brevity. Order, in the present context, implies that there exist certain "special" initial conditions in the state space (indicated by spheres in Fig. 1.1) leading to asymptotic dynamics that are nonchaotic. For example, there are fixed points in the state space which correspond to initial conditions that do not evolve[8], i.e., $\dot{\mathbf{s}} = 0$, or periodic orbits which result in the state of the system recurring exactly after a finite time T, i.e., $\mathbf{s}(t+T) = \mathbf{s}(t)$ for any t. Furthermore, there can be homoclinic and heteroclinic connections, which are trajectories that originate in the neighborhoods of these nonchaotic solutions and asymptotically approach the same or a different nonchaotic solution, respectively. These types of solutions, demonstrate

[8]For example, the Lorenz system has fixed points $(0,0,0)$ and $(\pm\sqrt{b(r-1)}, \pm\sqrt{b(r-1)}, r-1)$ for $r > 1$. Even when the dynamics are chaotic, starting at this fixed-point will result in no change in the system.

a certain degree of order present in the system. However, being unstable, these states are not realized in experiments or numerical simulations starting from arbitrary initial conditions, since infinitesimal amount of (random) noise will grown in amplitude eventually leading to chaotic evolution of the system. For example, while the inverted position of a static double pendulum is an unstable equilibrium, a tiny push quickly leads to chaotic dynamics (if one ignores dissipation) [38].

The presence of nonchaotic solutions embedded in the regions of state-space visited by chaotic or turbulent trajectories has important applications, both from dynamical and statistical standpoints. These solutions are hyperbolic, i.e., their state-space neighborhoods have a saddle-like structure. The trajectories in their vicinity are attracted towards the solution along a combination of contracting directions which constitute the stable manifold, and depart the neighborhood following a combination of repelling directions which constitute the unstable manifold. Hence, computing the stable and unstable manifolds in state space should facilitate forecasting evolution in the neighborhoods of these solutions. Furthermore, the dynamically important solutions are expected to be the least unstable or least repelling ones, suggesting that the chaotic/turbulent trajectories spend a greater part of their evolution in the neighborhoods of these solutions. Consequently, nonchaotic solutions should facilitate retrieving statistical measures, which are otherwise available only from time-integration of the governing equations or long time observations.

In low-dimensional systems, the statistical as well as dynamical importance of nonchaotic solutions has been explored, rather extensively. It was shown [24, 39–41] that the chaotic attractor is dense in periodic orbits, i.e., for any given point $\mathbf{s}$ on the attractor one can, for any $\epsilon > 0$, identify a point $\tilde{\mathbf{s}}$ in the neighborhood of $\mathbf{s}$ which lies on a periodic orbit, where $\|\tilde{\mathbf{s}} - \mathbf{s}\| \leq \epsilon$. Consequently, temporal averages of observables can be retrieved as weighted averages (cycle expansion) of the observables computed using unstable periodic orbits [39, 41–46]. This result is very

much along the lines of what Hopf had envisaged for the problem of turbulence. From a dynamical standpoint, unstable solutions were shown to be crucial in controlling chaos, as was proposed by Ott *et al.* (OGY method) [47]. By iteratively perturbing[9] a chaotic trajectory to fall into the stable manifold of a nearby equilibrium or a periodic solution, one can dramatically change the nature of the asymptotic dynamics from being chaotic to nonchaotic. Since tiny perturbations can lead to large changes in the trajectory, these solutions play pivotal role in developing efficient ways to control chaotic dynamics. Controlling chaos using unstable periodic orbits has been successfully implemented in mechanical systems [48], lasers [49, 50], cardiac dynamics [51], as well as chemical reactions [52].

1.3.1 Exact Coherent Structures

Unlike in low-dimensional systems, understanding the role of unstable nonchaotic solutions of Navier-Stokes equation in turbulence, which are now referred[10] to as Exact Coherent Structures, is still in its adolescence. The lack of computational power and root finding algorithms for high-dimensional systems has severely impeded progress on this front [9, 53–55]. The identification of ECS in fluid turbulence has its roots in the observation of "coherent structures" in turbulence, flow features like vortices which remain relatively steady and easily discernible as in the wake of the flow past a cylinder [56–58]. Furthermore, the presence of well-organized structures, in turbulent boundary layers have been identified in experiments dating back to 1960s [59–61]. However, only recently, such coherent structures have been found to play a crucial role in the sustaining of near-wall turbulence in shear flows such as plane-Couette[11] and pipe flows [62–64].

[9] In his article, Prof. Ott suggests the perturbation of a "parameter" rather than the state of the system.

[10] They are also often referred to as recurrent flows or invariant solutions.

[11] Flow of a fluid between two solid parallel planar surfaces with normal along $\hat{\mathbf{z}}$, and moving in opposite directions along $\hat{\mathbf{x}}$

For instance, the studies of coherent structures in near-wall turbulence ultimately lead to the discovery that these structures were related to traveling-wave solutions of the Navier-Stokes equation [64–68]. Traveling-waves are (exact) equilibrium solutions of the governing equation in a co-moving frame, to account for advection of the structures of interest by the flow, as in the case of flow in pipes and channels. The subsequent major breakthrough[12] concerning the role of nonchaotic solutions was due Kawahara *et al.* [7], who computed two periodic solutions from turbulent DNS data of plane-Couette flow[13], and showed that the turbulent trajectory wanders around one of the orbits for an extended duration. Statistical measures like mean flow profile, mean energy input and dissipation of the turbulent flow were found to be in good agreement with those computed using just this single periodic solution. Following this computation, the existence and relevance of unstable periodic orbits in turbulent dynamics has received further validation through several studies of 3D shear flows[14] [8–12]. However, unlike in low dimensional chaos where the attractor is dense in periodic orbits, it is not known *a priori* in turbulence if all the dynamically relevant periodic orbits have been computed. Consequently, systematic procedures to retrieve turbulent statistics from the available unstable solutions have begun only very recently [72, 73].

These recent developments in identifying and understanding the role of nonchaotic solutions has renewed the hope of applying ideas from low dimensional chaos theory to develop a tractable description of turbulence. Since a turbulent trajectory in the

[12]Early studies of nonchaotic solutions (periodic orbits) in spatially extended (≈100 degrees of freedom) systems were due Christiansen *et al.* [69] and Zoldi *et al.* [70], who studied Kuramoto-Shivashinski[71] equation and identified several unstable periodic orbits. Applying averaging procedures from periodic orbit theory of low-dimensional systems, it was found that global averages characterizing chaotic dynamics as well as the fractal dimensionality of the attractor were retrieved using only a few unstable solutions.

[13]It appears all previous computations of TW solutions were performed by continuing solutions across Re, and other simulation parameters like domain sizes.

[14]Besides computing periodic orbits, this article contains visually beautiful state space representations of turbulent trajectories visiting neighborhoods of ECS.

vicinity of an ECS mimics both its spatial and temporal features, it is reasonable to expect that ECS may constitute a finite set of building blocks, using which the turbulence on the finite dimensional inertial manifold can be described.

1.4 Motivation for the Present Study

Practical applications, as well as numerical convenience, have motivated the vast majority of researchers to study ECS in numerical simulations of three-dimensional (3D) shear flows in simple geometries, such as pipe flow, plane-Couette flow, and channel flow. Numerical simulations of such open flows are often performed on small computational domains – the largest dimension of the domain being only a few spatial correlation lengths – and assuming periodic boundary conditions[15]. Such idealized boundary conditions pose serious challenges in comparing numerical results with experiments. Consequently, there have been only four studies [74–77] prior to the work in this dissertation [78] which have aimed to find evidence of ECS in experiments. Spatial structures reminiscent of traveling wave solutions were detected in pipe flow (Hof *et al.* and Dennis *et al.*) and channel flow experiments (Lemoult *et al.*), while that similar to an edge-state was detected in pipe flow experiments (de Lozar *et al.*). While demonstrating their existence is a significant step forward, the dynamical role of these solutions in the evolution of turbulence experiments was not explored; the solutions were identified by comparing experimental flow fields with previously computed ECS from numerical studies[16].

The scarce evidence for the role of ECS also stems in part from experimental limitations posed by open flows. For example, in both pipe and channel flow experiments, imaging has been performed within a two-dimensional (2D) slice transverse to the direction of flow (e.g., if a pipe is along x direction, the imaging plane is yz). 3D

[15]Periodicity of a domain implies the velocity field, say in a pipe, on the left end is identical to the one on the right end.

[16]The identification of the edge-state is a deviation from this, in some sense, since techniques of relaminarization were employed to realize the state in experiments.

velocity components of fluid within the 2D slice are then computed using either particle tracking or particle image velocimetry (which will be discussed in section (2.1.1)). The limitations from such imaging setups[17] is that the structures of interest advect past them, rather quickly, and invoking Taylor's frozen hypothesis [79] is necessary to construct 3D velocity fields from 2D measurements. This severely limits the scope of simultaneously studying the spatial and temporal evolution of velocity fields. This implies that neither the dynamical role of ECS nor their utility in retrieving turbulent statistics can be tested satisfactorily in open flows, at least with existing technical capabilities.

To circumvent these limitations, the research presented herein employs a *shallow* layer of electrolyte in a flat bottomed container, as shown in Fig. 1.3, to generate turbulence at moderate Re. The fluid is driven using an electromagnetic body force whose direction is horizontal. For sufficiently shallow layers of electrolytes, it was shown [80–82] that the resulting velocity field is *nearly* horizontal in the entire volume of fluid. However, its magnitude varies along the layer depth which makes the flow "quasi-two-dimensional" (Q2D), i.e., a plane-parallel velocity field that varies along all three spatial coordinates. In a Q2D flow, the 2D velocity field at the electrolyte-air interface provides quantitative measure of both spatial and temporal dynamics of the flow. Unlike in 3D open flow experiments which were previously employed for studies of ECS, the Q2D flow is bounded by solid walls in both the horizontal directions, resulting in well-defined zero-velocity boundary conditions which is convenient when modeling the flow theoretically. Additionally, the evolution of horizontal flow can be measured *quantitatively* over the entire lateral expanse of the experimental domain for arbitrarily long durations, which is extremely advantageous in studying the dynamical role of ECS.

[17]Imaging and computing three components in a 3D volume of fluid is computationally very demanding, even with the technologically advanced Tomographic PIV setups. The restriction in such cases is the duration of data that can be recorded.

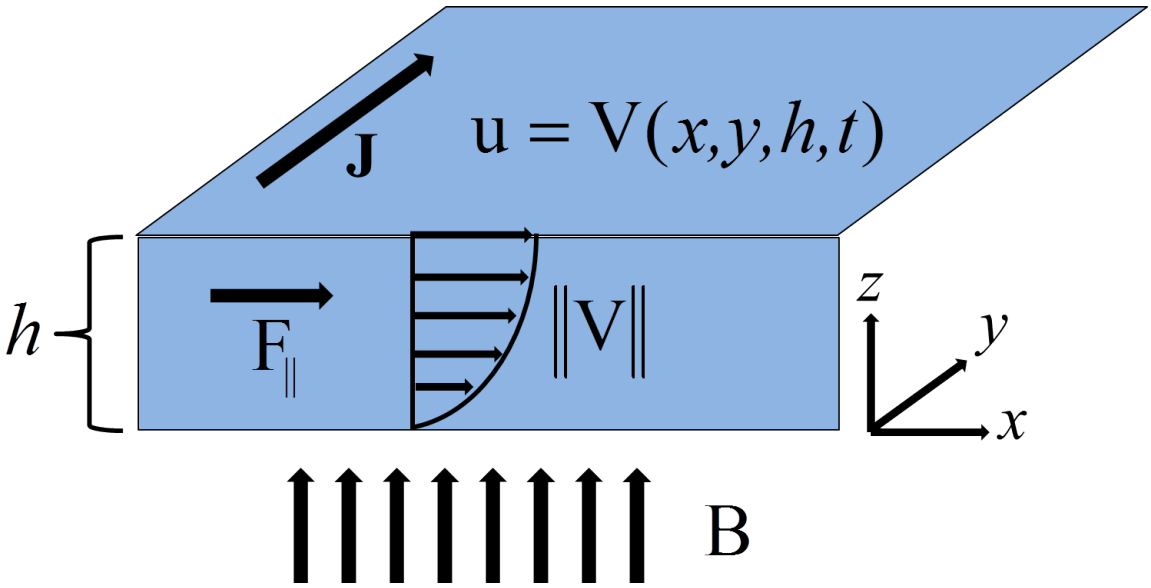

Figure 1.3: A figure illustrating a nearly 2D flow generated in a shallow electrolyte layer of depth h. $\mathbf{B}$ represents a magnetic field whose direction ($\hat{\mathbf{z}}$) is perpendicular to the xy plane, defined by the lateral expanse of the fluid layer. The direction of current density, for convenience of visualization, is chosen to align with $\hat{\mathbf{y}}$. The resulting Lorentz force $\mathbf{F}_{\parallel}$ is along $\hat{\mathbf{x}}$. The gradient in the magnitude of the horizontal velocity is indicated by the parabola-like curve with arrows of decreasing length.

Numerical simulations of the flow can in principle be performed by discretizing the full 3D Navier-Stokes equation (cf. equation (1.1)) on a 3D grid, which however is notoriously time-consuming. However, Q2D flows have been previously modeled using empirically derived strictly 2D equations [80, 83], which *approximate* the evolution of the flow measured at the electrolyte-air interface in the experiment. Numerical simulation of such 2D equations is computationally significantly less expensive compared to their 3D counterparts, which motivates modeling the flow in the experiment using a strictly 2D equation in the present study.

In the context of ECS in 2D domains, the work of Kerswell and co-workers on strictly 2D "Kolmogorov-flow" is worth mentioning [72, 84]. Chandler *et al.* have identified several tens of ECS, both equilibrium and periodic solutions, in numerical simulations of a sinusoidally forced fluid layer confined to a plane. The evolution of the flow is described using the 2D Navier-Stokes equation and numerical simulations

were performed on a domain periodic in both spatial directions. Despite being one of the most complete studies on ECS to date [85], the results from Chandler *et al.* [72] are not directly applicable to experiments, since the Q2D flow in experiment cannot be described by the 2D Navier-Stokes equation. The interaction of the fluid layer with a solid bottom of the container introduces a gradient in the magnitude of the horizontal velocity along the layer depth (cf. Fig. 1.3), whose effects should be systematically included into the 2D governing equation.

The goal of the study presented here is to understand the dynamical role of ECS in experiments as well as numerical simulations. The focus lies, almost exclusively, on exploring the state-space geometry shaped by ECS, their unstable manifolds, and the dynamical connections between ECS. Using such nonchaotic solutions in state space, the feasibility of developing a low-dimensional, tractable description of turbulent evolution is tested. Since ECS are observed only fleetingly in experiments, developing a theoretical model that accurately describes the evolution of the flow is fundamental to accomplishing this goal. However, since no previous study demonstrated quantitative agreement between a 2D model and a Q2D flow, a portion of this thesis focuses on deriving and validating such a model.

1.5 Quasi-Two-Dimensional Flows in Shallow Electrolyte Layers

Fluid flows in two spatial dimensions have been the subject of substantial research efforts in recent decades. For the greater part of the twentieth century, it was generally considered that two-dimensional (2D) flows are merely a theoretical idealization with limited practical relevance. This conception has changed drastically since the 1980s, when experiments in thin fluid layers [80], soap films [86], and liquid metals [87] demonstrated that nearly 2D flows can indeed be realized in the laboratory. Today, experimental approximations of 2D flows are widely employed as models of atmospheric and oceanic flows [88, 89]. For example, the formation of the red spot of

Jupiter was explored and explained using a laboratory approximation of 2D flows in liquid metals [90]. Being theoretically and experimentally more amenable than their 3D counterparts, 2D flows have also served as platforms for studying new phenomena such as turbulent cascades [91], coherent structures [90], and mixing [92].

Laboratory approximations use various techniques to create a flow that is nearly two-dimensional, in which the velocity along one of the spatial directions is strongly suppressed, say along $\hat{\mathbf{z}}$, i.e.,

$$\begin{aligned} \mathbf{V}(x,y,z,t) &= V_x(x,y,z,t)\,\hat{\mathbf{x}} + V_y(x,y,z,t)\,\hat{\mathbf{y}} + \underbrace{V_z(x,y,z,t)}_{\approx 0}\,\hat{\mathbf{z}} \qquad (1.5) \\ &\approx V_x(x,y,z,t)\,\hat{\mathbf{x}} + V_y(x,y,z,t)\,\hat{\mathbf{y}}. \qquad (1.6) \end{aligned}$$

Here V_x, V_y, V_z are the velocity components along the spatial directions x, y, z, respectively. To accomplish such suppression experiments often employ rotation, a strong magnetic field, geometric confinement, (density) stratification, immiscibility, or a combination of these, depending on the problem of study. The range of Re achievable, the feasibility of obtaining quantitative velocity field measurements, as well as the mechanism that suppresses the velocity component in each of these techniques is different. The experiments discussed in this thesis employ only geometric confinement and immiscibility to create a Q2D flow.

The first experimental realization of flow in a shallow electrolyte layer, as an approximation of a strictly 2D flow, was due Bondarenko *et al.* in 1979 [80]. The intended problem of study was a strictly 2D shear flow driven by a sinusoidal forcing, originally proposed by Andrey Kolmogorov as a mathematical problem of hydrodynamic stability. The evolution of the strictly 2D flow is governed by the Navier-Stokes equation[18]

$$\partial_t \mathbf{u} + \mathbf{u}\cdot\nabla\mathbf{u} = -\frac{1}{\rho}\nabla p + \nu\nabla^2\mathbf{u} + \mathbf{f}. \qquad (1.7)$$

[18]The form of the equation shown here is dimensional, which is different from the nondimensional 3D form discussed earlier. The dimensional form is employed extensively in this thesis, since it explicitly displays fluid properties.

Here, $\mathbf{u}$ is a 2D[19] incompressible ($\nabla \cdot \mathbf{u} = 0$) velocity field of the fluid confined to the xy plane, p is the 2D pressure, and $\mathbf{f}$ is the 2D body force. For the Kolmogorov problem $\mathbf{f}$ varies sinusoidally in y, i.e., $\mathbf{f} = \chi \sin(\kappa y)\,\hat{\mathbf{x}}$, where χ and κ are the amplitude and wavenumber of forcing which is directed in the $\pm\hat{\mathbf{x}}$ directions. The parameters ν and ρ are the kinematic viscosity and density, respectively, of the 2D fluid.

Bondarenko's experimental setup used a homogeneous layer of electrolyte (0.5M aqueous copper sulfate solution) with depth h ($\approx$ 3mm) in a flat bottomed container, placed over an array of permanent magnets, as shown in Fig. 1.3. The direction of the magnetic field due to the array is nearly perpendicular (along z) to the lateral expanse of the fluid layer (xy plane) with a sinusoid like profile along y, i.e., $\mathbf{B} \approx B_z(x, y, z)\ \hat{\mathbf{z}} \sim e^{-\kappa z}\sin(\kappa y)\,\hat{\mathbf{z}}$. When a direct current $\mathbf{J} = J_y\,\hat{\mathbf{y}}$ is passed through the electrolyte layer, its interaction with the magnetic field generates a *horizontal* Lorentz force, $\mathbf{F}_{\parallel} = \mathbf{J} \times \mathbf{B} \approx J_y B_z\,\hat{\mathbf{x}}$, which drives the electrolyte layer. The rationale behind the setup was that, for a sufficiently thin fluid layer *geometric confinement* suppresses the vertical component of velocity V_z, resulting in a flow that is nearly horizontal too. The expectation was that the evolution of the velocity field at the free surface ($z = h$), $\mathbf{u}(x, y, t) = \mathbf{V}(x, y, h, t)$, can be described using the 2D Navier-Stokes equation (1.7).

Theoretical results using equation (1.7), however, showed significant disagreement in predicting the response and stability of the nearly sinusoidal shear flow realized in experiments [80] with $\mathbf{F}_{\parallel} \sim e^{-\kappa z}\sin(\kappa y)\,\hat{\mathbf{x}}$. Bondarenko *et al.* [80] traced the disagreement to the inherent three-dimensionality of the flow in the experiment. The presence of a solid boundary at the bottom of the fluid layer results in a no-slip boundary condition on the velocity, i.e., $\mathbf{V} = 0$ at $z = 0$. This creates a gradient in the magnitude of velocity along the fluid layer depth, shown in Fig. 1.3, resulting

[19]For ease of distinguishing, lower and upper case bold characters are used to indicate fields in 2D and 3D, respectively.

in additional dissipation not accounted for in the 2D Navier-Stokes equation. Bondarenko *et al.* assumed that the effect of this bottom friction was linear deceleration of the horizontal velocity and proposed the following 2D equation to describe the evolution of free surface of the flow in experiments [80].

$$\partial_t \mathbf{u} + \mathbf{u} \cdot \nabla \mathbf{u} = -\frac{1}{\rho}\nabla p + \nu \nabla^2 \mathbf{u} - \alpha \mathbf{u} + \frac{1}{\rho}\langle \mathbf{F}_{\parallel} \rangle_z, \tag{1.8}$$

where α is the friction coefficient, commonly termed "Rayleigh" friction coefficient. $\langle \mathbf{F}_{\parallel} \rangle_z$ is the net 2D electromagnetic force computed by integrating the 3D plane-parallel force over the confined direction z. The friction coefficient was estimated to scale as $\alpha = \eta\, 2\nu/h^2$, where η was a fitting parameter to match experimental observations with theoretical predictions.

Since the 1980s, theoretical studies have employed equation (1.8) to compared results from experiments of nearly 2D flows generated in homogeneous electrolyte layers. Several studies exploring the effects of varying the form and strength of forcing, as well the geometry of the setup, were carried out in the context of understanding transition to turbulence [83, 93–98]. Moreover, nearly 2D flows using the single layer setup were also used in studies aimed at validating statistical descriptions of 2D turbulence [91, 99, 100].

Flows in shallow electrolyte layers, have, for a long time have been realized in homogeneous electrolyte layers driven by (near) plane-parallel forcing. The vertical velocity (V_z) in such systems, as discussed earlier, is never identically zero. Hence, to further suppress the vertical motion, Marteau *et al.* [101] suggested[20] a modification to the single layer setup which uses two layers of electrolyte (salt water) with different densities, in the context of studying decaying turbulence. The rationale behind using two fluid layers is that the lighter top layer — which is used for all the measurements — is shielded from the no-slip boundary condition at the bottom by a

[20]Specific motivation was not provided in the article, but Paret *et al.* mention that density stratification is the motivation to use this setup.

heavier lubricating layer. It was reasoned that *stratification* should suppress vertical motion, enhancing the two-dimensionality of the flow in the top layer. A variation of this two-miscible layer setup with the electrolyte in the top layer substituted with pure water was also used to realize nearly 2D flows [102, 103]. The stratification in the two-miscible layer setup, however, *may* deteriorate during the course of the experiment due to diffusive as well as advective mixing between the two layers[21]. This limitation was overcome by Rivera *et al.* [104] using two layers of immiscible fluids, the bottom being a heavy fluorocarbon-based fluid and the top being an aqueous electrolyte, in the context of studying pair dispersion statistics in 2D turbulence. In such a setup *immiscibility* rules out vertical mixing, thus improving the two-dimensionality in the top layer. While a systematic, quantitative comparison of vertical motion in the three (single, two-miscible, and two-immiscible layer) setups is yet to be performed, numerical [82] and experimental [105] studies of decaying vortices suggest that two-immiscible layer setup, indeed, fares better in suppressing vertical motion. Consequently, the quasi-two-dimensional flow studied in this thesis is realized in the two-immiscible layer setup proposed by Rivera *et al.* [104].

These refinements to experimental setups, however, were not accompanied by updates to the 2D model (1.8), which for stratified layers should account for the inhomogeneity of fluid properties in the confined direction z. Theoretical studies employing equation (1.8) have, instead, computed ν, α, and ρ from dimensional and geometrical considerations [81, 89, 106]. Specifically, estimates for friction coefficient α varied by a factor of 2 across studies employing nearly identical stratified layer setups [82, 102]. To address such limitations of previous 2D models of Q2D flows, a systematic study of the inherent three-dimensionality of the flow in experiments and

[21] Quantitative estimates of this from literature are unavailable regarding which effect dominates at low driving. Kelley's 2011 article [103] does not mention if fluid properties change during the course of the experiment, despite reporting Ekman pumping in time independent vortex patterns. In personal communication, Kelley reported that Ekman pumping could be the dominant mechanism leading to the mixing of the two layers.

the derivation of a 2D model to quantitatively study Q2D flows is included in this thesis.

1.6 Thesis Outline

The outline of this thesis is as follows: Chapter 2 includes details of the experimental setup. Additionally, a combined analytical and experimental study of the inherent three-dimensionality of a Q2D flow is presented. In chapter 3 the derivation of a 2D model that is expected to capture the evolution of Q2D flow in the experiment accurately is provided. Also, a detailed discussion of the numerical discretization of the 2D equation is provided. To study the effects of confinement three different numerical domains, two periodic and one with lateral dimensions and boundary conditions identical to those in experiment, are discussed. Chapter 4 includes validation of the 2D model by comparing the flow fields as well as the bifurcation sequence in experiment with the numerical simulations as the strength of the forcing is increased. Following this validation, the role of ECS in the turbulent regime, in both simulations and experiments, is discussed in chapter 5. The geometry of state space shaped by the ECS, and the feasibility of developing simplified models of evolution in their vicinity is explored. Finally, in chapter 6 a summary of scientific contributions accomplished through this study is presented, along with a discussion of possible limitations and future directions.

CHAPTER II

VELOCITY PROFILE IN A Q2D KOLMOGOROV FLOW

This chapter presents a detailed description of the experimental setup used to generate a nearly 2D flow in a shallow electrolyte layer (section (2.1)). Also included is a brief description of particle image velocimetry, the imaging technique employed to obtain quantitative measurements of velocity fields. The quasi-two-dimensional approximation of the flow in the experiments is then introduced, and its validity is tested using experimental measurements (section (2.2)). Following this, the variation in the magnitude of the horizontal velocity along the fluid layer depth is analytically computed and compared against experimental velocity measurements (section (2.3)). Finally, the inherent three-dimensionality of the flow in a two-immiscible-layer setup is discussed, and the procedure to create a nearly-perfect 2D flow in experiment is presented (section (2.4)).

2.1 Experimental Setup: Kolmogorov-Like Flow

The experimental setup[1] to generate a sinusoidal shear flow consists of an array of 14 NdFeB magnets[2] (Grade N42), each 15.24 cm long and 1.27 cm wide, with a thickness of 0.32 ± 0.01 cm, shown in Fig. 2.1. The magnets are positioned side-by-side with adjacent magnets aligned along their longest dimensions[3] to form a 15.24

[1]Over the years, the experimental setup has undergone several changes, most of which were aimed at improving control and reproducibility of results. While it may be useful to list all the changes, it would prove too much of a digression to provide the motivation behind each. The setup presented here is chosen to be the one relevant to a vast majority of data presented in this thesis. Henceforth, where applicable and necessary, a footnote is added to indicate details of the setup used to obtain the specific data set.

[2]The magnets were purchased from K&J Magnetics, Inc.

[3]The dimensions are specified in SI units here. However, the commercial specification of magnet dimensions are in inches 6"×0.5"×0.125". The dimensions of the setup are 7"×9".

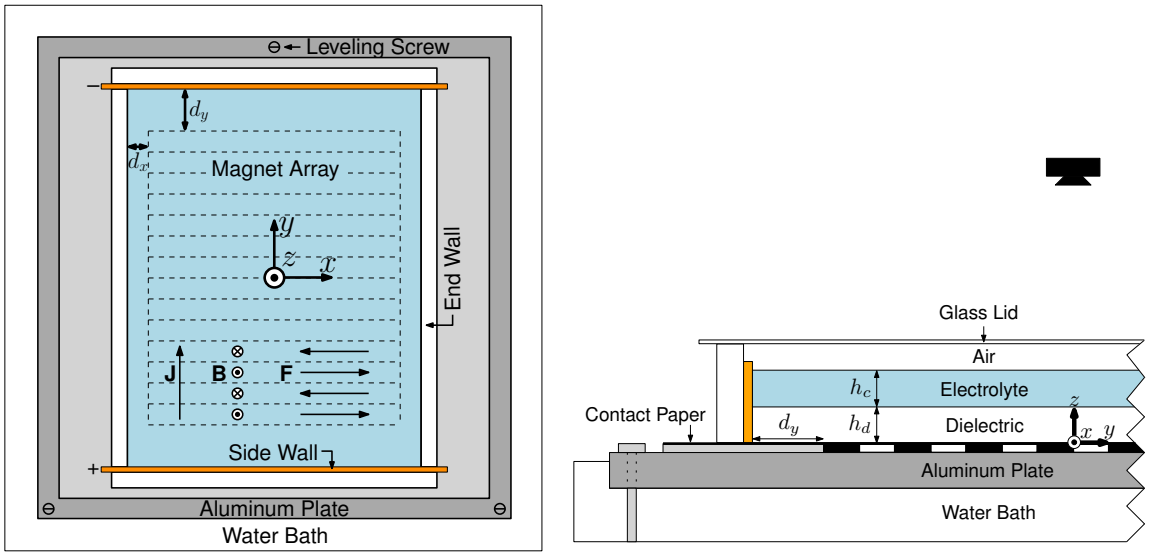

Figure 2.1: A schematic diagram of the two-immiscible-layer experimental setup for generating Kolmogorov-like flow viewed (a) from above and (b) from the side. The vectors **J**, **B**, and **F** denote, respectively, the directions of the electric current density, magnetic field, and the resulting Lorentz force. The flow is bounded in the longitudinal direction using two acrylic end walls, and in the transverse direction using two side walls (electrodes). The bottom of the dielectric rests on a solid surface, while the top surface is the free electrolyte-air interface. This container is mounted on an aluminum plate which is leveled and submerged in a water bath that is temperature-regulated such that the electrolyte is maintained at 23.0 ± 0.2°C.

cm × (14 × 1.27 cm) × 0.32 cm array such that the adjacent magnets have fields pointing in opposite directions, normal to the plane of the array. This configurations of the magnets is mechanically stable, and each magnet stays attached (naturally) to the adjacent ones.

This magnet array is placed on a flat aluminum plate of dimensions 30.5 cm × 30.5 cm × 1.0 cm, and rectangular pieces of aluminum with the same thickness as the magnets (0.32 ± 0.02 cm) are placed beside the magnet array to create a level surface. A thin layer of black, adhesive contact paper[4] (with approximate thickness 0.005 cm)

[4]Contact paper is often manufactured with a bumpy surface to improve grip. The specific one chosen here, however, is smooth with a non-reflecting finish. Sticking the contact paper on to the magnets requires a little care and patience. Dust particles and lint often stick to the adhesive side of the contact paper, once the protecting paper is peeled off. This traps air between magnets and the contact paper, which may create an uneven surface, which should be avoided.

is placed on top of the magnets to serve as a dark background for imaging. The surface of the contact paper serves as the bottom boundary for the fluids. The origin of the coordinate system is placed at this height and the lateral center of the magnet array, with the x-coordinate aligned with the magnets' longest side, the y-coordinate pointing in the direction of the magnet array periodicity, and the z-coordinate in the vertical direction. A schematic diagram is shown in Fig. 2.1.

Rectangular bars of acrylic are affixed directly onto the contact paper to create the lateral boundaries of the container that holds the fluids. Parallel to the y-direction, two bars are placed at a distance of $L_y = 17.8$ cm apart, centered about the origin[5]. These solid boundaries for the fluid are henceforth referred to as the "end walls." Similarly, running parallel to the x-direction, two electrodes mounted on rectangular bars of acrylic are placed at a distance $L_x = 22.9$ cm apart, symmetrically relative to the origin. These boundaries are henceforth referred to as the "side walls" and are used to drive the current through the electrolyte. The placement of the end walls and side walls leaves a buffer region of $d_x = 1.3$ cm and $d_y = 2.5$ cm, respectively, between the edge of the magnet array and these solid boundaries. The aluminum plate upon which the magnets are mounted is supported by three screws, which are adjusted to level the system.

The region $0 < z < h_d$ is filled with perfluorooctane[6] (PFO), a dielectric fluid of viscosity $\mu_d = 1.30$ mPa·s and density $\rho_d = 1769$ kg/m^3. The volume of the dielectric fluid (V_d) required to obtain the desired layer thickness h_d is computed from the

[5]Once the contact paper is glued down, the true location of the origin – the longitudinal center of the intersection of the middle two magnets – is no longer visible. The method followed by Jeff Tithof is ensuring the padding aluminum is machined, so that each padding bar is a rectangle cut to the desired dimensions. The outer edges and corners of the aluminum padding then serve as reference points when gluing the acrylic bars. Alternatively, when precise machining is not available (like during the hands-on workshop), one can make (extended) reference markings on the padding using pencil/scribe, *before* the contact paper is glued, to use as references.

[6]Recycled perfluorooctane was purchased from TMC Industries, Inc. Since its industrial use is waning, it has become increasingly difficult to find recycled PFO for purchase in large quantities. Alternatives to PFO with similar fluid properties, like FC-3283, Galden HT-110, HT-135, and Novec HFE-7100, HFE 7200 may be used as lubricants.

geometry of the setup, i.e., $V_d = h_d \times L_x \times L_y$. For all experimental runs, the height of the dielectric fluid is chosen to be $h_d = 0.3 \pm 0.01$ cm. Above the dielectric fluid, a layer of an immiscible conducting fluid (electrolyte) of thickness h_c ($h_d < z < h_d + h_c$) is poured. For the runs exploring the variation in velocity along z, the thickness of the conducting layer is varied from $h_c = 0.2 \pm 0.01$ cm to $h_c = 0.4 \pm 0.01$ cm; for all other runs a layer of thickness $h_c = 0.3 \pm 0.01$ cm is used. The volume[7] of the conducting fluid (V_c), as in the case of the dielectric, is computed using $V_c = h_c \times L_x \times L_y$. For the conducting layer, one of the two fluids is used: a "low-viscosity electrolyte" consisting of a 0.3 M solution of $CuSO_4$ (with viscosity $\mu_c = 1.12$ mPa·s and density $\rho_c = 1045$ kg/m^3) or a "high-viscosity electrolyte" consisting of a 1 M solution of $CuSO_4$ with 50% glycerol by weight (with viscosity $\mu_c = 5.8 \pm 0.1$ mPa·s and density $\rho_c = 1160 \pm 15$ kg/m^3). Immiscibility and density stratification maintain the relative configuration of the two layers. A small amount of viscosity-matched surfactant (dish-soap) is added to the electrolyte to lower the surface tension, and a glass lid is placed on top of the container to limit evaporation.

When a direct current is passed through the electrolyte layer, its interaction with the spatially alternating magnetic field $\mathbf{B} \sim B_z\,\hat{\mathbf{z}}$ results in a spatially alternating Lorentz force $\mathbf{F}_{||}$, which drives the electrolyte (cf. Fig. 2.1(a)). The viscous coupling between the electrolyte and the dielectric fluid sets the latter in motion as well. The direct current is maintained constant using LM317, a three terminal positive voltage regulator via the circuit shown in Fig. 2.2. Under normal operation[8], the LM317 maintains a constant voltage difference between the "OUT" and "ADJ" terminals, i.e., $V_{\rm OUT} - V_{\rm ADJ} = V_{ref} = 1.25$ V, when an input voltage $V_{\rm IN} (\approx 15V)$ is applied to

[7]The actual volumes of dielectric and electrolyte necessary to set the system up (carefully) are nearly twice as large compared to V_c and V_d used to run the experiment. A larger initial thickness of dielectric is needed to prevent the electrolyte from touching the contact paper and also to account for evaporative losses. A larger volume of electrolyte is necessary to "close" the free surface before adding soap and seeding. The excess volumes are removed before running the experiment.

[8]For more details about LM317, refer to `http://www.ti.com/lit/ds/symlink/lm317.pdf` (page 8,9). The constant current circuit with automated control is described in [107]

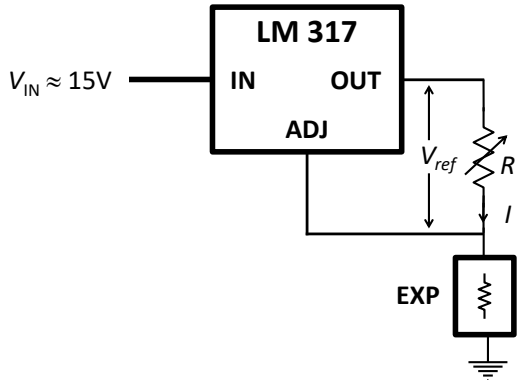

Figure 2.2: Circuit diagram for a constant current source using LM317 voltage regulator. For an input voltage between 1.25V and 30V, the voltage difference between the "OUT" and "ADJ" terminals is $V_{ref} = 1.25$ V. For a desired constant current I thought the experimental setup, the resistance R on the potentiometer should be set to $R = V_{ref}/I$.

the "IN" terminal. When a resistor R is connected across the "OUT" and "ADJ" terminals, a current $I = V_{ref}/R$ passes through it. The impedance of the "ADJ" terminal is very large such that very little current ($\approx 50\mu$A) can pass though it. Hence, when routed to ground via the experimental setup the constant current I passes though the electrolyte solution. Note that the current through the experiment is independent of the (load) resistance of the electrolyte, and hence remains fairly constant. By using a trimmer potentiometer to vary R, the desired current can be set up, which serves as the control parameter for driving. The current density in the electrolyte $J = J\,\hat{\mathbf{y}}$ can be computed using $J = I/(L_x \times h_c)$; J ranges from about 2 to 40 A/m^2 for the data presented in this thesis.

Since passing a current through a resistive conductor (the electrolyte) results in Joule heating, a calibrated thermistor is placed in the corner of the fluid domain to monitor the temperature, and the aluminum plate is immersed in a temperature-controlled water bath. The water bath is regulated such that the temperature of the electrolyte is maintained to 23.0 ± 0.2°C. By limiting the temperature fluctuations, the associated change in viscosity (3% per ∘C) of the fluids is kept to a minimum.

2.1.1 Measuring Velocity Fields

For flow visualization and measurement, hollow glass microspheres are added to the fluid which are illuminated with white light-emitting diodes,[9] placed parallel to the end-walls. Two separate methods are used to seed the flow with particles, either at the free surface or at the dielectric-electrolyte interface. For seeding at the free surface, Glass Bubbles (K15) manufactured by 3M and sieved to obtain particles with mean radius 24.5 ± 2 μm and mean density 150 kg/m^3 are used. For seeding the interface Soda Lime Solid Glass Microspheres manufactured by Cospheric with mean radius $r = 38 \pm 4$ μm and mean density $\rho = 2520$ kg/m^3 are used. The soda lime microspheres, though denser than the dielectric fluid, stay trapped between the dielectric and electrolyte layers due to interfacial tension. This method is particularly useful for experiments running continuously for extended periods of time, since particles seeded at the interface remain evenly distributed much longer. Lastly, the top surface of the electrolyte and the interface are not seeded simultaneously, but in separate experimental realizations.

The seeded flow, shown in Fig. 2.3(a), is imaged at 30 Hz with a DMK 31BU03 camera manufactured by The Imaging Source, with a 1024×768 pixel CCD sensor. The camera is positioned above the magnet array near the lateral center of the experimental domain, as shown in Fig. 2.1(b). Imaging the full lateral extent of the box yields a resolution of about 53 pixels per magnet width, i.e., about 41 pixels per centimeter length of the experimental domain. By zooming into a smaller region within the flow domain one can increase the pixel count per centimeter, however, at the expense of limiting the field of view. Flow images are recorded in the uncompressed

[9]The LEDs are placed along the end walls, outside the setup. Ideally, a high intensity of light from LEDs will help capture images at a high frame rate. However, if the LEDs are too close to the setup they heat the fluid close to the end walls quite a bit, which may affect uniformity of temperature and its control. Hence, the (approximate) particle density for seeding, frame rate, and LED brightness should be optimized simultaneously. One may measure temperature at different places in the setup to estimate the spatial variation due to LED heating.

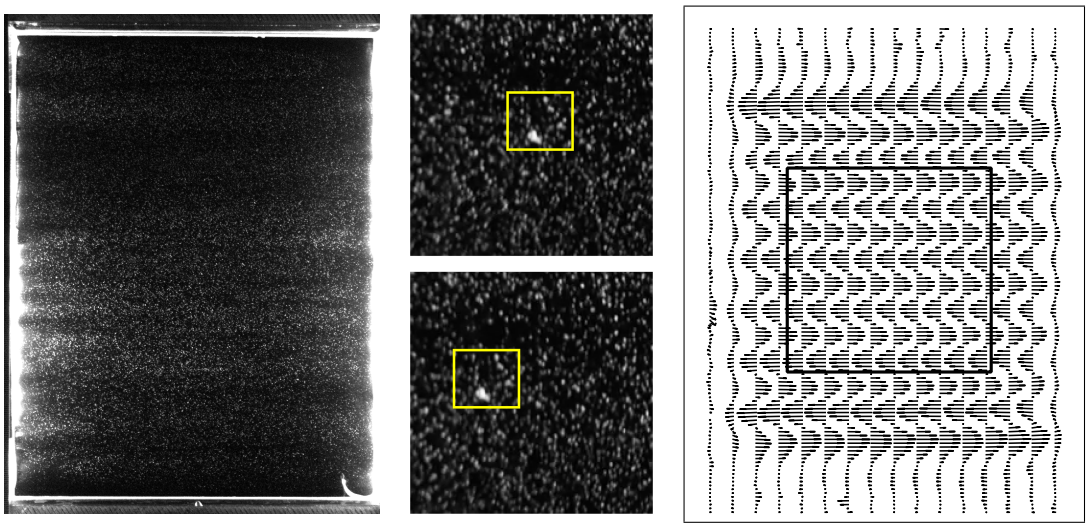

Figure 2.3: Illustration of velocity fields obtained by tracking groups of particles using particle image velocimetry. Panel (a) shows the image of tracer particles spread across the entire domain at an instant. Panel (b) shows identical regions from two images separated in time by Δt, cropped and zoomed for clarity. The yellow frame indicates the "window" whose displacement is tracked across images by matching particle patterns within it. The displacement of the center of the window in pixel units yields the local flow velocity in pixels per unit time, which can be converted to physical units using a scale factor. By applying this procedure to several small windows which uniformly sample the domain, one can obtain the spatiotemporally resolved velocity fields, like the one shown in panel (c). The actual resolution of the PIV grid used was 169×126. The velocity vectors have been scaled by a factor of 6 to highlight the spatial profile which is nearly sinusoidal along y. The box in the center indicates the region over which the root-mean-squared velocity is computed.

AVI video format, which are subsequently extracted for computing velocity fields.

Velocity fields from the seeded flow images are extracted using a technique called particle image velocitmetry (PIV), which relies on computing displacement of tracer particles across images [108]. A simplistic description of how PIV works is as follows: Consider two images of the seeded flow, captured Δt seconds apart in time, as shown in Fig. 2.3 (b). The first of these two images records the spatial arrangement of tracer particles in the flow at an instant t. Over the duration Δt that follows, each tracer particle is advected by the fluid element it is floating on. If Δt is sufficiently small, this motion can be approximated as being along a straight line. The second image, then,

records the new spatial arrangement of tracer particles in the flow. Given the near unique correspondence between spatial location in the flow and pixels on the camera, computing the pixel displacement of a certain tracer particle should, in principle, facilitate computing the corresponding *local* flow velocity.

Tracking the "identity" of each particle in the flow across the two images, with reasonable confidence, results in significant computational overhead. PIV circumvents this computational difficulty by dividing the image into pixel windows, say 8 pixels $\times$8 pixels in dimension (yellow box in Fig. 2.3(b)), and tracking the displacement of the window across the images, by computing spatial correlations. The rationale behind this is, for a sufficiently small region in the flow the local variation in the velocity field is small. Consequently, all the tracer particles in that region are displaced in the same direction, retaining their relative positions across the two images as can be seen in Fig. 2.3(b). By computing the displacement of a pixel window across images, one can compute the *mean-local* velocity of the flow in the physical space that maps to the pixel window. By choosing a sufficiently high pixel-to-length ratio, one can obtain accurate spatially resolved velocity fields. The PIV package PRANA [109, 110] was used for computing the velocity fields, which employs a multigrid PIV algorithm that additionally deforms pixel windows to better resolve flows with high shear. For the experimental domain discussed earlier, the velocity field is resolved on a 169 $\times$ 126 grid, with about 9 points per magnet width.

2.2 Testing the Validity of the Q2D Approximation

The PIV data obtained in the experiment measures the velocity field only at the free surfaces, i.e., either the electrolyte-air or the electrolyte-dielectric interfaces. Reconstructing full 3D volumetric velocity fields from such 2D measurements is not feasible, yet. However, for sufficiently shallow layers of fluid driven by *weak, horizontal* forcing, the characteristic times ($\rho_i h_i^2/\mu_i$) describing equilibration of momentum in the

vertical direction within each layer is much smaller than that ($\rho_i L^2/\mu_i$) associated with the horizontal direction. Here $\mu_i = \mu_c\,, \mu_d$ and $\rho_i = \rho_c\,, \rho_d$ are the dynamic viscosity and density for each layer, while $h_i = h_c\,, h_d$ indicates layer thickness. L is the characteristic horizontal length scale, equal to the width of the magnet in the present case. If the *direction* of the forcing $\mathbf{F}_\parallel$ is independent of z, it tends to drive the flow at a particular horizontal position (x, y) and different z along the same direction. Consequently, one can assume the direction of the velocity to be horizontal (cf. Fig. 1.3) and independent of the height z. Furthermore, if the forcing *profile* does not change substantially in the confined direction, i.e., $\mathbf{F}_\parallel(x, y, z)$ for various z (nearly) collapse to a single profile when scaled, viscous coupling between different layers of fluid will ensure that the velocity field can be factored as [111, 112]

$$\mathbf{V}(x, y, z, t) \approx P(z)\mathbf{u}(x, y, t) \equiv P(z)[u(x, y, t)\,\hat{\mathbf{x}} + v(x, y, t)\,\hat{\mathbf{y}}]. \tag{2.1}$$

where $P(z)$ describes the variation of the 2D horizontal velocity $\mathbf{u}$ along z. A 3D velocity field which can be approximated using equation (2.1) is henceforth called "quasi-two-dimensional" (Q2D). For the two-fluid layer configuration in the experiment, the boundary conditions that $P(z)$ must satisfy are no-slip at the bottom of the dielectric ($z = 0$), the continuity of the velocity and stress at the dielectric-electrolyte interface ($z = h_d$), and the stress-free boundary condition at the top (free) surface of the electrolyte ($z = h_d + h_c$):

$$P(0) = 0, \quad P(h_d^-) = P(h_d^+), \quad \mu_d P'(h_d^-) = \mu_c P'(h_d^+), \quad P'(h_d + h_c) = 0, \tag{2.2}$$

where the prime indicates derivative with respect to z.

Furthermore, to ensure the factorization is unique, the normalization condition

$$P(h_d + h_c) = 1 \tag{2.3}$$

is imposed, so $\mathbf{u}(x, y, t)$ can be interpreted as the velocity of the free surface ($z = h_d + h_c$), i.e., $\mathbf{u}(x, y, t) = \mathbf{V}(x, y, h_d + h_c, t)$, as shown in Fig. 1.3 with $h = h_d + h_c$.

To test the robustness of the forcing profile within the electrolyte layer the net magnetic field $\mathbf{B}(x, y, z) \approx B_z(x, y, z)\,\hat{\mathbf{z}}$ in the experiment is measured using a F. W. Bell Model 6010 Gaussmeter. Experimental measurements show that close to the surface of the magnets and the ends of the array $B_z(x, y, z)$ has a complicated profile. However, B_z near the center of the magnet array varies approximately sinusoidal in y, beyond a height of $z = 0.25$ cm; the measurements for the center pair of magnets are shown in Fig. 2.4(a). It can be seen that, the rescaled profiles collapse on to each other, validating that the forcing is *approximately* Q2D. Consequently, the forcing as well as the resulting flow are henceforth termed as "Kolmogorov-like". A detailed discussion on the deviation of forcing profile and the flow from being Q2D is included in Appendix D. Within the typical position of the electrolyte layer (0.3 cm $\leq z \leq$ 0.6 cm) (see Fig. 2.4(b)) the magnetic field decays approximately linearly, as shown in Fig. 2.4(b). The parameters found for the fit[10] $B_z = B_1 z + B_0$ at $y \approx 0.63$ cm in Fig. 2.4(a) are $B_1 = -30.6 \pm 0.5$ T/m and $B_0 = 0.276 \pm 0.01$ T. Following this observation one can approximate the functional dependence of B_z near the center of the array as,

$$B_z = (B_1 z + B_0)\sin(\kappa y). \tag{2.4}$$

For a current density J smaller than some critical value, the direction of the horizontal flow profile $\mathbf{u}(x, y, t)$ observed at the free surface follows that of the forcing (2.4), so the velocity profile, measured at the free surface, is expected to be nearly sinusoidal,

$$\mathbf{u}(x, y, t) = u_0 \sin(\kappa y)\,\hat{\mathbf{x}}. \tag{2.5}$$

If the Q2D ansatz in equation (2.1) is applicable to the base flow, then the 3D

[10]The decay of the magnetic field in the experiment above the center of the array can be modeled as $B_1 e^{-\kappa z}\sin(\kappa y) + B_3 e^{-3\kappa z}\sin(3\kappa y)$, with B_3 being about 10% of B_1 at $z = 0.3$ cm. Such a fit follows from the solution to Laplace's equation for magnetic field, $\nabla \cdot \mathbf{B} = 0$ and $\nabla \times \mathbf{B} = 0$. The two-harmonic approximation provides a direct estimate for deviation of forcing from being Q2D. A linear fit was employed for analytical simplification in computing $P(z)$.

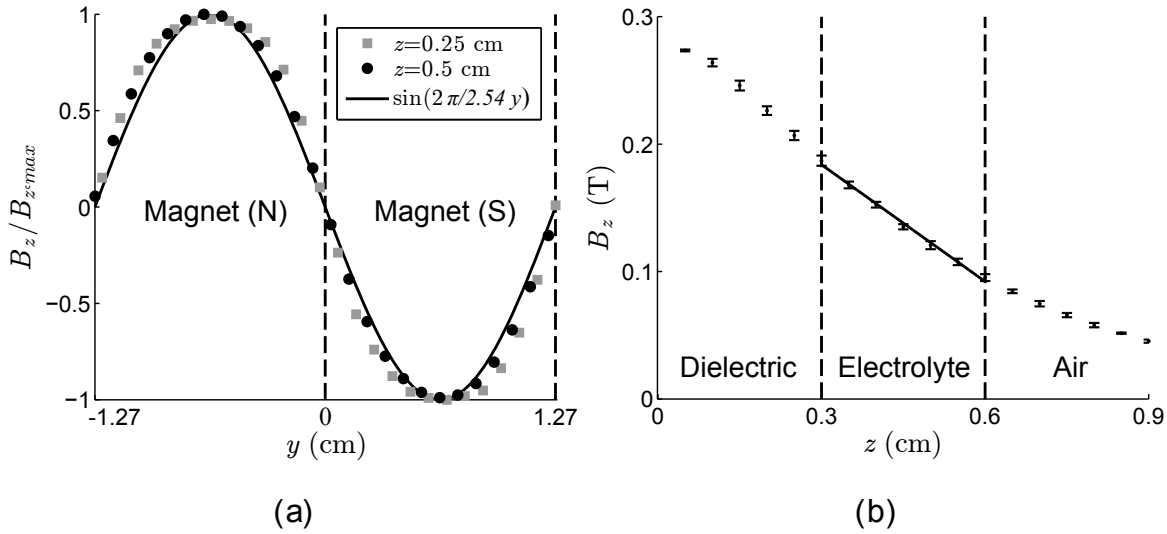

Figure 2.4: Validating the Q2D approximation for the magnetic field near the center of the domain. In panel (a) transverse (y) cross-section of normalized profile of magnetic field component B_z, is plotted. These profiles are obtained by measuring B_z at two different heights z over the middle two magnets of the array, and normalizing each to have peak of unity. A sine wave with periodicity equal to the width of one magnet pair is shown for comparison. (b) Experimental measurements of the decay of B_z with increasing height (z) from the magnets' surface. Within the electrolyte, the field decays approximately linearly. Error bars indicate one standard deviation.

velocity field near the center of the domain can be approximated as $\mathbf{V}(x, y, z, t) = P(z)\mathbf{u}(x, y, t) = u_0 P(z) \sin \kappa y \, \hat{\mathbf{x}}$. Fig. 2.5 validates the Q2D ansatz for the flow in the experiment, wherein the velocity cross sections measured at the electrolyte-air free surface and the dielectric-electrolyte interface for sufficiently low values of current (2.0mA) are plotted. The thickness of the dielectric and electrolyte layers used for this run are $h_c = h_d = 0.3 \pm 0.1$ cm, with the conducting fluid being the low-viscosity-electrolyte. Each data point is the time-averaged (over 300 seconds) PIV

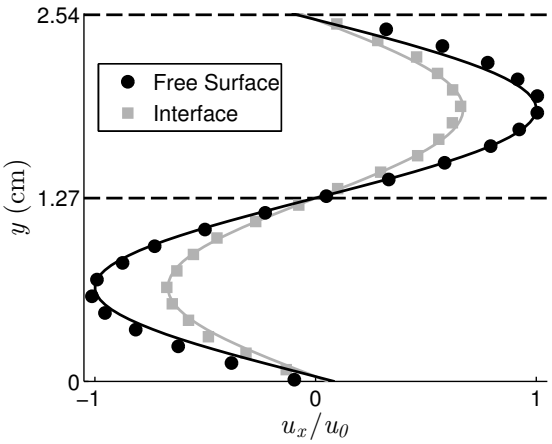

Figure 2.5: (a) Experimental measurements of the sinusoidal flow profile, near the center of the domain, taken in separate runs by seeding the electrolyte-air (black circles) and the electrolyte-dielectric (gray squares) interfaces. The thickness of each fluid layer in the setup is 0.3 cm. The velocities are normalized by the amplitude u_0 of a sinusoidal fit (solid lines) for the profile at the electrolyte-air interface. The sinusoidal fit for each height shows that the shape of the velocity profile does not change substantially, i.e., it is quasi-two-dimensional.

measurement[11], spatially averaged over 4.5 cm along the x-direction to obtain an accurate estimate of the mean profile. While the amplitudes of the horizontal velocity profiles at different heights z are different, when rescaled to have a unit amplitude, they confirm the flow is nearly Q2D. This, for instance, can be inferred by comparing the profiles at each interface with the purely sinusoidal fit. This demonstrates the usefulness of the Q2D approximation; by measuring a 2D velocity field at the electrolyte-air interface, one can recover the horizontal velocity at various heights within the fluid layer if $P(z)$ can be estimated.

[11]This data was captured using a setup slightly different than the one described previously. The lateral dimensions of the domain are $L_x = 25.4$ cm and $L_y = 20.3$ cm. Nevertheless, far away from the boundaries the profile is fairly robust to end effects. The images of the flow are recorded using a Unibrain Fire-i Board B/W digital camera which has a CCD sensor with a resolution of 640 × 480 pixels. The field of view corresponds to a region at the center of the magnet array with dimensions 4.7 cm × 3.5 cm. Images are captured at equal intervals of 0.133 seconds, which corresponds to a frame rate of 7.5 Hz. PIV was performed on the recorded images using Open Source Image Velocimetry software package (version 2.1, available at http://osiv.sourceforge.net/).

2.3 Vertical Profile in the Kolmogorov-Like Flow

To construct the Q2D velocity field using 2D velocity measurements, one requires the knowledge of $P(z)$ associated with the sinusoidal flow, which was not provided in the discussion above. To address this, the vertical profile $P(z)$ of the horizontal velocity $\mathbf{u}$ (cf. equation 2.1) in the Q2D Kolmogorov-like flow is derived analytically, and validated using experimental measurements here. To begin with, the exact evolution of the velocity field $\mathbf{V}$ in the experiment is governed by the 3D Navier-Stokes equation for an incompressible fluid ($\nabla \cdot \mathbf{V} = \mathbf{0}$)

$$\rho(\partial_t \mathbf{V} + \mathbf{V} \cdot \nabla \mathbf{V}) = -\nabla p + \mu \nabla^2 \mathbf{V} + \mathbf{F} + \rho \mathbf{g}, \tag{2.6}$$

where p is the pressure, and $\mathbf{g} = -g\,\hat{\mathbf{z}}$ is the acceleration due to gravity. In the two-layer setup under consideration ρ and μ are (stepwise) functions of z.

The electromagnetic forcing within the dielectric is zero, while that in the conducting electrolyte is approximated using $\mathbf{F}_{\parallel} = JB_z(z) \sin \kappa y\, \hat{\mathbf{x}}$, only near the center of the domain. Substituting the Q2D form of the velocity for the sinusoidal flow $\mathbf{V}(x, y, z, t) = u_0 P(z) \sin \kappa y\, \hat{\mathbf{x}}$ one obtains a boundary value problem for the vertical profile $P(z)$:

$$\begin{aligned} P'' - \kappa^2 P &= -\frac{J}{u_0 \mu_c}(B_1 z + B_0), \quad h_d < z < h_d + h_c, \\ P'' - \kappa^2 P &= 0, \qquad\qquad\qquad\qquad 0 < z < h_d \end{aligned} \tag{2.7}$$

where the prime denotes differentiation with respect to z. The solution to the above equation, with boundary conditions given by equation (2.2), should describe the vertical profile close to the center of the domain in the experiment. Note that the 1D equation results from only the x momentum equation, since the y momentum equation is identically zero, while that in the z direction yields hydrostatic pressure balance, which is discussed later.

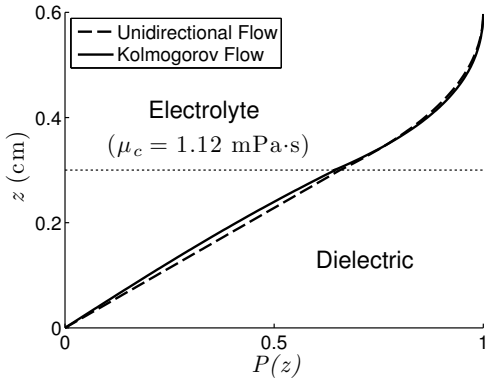

Figure 2.6: Theoretically computed profile $P(z)$ for the sinusoidal shear flow in the two-immiscible layer setup for $h_d = h_c = 0.3$ cm. Also plotted using the dashed lines is the profile for the limiting case $\kappa \to 0$, which corresponds to a unidirectional flow.

The solution to the differential equations (2.7) is given by

$$P = \begin{cases} Ce^{\kappa z} + De^{-\kappa z} + \frac{JB_1}{u_0 \mu_c \kappa^2} z + \frac{JB_0}{u_0 \mu_c \kappa^2}, & h_d < z < h_d + h_c, \\ Ee^{\kappa z} + Fe^{-\kappa z}, & 0 < z < h_d. \end{cases} \tag{2.8}$$

In equation (2.8), in addition to the coefficients C, D, E, and F, the amplitude u_0 of the sinusoidal velocity profile at the free surface of the electrolyte is not known *a priori*. To uniquely define $P(z)$ the normalization condition $P(h_c+h_d) = 1$ is imposed (cf. 2.3). This gives the fifth equation, in addition to the four defined by equation (2.2), necessary to solve for the five unknowns C, D, E, F, and u_0.

Fig. 2.6(a) shows the theoretically computed vertical profile $P(z)$ for the "low-viscosity-electrolyte". The dynamic viscosity and density of the conducting layer are 1.12 mPa.s and 1045 kg/m^3, while those of the dielectric fluid are 1.30 mPa.s and 1769 kg/m^3, respectively. These properties chosen for the profile computation are typical of those used in immiscible layer setups in several previous studies [104, 105]. The profile in the dielectric is close to being linear (Couette-like). The profile in the electrolyte, however, is fairly curved. It is vertical close to the electrolyte-air interface owing to the free-slip boundary condition $P'(h_d + h_c) = 0$, but shows a steep gradient as one moves towards the dielectric-electrolyte interface. For $h_d = h_c = 0.3\,$cm, $P(z)$ at the electrolyte-dielectric interface is roughly 0.6 times that at the electrolyte-air

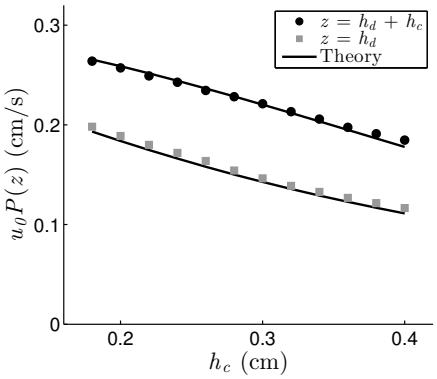

Figure 2.7: Amplitudes of the sinusoidal velocity profile at electrolyte-air (black circles) and electrolyte-dielectric (gray squares) interfaces, measured using two separate runs. For each run, the thickness of the electrolyte layer is varied from 0.2cm to 0.4cm, by keeping the current I though it constant at 2.1mA. The thickness of the dielectric layer is $h_d = 0.3$cm. The solid lines correspond to the analytical estimates u_0 and $P(h_d)u_0$, which correspond to the amplitudes of sinusoidal velocity profiles at the two interfaces. Note that $P(z)$ depends on h_c, hence for each height h_c a separate profile is computed to estimate u_0 and $u_0P(h_d)$.

interface. This implies that the amplitudes of the velocity profiles measured at the two interfaces are scaled similarly, which is confirmed by Fig. 2.5.

The vertical profile $P(z)$ depends on the decay of the magnetic field, fluid properties, as well as layer thicknesses. Direct measurements of the velocity along the fluid layer depth are tedious, especially in the dielectric layer [112]. An easier (albeit indirect) alternative is to vary the thickness of the fluid layers in the experiment and measure amplitudes of the horizontal velocity profiles at the electrolyte-air and electrolyte-dielectric interfaces. This shows the functional dependence of the profile on one of the parameters. Fig. 2.7 shows the velocity amplitudes measured at the electrolyte-air (black symbols) and electrolyte-dielectric (gray symbols) interfaces when the thickness h_c of only the electrolyte layer is varied from 0.2 cm to 0.4 cm, keeping the current I constant at 2.1 mA. This results in the decrease of current density from $J = 4.26$ A/m^2 to $J = 2.13$ A/m^2. These measurements are compared with analytical predictions for $u_0P(h_d + h_c)$ and $u_0P(h_d)$, which denote the velocity amplitude at the electrolyte-air and electrolyte-dielectric interfaces, respectively.

Since $P(z)$ and u_0 depend on h_c the profile for each value of the thickness realized in experiment is computed using equation (2.8) and the boundary conditions given in equation (2.2). As can be seen from the plots, the relative difference between theory and experiment is less than 5%. *All* the parameters used in the theoretical calculations have been measured experimentally. This comparison for different h_c validates that $P(z)$ given by equation (2.8) should capture the variation in the magnitude of horizontal velocity as a function of z. A similar validation by varying h_d, as well as I, were carried out but are not presented here.

2.4 Creating a Nearly Perfect 2D Flow

With the profile $P(z)$ in hand, one can attempt to address the inherent three-dimensionality of the flow in two-fluid layer systems, immiscible in the present case, which was previously not explored. The motivation behind using stratified layers of fluids to realize Q2D flows is that the top layer is shielded from the no-slip boundary condition at the bottom by a lubricating layer. For a perfectly 2D flow, one would expect the velocity field in the top layer to be independent of the z coordinate, i.e., $P(z > h_d) = 1$. Hence, for the two-immiscible-layer setup one can use the ratio of velocities at the electrolyte-air and electrolyte-dielectric interfaces as a measure that characterizes the inherent deviation from two-dimensionality:

$$r = \frac{P(h_d + h_c)}{P(h_d)}. \tag{2.9}$$

For a monotonically varying profile, the value of r describes how strongly the magnitude of the horizontal velocity field varies with z in the electrolyte, with $r = 1$ corresponding to a z-independent velocity profile. This measure of deviation from two-dimensionality is different from the one used in previous studies [82, 113], where the ratio of kinetic energy contained in the secondary (vertical) flow to that in the primary (horizontal) flow was chosen as a measure within each layer.

The profile $P(z)$ and r computed for the flow in the experiment have very complicated analytical dependence on the fluid properties and layer thicknesses. To elicit the dependence of r on fluid layer properties, one can study the limiting case of the Kolmogorov-like flow when the magnets are very wide ($\kappa \to 0$), and one confines observation to a small region near the centers of the magnets ($\kappa y \to n\pi/2$). This eliminates the y dependence of the problem, resulting in a magnetic field $B_z = B_1 z + B_0$ and unidirectional uniform flow $\mathbf{u}(x, y, t) = u_0\,\hat{\mathbf{x}}$. The vertical profile for such a flow can be computed solving equation (2.7) with $\kappa = 0$, which yields,

$$P_0 = \begin{cases} -\frac{JB_1}{6u_0\mu_c}z^3 - \frac{JB_0}{2u_0\mu_c}z^2 + Cz + D, & h_d < z < h_d + h_c, \\ Ez + F, & 0 < z < h_d, \end{cases} \tag{2.10}$$

the subscript zero indicating the wavenumber has been set to zero. The unknown coefficients C, D, E, F and u_0 in the above equation can be computed using the boundary conditions (2.2) [114].

Although the functional forms (2.8) and (2.10) of the vertical profile are quite different for the Kolmogorov and uniform flows, their shape is virtually indistinguishable, as Fig. 2.6 illustrates. Consequently, one can evaluate the analytical form for equation (2.9) using $P_0(z)$ in place of $P(z)$, which results in

$$r = 1 + \frac{1}{2}\frac{\mu_d h_c}{\mu_c h_d}\left(1 + \frac{1}{6}\frac{\Delta B}{\langle B\rangle}\right), \tag{2.11}$$

Here $\Delta B = B_1 h_c$ is the change in magnetic field across the electrolyte and $\langle B\rangle = B_0 + B_1 h_d + \frac{1}{2}B_1 h_c$ is the mean magnetic field in the electrolyte.

Expression (2.11) suggests that even if the magnetic field across the electrolyte were uniform, i.e. $\Delta B = 0$, for the typical case where $\mu_c \approx \mu_d$ and $h_c = h_d$ [104, 105], the flow in the electrolyte would still deviate significantly from being perfectly 2D, with $r = 1.5$. Instead, using $\Delta B/\langle B\rangle = -0.6$ which corresponds to the experiment gives $r = 1.45$. Hence, the decay in the magnetic field does not contribute

significantly to the deviation from two-dimensionality. Expression (2.11) also suggests that the shallower the electrolyte layer is (relative to the dielectric layer), the closer one comes to a vertically uniform profile in the electrolyte ($r = 1$). However, electrolyte layers with thickness less than 0.25 cm are found to be unstable in the experiment, as they break up to form configurations that correspond to lower total surface energy. Alternatively, one may increase the thickness h_d of the dielectric layer. This has the drawback that one moves the electrolyte layer farther from the magnets, requiring larger currents to drive the flow. Also, the Q2D approximation, an assumption whose validity depends partially on strong geometric confinement, is compromised. Hence, the most straightforward way to make the flow in the electrolyte nearly two-dimensional is by increasing the ratio of viscosities. The optimal choice of the electrolyte viscosity is not obvious. For the variation in the velocity of the electrolyte to be at most 10%, μ_c should exceed the solution of (2.11) with $r = 1.1$. Substituting $\mu_d = 1.30$ mPa·s for the dielectric (PFO) viscosity, $\Delta B/\langle B\rangle = -0.6$ for the magnatic field decay and $h_d = h_c = 0.3$ cm gives $\mu_c \geq 5.8$ mPa·s. Indeed, the analytical velocity profile $P(z)$ presented in Fig. 2.8 (a) shows that the uniformity of the velocity in the conducting layer is substantially enhanced when a more viscous electrolyte (with $\mu_c = 6.06$ mPa·s) is used. The value of r for these parameters is 1.08. Also plotted for comparison is the velocity profile computed for the uniform flow, which remains practically indistinguishable from the Kolmogorov-like one, which validates the function dependence of the profile on μ_c and h_c.

The uniformity of the profile in the electrolyte layer is experimentally validated by comparing the measured horizontal velocity of the laminar flow at the electrolyte-air and electrolyte-dielectric interfaces, which is shown in Fig. 2.8(b). The height of the conducting layer h_c is varied from 0.2 cm to 0.4 cm, similar to that discussed in section 2.3, while a constant current of 5.0 mA is passed through it. Also plotted for comparison are the theoretical estimates u_0 and $u_0 P(h_d)$ for the velocity at the

electrolyte-air and the electrolyte-dielectric interfaces, respectively.

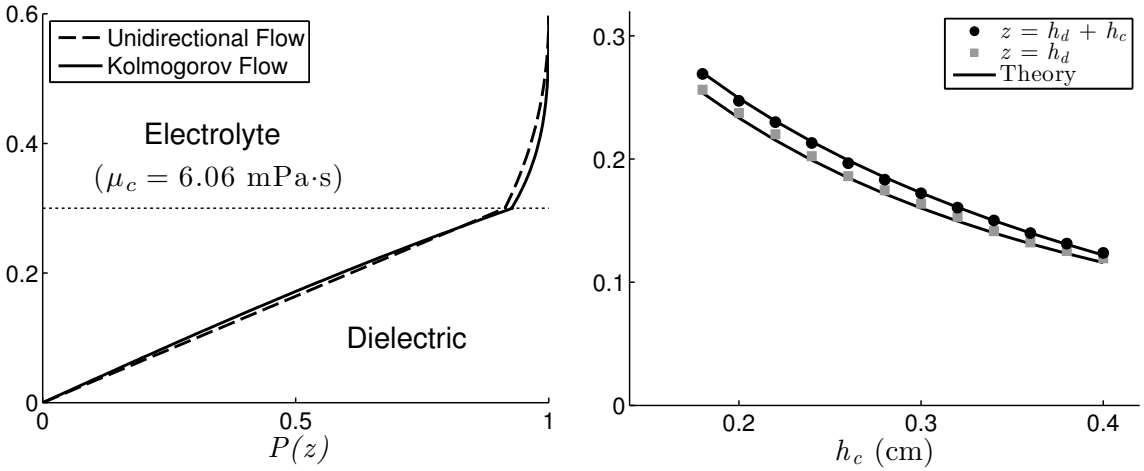

(a) (b)

Figure 2.8: Plots showing the effect of increasing the viscosity of the electrolyte layer with respect to the dielectric. In (a) the vertical profile $P(z)$ is plotted as a function of z. The profile, and hence the velocities, at the electrolyte-air and electrolyte-dielectric interfaces differ by less than 10%. Plot in (b) shows experimental measurements of the amplitude of the sinusoidal velocity measured at the two interfaces as the thickness of the high-viscosity-electrolyte layer is varied from 0.2 cm to 0.4 cm. A constant current of 5.0 mA is passed through the electrolyte layer. The height of the dielectric layer h_d was maintained constant at 0.3cm. The error bars are the size of the symbols.

Increasing the ratio of viscosity is advantageous from dynamical considerations. Since the time scales of momentum equilibration are $\rho_c h_c/\mu_c$ and $\rho_d h_d/\mu_d$, in the electrolyte and dielectric layers respectively, increasing the viscosity of the electrolyte layer decreases the associated equilibration time. For the "low-viscosity-electrolyte" the equilibration time is $\approx$ 10 seconds, which is much larger compared to $\approx$ 2s for "high-viscosity-electrolyte" case. This implies that the velocity fields measured simultaneously at the electrolyte-air and electrolyte-dielectric interfaces should be very similar in time-dependent regimes due to the increased viscosity of the electrolyte which, however, is not guaranteed in the low viscous case.

As a note of caution, a higher viscosity (dissipation) means a higher current (driving) is necessary to reach a desirable horizontal velocity. A potential drawback of this

is excess Joule heating, which can cause significant variation in the viscosity; there is a 4% decrease in μ_c for every 1 °C increase in temperature. Experimental runs with the high-viscosity electrolyte lasting for about sixty minutes with a current ≈ 30 mA show that the fluid temperature increases by around 1 °C. These runs performed with no thermal reservoir in place demonstrate the necessity to include one to maintain the fluid properties when using the high-viscosity electrolyte.

2.5 Summary

In this chapter a detailed description of the two-immiscible-layer experimental setup used to generate a nearly horizontal flow was presented. A brief overview of the imaging technique employed to obtain 2D velocity fields at the free surfaces was discussed. By providing experimental measurements of the magnetic field near the center of the domain, as well as those of the 2D sinusoidal velocity fields at the electrolyte-air and electrolyte-dielectric interfaces, it was shown that one can describe the flow using the Q2D approximation[12]. By assuming the flow to be purely sinusoidal, the vertical variation in the magnitude of the horizontal velocity was computed and validated against experimental measurements. It was shown that this profile is fairly robust, using the test case of uniform flow. Following the computation of the vertical profile, it was demonstrated that by increasing the ratio of electrolyte viscosity relative to the dielectric's, one can create a near perfect 2D flow in the electrolyte.

The results provided in this chapter were part experimental and part analytical, but limited to the study of the sinusoidal flow. However, as the strength of the current is increased the flow no longer remains sinusoidal and one cannot solve a simple linear, ordinary differential equation to compute $\mathbf{u}(x, y, t)$. This demands developing a general methodology which includes the description of a Q2D flow in

[12]The validation of the flow being Q2D was provided here only for the sinusoidal flow at low driving. As the strength of the forcing is increased, the flow bifurcates to a steady pattern of vortices. The Q2D nature of the flow was validated in that regime as well, but the data is not presented here.

the experiment using a strictly 2D equation which captures the evolution of the velocity at one of the free surfaces. The derivation of such an equation, as well as its numerical discretization, will be discussed in the following chapter.

CHAPTER III

THEORETICAL MODELING OF Q2D FLOWS

In the previous chapter, the sinusoidal Q2D flow realized in the two-immiscible layer setup was studied experimentally as well as analytically. In this chapter, a strictly 2D model (section (3.1)) that is expected to describe the evolution of a Q2D flow, even when the horizontal velocity profile is complicated, is developed. While this 2D model, in principle, can be numerically simulated using periodic domains, the goal here is to develop a numerical simulation with lateral dimensions and boundary conditions identical to those in the experiment. As a first step towards this a 3D numerical model of the magnetic field and its validation using experimental measurements is presented in section (3.2). In sections 3.3.1, 3.3.2, and 3.3.3 a detailed exposition of developing a realistic numerical integrator of the 2D model is presented. Finally, in section (3.3.6) two domains with periodic boundary conditions are discussed; these domains, despite being not experimentally realizable, will be employed to systematically study effects of confinement.

3.1 Depth-Averaged 2D Model Describing Q2D flows

As mentioned earlier, Q2D flows in shallow electrolyte layers have been previously modeled by adding a linear friction term to the 2D Navier-Stokes equation. The friction coefficient as well as the effective fluid properties in the case of two-fluid-layer setups have been determined using geometrical and dimensional considerations. These shortcomings are addressed here through a systematic derivation of a 2D model, applicable to *both* miscible and immiscible layer setups. For reasons of completeness, a few details which have been previously mentioned are repeated in the following text.

Consider a shallow layer of liquid — homogeneous or stratified — with total

thickness h, in a laterally extended container with a flat bottom. Here, shallow implies that the characteristic horizontal length scale L (related to the forcing wavelength in the Kolmogorov problem) is substantially larger than the thickness h. For the two-immiscible-layer setup described in the previous chapter $h = h_d + h_d$ and L is the width of a magnet (cf. section (2.1)). As shown in Fig. 2.1(a), the coordinate system is chosen with the xy-plane parallel to the lateral expanse of the fluid layer and the z-axis in the vertical direction, opposite to gravity. $z = 0$ is chosen at the bottom of the fluid layer and $z = h$ corresponding to the liquid-air interface. A body force ($\mathbf{F}_\parallel$) parallel to the xy plane applied to the fluid layer(s) results in a velocity field that depends, in general, on all three coordinates, $\mathbf{V} = \mathbf{V}(x, y, z, t)$, whose evolution is described by the 3D Navier-Stokes equation for an incompressible fluid ($\nabla \cdot \mathbf{V} = \mathbf{0}$)

$$\rho(\partial_t \mathbf{V} + \mathbf{V} \cdot \nabla \mathbf{V}) = -\nabla p + \mu \nabla^2 \mathbf{V} + \mathbf{F}_\parallel + \rho \mathbf{g}. \tag{3.1}$$

For the single homogeneous layer setup ρ and μ correspond to the density and dynamic viscosity of the fluid under consideration. For stratified layers, however, ρ and μ depend on z, either in a piecewise constant or continuous manner depending on how the stratification is achieved. Henceforth, unless otherwise stated, ρ and μ are functions of z. $\rho\mathbf{g}$ is the gravitational force (along the z-axis) per unit volume of the fluid at any given location and $\mathbf{F}_\parallel$ is the *local* electromagnetic plane-parallel force density. For stratified fluid layers the electromagnetic force density is also a function of z; within the layers composed of pure-water or dielectric fluids it is zero.

For a Q2D flow which satisfies the criteria discussed in section (2.2), the 3D velocity is approximated as $\mathbf{V}(x, y, z, t) \approx P(z)\mathbf{u}(x, y, t)$, where $\mathbf{u}(x, y, t)$ is a 2D velocity field. As was demonstrated in the previous chapter, such an approximation is accurate at moderate Re. For the normalization $P(h) = 1$, $\mathbf{u}(x, y, t)$ corresponds to the velocity field at the liquid-air interface. Substitution of the Q2D form of the

velocity field into (3.1) gives

$$\begin{aligned} \rho P \partial_t \mathbf{u} + \rho P^2 \mathbf{u} \cdot \nabla_\parallel \mathbf{u} &= -\nabla_\parallel p + P\mu \nabla_\parallel^2 \mathbf{u} + \mathbf{u}\mu \nabla_\perp^2 P + \mathbf{F}_\parallel, \\ \nabla_\perp p &= \rho \mathbf{g}, \end{aligned} \tag{3.2}$$

along with $\nabla_\parallel \cdot \mathbf{u} = 0$, where the subscript $\parallel$ and $\perp$ represent the operators in horizontal (x, y) and vertical (z) coordinates, respectively. In general, the profile $P(z)$ is time-dependent and depends on the horizontal flow profile $\mathbf{u}$. Hence, for a general flow $\mathbf{u}(x, y, t)$, the factorization is not mathematically rigorous. However, for sufficiently shallow electrolyte layers, if the characteristic spatial scales associated with $\mathbf{F}_\parallel$ and $\mathbf{u}$ are much larger than the fluid layer thickness, then $P(z)$ turns out to be fairly robust, and practically time-independent, as shown in Appendix D.

Integrating the first of the two equations in (3.2) over the z coordinate from $z = 0$ to $z = h$, i.e., from the bottom of the fluid layer to the electrolyte-air interface, one obtains

$$\partial_t \mathbf{u} + \beta \mathbf{u} \cdot \nabla \mathbf{u} = -\frac{1}{\bar{\rho}} \nabla p + \bar{\nu} \nabla^2 \mathbf{u} - \alpha \mathbf{u} + \frac{1}{\bar{\rho}} \langle \mathbf{F}_\parallel \rangle_z. \tag{3.3}$$

The above strictly 2D equation is expected to describe the evolution of the velocity field measured at the liquid-air interface in a Q2D flow (following the normalization $P(h) = 1$). The parameters in the 2D model β, $\bar{\nu}$, $\bar{\rho}$, and α are defined as follows

$$\beta = \frac{\int_0^h \rho P^2 dz}{\int_0^h \rho P dz}, \quad \bar{\nu} = \frac{\int_0^h \mu P dz}{\int_0^h \rho P dz}, \quad \bar{\rho} = \frac{\int_0^h \rho P dz}{h}, \quad \alpha = \frac{(\mu P')_{z=0}}{\int_0^h \rho P dz}. \tag{3.4}$$

The forcing term $\langle \mathbf{F}_\parallel \rangle_z$ on the right-hand side of (3.3) is related to the depth-averaged force density:

$$\langle \mathbf{F}_\parallel \rangle_z = \frac{\int_0^h \mathbf{F}_\parallel dz}{h}. \tag{3.5}$$

For electromagnetically driven shallow electrolytic layers, $\mathbf{F}_\parallel$ is usually a result of the interaction of the magnetic field and a current through the electrolyte. The magnetic field usually decays within the electrolyte layer, resulting in $\mathbf{F}_\parallel$ that depends on z.

Additionally, in two-layer setups, the current density may vary discretely with z, as mentioned before. Both these scenarios are taken into account in the above integral.

In equation (3.3), since $P(z) \in [0, 1]$ following normalization defined in equation (2.3), $\beta \neq 1$. This, distinguishes the above 2D model from all previous empirical modifications of 2D Navier-Stokes which assumed $\beta = 1$ [80, 83]. The effective non-linearity of a Q2D flow is different from what one estimates using 2D measurements at the free-surface due to the gradient in the magnitude of the velocity along z. $\beta \neq 1$ models this effective change in the inertia of the Q2D flow using the strictly 2D model.

The linear friction term $-\alpha\mathbf{u}$, which accounts for the presence of a solid boundary at the bottom of the fluid layer, is a direct consequence of *ansatz* (2.1) and depth-averaging. This is distinctly different from how previous studies have included this term in the 2D model. While Bondarenko *et al.* [80] have assumed the linear form, an alternative derivation using Taylor series expansion of the velocity field about the free surface was suggested by Dolzhanskii *et al.* [115], neither of which are accurate. Note that both equations (1.7) and (1.8) can be considered a special cases of equation (3.3) for suitable choice of α and β.

Lastly, the parameters $\bar{\nu}$ and $\bar{\rho}$ are the depth-averaged kinematic viscosity and density, respectively. For stratified layers, where fluid properties (μ, ρ) depend on z, the integrals in equations (3.4) and (3.5) are computed taking the variation in ρ and μ into account. This addresses the earlier stated concern that the parameters in previously employed 2D models have not systematically accounted for inhomogeneity in fluid properties for stratified setups.

Before proceeding to the discussion of the numerical estimates of parameters, a short explanation on the physical meaning of the pressure p in the 2D model is presented here. The discussion, for reasons of simplicity, is restricted to homogeneous electrolyte layers. Using the second equation in 3.2, the solution to the 3D pressure

is given by

$$p(x,y,z,t) = -g\int_0^z \rho dz + p_{\parallel}(x,y,t) = -\rho g z + p_{\parallel}(x,y,t), \tag{3.6}$$

where $p_{\parallel}$ is the complementary function which does not depend on z. The pressure at the electrolyte-air interface, where the velocity $\mathbf{u}$ is measured, is constant and equal to atmospheric pressure $p(x,y,z_{max},t) = p_a$. If the liquid-air interface were flat, i.e., $z_{max} = h \,\forall\, (x,y)$, one obtains $p_{\parallel}(x,y,t) = p_a + \rho g h$ which is a constant with zero gradient ($\nabla_{\parallel} p_{\parallel} = \nabla_{\parallel} p = 0$). The inconsistency in the above argument, however, is in assuming that the electrolyte-air interface is flat for an arbitrary $\mathbf{u}(x,y,t)$ (violation of cyclostrophic balance) [82]. In reality, the liquid-air interface is deformed, with $z_{max} = h + \delta h(x,y,t)$, where δh is the deformation about the mean height h, which results in

$$p_{\parallel}(x,y,t) = p_a + \rho g h + \rho g \delta h(x,y,t). \tag{3.7}$$

Taking the gradient of the above equation yields,

$$\nabla_{\parallel} p_{\parallel}(x,y,t) = \nabla_{\parallel} p = \rho g \nabla_{\parallel} \delta h(x,y,t). \tag{3.8}$$

This implies that the pressure in the 2D model is related to deformations of the electrolyte-air interface which tends to act like a deformed membrane. This implies that the velocity field $\mathbf{u}(x,y,t)$ measured at the free surface is only approximately incompressible, i.e., $\nabla \cdot \mathbf{u} \approx 0$. It can be shown that, across the dynamical regimes tested in this thesis, the maximum δh is of the order of a few (≤ 10) microns for the two-immiscible-layer setup. Hence the effects of deformations are not included in the mass conservation, and the velocity field is assumed incompressible at the liquid-air interface. Lastly, when the characteristic spatial scales become comparable to capillary length scales the effects of surface tension cannot be ignored, which are not included in the 2D model derived herein.

3.1.1 Numerical Estimates of Depth-Averaged Parameters

For sufficiently shallow fluid layers, one can use the vertical profile $P(z)$ associated with a simple horizontal profile, like the sinusoidal one, to estimate the depth-averaged parameters using equation (3.4). For the two-immiscible-layer setup with $h_c = h_d = 0.3$ cm, the depth-average parameters β, α, $\bar{\nu}$, $\bar{\rho}$, and the measure r of deviation from two-dimensionality are provided in Table 3.1. These parameters are computed using the profile $P(z)$ for the sinusoidal Kolmogorov-like flow discussed in section (2.3) for both for the low-viscosity-electrolyte (LVE) ($\mu_c = 1.12$ mPa·s and $\rho_c = 1045$ kg/m^3) and the "high-viscosity-electrolyte" (HVE) ($\mu_c = 5.80$ mPa·s and $\rho_c = 1160$ kg/m^3) cases.

Table 3.1: Numerical estimates of the depth-averaged 2D parameters. LVE corresponds to "low-viscosity-electrolyte", HVE corresponds to "high-viscosity-electrolyte". The parameters are computed using the vertical profile $P(z)$ of the Kolmogorov-flow, as well as $P_0(z)$ corresponding to the unidirectional flow .

Parameter	LVE $P(z)$	HVE $P(z)$	LVE $P_0(z)$	HVE $P_0(z)$
β	0.73	0.83	0.73	0.82
α (s^{-1})	0.057	0.064	0.063	0.069
$\bar{\nu}$ (mm^2/s)	0.95	3.23	0.94	3.19
$\bar{\rho}$ (kg/m^3)	743	959	758	964
r	1.54	1.08	1.52	1.10

The most striking finding from computing the depth-averaged parameters is the significant deviation of β from unity, for both the low and high viscosity setups. Also, the data suggests that the friction coefficient $\alpha \approx 0.065$ is fairly insensitive to the viscosity of the electrolyte. This has a significant consequence that one can change the relative importance of the diffusion term ($\bar{\nu}\nabla_{\parallel}^2\mathbf{u}$) and the friction term ($-\alpha\mathbf{u}$) in the 2D model (3.3) by changing the viscosity of the upper layer in the experiment. The estimate for α is a factor of two smaller than the one suggested by Rivera *et*

al. [104] using dimensional arguments for nearly identical fluid layer properties as the "low-viscosity-electrolyte" setup. Lastly, as expected, the depth-averaged fluid properties $\bar{\nu}$ and $\bar{\rho}$ are different from the viscosity and density of each fluid layer.

The procedure to compute the depth-averaged parameters, once the profile $P(z)$ is known, is applicable to stratified as well as single layer setups. For example, in the homogeneous single-layer setup which was employed extensively in early studies of Q2D flows [80, 81, 93] the vertical velocity gradient has been approximated using a Poiseuille-like profile [81, 82]

$$P(z) = \sin\left(\frac{\pi z}{2h}\right). \tag{3.9}$$

Using such profile one arrives at $\beta = \pi/4 \approx 0.79$ which is also significantly different from unity, showcasing the difference in the equations (1.8) and (3.3) for the single layer setup. The expression $\alpha = \pi^2\nu/4h^2$ for the Rayleigh friction coefficient using equation (3.4), can be recovered without assuming a decaying flow [81, 82]. Furthermore, this expression approximates $\eta 2\nu/h^2$ with the choice $\eta \approx 1.2$, recovering the estimates of Bondarenko *et al.* [80]. By choosing $h = h_c + h_d = 0.6$ cm, i.e., a homogeneous layer with thickness equal to the combined thickness of the dielectric and electrolyte layers, and $\bar{\nu} \approx 1.07 \times 10^{-6}$ m$^2\cdot$ s^{-1}, the same viscosity as the "low-viscosity-electrolyte", one obtains $\alpha = \pi^2\bar{\nu}/4h^2 \approx 0.073$ s^{-1}. Interestingly, the Rayleigh friction coefficient for the single layer setup is *not* very different from the two-immiscible-layer one. However, the latter provides the flexibility to adjust the relative strengths of linear and viscous dissipation.

3.1.2 Analytical Expressions for Depth-Averaged Parameters

The functional dependence of $P(z)$, and consequently of the depth-averaged parameters, on fluid layer properties is fairly complicated. To obtain closed form analytical expressions for the depth-averaged parameters, one can instead use the vertical profile $P_0(z)$ for the unidirectional flow. The parameters computed in this way should

provide very good estimates for α, β, $\bar{\rho}$, $\bar{\nu}$, from the mere knowledge of the setup geometry and fluid properties.

For the Rayleigh friction coefficient, using the velocity profile $P_0(z)$ one obtains:

$$\alpha = \frac{\frac{\mu_d}{\rho_c}\frac{1}{h_d h_c}}{1 + \frac{1}{2}\frac{h_d}{h_c}\frac{\rho_d}{\rho_c} + \frac{1}{3}\frac{h_c}{h_d}\frac{\mu_d}{\mu_c}\left(1 + \frac{1}{8}\frac{\Delta B}{\langle B\rangle}\right)}. \tag{3.10}$$

Here $\Delta B = B_1 h_c$ is the change in magnetic field across the electrolyte and $\langle B\rangle = B_0 + B_1 h_d + \frac{1}{2}B_1 h_c$ is the mean magnetic field in the electrolyte.

For the depth-averaged kinematic viscosity, one obtains:

$$\bar{\nu} = \nu_c \frac{1 + \frac{1}{2}\frac{h_d}{h_c}\frac{\mu_d}{\mu_c} + \frac{1}{3}\frac{h_c}{h_d}\frac{\mu_d}{\mu_c}\left(1 + \frac{1}{8}\frac{\Delta B}{\langle B\rangle}\right)}{1 + \frac{1}{2}\frac{h_d}{h_c}\frac{\rho_d}{\rho_c} + \frac{1}{3}\frac{h_c}{h_d}\frac{\mu_d}{\mu_c}\left(1 + \frac{1}{8}\frac{\Delta B}{\langle B\rangle}\right)}. \tag{3.11}$$

The expression for the depth-averaged density is given by

$$\bar{\rho} = \rho_c \frac{h_c}{h_d + h_c} \frac{1 + \frac{1}{2}\frac{h_d}{h_c}\frac{\rho_d}{\rho_c} + \frac{1}{3}\frac{h_c}{h_d}\frac{\mu_d}{\mu_c}\left(1 + \frac{1}{8}\frac{\Delta B}{\langle B\rangle}\right)}{1 + \frac{1}{2}\frac{h_c}{h_d}\frac{\mu_d}{\mu_c}\left(1 + \frac{1}{6}\frac{\Delta B}{\langle B\rangle}\right)}. \tag{3.12}$$

The exact expression for β is too complicated to yield much insight, but it can be evaluated using the profile $P_0(z)$ and the coefficients for any set of experimental parameters. However, for the values of parameters used in the experiment β as well as the other coefficients have a very weak dependence on $\Delta B/\langle B\rangle$; setting $\Delta B/\langle B\rangle = 0$ changes the values by less than 5%. In that limit, one finds

$$\beta = \frac{1 + \frac{1}{3}\frac{h_d}{h_c}\frac{\rho_d}{\rho_c} + \frac{2}{3}\frac{h_c}{h_d}\frac{\mu_d}{\mu_c} + \frac{2}{15}\frac{h_c^2}{h_d^2}\frac{\mu_d^2}{\mu_c^2}}{1 + \frac{1}{2}\frac{h_d}{h_c}\frac{\rho_d}{\rho_c} + \frac{5}{6}\frac{h_c}{h_d}\frac{\mu_d}{\mu_c} + \frac{1}{4}\frac{\rho_d}{\rho_c}\frac{\mu_d}{\mu_c} + \frac{1}{6}\frac{h_c^2}{h_d^2}\frac{\mu_d^2}{\mu_c^2}}. \tag{3.13}$$

The numerical estimates of the depth-averaged parameters, computed using the above analytical expressions, are presented in Table 3.1 under the columns "LVE $P_0(z)$" and "HVE $P_0(z)$" for both the low and high viscosity electrolytes. These parameters differ from those computed using the exact profile $P(z)$ for the sinusoidal flow by less than 5%, except for α which differs by about 10%.

3.1.3 Nondimensional Form of the 2D Model

The dimensional form of the governing equation (3.3) highlights the physical mechanisms β and α capture, besides highlighting that $\bar{\nu}$ and $\bar{\rho}$ are depth-averaged parameters as opposed to being fluid properties. A vast majority of numerical studies of Q2D flows have, instead, used nondimensional forms of governing equations. To facilitate comparison with such studies equation (3.3) is presented in the nondimensional form here. To begin, the width of a magnet w is chosen as the horizontal length scale L (cf. section (3.1)). In the nondimensional units, the lateral dimensions of the experiment are 14×18. The root-mean-squared (rms) velocity computed over a square region spanning 8 magnets $|x| \leq 4$ and $|y| \leq 4$, shown in Fig. 2.3 (c), is chosen as the velocity scale U. By choosing the interior region alone for computing the rms velocity, one can compare the results obtained from the current study with previous ones employing simulations on periodic domains [72]. The ratio of the length and velocity scales then serves as the time scale. The corresponding nondimensional form of the governing equation and the incompressibility condition is,

$$\begin{aligned} \partial_t \mathbf{u} + \beta \mathbf{u} \cdot \nabla \mathbf{u} &= -\nabla p_0 + \frac{1}{Re}\left(\nabla^2 \mathbf{u} - \gamma \mathbf{u}\right) + \mathbf{f}_0 \\ \nabla \cdot \mathbf{u} &= 0 \end{aligned} \tag{3.14}$$

Here Re is the Reynolds number defined as

$$Re = \frac{UL}{\bar{\nu}} = \frac{Uw}{\bar{\nu}}. \tag{3.15}$$

The parameter $\gamma = \alpha L^2/\bar{\nu}$ describes the relative strength of the Rayleigh friction and viscous terms in equation (3.3). Setting $\gamma = 0$ and $\beta = 1$ results in the familiar 2D Navier-Stokes equation. $p_0 = p(LU^2/\bar{\rho})$ is the nondimensional pressure and $\mathbf{f}_0 = \langle \mathbf{F}_{\|} \rangle_z (L/\bar{\rho}U^2)$ is the nondimensional 2D forcing profile.

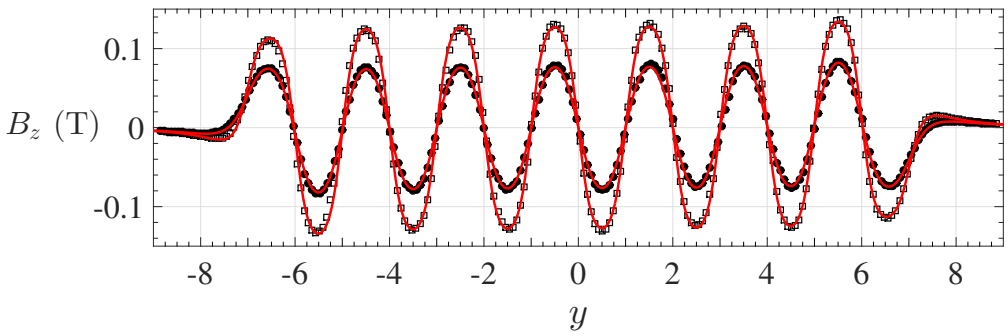

(a)

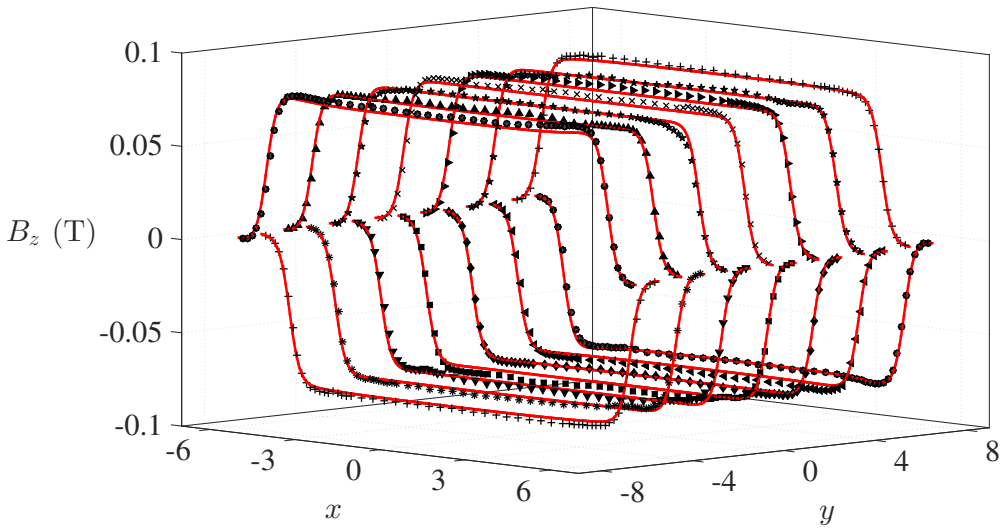

(b)

Figure 3.1: The z-component of the magnetic field, B_z, (a) at the longitudinal center of the domain ($x = 0$) and (b) along the magnet centerlines at $y = \pm\{0.5, 1.5, 2.5, 3.5, 4.5, 5.5, 6.5\}$. In (a), the experimental measurements at a height $z = 0.265$ (just above the dielectric-electrolyte interface) and at $z = 0.438$ (just below the electrolyte free surface) are shown, respectively, as open squares and filled circles. In (b), each type of black symbols indicates the experimental measurements at a height $z = 0.438$ along a specific magnet centerline. A least-squares fit has been performed using the data in (a) to determine the scaling factor for the dipole summation; the scaled dipole summation magnetic field is shown as the red lines. The experimental uncertainties are the size of the symbols or smaller.

3.2 Numerical Model of the Magnetic Field

In the discussion so far, the magnetic field profile as well as the resulting velocity field at very low driving near the center of the domain were modeled as being strictly

sinusoidal, for reasons of analytical convenience. The magnetic field away from the center of the domain, however, is fairly complicated. Fig. 3.1 shows the experimentally measured magnetic field spanning the entire transverse and longitudinal dimensions of the experimental domain. In Fig. 3.1 (a) the black symbols are the experimental measurements of B_z along the line $x = 0$, passing above the center of the magnet array at two different heights. Clearly, away from the center, the magnetic field profile deviates significantly from being a pure sinusoid. In Fig. 3.1 (b) the black symbols correspond to the magnetic field measurements along centerlines of the magnets. While the field is fairly uniform near the center of each magnet, which validates the analytical model for B_z used in section (2.2), it decays towards the ends of the magnet array.

To obtain a magnetic field profile that closely resembles the one in the experiment one can use a Hall-probe to measure the z-component of the magnetic field (B_z) across the entire flow domain at various heights above the magnet array. Using the measured field, one can then compute the depth-averaged forcing profile using a discrete version of equation (3.5). However, measuring B_z on a 3D grid is not only an extremely tedious process but also difficult, since the Hall-probe needs to be scanned along near-parallel planes above the magnet array. Moreover, Hall-probe measurements yield a vertically-averaged magnetic field strength as opposed to the true local field due to the finite thickness of the sensor (≈ 0.25 mm). To circumvent this difficulty, the magnetic field is numerically computed using a 3D model of the magnet array as described below.

To obtain a magnetic field everywhere within the electrolyte layer, each magnet is modeled as a 3D cubic lattice of identical dipoles, each with a dipole moment $\mathbf{m} = m\hat{\mathbf{z}}$, as shown in Fig. 3.2. Changing the sign of m across adjacent magnets accounts for the alternating direction of magnetization. Along each spatial direction, the magnet is resolved using 32 dipoles per unit length ($L = 1.27$ cm). Since the

dimensions of the array are $12 \times 14 \times 1/4$, approximately 2×10^6 dipoles are used to sample the magnet array. This resolution was tested to be sufficient to capture the spatial variation in the magnetic field.

The magnetic field at a location $\mathbf{r} = (x, y, z)$ within the electrolyte layer can then be approximated as the linear superposition of field contribution from all of the dipoles modeling the array, as follows:

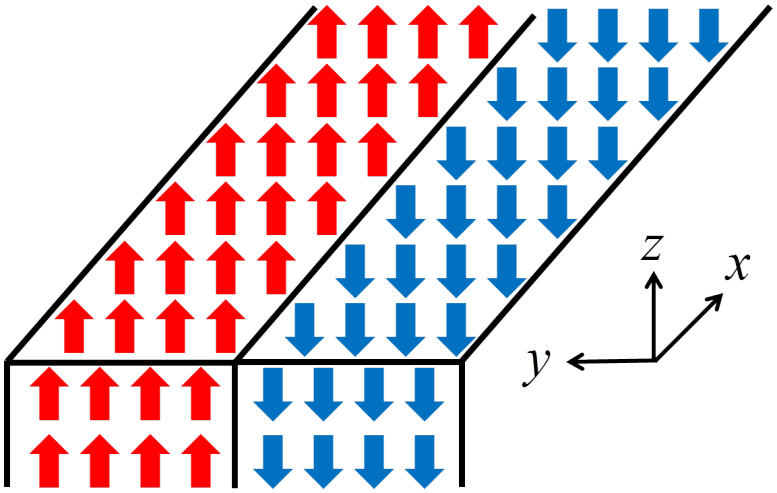

(a)

Figure 3.2: An illustration of the dipole model of the magnet array. The red and blue arrows indicate opposite directions of magnetization in adjacent magnets. A dipole density of 32 dipoles per magnet width (1.27 cm) is used to construct this 3D cubic lattice.

$$\mathbf{B}(\mathbf{r}) = \frac{\mu_0}{4\pi} \sum_{\mathbf{r}'} \left(\frac{3(\mathbf{r} - \mathbf{r}')\mathbf{m} \cdot (\mathbf{r} - \mathbf{r}')}{\|\mathbf{r} - \mathbf{r}'\|^5} - \frac{\mathbf{m}}{\|\mathbf{r} - \mathbf{r}'\|^3} \right). \tag{3.16}$$

Here, $\mathbf{r}'$ indicates the location of a point dipole within the lattice representing the magnet array. Since the field is the contribution from point-dipoles, this procedure shall be hereafter referred to as "dipole-summation".

Since the strength of the dipole m cannot be measured experimentally, a single scaling parameter is calculated from a least-squares fit with the experimental measurements, taken at the two heights shown in Fig. 3.1(a). The rescaled dipole summation magnetic field is shown in Fig. 3.1 (a) (red lines), along with the experimental measurements of B_z (black symbols), corresponding to the line $x = 0$ at heights $z = 0.265$

and $z = 0.438$. Fig. 3.1 (b) shows the magnetic field comparison at $z = 0.438$ along the magnet centerlines. This comparison confirms that the dipole-summation accurately captures the variation of the magnetic field both in the horizontal (x, y) as well as the vertical (z) directions in the electrolyte layer.

By computing the magnetic field $B_z(x, y, z)$ using the dipole summation at various heights, spaced Δz apart in the region $h_d < z < h_d + h_c$, one can compute the depth-averaged plane-parallel forcing $\langle \mathbf{F}_\parallel \rangle_z$ using a discrete version of the expression (3.5),

$$\langle \mathbf{F}_\parallel \rangle_z = \frac{J\Delta z}{h_d + h_c} \sum_{k=0}^{h_c/\Delta z} B_z(x, y, h_d + k\Delta z)\, \hat{\mathbf{x}}. \tag{3.17}$$

J is the magnitude of the current density calculated from geometrical considerations (cf. section (2.1)).

While the functional dependence of depth-averaged magnetic field, and consequently the forcing $\langle \mathbf{F}_\parallel \rangle_z$, on the horizontal coordinates x, y is fairly complicated near the end-walls and side-walls, it is accurately approximated using the equation

$$\langle \mathbf{F}_\parallel \rangle_z \cdot \hat{\mathbf{x}} \approx B_{0\kappa}(\kappa y) + B_\kappa \sin(\kappa y) + B_{3\kappa} \sin(3\kappa y) + B_{5\kappa} \sin(5\kappa y), \tag{3.18}$$

in the region $|x| \leq 4$ and $|y| \leq 4$. The amplitudes $B_{0\kappa}, B_{3\kappa}, B_{5\kappa}$, relative to the amplitude B_κ of the $\sin(\kappa y)$ term, are approximately 0.001, 0.045, and 0.003, respectively. Hence, the contribution from the fifth and higher harmonics is negligible compared to the first and third ones. Lastly, over the span of 8 magnets, the change in the local amplitude of the sinusoidal profile relative to B_κ, given by $8\pi B_{0\kappa}$, is approximately 0.01.

Lastly, the dipole summation yields all three components of the Lorentz force density at any location (x, y, z) within the electrolyte layer; $\mathbf{F} = \mathbf{J} \times \mathbf{B} = JB_z\hat{\mathbf{x}} - JB_x\hat{\mathbf{z}}$, where B_x is the x component of the magnetic field. The numerical model, as well as the experimental measurements, show that the typical value of B_x is less than 3% of the value of B_z at any given location within the electrolyte away from the walls. This component of the Lorentz force, the gravitational force, and the vertical gradient in

the pressure add to zero approximately (cf. equation (3.2)). Hence, the Lorenz force density, for all practical purposes, can be treated as being horizontal.

3.3 Numerical Simulations of the 2D Model

A realistic model of the forcing, like the one discussed above, has not been employed in previous studies of Kolmogorov-like flows [80, 95]. This was, in part, because the governing equations were exclusively solved on domains periodic in both horizontal directions. The rationale behind assuming periodicity is that for sufficiently large domains, the dynamics at the center are unaffected by the boundaries. While this may be a valid assumption for testing statistical properties, there has been no validation that periodic simulations quantitatively capture flow structure and dynamics observed in experiments. To address this shortcoming of previous studies, a numerical simulation with realistic no-slip boundary conditions is developed in the following sections, with the goal of quantitative comparison between simulation and experiment.

3.3.1 Temporal Discretization: P2 Projection Scheme

Temporal integration of the governing equation (3.14) corresponds to the following problem: given the velocity $\mathbf{u}(x, y, t)$ and pressure $p(x, y, t)$ fields at an instant t, how does one compute the fields $\mathbf{u}(x, y, t+\Delta t)$ and $p(x, y, t+\Delta t)$ at a later instant $t+\Delta t$, with $\nabla \cdot \mathbf{u}(x, y, t + \Delta t) = 0$? By repeating such updating procedure, one should be able to approximate the spatiotemporal evolution of the flow governed by equation (3.14) for arbitrarily long times.

Historically, the difficulty associated with accomplishing such integration for incompressible flows was traced [116] to the lack of an equation which governs the evolution of pressure p. To elaborate, consider a discrete sampling of the velocity $\mathbf{u} = u\,\hat{\mathbf{x}} + v\,\hat{\mathbf{y}}$ at points on a rectangular grid of dimensions $n_x \times n_y$, similar to that in the experiment (Fig. 2.3(c)). The governing equation (3.14) yields $2 \times n_x \times n_y$ coupled equations which determine the update of the local velocities u and v at these $n_x \times n_y$

locations. However, one needs an additional $n_x \times n_y$ equations that govern the update of pressure, which are missing. The workaround, originally proposed by Chorin and Temam [116, 117], is relating these "missing" $n_x \times n_y$ equations to the additional $n_x \times n_y$ equations arising from the incompressibility condition[1]. Numerical schemes solving incompressible flows [118, 119] developed along the lines of Chorin-Temam's idea have come to be known as "projection" or "fractional-step" schemes, for reasons that will become obvious in the following paragraphs.

For reasons of notational brevity, the governing equation will henceforth be written as

$$\begin{aligned} \partial_t \mathbf{u} &= -\nabla p + \mathcal{L}\mathbf{u} - \mathcal{N}\mathbf{u} + \mathbf{f}_0, \\ \nabla \cdot \mathbf{u} &= 0, \end{aligned} \tag{3.19}$$

where,

$$\mathcal{L}\mathbf{u} = \frac{1}{Re}\left(\nabla^2 \mathbf{u} - \gamma \mathbf{u}\right) \quad \text{and} \quad \mathcal{N}\mathbf{u} = \beta \mathbf{u} \cdot \nabla \mathbf{u} \tag{3.20}$$

represent the linear and nonlinear terms in the evolution equation.

The specific fractional-step scheme employed in this work is popularly known as the P2 projection scheme [120], originally proposed by Van Kan [119]. A clear description of this second-order scheme, as well as a couple of other projection schemes, can be found in Armfield *et al.* [121, 122]. Consider the following *semi-implicit* temporal discretization of the governing equation (3.19)

$$\begin{aligned} \frac{\mathbf{u}^{k+1} - \mathbf{u}^k}{\Delta t} &= -\nabla p^{k+1} + \frac{1}{2}\left(\mathcal{L}\mathbf{u}^{k+1} + \mathcal{L}\mathbf{u}^k\right) - \left(\frac{3}{2}\mathcal{N}\mathbf{u}^k - \frac{1}{2}\mathcal{N}\mathbf{u}^{k-1}\right) + \mathbf{f}_0, \\ \nabla \cdot \mathbf{u}^{k+1} &= 0 \end{aligned} \tag{3.21}$$

In the above equation, k quantifies a discrete instant of time $t = k\Delta t$; the velocity and pressure fields at the instant $k\Delta t$ are denoted by $\mathbf{u}^k$ and p^k, respectively. As can

[1] A nice introduction to numerical aspects of incompressible flows can be found in Prof. James M. McDonough's lecture notes available at `http://www.engr.uky.edu/~acfd/lecturenotes.html`

be seen, the linear terms in the momentum equation are updated using the second-order implicit Crank-Nicolson method, while the nonlinear term is updated using the second-order explicit Adams-Bashforth method. Note that the spatial and temporal discretizations in the above formulation are decoupled, making it a semi-discrete form [123] of equation (3.19).

The basic idea behind the P2, as well as other projection/fractional-step methods, is to split the momentum equation (3.19) into two or more sub-equations/sub-steps, which, when "added", satisfy the discrete form given by equation (3.21). In the following paragraphs, references to the first-order Chorin-Temam P1 scheme are also made. The P1 scheme follows a similar discretization as that in equation (3.21), except that Crank-Nicholson and Adams-Bashforth methods are replaced with the first-order forward Euler method.

In the first step of the P2 scheme, the initial velocity field is updated to an intermediate field $\mathbf{u}^*$ as follows:

$$\frac{\mathbf{u}^* - \mathbf{u}^k}{\Delta t} = -\nabla p^k + \frac{1}{2}\left(\mathcal{L}\mathbf{u}^* + \mathcal{L}\mathbf{u}^k\right) - \left(\frac{3}{2}\mathcal{N}\mathbf{u}^k - \frac{1}{2}\mathcal{N}\mathbf{u}^{k-1}\right) + \mathbf{f}_0, \tag{3.22}$$

where the intermediate velocity field is not divergence free $\nabla \cdot \mathbf{u}^* \neq 0$. The above update using the implicit viscous term $\mathcal{L}\mathbf{u}^*$ (cf. equation (3.20)) requires specifying the boundary conditions on $\mathbf{u}^*$ which are related to spatial discretization. There have been quite a few suggestions [116–120] in the literature regarding how these can be chosen, depending on the exact spatial discretization of the fields, a discussion of which is far too complicated in the present context. For the discretization on a "staggered" grid, which will be presented in the next section, the procedure suggested in [119, 121] is followed, wherein a zero-velocity Dirichlet condition is imposed on $\mathbf{u}^*$ on the boundary ($\partial\Omega$), i.e.,

$$\mathbf{u}^*|_{\partial\Omega} = 0. \tag{3.23}$$

Using Helmholtz-Hodge decomposition, one can then express $\mathbf{u}^*$ as a sum of a "divergence-free/solenoidal" vector field and a "gradient/conservative" vector field as below:

$$\mathbf{u}^* = \nabla \times \mathbf{A} + \nabla\Psi, \tag{3.24}$$

wherein, the first term represents the divergence free part, since $\nabla \cdot (\nabla \times \mathbf{A}) = 0$ for a smooth vector field, while the second term represents the conservative part, since $\nabla \times \nabla\Psi = 0$ for a scalar field Ψ. Using the interpretation $\mathbf{u}^{k+1} = \nabla \times \mathbf{A}$ and $\nabla\Phi = 1/\Delta t\ \nabla\Psi$, one can write

$$\mathbf{u}^* = \mathbf{u}^{k+1} + \Delta t \nabla\Phi, \tag{3.25}$$

such that $\nabla \cdot \mathbf{u}^{k+1} = 0$.

Φ can be obtained by solving the Poisson's equation resulting from taking the divergence of the above equation:

$$\nabla^2\Phi = \frac{1}{\Delta t}\nabla \cdot \mathbf{u}^*. \tag{3.26}$$

The boundary conditions on Φ are homogeneous Neumann type, which result directly from equation (3.25), since $\mathbf{u}^*|_{\partial\Omega} = 0$, i.e.,

$$\nabla\Phi \cdot \hat{\mathbf{n}}|_{\partial\Omega} = (\mathbf{u}^*|_{\partial\Omega} - \mathbf{u}^{k+1}|_{\partial\Omega}) \cdot \hat{\mathbf{n}} = 0, \tag{3.27}$$

where $\hat{\mathbf{n}}$ is the unit vector normal to the boundary. Finally, $\mathbf{u}^{k+1}$ can then be computed using equation (3.25), $\mathbf{u}^{k+1} = \mathbf{u}^* - \Delta t\nabla\Phi$.

The equation for pressure update is obtained by substituting the expression for $\mathbf{u}^*$ from equation (3.25) into equation (3.22) and rearranging the terms, which results in the following equation:

$$\frac{\mathbf{u}^{k+1} - \mathbf{u}^k}{\Delta t} = \left(-\nabla p^k - \nabla\Phi + \frac{\Delta t}{2}\nabla\mathcal{L}\Phi\right) + \frac{1}{2}\left(\mathcal{L}\mathbf{u}^{k+1} + \mathcal{L}\mathbf{u}^k\right) - \left(\frac{3}{2}\mathcal{N}\mathbf{u}^k - \frac{1}{2}\mathcal{N}\mathbf{u}^{k-1}\right) + \mathbf{f}_0 \tag{3.28}$$

which, on comparison with equation (3.21), yields the pressure update formula,

$$p^{k+1} = p^k + \Phi - \frac{\Delta t}{2}\mathcal{L}\Phi. \tag{3.29}$$

In the above equation, the last term is a higher order correction, and hence, for all practical purposes can be omitted without compromising the accuracy of the update, as suggested in [121].

An important distinction between the P1 and P2 schemes, besides the temporal discretization of the linear and nonlinear terms, is the interpretation of pressure; the P1 scheme treats it as a mathematical artifact [124], by setting $p^{k+1} = \Phi$ after the velocity correction given by equation (3.25)[121]. In contrast, the P2 scheme uses Φ to correct the pressure with the update formula (3.29), giving a more accurate computation. The difference in the velocity fields $\mathbf{u}^{k+1}$ is rather negligible, since the correction equation (3.25) is identical across the two schemes and is performed after the velocity is rendered divergence free. The difference, in the velocity fields, however, if any, is localized to a narrow layer of thickness $\sqrt{\nu \Delta t}$ near the boundary [119, 121].

The P2 projection scheme requires the nonlinear term at $k = -1$, i.e., $\mathcal{N}\mathbf{u}^{(-1)}$, to update the initial velocity $\mathbf{u}^0$. In such case, setting $\mathcal{N}\mathbf{u}^{(-1)} = \mathcal{N}\mathbf{u}^0$ offers an easy fix, wherein one converts the second-order Adams-Bashforth scheme to a first-order forward Euler scheme, resulting in a P1 projection step. However, as an after fix, one can still recover the P2 projection by repeating the first update step, by replacing $3/2\,\mathcal{N}\mathbf{u}^0 - 1/2\,\mathcal{N}\mathbf{u}^{-1}$ with the mid-point rule $3/2\,\mathcal{N}\mathbf{u}^0 + 1/2\,\mathcal{N}\mathbf{u}^1$, wherein $\mathcal{N}\mathbf{u}^1$ is computed using P1, as suggested by Van Kan [119]. This trick is very useful when initializing the integrator with velocity fields from the experiment.

3.3.2 Spatial Discretization Using Finite Differences

The velocity and pressure fields in equation (3.14) are discretized on a "staggered" or marker and cell (MAC) grid, originally proposed by Harlow *et al.* [125] in the context of numerical simulation of free-surface flows. A schematic of the grid is shown in Fig. 3.3(a). The domain, with dimensions identical to the experiment and indicated by the red boundary in Fig. 3.3(a), is divided into $n_x \times n_y$ cells. The pressure p is

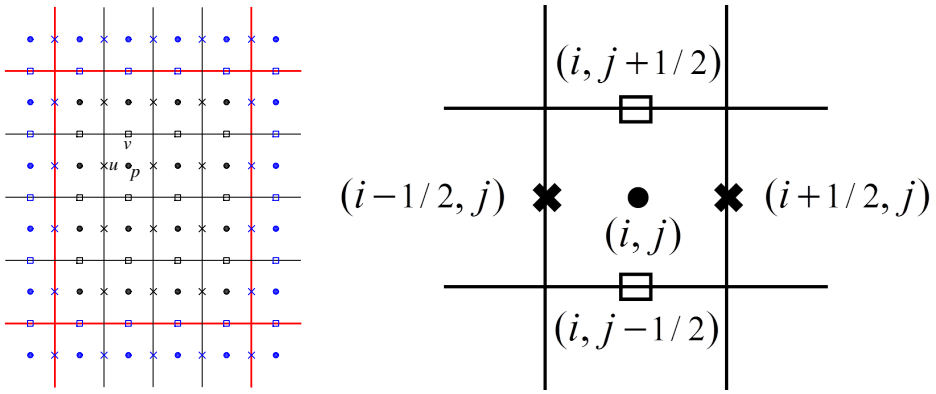

(a) (b)

Figure 3.3: An illustration of the staggered grid used for the numerical simulation. In (a) the red lines indicate the boundaries of the domain, which is identical in lateral dimensions to the one used in the experiment Fig. 2.1(a). The dots represent cell centers where the pressure is defined. The crosses represent locations of the $u-$velocity, and the squares represent locations of $v-$velocity grid points. Black symbols represent the interior grid, which is numerically solved for. The blue symbols represent "ghost" points in the exterior, which are updated to enforce boundary conditions. In (b) a zoomed in version of an interior cell is shown, along with indices used to denote the various locations.

defined at the center of the cells, while the velocities are defined on the cell faces; the $u-$velocity on the left and right faces, and the $v-$velocity of the top and bottom faces, as highlighted in Fig. 3.3(b). The staggered grid is an overlap of three rectangular grids, shifted relative to one another. The p grid has dimensions $n_x \times n_y$, while the u and v grids have dimensions $(n_x - 1) \times n_y$ and $n_x \times (n_y - 1)$, respectively. Owing to the different sizes and positions of the three grids, it is conventional to refer to the number of cells $n_x \times n_y$ as the grid dimensions. Consequently, the cell centers are denoted using (i, j), the right and left faces using $(i \pm 1/2, j)$, and the top and bottom faces using $(i, j \pm 1/2)$, respectively. Since the Kolmogorov forcing points only in the x direction, $\mathbf{f_0} = f_x\,\hat{\mathbf{x}}$ in equation (3.14) is computed on the u grid, to avoid interpolating the forcing profile. While a co-located grid, wherein u, v and p are all defined at the same location, is convenient with regard to setting up the simulation, it is known to suffer from "odd-even" decoupling, which is avoided by

using the staggered grid [125].

Using the above notation, the interpolations of the u and v velocity fields at the cell centers is given as below:

$$u(i,j) = \frac{u(i+1/2,j) + u(i-1/2,j)}{2}, \quad v(i,j) = \frac{v(i,j+1/2) + v(i,j-1/2)}{2}. \tag{3.30}$$

Note that the corners of cells – the nodes – are denoted by the indices $(i \pm 1/2, j \pm 1/2)$, where similar averaging formulas for u, v can be derived; for example,

$$\begin{aligned} u(i-1/2,j+1/2) &= \frac{u(i-1/2,j) + u(i-1/2,j+1)}{2}, \\ v(i-1/2,j+1/2) &= \frac{v(i-1,j+1/2) + v(i,j+1/2)}{2}. \end{aligned} \tag{3.31}$$

The advantage of using a staggered grid becomes apparent when using "finite-differences" to approximate the spatial derivatives required at various stages of the numerical scheme. For example, the update of a velocity component u, following equation (3.22), requires computing the quantities $\partial_x p$, $\nabla^2 u$, as well as the nonlinear term $u\partial_x u + v\partial_y u$, all at the same location as u is defined. For the u update, the pressure gradient is discretized using the following approximation, which maps $\partial_x p$ onto the u grid (cf. Fig. 3.3(b)).

$$\partial_x p(i+1/2,j) = \frac{p(i+1,j) - p(i,j)}{\Delta x}. \tag{3.32}$$

The Laplacian $\nabla^2 = (\partial_x^2 + \partial_y^2)$ of u in the diffusion term is discretized using the second-order five-point stencil formula as,

$$\begin{aligned} \nabla^2 u(i+1/2,j) = &\frac{u(i+3/2,j) + u(i-1/2,j) - 2u(i+1/2,j)}{(\Delta x)^2} + \\ &\frac{u(i+1/2,j+1) + u(i+1/2,j-1) - 2u(i+1/2,j)}{(\Delta y)^2}, \end{aligned} \tag{3.33}$$

with the two terms in the right hand side of the equation representing $\partial_x^2 u$ and $\partial_y^2 u$, respectively.

The discretization of the nonlinear term, however, requires some explanation, both from theoretical and numerical standpoints. To begin with, consider the nonlinear

term in the u equation which is given by $u\partial_x u + v\partial_y u$. The operators $u\partial_x$ and $v\partial_y$ acting on u denote the net flux of u along the x and y directions, as transported by u and v velocities. Using the three point central difference formula for $u\partial_x u$, one obtains,

$$u\partial_x u(i+1/2,j)\big|_{cd} = u(i+1/2,j)\left(\frac{u(i+3/2,j)-u(i-1/2,j)}{2\Delta x}\right). \tag{3.34}$$

The concern with the central differencing approximation is that it is inaccurate in modeling the transport nature of convective terms [123]. When $|u(i+1/2,j)|\Delta t$ becomes nearly equal to Δx in magnitude, the fluid particles are carried about one cell width in one time step Δt. This results in the central difference approximation yielding unphysical[2] results since, if $u(i+1/2,j)$ is positive, the above discretization includes transport from a"downstream" location $u(i+3/2,j)$. In such case, one should modify the approximation in equation (3.34) to include transport from "upstream" points. The simplest alternative, in such case, is to use an *upwind* approximation of the derivative, given by

$$u\partial_x u\big|_{\text{uw}} = \begin{cases} u(i+1/2,j)\left(\dfrac{u(i+1/2,j)-u(i-1/2,j)}{\Delta x}\right) \forall u(i+1/2,j) > 0, \\ u(i+1/2,j)\left(\dfrac{u(i+3/2,j)-u(i+1/2,j)}{\Delta x}\right) \forall u(i+1/2,j) < 0. \end{cases}$$

Another motivation behind employing upwinding is to add numerical dissipation to stabilize the central differencing scheme[126]. This becomes obvious in the discretization of term $v\partial_y u$, which, using central differencing results in,

$$v\partial_y u(i+1/2,j)\big|_{\text{cd}} = v(i+1/2,j)\left(\frac{u(i+1/2,j+1)-u(i+1/2,j-1)}{2\Delta y}\right). \tag{3.35}$$

The above discrete approximation is independent of the $u-$velocity at $(i+1/2,j)$, where the quantity is being computed, rendering it neutrally stable to perturbations/noise in $u(i+1/2,j)$ [127]. While its accuracy as an approximation is not

[2]This unphysical nature of discretization is always present, irrespective of the flow speed, it is most easily explained when $U\Delta t/\Delta x \approx 1$

questionable, it is well-established that central difference approximations to model convective derivatives, even those computed using higher-order stencils, result in undamped oscillations [126–128]. The truncation terms from the upwinding act as "numerical" diffusion which suppresses such oscillations.

Since a pure upwinding approximation can lead to significant diffusion[3] one workaround, to include the merits of both the schemes as (originally) proposed by Spalding [129] and (later) by Hirt [126], is to blend central differencing with the upwinding as follows:

$$u\partial_x u = (1-b)\cdot u\partial_x u\big|_{\text{cd}} + b\cdot u\partial_x u\big|_{\text{uw}} \tag{3.36}$$

where, b is the blending parameter given by

$$b = \min(1.2\max(|u|\Delta t/\Delta x, |v|\Delta t/\Delta y), 1). \tag{3.37}$$

As the flow becomes strongly convective, b tends to unity and the scheme smoothly transitions from central differencing to upwinding. The term, $\max(|u|\Delta t/\Delta x, |v|\Delta t/\Delta y)$, called the Courant–Friedrichs–Lewy (CFL) number of the flow, needs to be maintained below unity and provides an upper limit on the time step [130]. A safety factor of 1.2 is chosen [126, 131] to ensure one does not encounter CFL ≥ 1. For all the simulations presented in the thesis, CFL ≤ 0.5 was maintained to ensure the finite difference approximation yields physically meaningful results.

The above discussion of discretization entirely focused on the update of u; the discretization of operators in the v velocity update as well as the other steps (the solution to Poisson's equation (3.26) in the P2 projection scheme) are dealt with in a similar manner. Lastly, the above index notation for the cells leaves the boundaries on half-index points, much like the velocities. The location of the end-walls (cf. section (2.1)) on the grid corresponds to indices $(1/2, j)$ and $(n_x + 1/2, j)\,\forall j$, while that of the side-walls corresponds to indices $(i, 1/2)$ and $(i, n_y + 1/2)\,\forall i$. The "ghost" points,

[3]Both central differencing and upwinding give identical results in the asymptotic limit of grid resolution going to infinity.

which store the boundary conditions of u and v are then assigned the values given in Table 3.2

Table 3.2: Updating the ghost point values of u and v using the interior points in the bounded simulation.

	u	v
$x = -L_x/2$	$u(1/2, j) = 0$	$v(0, j + 1/2) = -v(1, j + 1/2)$
$x = L_x/2$	$u(n_x + 1/2, j) = 0$	$v(n_x + 1, j + 1/2) = -v(n_x, j + 1/2)$
$y = -Ly/2$	$u(i + 1/2, 0) = -u(i + 1/2, 1)$	$v(j, 1/2) = 0$
$y = L_y/2$	$u(i + 1/2, n_y + 1) = -u(i + 1/2, n_y)$	$v(i, n_y + 1/2) = 0$

Lastly, note that the update to u requires computing $\partial_x p$, while the update to v requires computing $\partial_y p$. Since the interior points uniquely define the flow, the position of the u, v grids ensures there is no explicit specification of boundary condition for pressure [122]. Only equation (3.26) requires specifying boundary conditions on the pressure grid, which are implicitly handled in the numerical implementation.

3.3.3 Spatiotemporal Integration

The experimental domain, of size $L_x = 14$ and $L_y = 18$ in units of characteristic length scale $L = 1.27$ cm, is discretized using 20 cells per unit length, resulting in a grid of dimensions 280×360 for the interior of the domain. The grid spacing, in both the directions, is $\Delta x = \Delta y = 0.05$. The dimensions of the pressure grid are the same as that of the number of cells. The dimensions of the u and v grids in the interior of the domain are $(n_x - 1) \times n_y = 279 \times 360$ and $n_x \times (n_y - 1) = 280 \times 359$, respectively. Details of convergence tests demonstrating the adequacy of the spatiotemporal resolution is included in Appendix B.

The numerical implementation of the integrator is performed using MATLAB[4],

[4]A detailed discussion of the implementation of a Navier-Stokes solver (P1-scheme) is presented in Gilbert Strang's Computational Science and Engineering.

which is very efficient in solving linear equations, like those for the velocity update in equation (3.22) and the solution to Poisson's equation (3.26). Herein, a detailed discussion of solving the u equation is provided; the solution to v equations follows an identical procedure. If $\mathbf{I}$ is the identity matrix, and $\mathbf{L}_u$ is the matrix representation of the Laplacian acting on the discretized field u, as in equation (3.33), the update from u to u^* is the solution to the linear equation,

$$\underbrace{\left(\mathbf{I} + \frac{\gamma \Delta t}{2Re}\mathbf{I} - \frac{\Delta t}{2Re}\mathbf{L}_u\right)}_{=\mathbf{A}} u^*(:) = b(:), \tag{3.38}$$

where,

$$b = u^k + \Delta t \left(-\partial_x p^k + \frac{1}{2}\mathcal{L}u^k - \left(\frac{3}{2}\mathcal{N}u^k - \frac{1}{2}\mathcal{N}u^{k-1}\right) + f_x\right), \tag{3.39}$$

is the right-hand-side of the linear update in which the terms are computed using the difference formulas in equations (3.32), (3.40), (3.36), requiring no matrix multiplications.

In the above equations, following MATLAB notation, (:) denotes recasting a 2D grid[5] into a 1D column vector, such that the columns of the 2D grid are placed one below the other; for u the 2D grid is of dimensions $(n_x - 1) \times n_y$ and $u(:)$ is of dimensions $(n_x - 1)n_y \times 1$. Consequently, the matrices $\mathbf{I}$ and $\mathbf{L}_u$ acting on $u(:)$ have dimensions $(n_x - 1)n_y \times (n_x - 1)n_y$. For a sample grid of dimensions 4×4 cells shown in Fig. 3.3 the corresponding u grid has dimensions 3×4, leading to $\mathbf{I}$ and $\mathbf{L}_u$ having dimensions 12×12. Since $\nabla^2 = \partial_x^2 + \partial_y^2$, using the notation $\mathbf{D}_{xu} = \partial_x^2$ and $\mathbf{D}_{yu} = \partial_y^2$ on the u grid, $\mathbf{L}_u u(:)$ can be expressed as $\mathbf{D}_{xu}u(:) + \mathbf{D}_{yu}u(:)$, where $\mathbf{D}_{xu}u(:)$

[5]The actual implementation of this in MATLAB is a little different, since the rows indicate the y coordinates in the physical grid, and columns indicating the x coordinate. Hence a point (i, j) on the grid corresponds to index (j, i) in the 2D matrix. This additional level of complexity is being ignored for illustration purposes and u, as well as other variables, are denoted using the physical grid coordinates.

and $\mathbf{D}_{yu}u(:)$ are given by,

$$\mathbf{D}_{xu}u(:) = \frac{1}{(\Delta x)^2}\begin{bmatrix} -2 & 0 & 0 & 0 & 1 & 0 & 0 & 0 & 0 & 0 & 0 & 0 \\ 0 & -2 & 0 & 0 & 0 & 1 & 0 & 0 & 0 & 0 & 0 & 0 \\ 0 & 0 & -2 & 0 & 0 & 0 & 1 & 0 & 0 & 0 & 0 & 0 \\ 0 & 0 & 0 & -2 & 0 & 0 & 0 & 1 & 0 & 0 & 0 & 0 \\ 1 & 0 & 0 & 0 & -2 & 0 & 0 & 0 & 1 & 0 & 0 & 0 \\ 0 & 1 & 0 & 0 & 0 & -2 & 0 & 0 & 0 & 1 & 0 & 0 \\ 0 & 0 & 1 & 0 & 0 & 0 & -2 & 0 & 0 & 0 & 1 & 0 \\ 0 & 0 & 0 & 1 & 0 & 0 & 0 & -2 & 0 & 0 & 0 & 1 \\ 0 & 0 & 0 & 0 & 1 & 0 & 0 & 0 & -2 & 0 & 0 & 0 \\ 0 & 0 & 0 & 0 & 0 & 1 & 0 & 0 & 0 & -2 & 0 & 0 \\ 0 & 0 & 0 & 0 & 0 & 0 & 1 & 0 & 0 & 0 & -2 & 0 \\ 0 & 0 & 0 & 0 & 0 & 0 & 0 & 1 & 0 & 0 & 0 & -2 \end{bmatrix}\begin{bmatrix} u(3/2,1) \\ u(3/2,2) \\ u(3/2,3) \\ u(3/2,4) \\ u(5/2,1) \\ u(5/2,2) \\ u(5/2,3) \\ u(5/2,4) \\ u(7/2,1) \\ u(7/2,2) \\ u(7/2,3) \\ u(7/2,4) \end{bmatrix} \tag{3.40}$$

$$\mathbf{D}^2_{yu}u(:) = \frac{1}{(\Delta y)^2}\begin{bmatrix} -3 & 1 & 0 & 0 & 0 & 0 & 0 & 0 & 0 & 0 & 0 & 0 \\ 1 & -2 & 1 & 0 & 0 & 0 & 0 & 0 & 0 & 0 & 0 & 0 \\ 0 & 1 & -2 & 1 & 0 & 0 & 0 & 0 & 0 & 0 & 0 & 0 \\ 0 & 0 & 1 & -3 & 0 & 0 & 0 & 0 & 0 & 0 & 0 & 0 \\ 0 & 0 & 0 & 0 & -3 & 1 & 0 & 0 & 0 & 0 & 0 & 0 \\ 0 & 0 & 0 & 0 & 1 & -2 & 1 & 0 & 0 & 0 & 0 & 0 \\ 0 & 0 & 0 & 0 & 0 & 1 & -2 & 1 & 0 & 0 & 0 & 0 \\ 0 & 0 & 0 & 0 & 0 & 0 & 1 & -3 & 0 & 0 & 0 & 0 \\ 0 & 0 & 0 & 0 & 0 & 0 & 0 & 0 & -3 & 1 & 0 & 0 \\ 0 & 0 & 0 & 0 & 0 & 0 & 0 & 0 & 1 & -2 & 1 & 0 \\ 0 & 0 & 0 & 0 & 0 & 0 & 0 & 0 & 0 & 1 & -2 & 1 \\ 0 & 0 & 0 & 0 & 0 & 0 & 0 & 0 & 0 & 0 & 1 & -3 \end{bmatrix}\begin{bmatrix} u(3/2,1) \\ u(3/2,2) \\ u(3/2,3) \\ u(3/2,4) \\ u(5/2,1) \\ u(5/2,2) \\ u(5/2,3) \\ u(5/2,4) \\ u(7/2,1) \\ u(7/2,2) \\ u(7/2,3) \\ u(7/2,4) \end{bmatrix} \tag{3.41}$$

The subscripts, for example in $\mathbf{D}_{xu}$ matrix, indicate that the derivative is computed along the x direction specifically for the u grid. The boundary conditions on $\mathbf{u}^*$, analogous to the ones given by Table 3.2, are implicit in the construction of the $\mathbf{L}_u$. The above matrix multiplication yields the five-point stencil formula given by equation (3.33) for every interior point of the u grid.

For $n_x = 280, \quad n_y = 360$, as is the case with the simulations presented in this thesis, $n_x n_y$ is of the order 10^5. The velocity update, given in equation (3.38), corresponds to solving the linear equation $\mathbf{A}u^*(:) = b(:)$, with $\mathbf{A}$ having dimensions

$\approx 10^5 \times 10^5$. Since $\mathbf{L}_u$ and $\mathbf{I}$ are symmetric sparse matrices, i.e., they have few non-zero elements, one can solve the system of linear equation using MATLAB's "A solve b" command, i.e., $u^*(:) = \mathbf{A}\backslash b(:)$. However, the efficiency of the computation can be increased using "Cholesky" decomposition of $\mathbf{A}$, resulting in $u^*(:) = \mathbf{T}^u\backslash\mathbf{T}_u\backslash b(:)$, where $\mathbf{T}^u, \mathbf{T}_u$ are upper and lower triangular matrices such that $\mathbf{A} = \mathbf{T}_u\mathbf{T}^u$. Similar matrix representations for the v velocity update, as well as the solution of the projection-step in equation (3.25), can be constructed.

3.3.4 Numerical Aspects of Solving Poisson's Equation

For the solution of the Poisson's equation, given by equation (3.26) however, there are a few subtleties that deserve attention. The first of these is the "compatibility condition" that should be satisfied for the Poisson-Neumann problem [132]. Consider a general form of the Poisson's equation with a source term g, with Neumann type conditions ($\nabla\Phi \cdot \hat{\mathbf{n}}$) defined on the boundary ($\partial\Omega$),

$$\nabla^2\Phi(x, y) = g(x, y), \tag{3.42}$$

Setting $g = \frac{1}{\Delta t}\nabla \cdot \mathbf{u}^*$ and $\nabla\Phi \cdot \hat{\mathbf{n}}\big|_{\partial\Omega} = 0$ yields equation (3.26). Taking a spatial integral of the above Poisson's equation over the domain Ω, one arrives at the compatibility condition[6]

$$\int_\Omega \nabla^2\Phi \, dx \, dy = \int_\Omega g \, dx \, dy \implies \int_{\partial\Omega} \nabla\Phi \cdot \hat{\mathbf{n}} = \int_\Omega g \, dx \, dy. \tag{3.43}$$

For homogeneous Neumann boundary conditions the compatibility condition requires $\int_\Omega g \, dx \, dy = 0$ for the solution Φ to exist. This requirement is satisfied in the formulation of the projection step, and its discrete approximation, since $\int_\Omega \nabla \cdot \mathbf{u}^* dx \, dy = \sum_{i,j}(\nabla\cdot\mathbf{u})(i, j) = 0$. For arbitrary test functions g, however, the problem may become ill-posed.

[6]For the physicist, the compatibility condition is 2D Gauss's law, which requires that the net charge in a region is equal to the net flux of the gradient field due to the charge crossing the enclosing boundary.

The second important aspect is the singularity of the discrete "Poisson-Neumann" matrix with homogeneous Neumann boundary conditions. The discrete Laplacian, for the sample 4×4 grid, is once again given as the summation $\mathbf{L}_p = \mathbf{D}_{xp}^2 + \mathbf{D}_{yp}^2$, with

$$\mathbf{D}_{xp}^2\Phi(:) = \frac{1}{(\Delta x)^2}\begin{bmatrix} -1 & 0 & 0 & 0 & 1 & 0 & 0 & 0 & 0 & 0 & 0 & 0 & 0 & 0 & 0 & 0 \\ 0 & -1 & 0 & 0 & 0 & 1 & 0 & 0 & 0 & 0 & 0 & 0 & 0 & 0 & 0 & 0 \\ 0 & 0 & -1 & 0 & 0 & 0 & 1 & 0 & 0 & 0 & 0 & 0 & 0 & 0 & 0 & 0 \\ 0 & 0 & 0 & -1 & 0 & 0 & 0 & 1 & 0 & 0 & 0 & 0 & 0 & 0 & 0 & 0 \\ 1 & 0 & 0 & 0 & -2 & 0 & 0 & 0 & 1 & 0 & 0 & 0 & 0 & 0 & 0 & 0 \\ 0 & 1 & 0 & 0 & 0 & -2 & 0 & 0 & 0 & 1 & 0 & 0 & 0 & 0 & 0 & 0 \\ 0 & 0 & 1 & 0 & 0 & 0 & -2 & 0 & 0 & 0 & 1 & 0 & 0 & 0 & 0 & 0 \\ 0 & 0 & 0 & 1 & 0 & 0 & 0 & -2 & 0 & 0 & 0 & 1 & 0 & 0 & 0 & 0 \\ 0 & 0 & 0 & 0 & 1 & 0 & 0 & 0 & -2 & 0 & 0 & 0 & 1 & 0 & 0 & 0 \\ 0 & 0 & 0 & 0 & 0 & 1 & 0 & 0 & 0 & -2 & 0 & 0 & 0 & 1 & 0 & 0 \\ 0 & 0 & 0 & 0 & 0 & 0 & 1 & 0 & 0 & 0 & -2 & 0 & 0 & 0 & 1 & 0 \\ 0 & 0 & 0 & 0 & 0 & 0 & 0 & 1 & 0 & 0 & 0 & -2 & 0 & 0 & 0 & 1 \\ 0 & 0 & 0 & 0 & 0 & 0 & 0 & 0 & 1 & 0 & 0 & 0 & -1 & 0 & 0 & 0 \\ 0 & 0 & 0 & 0 & 0 & 0 & 0 & 0 & 0 & 1 & 0 & 0 & 0 & -1 & 0 & 0 \\ 0 & 0 & 0 & 0 & 0 & 0 & 0 & 0 & 0 & 0 & 1 & 0 & 0 & 0 & -1 & 0 \\ 0 & 0 & 0 & 0 & 0 & 0 & 0 & 0 & 0 & 0 & 0 & 1 & 0 & 0 & 0 & -1 \end{bmatrix}\begin{bmatrix} \Phi(1,1) \\ \Phi(1,2) \\ \Phi(1,3) \\ \Phi(1,4) \\ \Phi(2,1) \\ \Phi(2,2) \\ \Phi(2,3) \\ \Phi(2,4) \\ \Phi(3,1) \\ \Phi(3,2) \\ \Phi(3,3) \\ \Phi(3,4) \\ \Phi(4,1) \\ \Phi(4,2) \\ \Phi(4,3) \\ \Phi(4,4) \end{bmatrix}$$

$$\mathbf{D}_{yp}^2\Phi(:) = \frac{1}{(\Delta y)^2}\begin{bmatrix} -1 & 1 & 0 & 0 & 0 & 0 & 0 & 0 & 0 & 0 & 0 & 0 & 0 & 0 & 0 & 0 \\ 1 & -2 & 1 & 0 & 0 & 0 & 0 & 0 & 0 & 0 & 0 & 0 & 0 & 0 & 0 & 0 \\ 0 & 1 & -2 & 1 & 0 & 0 & 0 & 0 & 0 & 0 & 0 & 0 & 0 & 0 & 0 & 0 \\ 0 & 0 & 1 & -1 & 0 & 0 & 0 & 0 & 0 & 0 & 0 & 0 & 0 & 0 & 0 & 0 \\ 0 & 0 & 0 & 0 & -1 & 1 & 0 & 0 & 0 & 0 & 0 & 0 & 0 & 0 & 0 & 0 \\ 0 & 0 & 0 & 0 & 1 & -2 & 1 & 0 & 0 & 0 & 0 & 0 & 0 & 0 & 0 & 0 \\ 0 & 0 & 0 & 0 & 0 & 1 & -2 & 1 & 0 & 0 & 0 & 0 & 0 & 0 & 0 & 0 \\ 0 & 0 & 0 & 0 & 0 & 0 & 1 & -1 & 0 & 0 & 0 & 0 & 0 & 0 & 0 & 0 \\ 0 & 0 & 0 & 0 & 0 & 0 & 0 & 0 & -1 & 1 & 0 & 0 & 0 & 0 & 0 & 0 \\ 0 & 0 & 0 & 0 & 0 & 0 & 0 & 0 & 1 & -2 & 1 & 0 & 0 & 0 & 0 & 0 \\ 0 & 0 & 0 & 0 & 0 & 0 & 0 & 0 & 0 & 1 & -2 & 1 & 0 & 0 & 0 & 0 \\ 0 & 0 & 0 & 0 & 0 & 0 & 0 & 0 & 0 & 0 & 1 & -1 & 0 & 0 & 0 & 0 \\ 0 & 0 & 0 & 0 & 0 & 0 & 0 & 0 & 0 & 0 & 0 & 0 & -1 & 1 & 0 & 0 \\ 0 & 0 & 0 & 0 & 0 & 0 & 0 & 0 & 0 & 0 & 0 & 0 & 1 & -2 & 1 & 0 \\ 0 & 0 & 0 & 0 & 0 & 0 & 0 & 0 & 0 & 0 & 0 & 0 & 0 & 1 & -2 & 1 \\ 0 & 0 & 0 & 0 & 0 & 0 & 0 & 0 & 0 & 0 & 0 & 0 & 0 & 0 & 1 & -1 \end{bmatrix}\begin{bmatrix} \Phi(1,1) \\ \Phi(1,2) \\ \Phi(1,3) \\ \Phi(1,4) \\ \Phi(2,1) \\ \Phi(2,2) \\ \Phi(2,3) \\ \Phi(2,4) \\ \Phi(3,1) \\ \Phi(3,2) \\ \Phi(3,3) \\ \Phi(3,4) \\ \Phi(4,1) \\ \Phi(4,2) \\ \Phi(4,3) \\ \Phi(4,4) \end{bmatrix}.$$

$\mathbf{L}_p$ has a null eigenvalue with an eigenvector $\Phi_e(i,j) = c \neq 0$, $\forall i, j$, i.e, $\mathbf{L}_p\Phi_e(:) = 0\Phi_e(:)$. This can be tested by noting that every row of matrices $\mathbf{D}_{xp}$ and $\mathbf{D}_{yp}$ adds up to zero. This implies that the Poisson equation for Φ is solved to within an arbitrary

constant c. This singularity poses issues with regard to the Cholesky decomposition in particular, and the uniqueness of Φ, in general. The workaround followed in this thesis is the regularization of the Poisson-Neumann problem (or computing the generalized-inverse), discussed in Pozrikidis [132]. This amounts to modifying a diagonal element, say $\mathbf{L}_p(1,1)$, with $\mathbf{L}_p$ remaining symmetric for the "Cholesky" decomposition to be carried out. This method is particularly elegant given the source term is left untouched[7].

Lastly, the modification to $\mathbf{L}_p$ to make it non-singular does not mean the compatibility condition can be violated. For example, the solution Φ to a rotationally symmetric source g, i.e., $g(x,y) = g(-x,-y)$ should remain rotationally symmetric. However, as a very first step the compatibility condition on g, i.e., $\int_\Omega g\,dx\,dy = 0$ should be tested, which, if not satisfied, will imply that the Poisson equation cannot be solved. One cannot expect $\mathbf{L}_p \backslash g(:)$ to be rotationally symmetric in such cases, since the problem is ill-posed. A detailed discussion of the solution to the discrete Poisson's equation and its validation is provided in Appendix A.

3.3.5 Initializing Numerical Simulation Using Experimental Data

The development of a numerical simulation that mimics the experiment in lateral dimensions and boundary conditions has the advantage that one can *directly* use experimental flow fields to initialize the simulation, i.e., $\mathbf{u^0}$ can be defined using PIV data. However, using experimental data to initialize the numerical simulation requires some processing. To begin, the u^{exp}, v^{exp} velocity fields in the experiment are measured on a collocated grid of dimensions 126×170, which is (about) 2 times coarser in resolution compared to the staggered grid used in simulation (cf. section (3.3.2)).

[7] Alternatively, one can modify the $\mathbf{L}_p$ matrix by pinning the value of Φ at any location in the domain, say $\Phi(1,1) = 0$. This modifies the first row of the L_p matrix to $[1, 0, 0, \cdots, 0]$, along with replacing the first element in the source term $g(1,1) = 0$ in the system of equations $\mathbf{L}_p\Phi(:) = g(:)$. $\mathbf{L}_p$ ceases to be symmetric, and one can compute the solution using LU decomposition. These two procedures result in identical solutions to the Poisson's equation, which differ only by a constant.

Hence, u^{exp} and v^{exp} are interpolated onto the respective simulation grids using the spline interpolation option in MATLAB. However, these interpolated velocity fields (as well as the raw PIV data) are not incompressible as is required in the simulation. Hence, they are projected onto a divergence-free (incompressible) space using Helmholtz-Hodge decomposition (cf. section (3.3.1)),

$$\mathbf{u}_{ic}^{exp} = \mathbf{u}_{interp}^{exp} - \nabla\Phi, \qquad \text{with} \qquad \nabla \cdot \mathbf{u}_{ic}^{exp} = 0. \tag{3.44}$$

Φ can be computed by solving the Poisson's equation resulting from taking the divergence of the above equation. The Dirichlet no-slip conditions for the velocity fields at the boundary ($\partial\Omega$), i.e., $\mathbf{u}_{ic}^{exp}|_{\partial\Omega} = \mathbf{u}_{interp}^{exp}|_{\partial\Omega} = 0$, result in homogeneous Neumann boundary condition for Φ, i.e., $\nabla\Phi \cdot \hat{\mathbf{n}}|_{\partial\Omega} = 0$.

The $\mathbf{u}_{ic}^{exp}$ generated are first tested for accurate interpolation by computing the change in the velocity field when evolved ($\mathbf{u}_{ic}^{exp} \rightarrow \mathbf{u}(\Delta T)$) using the numerical integrator, which can be quantified using the residual $r_{ic} = \|\mathbf{u}(\Delta T) - \mathbf{u}_{ic}^{exp}\|$. Here $\|\cdots\|$ represents the L2 norm and $\Delta T = 1$ is the duration of numerical integration. Typically, r_{ic} is less than 25, which is around 10% of the norm of the velocity field $\|\mathbf{u}_{ic}^{exp}\| \approx 250$. Misalignment in the centers of experimental and simulation domains, however, can lead to large values of $r_{ic} \approx 50$. Such misalignment is due to the error in determining the origin of the PIV grid exactly; the center of the experimental domain is determined only to within an accuracy of $\Delta x, \Delta y = \pm 0.035$ ($\approx \pm 0.5$ mm). While this uncertainty is the same in both x and y directions, minor misalignment in the x direction does not lead to a large increase in r_{ic} due to the relatively weak dependence of the forcing profile on x (cf. Fig. 3.1(b)). In contrast, a misalignment in the y direction results in the flow and forcing being oppositely directed over some region of every magnet, causing a large change in the velocity field when evolved using simulation even for a short duration ΔT. Hence, the origin of the PIV data should be shifted to coincide with that in the numerical simulation, especially in the y direction. The optimal y-shift can be estimated by calculating r_{ic} by shifting the experimental grid

in the y-direction within the limits of uncertainty $[-0.035, 0.035]$ and identifying the one yielding the minimum residual. This can be independently tested by computing the spatial shift that minimizes the difference between the temporal averages of the longitudinal velocity u in simulation and experiment, i.e., $\langle u^{exp} \rangle_t - \langle u^{sim} \rangle_t$.

3.3.6 Simulations on Spatially Periodic Domains

In the experimental Kolmogorov-like flow, vertical solid walls serve as the lateral boundaries, resulting in a no-slip boundary condition. As discussed in the previous section, the domain size for the simulations was chosen be identical to the experimental one with no-slip boundary conditions imposed on all four walls, as shown in Fig. 3.4. This simulation will be referred to as the Non-Periodic Simulations (NPS). However, for reasons of analytical and computational feasibility, Kolmogorov flow has been studied almost exclusively using unbounded or periodic domains. While periodic flows cannot be created in laboratories it is reasonable to conjecture that for large experimental domains the flow structures in a sub-region away from the walls *may* resemble those in smaller periodic domains. Hence, periodic simulations are useful in systematically studying the role of confinement in the longitudinal and transverse directions independently. The two different periodic domains studied in this thesis are as follows:

3.3.6.1 Singly-Periodic Simulation (SPS)

This simulation is performed on a computational domain of dimensions $L_x = 14$ and $L_y = 8$, that coincides with the region $|x| \leq 7$ and $|y| \leq 4$, indicated by the dashed red box in Fig. 3.4. The longitudinal dimension is the same as that of the experiment, while the transverse one spans a width equaling that of only 8 magnets. No-slip boundary conditions are imposed at the end walls, i.e., $\mathbf{u}(x = \pm L_x/2, y) = 0$, while periodic boundary conditions are imposed along the transverse direction, i.e., $\mathbf{u}(x, y = L_y/2) = \mathbf{u}(x, y = -L_y/2)$. The 2D forcing profile $\mathbf{f}_0 = f_x \hat{\mathbf{x}}$ over this

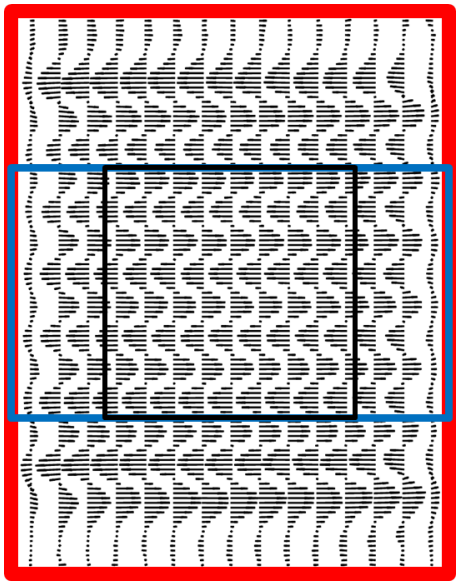

Figure 3.4: Three different computational domains employed to study the effects of confinement. The velocity field plotted using the black arrows corresponds to that measured over the entire experimental domain. The largest red box, coinciding with the experimental domain, is the one used for the Non-Periodic Simulation (NPS). The blue box extending all the way to the end walls $|x| = 7$, but confined to the central 8 magnets ($|y| \leq 4$) corresponds to the Singly-Periodic Simulation (SPS). The black square box, enclosing the region $|x| \leq 4$ and $|y| \leq 4$ corresponds to the Doubly-Periodic Simulation (DPS).

singly-periodic domain is constructed as a product of two one-dimensional profiles $f_x(x, y) = \mathcal{H}(x)\mathcal{S}(y)$. Along the y-direction the profile is constructed by retaining only two dominant Fourier (sinusoidal) modes of the depth-averaged magnetic field (cf. equation (3.18)), $\mathcal{S}(y) = 1.05\sin(\kappa y) + 0.05\sin(3\kappa y)$. Along the x-direction the horizontal profile $\mathcal{H}(x)$ is chosen to be the depth-averaged magnetic field profile from the dipole summation along the magnet centerline $|y| = 0.5$.

Numerical simulations over the singly periodic domains are performed using the finite-difference method described in the previous section. The NPS code, with some nontrivial effort, can be modified to simulate the flow on the singly-periodic domain. The periodicity of the domain requires redefining the interior points and ghost points, as well as the boundary conditions. Like in the NPS, the domain is discretized into $n_x \times n_y$ cells, with 20 cells chosen per unit length in both the x and y directions. The

dimensions of the u, v and p grids for the SPS and the comparison with their NPS counterparts is shown in the table below.

Table 3.3: Dimensions of the singly-periodic and non-periodic simulation grids.

Domain	p	u	v
NPS $(n_x = 280, n_y = 380)$	$n_x \times n_y$	$(n_x - 1) \times n_y$	$n_x \times (n_y - 1)$
SPS $(n_x = 280, n_y = 160)$	$n_x \times n_y$	$(n_x - 1) \times n_y$	$n_x \times n_y$

The difference in the number of grid points of the v grid is related to the periodicity of the domain and the definition of ghost points. The v grid is defined on half-integer points in the y direction, i.e., $(i, j + 1/2)$. The boundaries in the periodic direction y of the SPS domain are indicated using the indices $(x, -L_y/2) \rightarrow (i, 1/2)$ and $(x, L_y/2) \rightarrow (i, n_y{+}1/2)$. The v grid aligns with the boundaries in the y direction, which are periodic, i.e., $v(i, 1/2) = v(i, n_y{+}1/2)$. Hence, the v grid is uniquely defined from $y = -L_y/2$, only up to $y = L_y/2 - \Delta y$, i.e., $(i, 1/2)$ up to $(i, n_y - 1/2)$. Hence, the boundary conditions imposed using the ghost point relations for the SPS are given below.

Table 3.4: Boundary conditions imposed using ghost points on the staggered grid for the SPS.

$L_x = 14, L_y = 8$	u	v
$x = -L_x/2$	$u(1/2, j) = 0$	$v(0, j + 1/2) = -v(1, j + 1/2)$
$x = L_x/2$	$u(n_x + 1/2, j) = 0$	$v(n_x + 1, j + 1/2) = -v(n_x, j + 1/2)$
$y = -L_y/2$	$u(i + 1/2, 0) = u(i + 1/2, n_y)$	none
$y = L_y/2$	$u(i + 1/2, n_y + 1) = u(i + 1/2, 1)$	$v(i, n_y + 1/2) = v(i, 1/2)$

3.3.6.2 Doubly-periodic simulation (DPS)

This computational domain of size $L_x = 8$ and $L_y = 8$ for this simulation is chosen to coincide with the region of the experimental domain $|x| \leq 4$ and $|y| \leq 4$ (in nondimensional units). The simulated flow is constrained to be periodic in both the longitudinal and transverse directions, i.e., $\mathbf{u}(x = -L_x/2, y) = \mathbf{u}(x = L_x/2, y)$ and $\mathbf{u}(x, y = -L_y/2) = \mathbf{u}(x, y = L_y/2)$. Along the transverse direction it spans a width equaling that of 8 magnets. The 2D forcing profile $\mathbf{f}_0 = f_x(y)\hat{\mathbf{x}}$ over this doubly-periodic domain is constructed from the depth-averaged magnetic field by retaining only the two dominant Fourier modes, $\sin(\kappa y)$ and $\sin(3\kappa y)$, along the y-direction, where $\kappa = \pi$ in dimensionless units. Along the x-direction the profile is uniform: $f_x(y) = 1.05\sin(\kappa y) + 0.05\sin(3\kappa y)$.

Simulations on the doubly-periodic domain can be sped up using a spectral method [133], since solving linear equations is relatively straightforward. Furthermore, since the boundary conditions are periodic, i.e., there is no necessity to specify the value of velocity anywhere on the boundary, it is convenient to use the vorticity-stream function formulation instead of the velocity-pressure formulation. Taking the curl of equation (3.3), the following equation for the z-component of vorticity $\omega = (\nabla \times \mathbf{u}) \cdot \hat{\mathbf{z}}$ is obtained:

$$\partial_t \omega + \beta \mathbf{u} \cdot \nabla \omega = \frac{1}{Re}\left(\nabla^2 \omega - \gamma \omega\right) + W, \tag{3.45}$$

where $W = (\nabla \times \mathbf{f}_0) \cdot \hat{\mathbf{z}}$. The horizontal components of the velocity field $u_x = \partial\psi/\partial y$ and $u_y = -\partial\psi/\partial x$ can be computed using the stream function ψ, which satisfies the Poisson equation $\nabla^2 \psi = -\omega$.

The vorticity field ω is discretized in the Fourier space using 128 modes along each of the x- and y-directions, which corresponds to 16 Fourier modes per unit length L. Taking the Fourier transform of equation (3.45), the following equation is obtained:

$$\partial_t \Omega = -\beta \mathcal{F}[\mathbf{u} \cdot \nabla \omega] + \frac{1}{Re}\left(\nabla^2 \Omega - \gamma \Omega\right) + \mathcal{F}[W], \tag{3.46}$$

where $\mathcal{F}[\cdot]$ represents the Fourier transform and $\Omega = \mathcal{F}[\omega]$.

Equation (3.46) is stepped forward in time ($t \to t + \Delta t$) using a 3-substep semi-implicit Strang-Marchuk splitting algorithm [134] where the first and last substeps advance the vorticity field using the nonlinear term by means of a second-order explicit Runge-Kutta scheme (using a time step $\Delta t/2$), while the intermediate substep advances the vorticity field using the Crank-Nicholson scheme (using a time step Δt). A time step $\Delta t = 1/32$ s was used for all periodic simulations.

3.4 Summary

In this chapter, a 2D model that should closely approximate the evolution of a (near) Q2D flow in experiments, was derived. This model, applicable to both homogeneous and stratified layer setups, was derived by depth-averaging the 3D Navier-Stokes equation which describes the exact evolution of the flow in experiments. Analytical expressions for the coefficients that parametrize the 2D model were provided in terms of experimentally measurable fluid layer properties. Following this theoretical development, a numerical simulation of the 2D model with lateral dimensions and boundary conditions identical to those in experiment was developed to facilitate direct comparison between the experiment and simulation. Details of a numerical model for the electromagnetic body force, the spatiotemporal discretization of the velocity and pressure fields in the 2D model, as well as the numerical implementation of the integrator using MATLAB were discussed. Finally, two periodic numerical simulations were introduced, with the goal of systematically studying the effects of confinement. In the next chapter, the numerical simulations discussed here will be employed to test the accuracy of the 2D model in describing the flows observed in the experiment. A systematic exploration, using both experiments and simulations, of the various pre-turbulent flow regimes as well as the transitions between them will be presented.

CHAPTER IV

BIFURCATIONS IN THE KOLMOGOROV-LIKE FLOW

Previously in this thesis, the experimental realization of a quasi-two-dimensional flow was presented, following which, a 2D theoretical model and its numerical discretization were discussed. In this chapter, the accuracy of the 2D model in capturing the flow structure and its dynamics in the experiment are tested. This is performed by comparing the various flow regimes realized in the experiment and simulation as one increases the driving (current). The outline of this chapter is as follows: In section (4.1) a detailed discussion of the sinusoidal flow at low driving is presented. This flow was discussed earlier in chapter 2, but, only near the center of the domain where it was approximated as a pure sinusoid. Herein, the flow over the entire lateral span of the experiment is studied and compared to simulations[1]. In section (4.2), linear stability analysis of the sinusoidal flow is provided. In section (4.3), a discussion of the flow regime that is observed after the sinusoidal flow loses stability is presented. In section (4.5) the nature of the primary instability on each of the three numerical domains is discussed using symmetries of the governing equation (3.14). In section (4.4), the sensitivity of the primary instability in the NPS to changes in simulation parameters is discussed. In section (4.6), the secondary instability which leads a time-dependent flow is studied in both experiment and the NPS.

[1]All the numerical simulations in this chapter have been performed by setting the blending parameter "b" in the non-linear term to zero, i.e., by using central differencing scheme, cf. equation (3.36)

4.1 Straight Flow

For weak driving, the flow in the experiment[2] away from the walls mimics the forcing closely. One finds spatially alternating straight bands of fluid flow along the $\pm x$-directions, as can be seen in figure 4.1(d) for $Re = 8.1$. For this reason, this flow shall be referred to as the "straight flow" hereafter. In this figure, black vectors represent the velocity field $\mathbf{u}$, similar to those plotted in Fig. 2.3. The color map indicates the vorticity $\omega = (\nabla \times \mathbf{u}) \cdot \hat{\mathbf{z}}$ (cf. equation (3.45)). For the experiment (Fig. 4.1 (d)), the y-component of the velocity measured in the central region of the domain is close to zero. However, there are regions of strong recirculation near the end walls, characterized by a nonzero y-component of velocity. A closer inspection of the flow shows a slight tilt in the alignment of the flow bands. This tilt is due to the global circulation, resulting from confinement and the fluid flowing in opposite directions over the end magnets at $y = \pm 6.5$.

Figures 4.1 (a), (b), and (c) show the straight flows found in the DPS, SPS, and NPS, respectively. The depth-averaged parameters $\alpha = 0.064$ s^{-1}, $\beta = 0.83$, and $\bar{\nu} = 3.26 \times 10^{-6}$ m^2/s in these simulations are computed using equation (3.4) with the vertical profile $P(z)$ for the purely sinusoidal flow (cf. section (2.3)). It can be seen that flow fields in the DPS and SPS reproduce the experimental flow qualitatively, only away from the side walls. The SPS, unlike the DPS, captures the turnaround flow near the end walls. However, neither the SPS nor the DPS displays the tilt of the flow bands observed in the experiment since the periodic flows are devoid of global circulation. In contrast, the NPS generates a flow field that looks indistinguishable

[2]The experimental setup used to generate this data is slightly different from the one discussed in section (2.1). A 0.9 mm thick glass plate was glued to the magnet array to improve the smoothness of the bottom surface over which the fluid layers rest. Since $z = 0$ was chosen to coincide with the bottom of the dielectric layer, the z coordinates of the dielectric-electrolyte and electrolyte-air interfaces remain unchanged. However, the dipole-summation and the depth-averaged magnetic field profile were recomputed, since the position of the electrolyte layer relative to the magnet array is shifted by 0.9 mm

from the experimental one (cf. figure 4.1 (c)).

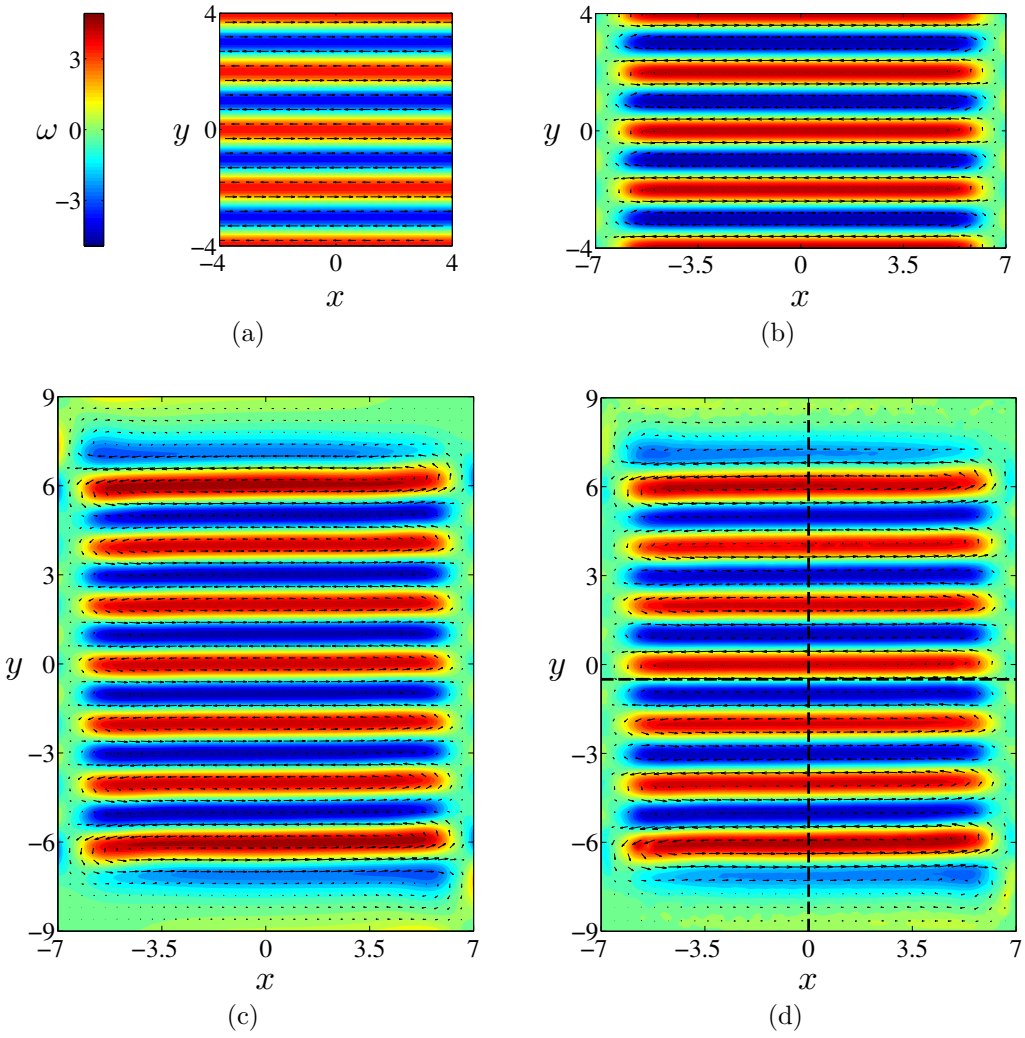

Figure 4.1: Straight flow fields at $Re = 8.1$ for the (a) DPS, (b) SPS, (c) NPS, and (d) experiment. The dashed lines in (d) indicate the locations of velocity profiles in the experiment that are compared to the simulations. The vorticity color scale plotted for (a) also applies to (b-d). The velocity vectors are downsampled in each direction by a factor of 8 for the simulations and 4 for the experiment.

For a quantitative description of the straight flow profile, the longitudinal component u^{exp} of the velocity along the line $x = 0$ in the experiment is plotted in figure 4.2 (a). The location of this cross section is indicated by the vertical dashed line in figure 4.1 (d). While the profile near the center is approximately sinusoidal, as was demonstrated in Fig. 2.5, the lack of strict periodicity introduces a slant in the peak

velocity. The difference in u between the experiment and the numerical simulations along this line is shown in figure 4.2 (b). The DPS and SPS, which are only defined for $|y| \leq 4$, show systematic deviation from the experiment as high as 18% since they do not capture global circulation. The periodic simulations amount to modeling the flow at the center as a strict sinusoid, much like equation (2.5), and the deviation stems from the change in the peak of the sine profile along y. In comparison, the NPS agrees to within about 5% over the same region, with no clear systematic deviation. The disagreement between the experiment and NPS in this region is a result of the dipole summation not accounting for the variation in the strength of each individual magnet as well as the slight ($\pm$0.1cm) differences in the widths of the magnets. Closer to the boundaries, at $y \approx 7$ and $y \approx -6$, the largest difference between the NPS and the experiment is around 12%. The analysis of this discrepancy is deferred to Appendix D.

The experimental longitudinal velocity component u^{exp} at $y = -0.5$ (along a central magnet centerline) is shown in figure 4.3 (a). The very slight asymmetry in the longitudinal velocity is a result of the global circulation. In contrast, the flow in the DPS is perfectly uniform and thus does not capture this asymmetry, as can be seen from the plot of its difference with the experimental profile in figure 4.3 (b). The SPS, which is defined all the way to the end walls, also does not capture this asymmetry due to the lack of global circulation. The NPS produces the closest agreement: the corresponding flow displays the asymmetry observed in the experiment, with no significant systematic deviation. In summary, the NPS succeeds in capturing the effects of confinement in the experiment with good accuracy, while the DPS and SPS show significant systematic deviations.

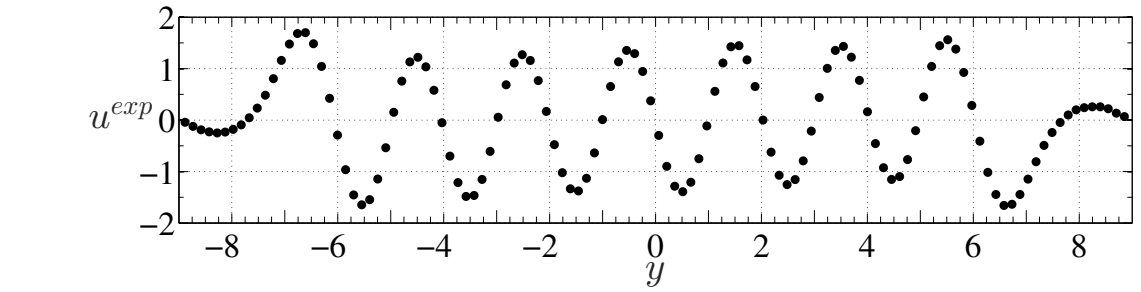

(a)

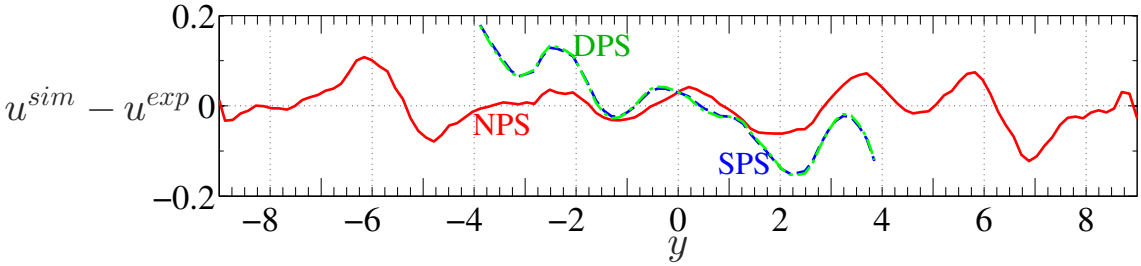

(b)

Figure 4.2: Comparison of the longitudinal velocity profiles along the y-direction in experiment and simulations at $Re = 8.1$. (a) u^{exp} as a function of y at the longitudinal center ($x = 0$), (b) the difference between the longitudinal velocity in the simulations and the experiment, $u^{sim} - u^{exp}$, as a function of y at the longitudinal centre ($x = 0$); note that the curves corresponding to the DPS and SPS are virtually indistinguishable in the region $-4 < y < 4$, where the DPS is defined. Experimental uncertainties are the size of the symbols or smaller.

4.2 Stability of the Straight Flow: Analytical Study

As the strength of the forcing increases, the flow in the experiment undergoes a qualitative change at $Re_c = 11.07 \pm 0.05$. The near uniformity of the flow bands (cf. figure 4.3 (a)) away from the end-walls is lost, with the flow profile developing modulations, as shown in Fig. 4.4. As the strength of the forcing is further increased this modulation grows in strength, eventually leading to the formation of vortices. Hence, this regime shall be referred to as the "modulated flow."

Several previous experimental studies have reported this transition and have characterized it using the critical Reynolds number (Re_c^{exp}) and wavenumber (k_c^{exp}) of the modulation [80, 93, 95, 135]. In the current experimental setup, the wavenumber

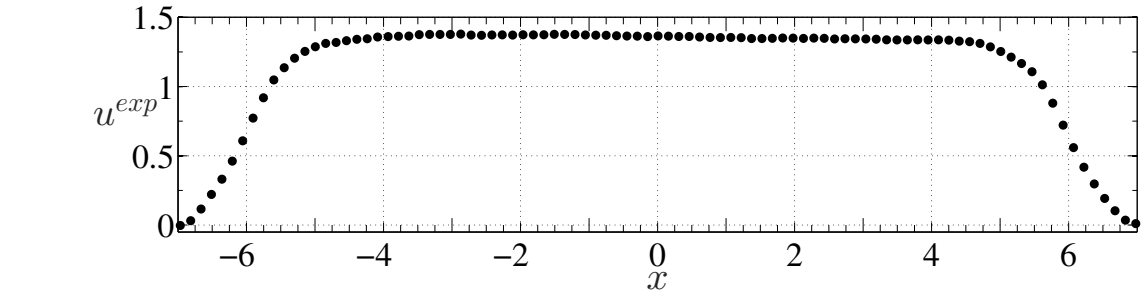

(a)

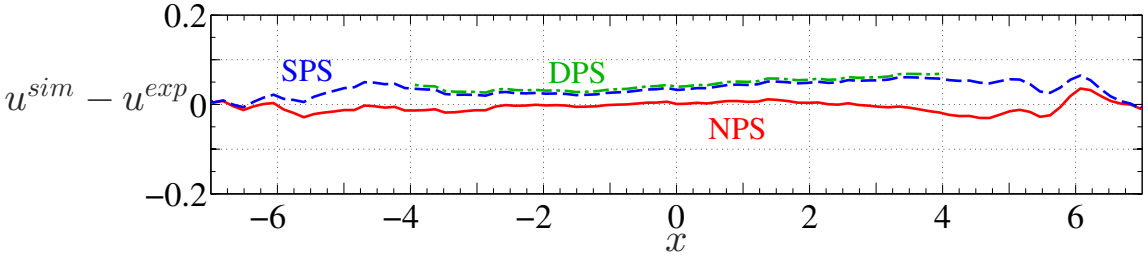

(b)

Figure 4.3: Comparison of longitudinal velocity profiles along the magnet centerlines. (a) u^{exp} as a function of x at the centerline of a middle magnet ($y = -0.5$), and (b) the difference between the longitudinal velocity in the simulations and the experiment, $u^{sim} - u^{exp}$, as a function of x at the centerline of a middle magnet ($y = -0.5$); note that the curves corresponding to the DPS and SPS are virtually indistinguishable in the region $-4 < x < 4$, where the DPS is defined. Experimental uncertainties are the size of the symbols or smaller.

just above this transition was measured to be $k_c^{exp} = 0.50\kappa$, where κ is computed using the width of a pair of magnets, i.e., $\kappa = \pi/L_s$. In virtually all the previous studies, theoretical estimates for these critical parameters have been obtained by using equation (1.8) by modeling the straight flow in experiment as a pure sinusoid[3] $\mathbf{u}_s \propto \sin(\kappa y)\,\hat{\mathbf{x}}$, like in equation (2.5). Also, many previous studies used a different nondimensionalization by choosing $L = 2\pi/\kappa$ as the length scale with $\kappa = 1$. Hence, the analytical results presented below can be compared to those from such studies by setting $q = k$.

The strictly sinusoidal straight flow governed by equation (3.3) on an unbounded

[3]This theoretical approach closely resembles the one employed in chapter 2, which stems from the observation that, away from the boundaries the flow is indeed close to being a sinusoid varying along y.

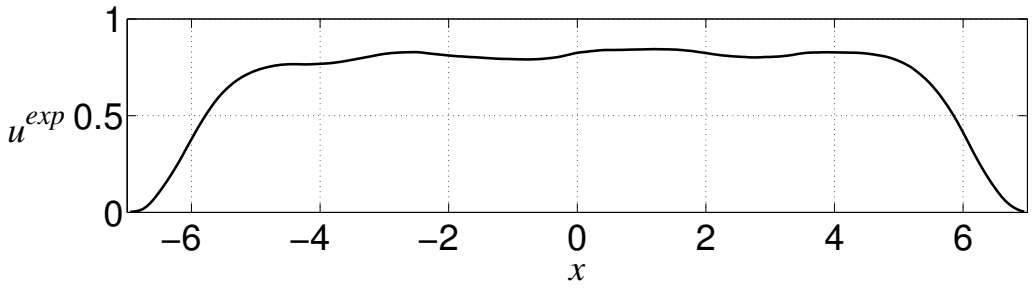

(a)

Figure 4.4: Plot of longitudinal velocity u versus x, showing the emergence of modulations along x in the longitudinal velocity u. Compare the flatness of the profile with the straight flow shown in Fig. 4.3(a)

domain becomes unstable with respect to perturbations with wavenumber q above the Reynolds number $Re = Re_n(q)$, which to a very good accuracy is given by:

$$Re_n(q) = \frac{\pi}{\beta}\frac{1}{q}\sqrt{\frac{(1+q^2)}{(1-q^2)}\left(q^2+\frac{\alpha}{\nu\kappa^2}\right)\left(1+q^2+\frac{\alpha}{\nu\kappa^2}\right)}. \tag{4.1}$$

This expression, whose derivation is included in Appendix C, was computed by linearizing equation (3.3) around $\mathbf{u}_s$ and calculating its stability with respect to perturbations including three modes [88],

$$\delta\mathbf{u}(y)e^{ikx} = \sum_{n=-1,0,1} \epsilon_n e^{i\kappa(ny+qx)}. \tag{4.2}$$

The critical Reynolds number $Re_c = \min_q Re_n(q)$ and the corresponding critical wavenumber $k_c = \kappa q_c$ computed using the expression (4.1) can then be compared with experimental observations.

The neutral stability curve (blue dot-dashed line) which corresponds to the experimental values of parameters α, β, and ν is shown in figure 4.5. The minimum of this neutral stability curve yields a critical Reynolds number $Re_c = 9.16$ and an associated critical wavenumber $q_c = 0.465$. The black dot on the plot indicates the critical values $Re_c^{exp} = 11.07$ and $q_c^{exp} = 0.50$ corresponding to the instability observed in the experiment. The relative difference $(Re_c^{exp} - Re_c)/Re_c^{exp}$ between the theoretical estimate for the critical Reynolds number and that measured in experiment is about 17%. The critical wavenumber, however, is in better agreement with

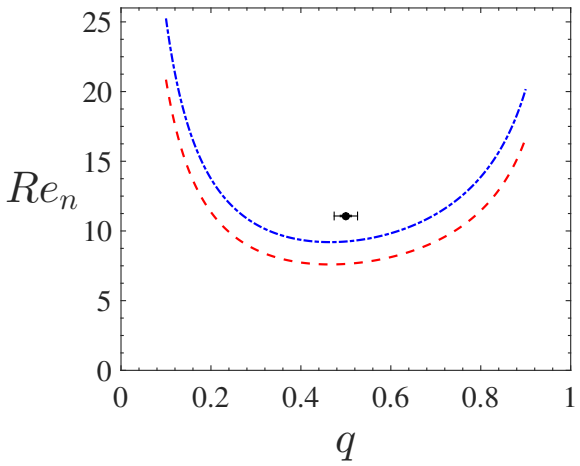

Figure 4.5: Neutral stability curves (4.1) describing the primary instability. The red dashed line corresponds to $\alpha = 0.064$ s^{-1} and $\beta = 1.00$, while the blue dot-dashed line corresponds to $\alpha = 0.064$ s^{-1} and $\beta = 0.83$. The experimental measurement is shown as a black dot; note that the uncertainty in Re_c^{exp} is smaller than the size of the black circle. In all the cases, $\nu = 3.26 \times 10^{-6}$ m^2/s is held constant.

the experimentally measured one, with a 7% relative error.

While the critical Reynolds number obtained from the linear stability analysis does not agree perfectly with the experimentally observed one, it is still a significant improvement over analytical estimates for a flow modeled using equation (1.8), which corresponds to setting $\beta = 1$ in equation (3.3). The corresponding neutral stability curve is indicated by the red dashed line in figure 4.5. From equation (4.1) it can be seen that the entire neutral stability curve scales as $1/\beta$. This implies that the critical wavenumber ($q_c = 0.465$) is independent of β, while the predicted critical Reynolds number for $\beta = 1$ is $Re_c = 7.60$. This is a 31% discrepancy with the experimental value, which is comparable to the 30% discrepancy reported by Bondarenko *et al.* [80] in a study based on equation (1.8). As discussed previously, the parameter β describes the effect of the vertical variation in the magnitude of the horizontal velocity on the effective inertia and nonlinearity of the flow. Equation (1.8) does not account for this effect, so it is natural that its predictions are substantially less accurate.

4.3 Primary Instability: Transition from Straight to Modulated Flow

Figure 4.6 (a-d) shows the modulated flow fields corresponding to the DPS, SPS, NPS, and experiment, respectively, at $Re = 14$. At this Reynolds number, the modulation is strong enough that the flow is visually quite distinct from the straight flow. It should be noted that the size of the DPS domain along x was chosen *a posteriori* to be commensurate with the critical wavenumber $q_c^{exp} = 0.50$ measured in the experiment. The counterclockwise global circulation in the experiment strongly affects the alignment of the vortices (see figure 4.6 (d)) as can be seen by comparing the modulated flows in the DPS and SPS with the relevant regions of the experimental flow. Unlike the DPS and SPS, the flow field in the NPS captures the features observed in the experiment remarkably well. This unambiguously demonstrates the importance of properly modeling the confinement effects in both the longitudinal and the transverse direction to reproduce the features of the flow in the experiment.

The onset of the modulated flow is characterized by the appearance of the transverse component v of the velocity throughout the flow domain; as the driving is increased, the magnitude of v also increases. A bifurcation diagram characterizing the transition from the straight to the modulated flow is shown in figure 4.7 (a). The spatial mean square transverse velocity, $\langle v^2 \rangle$, is used as the order parameter and is plotted as a function of Re. The spatial average is computed over the central region $|x| \leq 4$ and $|y| \leq 4$ for all simulations and experiment (cf. Fig. 3.4). In comparison to the experimental value of $Re_c^{exp} = 11.07$, the primary instability in the DPS and SPS occurs at much lower Reynolds numbers $Re_c = 9.39$ and $Re_c = 9.53$, respectively. In contrast, by imposing the correct (no-slip) boundary conditions in both the longitudinal and transverse directions, in addition to using a realistic model of the magnetic field, the transition can be predicted quite accurately. The laminar to modulated transition in the NPS occurs at $Re_c = 10.49$, which is within 5.2% of Re_c^{exp}. Another

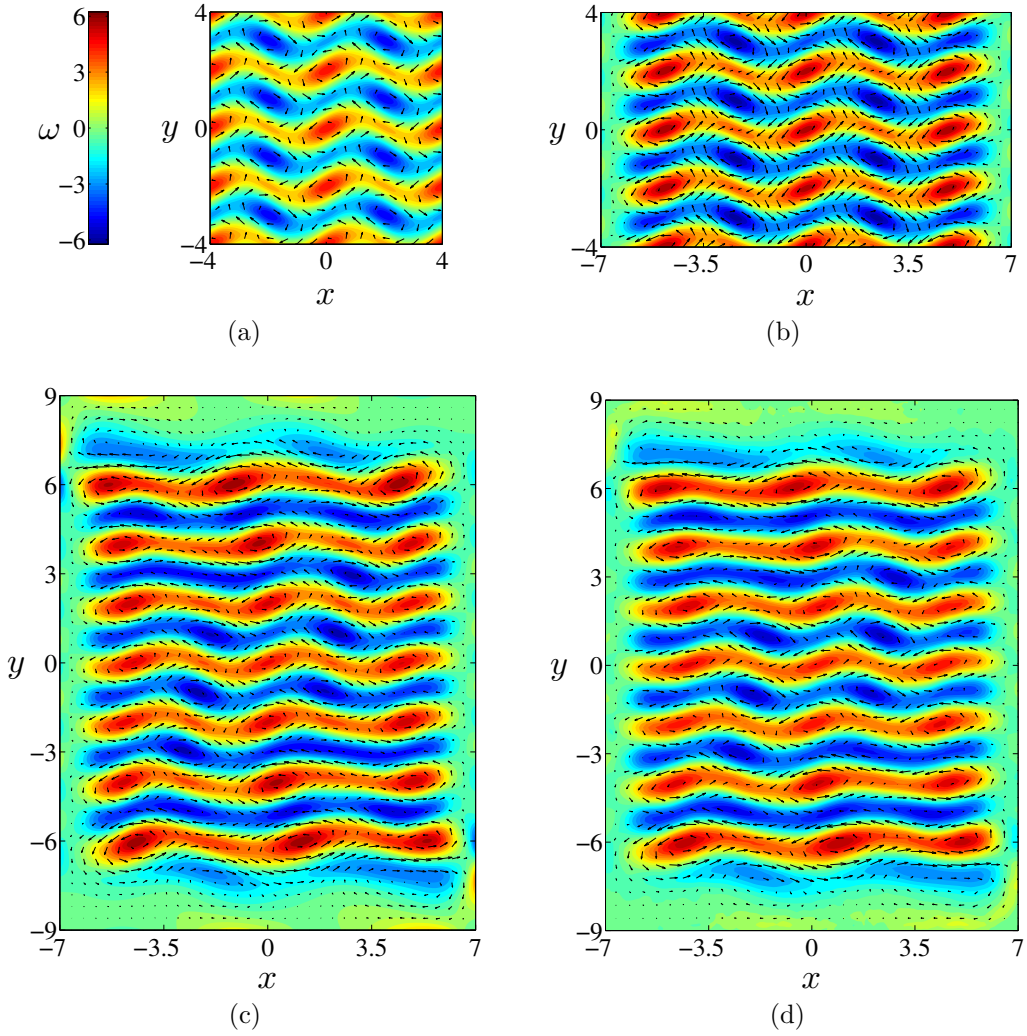

Figure 4.6: Modulated flow fields at $Re = 14$ for the (a) DPS, (b) SPS, (c) NPS, and (d) experiment. The vorticity color scale plotted for (a) also applies to (b-d). The velocity vectors are downsampled in each direction by a factor of 8 for the simulations and a factor of 4 for the experiment.

distinguishing feature of the straight to modulated transition in the experiment/NPS and the periodic simulations is the smooth manner in which the amplitude of v grows from the straight flow. This is related to the difference in the nature of the transition, which is discussed in greater detail in section (4.5). Finally, note that setting $\beta = 1$ results in a poor prediction $Re_c = 8.71$ even in the NPS, which corresponds to a 21% error.

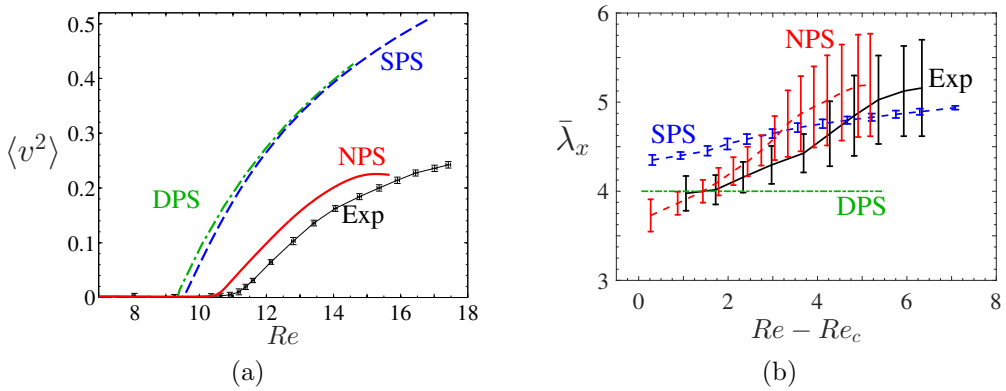

Figure 4.7: Characterizing the primary instability in the Kolmogorov-like flow. Panel (a) shows the bifurcation diagram where the growth of mean squared transverse velocity is plotted as a function of Re. In panel (b) the average wavelength of the pattern, $\bar{\lambda}_x$, as a function of Re for the modulated flow regime is plotted. At each Re, wavelength measurements are made in the central region $|y| \leq 4$ then averaged; the uncertainty bars indicate one standard deviation in the spatial measurements.

Given that the pattern of vortices in the experimental flow lacks perfect periodicity, the average longitudinal wavelength $\bar{\lambda}_x$ serves as a measure to facilitate a quantitative comparison between the flow patterns observed in the experiment and the simulations. This wavelength is defined as a spatial average of the separation between adjacent vortex centers in the region $|y| \leq 4$. The vortex centers are identified by searching for points with $u, v = 0$ within each vortex. Just above onset, the vortices in the experiment form a lattice with a fairly uniform separation, $\bar{\lambda}_x^{exp} \approx 4.0$. The spatial resolution of the PIV limits the accuracy with which one can identify the centers; for about 10 grid points per magnet-width, as is the resolution of PIV grid in the experiment (cf. section (2.1.1)), the uncertainty in identifying the vortex centers is about 0.1 nondimensional length units. As the forcing is increased, the mean separation between the vortices increases, as can be seen from the plot of $\bar{\lambda}_x$ versus $Re - Re_c$ shown in figure 4.7 (b). Additionally, the vortex lattice becomes spatially irregular, as can be seen in figure 4.6 (d). This spatial variation is quantified in the plot in figure 4.7 (b) wherein the uncertainty bars indicate one standard deviation in

the spatial variation of the separation between adjacent vortices. Note that immediately above onset, accurate identification of the vortex centers in the experiment is not possible because of the very weak modulation and coarse grid resolution; hence, experimental measurements are only plotted for $Re - Re_c \geq 1$.

For comparison, Fig. 4.7 (b) also shows the average wavelength of the flow pattern in the DPS, SPS, and NPS. Finer spatial resolution in the simulation, compared to that in experiment, facilitates measuring $\bar{\lambda}_x$ closer to onset. The domain size in the DPS was chosen *a posterori* to match the critical wavelength at onset of the modulated flow, resulting in (artificially) perfect agreement in the wavelength comparison at Re_c. However, the DPS does not capture the spatial variation of the wavelength or its variation with $Re - Re_c$ observed in the experiment. This is a consequence of the periodicity in the x direction. The SPS, however, shows a qualitatively similar trend for the dependence of $\bar{\lambda}_x$ on $Re - Re_c$. The periodicity in the transverse direction results in a uniform vortex pattern with smaller spatial variation in the separation between vortices compared to the experiment. In contrast, the NPS captures both the spatial variation of the wavelength and the distortion of the lattice with increasing forcing quite satisfactorily. At $Re - Re_c \approx 1$, the discrepancy is much smaller than the uncertainty bars, but for $Re - Re_c \gtrsim 1.5$, the NPS overestimates the wavelength compared to what is observed in the experiment. The largest discrepancy, which is 0.46 (a 10% relative error), occurs around $Re - Re_c = 3.7$. The slight difference in the flow patterns in the NPS and the experiment is partially due to the deviation of the latter from being perfectly Q2D. The analysis in Appendix D.1 further shows that the wavelength of the pattern also sensitively depends on relatively minor changes in the forcing profile, which could also be responsible for the observed discrepancy between the numerics and experiment.

4.4 Sensitivity of Primary Instability to Parameter Variation

While the NPS provides a fairly accurate description of the transition from straight to modulated flows in the experiment, it somewhat underestimates the critical Reynolds number Re_c. Furthermore, systematic deviations in the longitudinal wavelength $\bar{\lambda}_x$ measured in experiment and the NPS were observed. To resolve these discrepancies, the sensitivity of the transition in the NPS to magnetic field imperfections, as well as variations in parameters β, $\bar{\nu}$, and α was tested. In particular, it was found that Re_c is fairly insensitive to spatial variation in the strength of the magnets in the array. This testing was accomplished by including inhomogeneity of select types to the strength of dipoles in the dipole-summation model of the magnetic field.

Consequently, attention was turned to changing in the values of the parameters β, $\bar{\nu}$, and α in hopes of improving agreement in both Re_c and $\bar{\lambda}_x$ between experiment and NPS. In order to match Re_c in the NPS and experiment, β had to be decreased by 6%, while $\bar{\nu}$ and α had to be changed[4] by 7% and 22%, respectively. This suggests that Re_c is more sensitive to β and $\bar{\nu}$ than α. Figures 4.8 (a) and (b) show that the variation of parameters has a fairly weak effect on both the amplitude of the modulation and the wavelength of the pattern, suggesting that the disagreement between the simulation and experiment is primarily due to the deviation of the flow and/or forcing from quasi-two-dimensionality, which is discussed in Appendix D.

Before proceeding to discussing the nature of the transition from straight to modulated flows, the sensitivity of *any* bifurcation to changes in β deserves special attention. It is possible to eliminate the parameter β from equation (3.3) by redefining a

[4]The Reynolds number $Re = Uw/\bar{\nu}$ is defined using the measured rms velocity U and parameter $\bar{\nu}$ which cannot be measured, but has to be computed. While in the simulation the value of $\bar{\nu}$ is well-defined (it is one of the parameters of the model), in the experiment it is not, so the corresponding Re depends on the choice of $\bar{\nu}$. Hence, to enable a proper comparison of experiment with numerics, Re is defined in both cases using the analytically computed depth-averaged value $\bar{\nu} = 3.26 \times 10^{-6}$ m^2/s [114], regardless of the actual value of $\bar{\nu}$ used in the simulation. Matching Re using this convention is effectively equivalent to matching the rms velocity U.

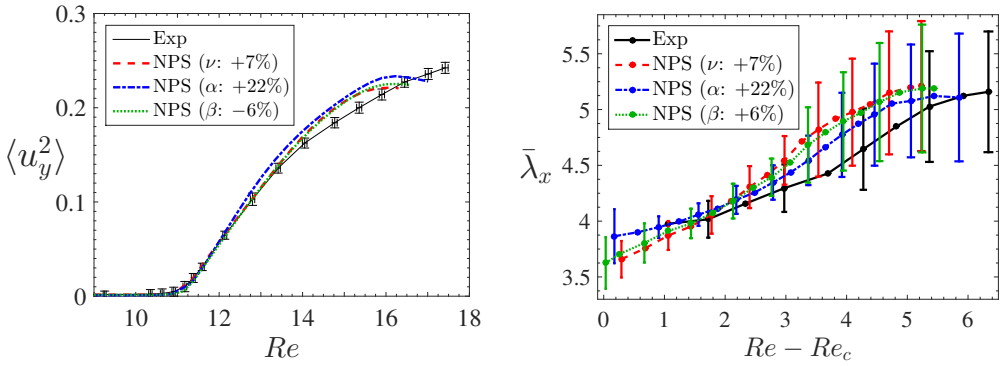

Figure 4.8: The effect of the variation in model parameters. (a) A bifurcation diagram and (b) the average wavelength of the pattern in the modulated flow regime. The numerical results correspond to either a 7% increase in $\bar{\nu}$, a 22% increase in α, or a 6% decrease in β compared with the depth-averaged values for the straight flow ($\alpha = 0.064$ s^{-1}, $\beta = 0.83$, and $\bar{\nu} = 3.26 \times 10^{-6}$ m^2/s). Note that the error bars in (b) have been downsampled by a factor of 2 for clarity.

scaled velocity $\tilde{\mathbf{u}} = \beta \mathbf{u}$. Multiplying equation (3.3) with β and redefining $\tilde{p} = \beta p$ and $\tilde{\mathbf{f}} = \beta \mathbf{f}$, one obtains

$$\frac{\partial \tilde{\mathbf{u}}}{\partial t} + \tilde{\mathbf{u}} \cdot \nabla \tilde{\mathbf{u}} = -\nabla \tilde{p} + \nu \nabla^2 \tilde{\mathbf{u}} - \alpha \tilde{\mathbf{u}} + \tilde{\mathbf{f}}, \tag{4.3}$$

The above equation is independent of β, which means the sequence of bifurcations for various values of $\beta \neq 0$ is identical. Moreover, the *scaled* Reynolds number $\tilde{Re} = \tilde{U}L/\bar{\nu}$ at which each of these bifurcations occurs is independent of β, where $\tilde{U} = \beta U$. Then, since $Re_c = 1/\beta \tilde{Re}_c$, the critical Re at which any bifurcation occurs is merely scaled when β is changed (cf. equation (4.1)). To match Re_c for a specific bifurcation in simulation with that found in experiment, one can simply modify the value of β. This change, however, will not improve agreement between simulation and experiment with regard to dynamical measures characterizing the bifurcation. However, such measures often can be matched to some extent by modifying $\bar{\nu}$ and α, as will be demonstrated shortly in the context of the secondary instability. This shows the flexibility that equation (3.3) offers over previous 2D models, where modifying α simultaneously changed Re_c, the sequence of bifurcations, and the dynamical

measures associated with each bifurcation.

4.5 Nature of the Primary Instability

An important consequence of bounding the flow in the longitudinal or transverse directions is that one restricts the set of coordinate transformations (symmetries) that leave the governing equation (3.3) equivariant. The symmetries of the governing equation, in turn, govern the number of and relations between the distinct modulated flow solutions. In this section, the nature of the primary instability observed in the experiment is understood from the standpoint of symmetry-breaking. The symmetries implicit in the DPS, SPS, and NPS, as well as the relations between their solutions corresponding to the modulated flow are discussed below.

4.5.1 DPS

On an unbounded or a doubly-periodic domain, equation (3.3) is equivariant under the following symmetry operations [72, 136]:

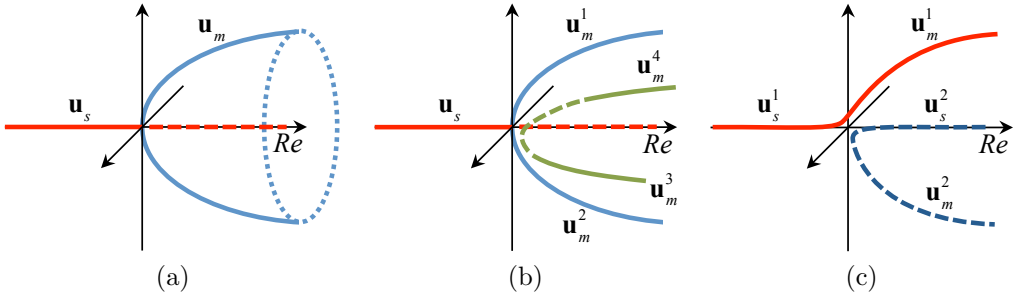

Figure 4.9: A schematic showing the bifurcations corresponding to the primary instability: (a) circle pitchfork in the DPS, (b) sequence of pitchfork bifurcations in the SPS, (c) imperfect pitchfork bifurcation in the NPS. Solid (dashed) lines indicate stable (unstable) solution branches.

1. Continuous translations in x: $\mathcal{T}_x^{\delta x}(x, y) \to (x + \delta x, y)$, where δx is an arbitrary translation along the longitudinal direction.

2. Reflection in x combined with a discrete shift of one magnet width or half a period in y: $\mathcal{R}_x \mathcal{T}_y^{w}(x, y) \to (-x, y + w)$.

3. Reflections in both x and y: $\mathcal{R}_y\mathcal{R}_x(x,y) \to (-x,-y)$.

The reflection $\mathcal{R}_y\mathcal{R}_x$ is equivalent to a rotation by an angle π about the z-axis, while the square of the symmetry operation $\mathcal{R}_x\mathcal{T}_y^w$ corresponds to a discrete shift[5] $\mathcal{T}_y^{2w}$ of one period (or two magnet widths) in the y-direction, i.e., $(\mathcal{R}_x\mathcal{T}_y^w)^2 = \mathcal{T}_y^{2w}$. The above transformations that leave the governing equation equivariant may leave the flow fields invariant. For example, the straight flow in Fig. 4.1 (a) remains unchanged when an arbitrary translation $\delta x \in [0, L_x]$ is applied along the x-direction, so there is a unique straight flow solution. However, when a flow field does not share a certain symmetry of the governing equation, one can generate – by applying the corresponding coordinate transformation – a dynamically-equivalent, symmetry-related copy of the flow. Since the primary instability breaks the translational symmetry, there are infinitely many copies of the modulated flow, all related by translations in the x direction. This instability therefore corresponds to a circle pitchfork bifurcation (cf. Fig. 4.9 (a)).

Figure 4.10 shows four (among the infinitely many) distinct solutions $\mathbf{u}_m^1$, $\mathbf{u}_m^3$, $\mathbf{u}_m^2$, and $\mathbf{u}_m^4$ of the modulated flow from the DPS. They are related by discrete translations $\mathcal{T}_x^{\Delta x}$ with $\Delta x = L_x/8$:

$$\mathbf{u}_m^3 = \mathcal{T}_x^{\Delta x}\mathbf{u}_m^1, \quad \mathbf{u}_m^2 = \mathcal{T}_x^{\Delta x}\mathbf{u}_m^3, \quad \mathbf{u}_m^4 = \mathcal{T}_x^{\Delta x}\mathbf{u}_m^2, \quad \text{and} \quad \mathbf{u}_m^1 = \mathcal{T}_x^{\Delta x}\mathbf{u}_m^4. \tag{4.4}$$

The equivariance of the governing equation under $\mathcal{T}_x^{\delta x}$ with arbitrary δx makes the choice of the coordinate origin $x = 0$ for the modulated flow arbitrary. This is fixed by requiring that $\mathbf{u}_m^1 = \mathcal{R}_y\mathcal{R}_x\mathbf{u}_m^1$. Since both the discrete symmetries $\mathcal{R}_y\mathcal{R}_x$ and $\mathcal{R}_x\mathcal{T}_y^w$ include reflection of the flow about the line $x = 0$, the choice of the origin determines whether a particular solution remains invariant under either of these discrete symmetries.

Each of these four solutions is invariant under $\mathcal{T}_y^{2w}$ and either $\mathcal{R}_y\mathcal{R}_x$ or $\mathcal{R}_x\mathcal{T}_y^w$. In particular, $\mathbf{u}_m^1$ and $\mathbf{u}_m^2$ are invariant under $\mathcal{R}_y\mathcal{R}_x$, while $\mathbf{u}_m^3$ and $\mathbf{u}_m^4$ are invariant

[5]In nondimensional units $w = 1$, however to avoid ambiguity with powers of symmetry operators and discrete shits the index w is used.

under $\mathcal{R}_x\mathcal{T}_y^w$. Furthermore, the states $\mathbf{u}_m^1$ and $\mathbf{u}_m^2$ are related to each other via $\mathcal{R}_x\mathcal{T}_y^w$, $\mathbf{u}_m^1 = \mathcal{R}_x\mathcal{T}_y^w\mathbf{u}_m^2$, while $\mathbf{u}_m^3$ and $\mathbf{u}_m^4$ are related via $\mathcal{R}_x\mathcal{R}_y$, $\mathbf{u}_m^3 = \mathcal{R}_y\mathcal{R}_x\mathbf{u}_m^4$. Note that the operator $\mathcal{R}_x\mathcal{T}_y^w$ contains a single reflection which causes the sign of the vorticity to change. In summary, by virtue of the continuous translational symmetry of the governing equation, the laminar flow in the DPS undergoes a circle pitchfork bifurcation with an infinite number of translation-related copies of a modulated flow. Only four of these copies, however, remain invariant under the discrete symmetries $\mathcal{R}_x\mathcal{T}_y^w$ and $\mathcal{R}_y\mathcal{R}_x$.

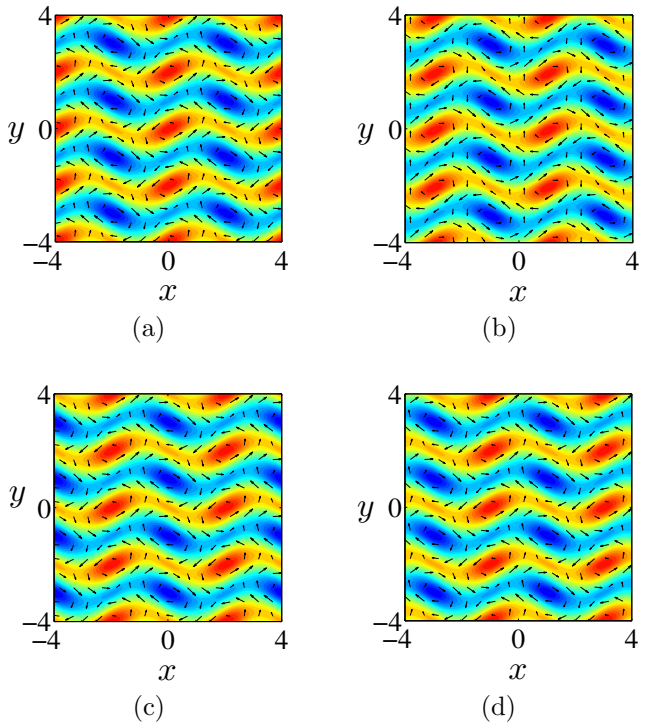

Figure 4.10: Modulated flow fields (a) $\mathbf{u}_m^1$, (b) $\mathbf{u}_m^3$, (c) $\mathbf{u}_m^2$, and (d) $\mathbf{u}_m^4$ at $Re = 14$ in the DPS. The vorticity color scale is the same as that in Fig. 4.6.

4.5.2 SPS

The no-slip boundary condition at $x = \pm L_x/2$ in the SPS destroys the equivariance under translation $\mathcal{T}_x^{\delta x}$. The governing equation, however, still remains equivariant under each of the discrete transformations $\mathcal{R}_x\mathcal{T}_y^w$ and $\mathcal{R}_y\mathcal{R}_x$. The loss of equivariance

under $\mathcal{T}_x^{\delta x}$, which connects the states $\mathbf{u}_m^w$, $\mathbf{u}_m^2$ with $\mathbf{u}_m^3$, $\mathbf{u}_m^4$ in the DPS, implies either of $\mathcal{R}_y\mathcal{R}_x$ or $\mathcal{R}_x\mathcal{T}_y^w$ is broken in the straight to modulated transition in the SPS. Breaking either of the discrete symmetries, $\mathcal{R}_x\mathcal{T}_y^w$ or $\mathcal{R}_y\mathcal{R}_x$ should generate (only) two branches, i.e, should result in a pitchfork bifurcation, since the modulated flow states in the SPS should remain symmetric with respect to $\mathcal{T}_y^{2w}$, which is not affected by confinement in x. Consequently, of the infinite number of modulated states in DPS only four, the counterparts of those shown in Fig. 4.10, will survive in the SPS, and should be formed via two distinct pitchforks.

This is indeed what is observed in the simulations, wherein two pairs of distinct solutions, shown in Fig. 4.11, are formed via two pitchfork bifurcations of the straight flow. Like in the DPS, $\mathbf{u}_m^1$ and $\mathbf{u}_m^2$ are invariant under $\mathcal{R}_y\mathcal{R}_x$, while $\mathbf{u}_m^3$ and $\mathbf{u}_m^4$ are invariant under $\mathcal{R}_x\mathcal{T}_y^w$. The branches formed in a given pitchfork are related via the broken symmetry, i.e, $\mathbf{u}_m^1 = \mathcal{R}_x\mathcal{T}_y^w\mathbf{u}_m^2$ and $\mathbf{u}_m^3 = \mathcal{R}_y\mathcal{R}_x\mathbf{u}_m^4$. Unlike in the DPS where $\mathcal{T}_x^{\delta x}$ relates all the distinct solutions corresponding to the modulated flow (cf. equation (4.4)), there is no coordinate transformation that maps $\mathbf{u}_m^1$ and $\mathbf{u}_m^2$ to $\mathbf{u}_m^3$ and $\mathbf{u}_m^4$.

On an infinite domain, all four branches of the modulated flow are created at exactly the same Re (as in DPS), however, on a finite domain, the pitchfork bifurcations that produce the two pairs of solutions would generally happen at different Re (cf. Fig. 4.9 (b)), which depends on the confinement in both x, y directions. However, since all the modulated flow states are periodic in y, the confinement (for $L_y \geq 4$) in y does not affect Re_c of the pitchfork bifurcations. In contrast, the confinement in the x direction affects the wavelength of modulation, which can lead to the two pitchforks occurring at different Re_c. For $L_x = 14$, chosen from experimental considerations, the instability which gives rise to $\mathbf{u}_m^3$ and $\mathbf{u}_m^4$ is suppressed, pushing the corresponding bifurcation to higher Re. For other choices of L_x, the sequence *may* reverse. Note

that the two modulated flow branches ($\mathbf{u}_m^3$ and $\mathbf{u}_m^4$) that are formed from the second pitchfork are initially unstable, because they originate from an already unstable straight flow.

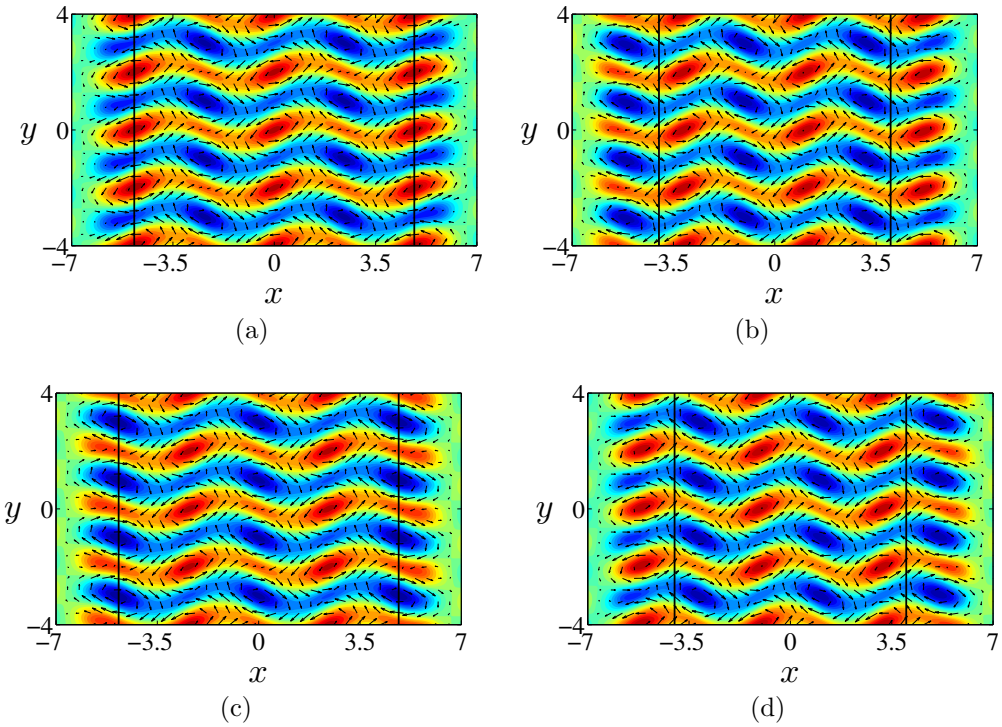

Figure 4.11: Modulated flow fields (a) $\mathbf{u}_m^1$, (b) $\mathbf{u}_m^3$, (c) $\mathbf{u}_m^2$, and (d) $\mathbf{u}_m^4$ at $Re = 14$ in the SPS. Vertical black lines indicate the central region which is analogous to the flow fields shown in Fig. 4.10. The vorticity color scale is the same as that of Fig. 4.6.

4.5.3 NPS

In the NPS, the additional no-slip boundary condition at $y = \pm L_y/2$ breaks the equivariance of the problem under $\mathcal{R}_x T_y^w$, leaving the governing equation equivariant only under $\mathcal{R}_y \mathcal{R}_x$. Since $\mathcal{R}_x T_y^w$ underlies the pitchfork bifurcation that gives rise to the solutions $\mathbf{u}_m^1$ and $\mathbf{u}_m^2$ in the SPS, when this symmetry is broken, one finds an imperfect pitchfork bifurcation, as shown in Fig. 4.9 (c). The straight flow $\mathbf{u}_s^1$ at lower Re smoothly transitions to the modulated flow $\mathbf{u}_m^1$ at higher Re without an instability taking place, i.e., the real part of the leading eigenvalue of the straight flow does not change sign as the one increases the Re in the NPS. The shapes of the

bifurcation curves close to Re_c (figure 4.7 (a)) capture this difference in the nature of the primary instability across the NPS and the two periodic simulations.

In the NPS, the $\mathbf{u}_m^2$ branch and the higher-Re branch of the straight flow $\mathbf{u}_s^2$ are created in a saddle-node bifurcation at $Re = 10.72$. The states $\mathbf{u}_m^1$ and $\mathbf{u}_m^2$, both of which are symmetric with respect to $\mathcal{R}_y\mathcal{R}_x$, are shown in Fig. 4.12. While $\mathcal{R}_x T_y^w$ is no longer an exact symmetry in NPS, given the large transverse extent of the domain compared with the period of the forcing ($L_y = 18$), near the center of the domain this approximate symmetry holds and consequently, $\mathbf{u}_m^2 \approx \mathcal{R}_x\mathcal{T}_y^w\mathbf{u}_m^1$. However, unlike $\mathbf{u}_m^1$, which remains stable up to $Re = 15.4$ in the NPS, $\mathbf{u}_m^2$ is unstable over the entire range of Re where it exists ($Re \geq 10.72$). This explains why numerical simulations starting from randomized initial conditions have always converged to the modulated flow $\mathbf{u}_m^1$ and why $\mathbf{u}_m^2$ was never found in the numerical simulations or observed in the experiment.

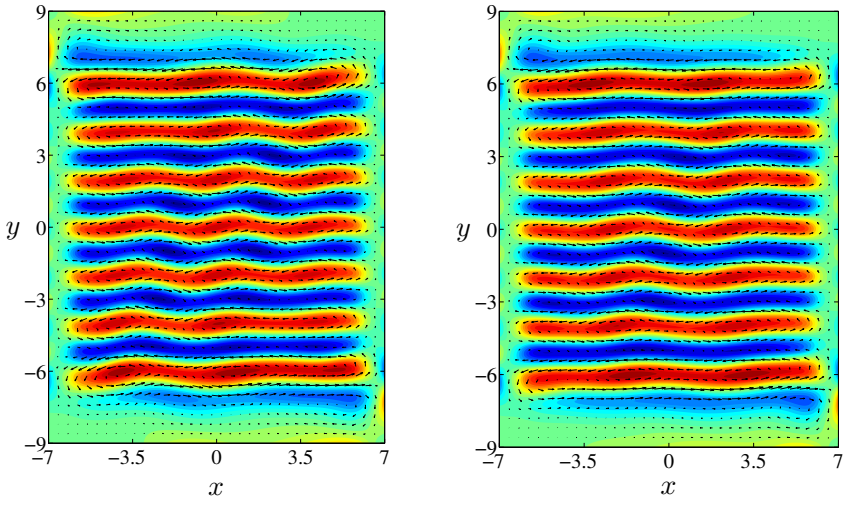

Figure 4.12: Modulated flow fields at $Re = 11.6$ in the NPS beyond the imperfect pitchfork bifurcation shown in Fig. 4.9 (c). The flow fields shown here are (a) $\mathbf{u}_m^1$ which emerges smoothly from the straight flow and (b) $\mathbf{u}_m^2$ which is formed through a saddle-node bifurcation.

The pitchfork bifurcation which gave rise to the branches $\mathbf{u}_m^3$ and $\mathbf{u}_m^4$ in the SPS

did not carry over into the NPS. This is possibly because the window of Reynolds numbers they exist in the NPS above the saddle node may be too small, requiring a much finer resolution in Re ($\Delta Re \leq 0.01$) to search for the branches. Such a computation is beyond the scope of the present study. Lastly, this suppression in window of Re is likely caused by transverse confinement, which has a more prominent effect on $\mathbf{u}_m^3$ and $\mathbf{u}_m^4$: these states are invariant under the $\mathcal{R}_x\mathcal{T}_y^w$ symmetry in the SPS, but this symmetry is broken in the NPS. While $\mathbf{u}_m^3$ and $\mathbf{u}_m^4$ are not observed in the NPS for the given domain parameters, the analogues of these solutions may appear for different model parameters, forcing profile, and/or the degree of confinement. Details regarding the computation of the unstable branches associated with the various pitchfork bifurcations are included in Appendix F.

4.6 Secondary Instability: Onset of Time-Dependent Dynamics

As the forcing is further increased, the modulated flow in the experiment becomes unstable at $Re_s = 17.6 \pm 0.1$ giving way to a time-periodic flow with a period of 42.8 ± 0.4 (120 ± 1 s in dimensional units) at onset. With a quasi-static increase in the driving, the amplitude of these oscillations grows while the period remains approximately constant. A sample of the power spectra spatially averaged over the region $|x| \leq 4$ and $|y| \leq 4$ is shown in Fig. 4.13 (a). The bifurcation diagram quantifying this transition is presented in Fig. 4.13 (b), which shows the peak intensity I of the temporal power spectrum as a function of $Re - Re_s$.

The modulated flow in the DPS and $\mathbf{u}^1$ in the SPS (which matches the experiment the closest, cf. Fig. 4.6), unlike in the experiment, do not transition directly to an oscillatory state. Instead, they undergo pitchfork bifurcations; the DPS at $Re_s = 14.7$ and $\mathbf{u}^1$ in SPS at $Re_s = 16.7$. This clearly demonstrates that periodic simulations fail to capture the dynamics in the experiment at higher Re. Hence, exploration of flow regimes with temporal dependence in DPS and SPS, as well as direct comparison

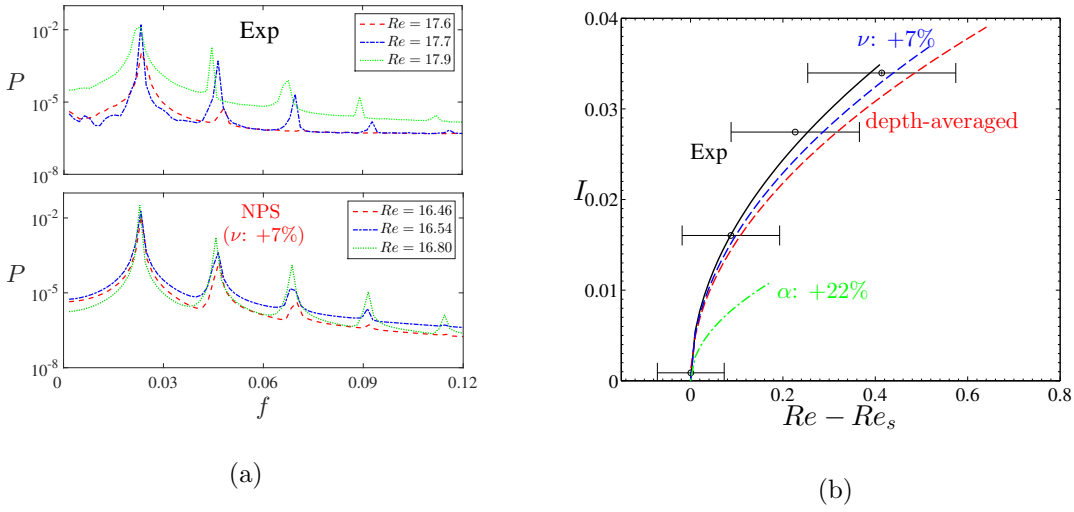

Figure 4.13: Quantifying the secondary instability of the Kolmogorov-like flow in the experiment and NPS which gives rise to an oscillatory vortex pattern. In Panel (a) the sample of the temporal power spectra P as a function of the temporal frequency f in the experiment (top) and NPS with ν increased by 7% (bottom) are included. The temporal power spectra for the depth-averaged parameters are similar as well. In (b) the bifurcation diagram showing the integrated power spectrum intensity I as a function of $Re - Re_s$ is presented. The temporal power spectrum is averaged over the central region $|x| \leq 4$ and $|y| \leq 4$. Note that although the NPS with α increased by 22% is plotted in (b), the associated power spectra are not provided.

with experiment, is not presented here[6].

The modulated flow in the NPS, with the depth-averaged ($\alpha = 0.064$ s^{-1}, $\beta = 0.83$, and $\bar{\nu} = 3.26 \times 10^{-6}$ m^2/s) as well as the adjusted parameters, undergoes a Hopf bifurcation as the forcing is increased, leading to an oscillatory state like in the experiment. For the depth-averaged and the adjusted parameter sets with $\bar{\nu} = +7\%$ and $\alpha = +22\%$ the plots of peak intensity I versus $Re - Re_s$ are shown in Fig. 4.13(b). For each parameter set shown in Fig. 4.13, Re_s is different and the values are indicated in Table 4.1. While changing β modifies Re_s, the variation of order parameter I as a function of $Re - Re_s$ is independent of β (cf. velocity scaling

[6]The steady flows in DPS and SPS eventually transition to oscillatory states at higher Re. The period of oscillations at onset in the DPS is around 30 seconds while that in the SPS is around 90 seconds, both of which differ significantly from that (120 seconds) observed in the experiment.

discussed in section (4.4)). This follows from the definition of I, which is the peak intensity of the spatially averaged temporal Fourier spectrum of $\mathbf{u}(t)/U$. Hence, the plot of I versus $Re - Re_s$ for the parameter set $\beta = -6\%$ is identical to that obtained using using depth-averaged parameters.

From Fig. 4.13 and Table 4.1 it is evident that Re_s, T_s, as well as the growth of the amplitude show very different sensitivity to changes in each of the parameters. Hence, while separately modifying $\bar{\nu}$, α, and β shows improvement in matching I versus $Re - Re_s$, T_s, and Re_s (trivially using β) it should be possible to obtain even better agreement by modifying *all* the model parameters simultaneously, each by only a few percent. For example, by increasing $\bar{\nu}$ by 7% and accordingly choosing a suitable value of β, one can match Re_s in simulation and experiment *exactly*, with only an 8% difference in period of oscillation. The growth of peak intensity I versus $Re - Re_s$ also shows excellent agreement for this choice, as can be seen from the blue curve in Fig. 4.13(b).

Note that the depth-averaged parameters are computed using the vertical profile $P(z)$ that corresponds to the straight sinusoidal flow. However, the values of $\bar{\nu}$, α, and β should vary slowly with Re, since $P(z)$ is weakly dependent on the horizontal flow profile, as shown in Appendix D. Hence, a different set of parameters is required to describe the two instabilities and, more generally, there is no universal set of parameters β, $\bar{\nu}$, and α that correctly describes the experimental flow at all Re. The necessity of modifying parameters across different dynamical regimes raises the question of how robust α, β, and $\bar{\nu}$ are to changes in the (local) wavenumber of the flow. To test this, the parameters were recomputed using the wavenumber $k \approx \sqrt{5/4}\kappa$ (1.18κ) associated with the modulated flow. It was found that β and $\bar{\nu}$ change by less than 1%, and α by about 3.5%, compared to those computed using $k = \kappa$. This robustness suggests that, once adjusted to match the experiment, the 2D model should provide a reasonably accurate description of the dynamics even in the weakly

Table 4.1: Critical transition parameters characterizing the stable periodic regime for the experiment and the NPS with different sets of parameters.

	Re_s	T_s
Experiment	17.6 ± 0.1	42.8 (120 ± 1 s)
NPS (Depth-Averaged)	15.6	43.2 (137 s)
NPS ($\bar{\nu}$: +7%)	16.4	43.2 (130 s)
NPS (α: +22%)	17.1	48.1 (139 s)
NPS (β: −6%)	16.5	45.8 (137 s)

turbulent regime where the wavenumber may vary in space and time [78].

4.7 Summary

In this chapter a detailed study of the laminar states in a Q2D Kolmogorov flow was performed, using both experiments and simulations. To test the importance of lateral confinement, experimental measurements were compared with numerical simulations with different boundary conditions. It was shown that global circulation plays a role in shaping the flow structure even at very low driving. The sinusoidal straight flow, its transition to a steady vortex pattern, and the onset of temporal dynamics with steady oscillations were studied experimentally and compared with numerical simulations. The nature of the transition from straight to modulated flows as the degree of confinement in the system is changed was studied from a symmetry-breaking standpoint. The 2D model derived in the previous chapter and its numerical discretization have been validated through the bifurcation study presented in this chapter, setting stage for studying weakly turbulent dynamics that follow as the driving is further increased. This study will form the next chapter in the thesis, where the role of ECS in experiments and NPS will be discussed.

CHAPTER V

DYNAMICAL ROLE OF EXACT COHERENT STRUCTURES

In the previous chapters of this thesis, the experimental realization of a quasi-two-dimensional flow and its modeling using a strictly-2D equation were discussed. The model was validated by studying laminar regimes of the Kolmogorov-like flow, and it was demonstrated that one can replicate the dynamics observed in the experiment remarkably well by employing simulations that include realistic no-slip boundary conditions; the periodic simulations fared poorly in this regard. In this chapter, the role of exact coherent structures in a weakly turbulent flow, which is observed as the driving is increased further, are studied in both the experiment and the non-periodic simulation.

The outline of this chapter is as follows: section (5.1) provides a brief discussion of the characteristics of chaotic dynamics observed in both experiments and numerical simulation of the Kolmogorov-like flow. The role of unstable equilibrium solutions is discussed in section (5.2) and their proximity to the turbulent trajectory is studied in section (5.3). The unstable manifolds associated with the solutions are constructed in section (5.4) and used to forecast turbulent evolution. Finally, in section (5.5) dynamical connections between unstable equilibria are presented.

5.1 Onset Of Spatiotemporally Chaotic Dynamics

As mentioned in the previous chapter, the modulated state remains stable until about $Re \approx 17$ in both the simulation (NPS) and the experiment. As the driving is increased further, one observes spatiotemporal evolution of the vortex pattern, i.e., the pattern

changes in time. The exact nature of the dynamics close to the onset of the temporal evolution is quite sensitive to the geometry of the setup[1]. However, for sufficiently large driving, $Re \geq 19$, the dynamics show complicated spatiotemporal behavior.

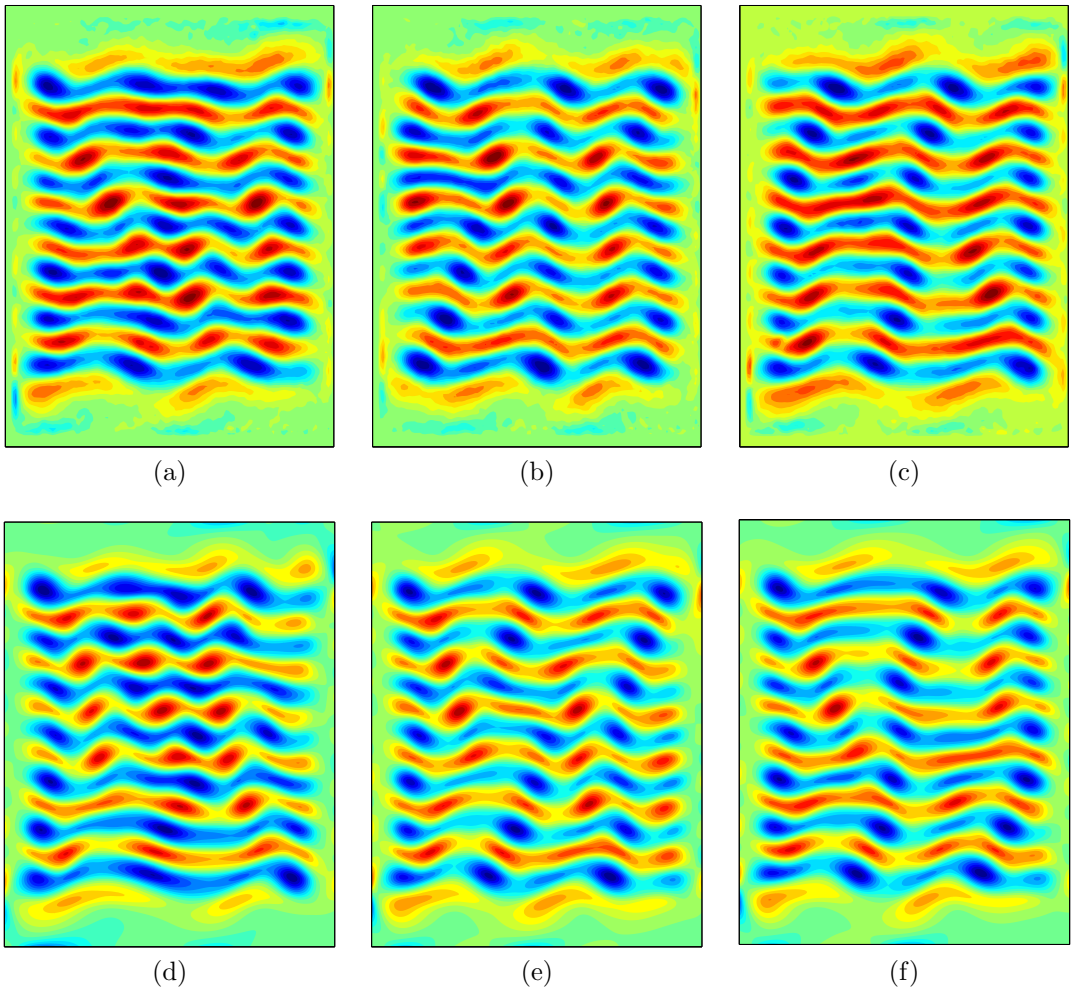

Figure 5.1: Contour plots of vorticity of sample turbulent flow fields at $Re = 22.5$. Panels (a), (b), and (c) show flow fields from the experiment while panels (d), (e), and (f) show flow fields from the NPS.

Fig. 5.1 shows contour plots of vorticity for sample flow fields at $Re = 22.5$ in both the experiment and NPS at different instants during turbulent evolution. While vortices rotating in opposite directions remain the building blocks of the flow, like in the modulated regime, their arrangement varies significantly over time. Furthermore,

[1]The data presented in this chapter was acquired using the setup described in chapter 2.

the flow fields cease to remain invariant under the rotational symmetry of the governing equations in the turbulent regime (cf. chapter 4). However, since the governing equation (3.14) remains equivariant under $\mathcal{R}_y\mathcal{R}_x$, a flow field (e.g., Fig. 5.1(c)) or its rotated copy (Fig. 5.1(f)) are equally likely to appear during turbulent evolution.

5.1.1 Temporal Auto-Correlation

The estimate for how long it typically takes for a turbulent flow field to change significantly in the course of its evolution can be computed using the temporal auto-correlation of the velocity fields, defined using the following equation:

$$C(\tau) = \frac{\langle \Delta\mathbf{u}(t) \cdot \Delta\mathbf{u}(t+\tau) \rangle_t}{\langle \Delta\mathbf{u}(t) \cdot \Delta\mathbf{u}(t) \rangle_t}, \tag{5.1}$$

where $\langle \cdots \rangle_t$ indicates temporal average, $\Delta\mathbf{u}(t) = \mathbf{u}(t) - \langle \mathbf{u}(t) \rangle_t$, and $\Delta\mathbf{u}(t) \cdot \Delta\mathbf{u}(t+\tau)$ is the vector dot product of the fields $\Delta\mathbf{u}(:)$ at instants t and $t+\tau$ [2].

Figure 5.2 shows a plot of the normalized temporal auto-correlation as a function of τ at $Re = 22.5$. The normalization criterion $C(0) = 1$, takes into account that a flow field at every instant is identical (and hence perfectly correlated) to itself. The correlation time τ_c is smallest root of $C(\tau) = 1/e$, denoted by the black dashed line in Fig. 5.2. For both the experiment and simulation the correlation time $\tau_c \approx 12.5$ (27s in dimensional units).

5.1.2 Recurrence Analysis

The auto-correlation yields a temporally global measure, with practically no information regarding instantaneous temporal behavior as well as spatial structure of the flow. To visualize both the spatial and instantaneous temporal complexity of a dynamical system, turbulence in the present case, "recurrence plots" are a powerful tool [137]. A 2D recurrence plot can be constructed by comparing the state ($\mathbf{u}$) at each

[2] The velocity field $\mathbf{u}$ is recast into a column vector $[u(:);v(:)]$ cf. section (3.3.3) to compute the vector dot product

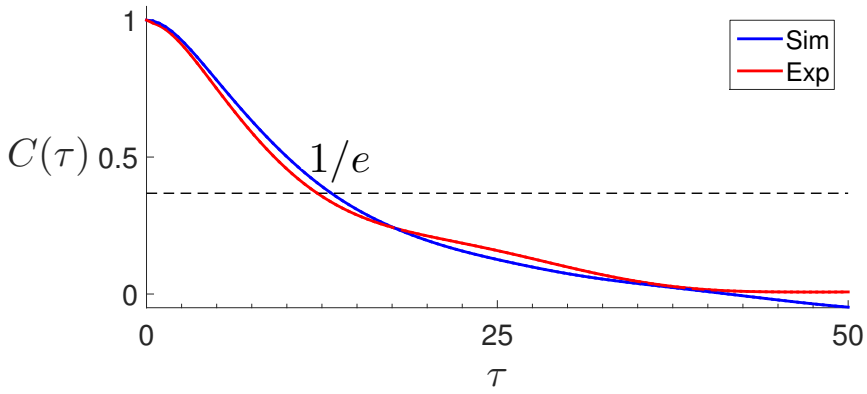

Figure 5.2: Plot of temporal auto-correlation of the velocity fields at $Re = 22.5$ in simulation (blue) and experiment (red). The correlation time τ_c corresponds to the smallest value of τ such that $C(\tau \geq \tau_c) \leq 1/e$. For both the experiment and simulation $\tau_c \approx 12.5$.

.

instant t with the state at a later[3] instant $t + \tau$, using the equation,

$$R(t, \tau) = \frac{\min\left(\|\mathbf{u}(t) - \mathbf{u}(t+\tau)\|, \|\mathbf{u}(t) - \mathcal{R}_y\mathcal{R}_x\mathbf{u}(t+\tau)\|\right)}{\|\mathbf{u}(t)\|}, \tag{5.2}$$

with $\tau > 0$. In the above equation $\|\cdots\|$ indicates the L2 norm. The equivariance of the governing equation under the symmetry $\mathcal{R}_y\mathcal{R}_x$ requires testing if the rotated copy of a flow field has recurred in time. This is accounted for in the above equation by choosing minimum of the differences between the state $\mathbf{u}(t)$ and $\mathbf{u}(t+\tau)$ or its rotated copy $\mathcal{R}_y\mathcal{R}_x\mathbf{u}(t+\tau)$. Small values of R indicate that the flow fields at the two instants are similar, while large values indicate they are very different.

Fig. 5.3 shows two sample recurrence plots at $Re = 22.5$, one each from simulation and experiment. Low values of R show up as blue regions, indicating that two flow fields at instants t and $t + \tau$ are similar. Red regions, which correspond to high value of R, indicate the flow fields at two instants are significantly different. In the experiment, a total of 4 runs were performed, each 1700 time units long ($\approx 125\tau_c$ or

[3]In this thesis recurrence plots are constructed for $\tau > 0$. One can construct plots using $\tau < 0$ to obtain more or less identical information.

3600s). In the numerical simulations a time series[4] 11,500 units ($\approx 900\tau_c$ or 25,000s) long was generated. The range $R \in [0, 1.2]$ for the recurrence values was found to be more or less constant for all recurrence searches at $Re = 22.5$.

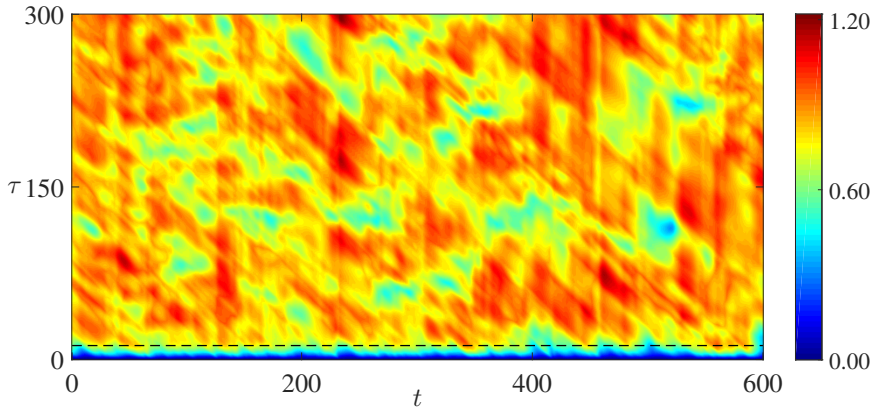

(a)

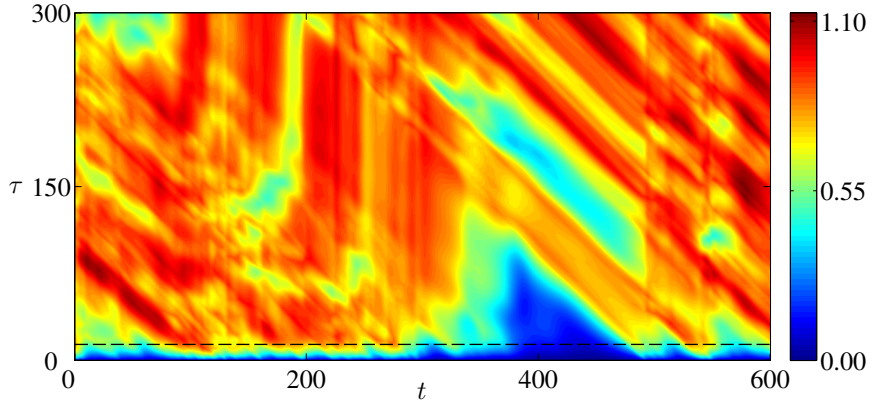

(b)

Figure 5.3: Recurrence diagrams of experimental and numerical time series of turbulent flow fields. The colormap indicates how similar (blue) or different (red) the velocity fields are at two instants t and $t + \tau$. The black dashed line at τ_c, the mean correlation time for the time series, indicates the typical duration beyond which a pattern ceases to resemble itself. In both the plots t is given in non-dimensional units.

[4]In the numerical simulations two additional time series, one 11,000 units ($\approx 900\tau_c$ or 25,000s) long (using P1 scheme), and another 22,000 units ($\approx 1800\tau_c$ or 50,000s) long (using P2 scheme) were generated. The recurrence analysis from all the three runs gave similar picture of the dynamics.

5.2 Computing Unstable Equilibrium Solutions

Recurrence plots can be used to infer two very distinct dynamical behaviors, depending on where a blue region is identified. Blue "bands/islands" far enough from the $\tau = 0$ axis (like one at $(t, \tau) \approx (500, 125)$ in Fig. 5.3(a)) indicate periodic motion, which help identify close passes to periodic or homoclinic orbits. Computing homoclinic cycles is fairly challenging and is not pursued herein. However, for both the numerical and experimental time series, there were very few (≤ 10) recurrences that suggested the presence of periodic orbits[5]. Initial guesses using Newton-Krylov solver did not result in their convergence either. However, the more common pattern found from recurrence plots is the presence of blue regions close to $\tau = 0$ axis. For a sufficiently fine temporal sampling ($\Delta\tau = 0.46$), the velocity fields do not change significantly across consecutive instants, resulting in low recurrence values (blue band) close to $\tau = 0$. However, as the value of τ increases one typically observes a rapid increase in values of R, indicated by the emergence of the yellow/red regions in the contour plot. This increase in R captures the loss of correlation between flow fields separated in time. However, one can identify from the recurrence plots special intervals during which the flow field changes significantly less over one correlation time (indicated by the black dashed line at $\tau = \tau_c$). These intervals appear as blue triangles with height approximately equal to τ_c at the bottom of the recurrence plots, as can bee seen in Fig. 5.3(a) at instants t $\approx 0, 400, 475, 500, 600$ and in Fig. 5.3(b) at $t \approx 25, 50, 310, 425, 525, 575$. For the most conspicuous triangle, at $t \approx 450$ in the simulation, the recurrence value at τ_c is $R(470, \tau_c) = 0.07$, which is a factor 8 smaller than the temporal mean recurrence value along $\tau = \tau_c$, $\langle R(\tau_c)\rangle_t = 0.65$, computed over the whole time series[6]. The recurrence plots suggest that in simulations as well

[5]This was not the case with the DPS, for example. Several periodic as well as relative periodic orbits were identified and computed.

[6]While not rigorous, $\langle R(\tau_c)\rangle_t \approx 1 - 1/e$, since the correlation after τ_c is 1/e, by definition.

as in the experiment, there are intervals during which the evolution of the turbulent flow slows down dramatically, resulting in longer temporal correlations.

In the state space picture of the turbulent trajectory visiting the neighborhoods of ECS, such slow-downs suggest that the trajectory *may* be in the vicinity of an unstable equilibrium solution. This inference can be rationalized using the analogy of a rotating pendulum slowing down at its inverted position (2D state space coordinates θ and $\dot{\theta}$) which is close to the unstable equilibrium state ($\theta = \pi$ and $\dot{\theta} = 0$). Since the near by equilibrium is not known *a priori* in the present case, it is hypothesized that the instant a turbulent trajectory is evolving the slowest is an instant it is *sufficiently* close to the equilibrium. The instantaneous "state space speed" of a turbulent trajectory[7], defined as

$$s(t) = \frac{1}{s_0} \left\| \frac{\partial \mathbf{u}}{\partial t} \right\| \approx \frac{1}{s_0} \frac{1}{\Delta t} \left\{ \iint \left[\mathbf{u}(t + \Delta t) - \mathbf{u}(t) \right]^2 \, \Delta x \, \Delta y \right\}^{1/2}, \tag{5.3}$$

yields the instantaneous rate of evolution of the turbulent flow field. The difference in velocity fields across successive instants[8] of sampled data is measured using the L2 norm. In both simulation and experiment, the rate of sampling Δt was chosen to be 0.46 ($\approx 0.03\tau_c$ or 1s). The scale factor s_0 in the above equation can be computed using normalization condition $\langle s \rangle_t = 1$. At $Re = 22.5$, $s_0 \approx 10$ which is the average speed of evolution of the turbulent trajectory in state space.

5.2.1 Close Passes in the Simulation

Fig. 5.4 shows the plot of normalized state space speed as a function of time from the simulation. The (open and filled) red symbols, indicate the local minima in s for $s \leq 1$, which correspond to instants of the slowest rates of evolution, locally in

[7]The idea to use the instantaneous rate of evolution ($d\mathbf{u}/dt$) follows from recurrence analysis, since $R(t, \tau = 1)$ gives the relative change in the velocity field $\Delta\mathbf{u}$ per sampling time unit Δt.

[8]Alternatively, the speed can be defined as $s(t) = \tau_c \frac{1}{\|u(t)\|} \left\| \frac{\partial \mathbf{u}}{\partial t} \right\|$. This definition has the advantage that it takes into account both the instantaneous norm of the velocity and the characteristic time scale of change in flow structures.

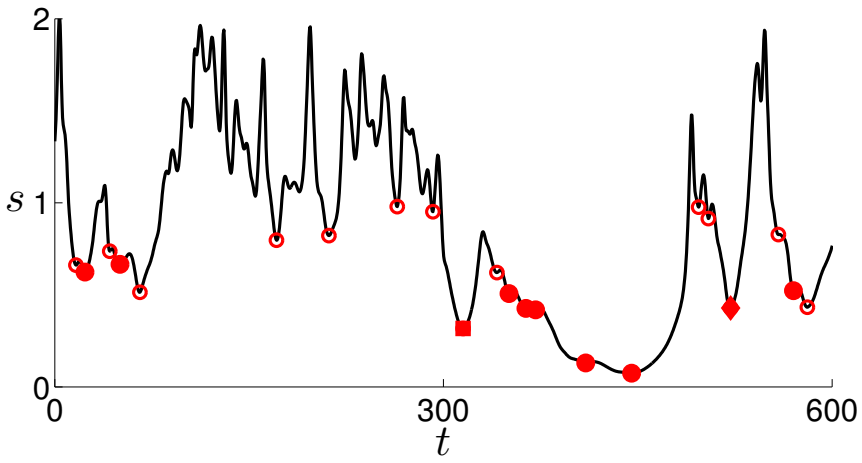

Figure 5.4: Plot of the state space speed (s) versus time (t) for the turbulent flow in the simulation. s measures how quickly turbulent flow fields change at a given instant. Very deep minima are conjectured to be close passes of the turbulent trajectory to unstable equilibrium solutions, like the one at $t \approx 450$. The filled symbols indicate the instants at which a nearby equilibrium was identified using a Newton-Krylov solver; different symbols (circle, diamond, and square) indicate convergence to distinct solutions. Open symbols indicate that the initial conditions at the minima have not not been tested for or resulted in convergence. Lastly, t in the above plot is given in non-dimensional units.

time. The very deep minima in the state space speed plot coincide with the intervals of prominent blue triangles observed in the recurrence plot Fig. 5.3(b). In the numerical simulation, all the local minima from the entire time series are extracted and sorted using their state space speed value. Each initial condition $\mathbf{u}_{ic}^{sim}$, in the sorted sequence, is input into a Newton-Krylov solver [133, 138] to test for convergence to an unstable equilibrium. The Newton-Krylov solver for computing equilibria iteratively modifies $\mathbf{u}_{ic}^{sim}$ to generate a sequence of states $\mathbf{u}_1, \mathbf{u}_2, \cdots, \mathbf{u}_k$ such that the residual $r_k = \|\mathbf{u}_k(\Delta T) - \mathbf{u}_k\|$ decreases as the iteration index k increases. Here $\|\cdots\|$ represents the L2 norm, and $\mathbf{u}_k(\Delta T)$ is computed by integrating $\mathbf{u}_k$ using the 2D equation (3.3) for a duration[9] $\Delta T = 0.45$. Convergence to an equilibrium implies $\mathbf{u}_k$

[9]The choice $\Delta T = 0.45$, the same as sampling rate, resulted from efficiency criteria. Too short a ΔT resulted in poor convergences while too long a ΔT increases computational time. For each simulation initial condition convergence was tested using $\Delta T = 0.45, 0.9, 1.8$, in that order. Initial conditions that did not converge using $\Delta T = 0.45$ rarely converged using higher ΔT.

ceases to evolve in time, i.e., $r_k \leq \epsilon$, where ϵ is very small (10^{-8} chosen for numerical convenience).

In Fig. 5.4 the closed symbols indicate the instants at which initial conditions converged to an equilibrium. Fig. 5.5 shows contour plots of vorticity at two different instants of minimum s, the equilibrium solutions each initial condition converged to, and the difference between $\mathbf{u}_{ic}^{sim}$ and the corresponding solution $\mathbf{u}_0$. The first set in Fig. 5.5(a) correspond to the slowing down near $t \approx 450$ in Fig. 5.4, indicated by the red filled circle; several initial conditions converged to this solution. Panel (b) shows the solution that corresponds to slowing down near $t = 330$ (indicated by the red square). The striking similarity between the equilibria and turbulent flow fields confirms that the turbulent trajectory comes fairly close to these ECS and evolves slowly when in their neighborhood.

Since the numerically generated trajectory is fairly long (duration of $11,500$ time units) around 1000 minima were identified. Since the true location of minimum identified a discrete time instant t_n can lie within the interval $t_n \pm \Delta t$, where Δt is the data sampling rate, the flow fields at $t_n + \Delta t$ and $t_n - \Delta t$ were also tested for convergence. Large number (3000) of initial conditions requires sorting to assign the slowest evolving states from across the entire time-series the highest priority to test for convergence. Consequently, several (higher) state-space minima were not tested, while others did not result in convergence. All these are represented using open circles in Fig. 5.4. In all, around 180×3 initial conditions from numerical simulations were tested, of which 30 minima converged ($\approx 16\%$) to an equilibrium, resulting in 10 distinct solutions.

5.2.2 Close Passes in the Experiment

The turbulent dynamics at $Re = 22.5$ in the experiment are similar to those observed in the simulation, as can be seen from the comparison of recurrence plots in

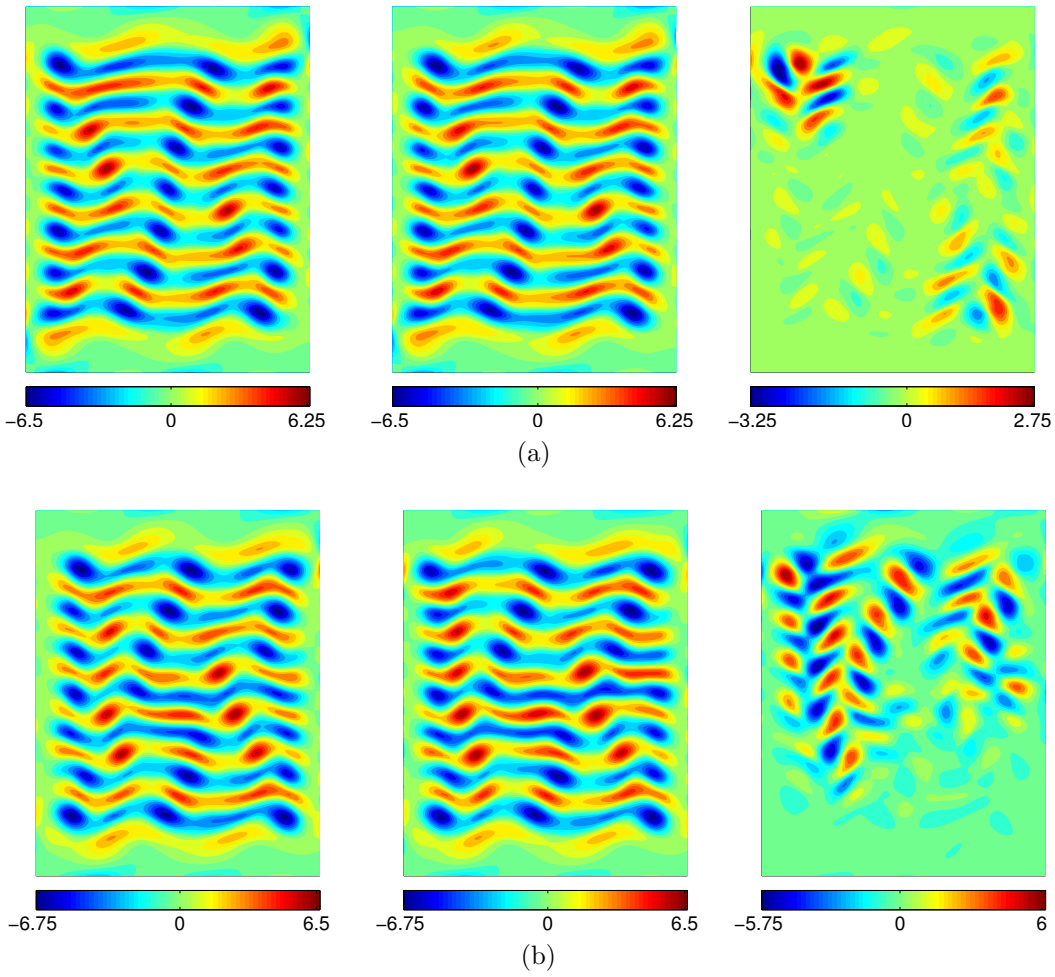

Figure 5.5: Unstable equilibrium solutions computed from numerical turbulent trajectory. The flow fields on the left column are from instants of slowest evolution, local minimum in s. The flow fields in the central pane are the equilibrium solutions the Newton-Krylov solver converged to and the contour plots on the right showcase the difference between $\mathbf{u}_{ic}^{sim}$ and $\mathbf{u}_0$

Fig. 5.3, with intervals of slow evolution. In principle, one can search through the experimental time-series for close passes to the 10 solutions computed from numerical initial conditions, and relate such instants to slowing down in evolution. However, the duration of each experimental run (1700 time units), is not long enough to observe a sufficiently close pass to any of the 10 solutions computed using the numerical turbulent trajectory. Moreover, there may be close passes to other solutions which

may not have been computed from numerical trajectory because of the sorting criteria employed. Hence, an alternative protocol of computing solutions *directly* using experimental initial conditions is developed.

The state space speed of the turbulent flow fields in the experiment is computed using PIV data, following which instants of local minima in s are identified and sorted separately for each run. However, unlike in the simulation, only the lowest minimum occurring within one correlation time (12.5 time-units or 27s) is retained for analysis to reduce possible duplication of initial conditions. This constraint would have excluded the numerical initial conditions marked by two open red circles in Fig. 5.4 at $t \approx 50$ from testing. In all, about 60×4 initial guesses from the 4 experimental runs were identified as initial conditions to test for convergence. These initial guesses were interpolated onto the simulation grid following the procedure described in section (3.3.5).

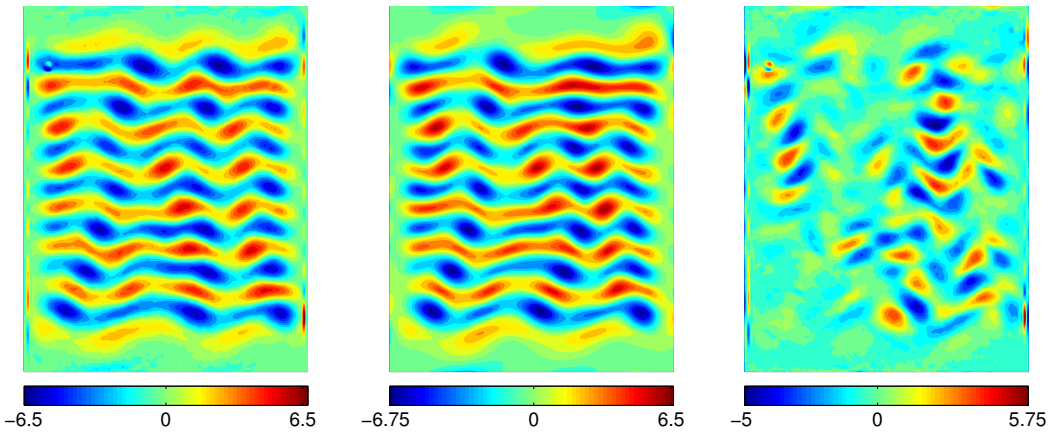

Figure 5.6: Equilibrium solution computed from experimental initial conditions. The flow field on the left is the initial condition from the experiment, the one in the middle is the equilibrium it converged to, and the contour plot on the right shows the difference between $\mathbf{u}_{ic}^{exp}$ and $\mathbf{u}_0$.

Fig. 5.6 shows a sample flow field (left column) from the experiment at an instant of slow evolution, the corresponding equilibrium it converged to (middle column), and the difference between the initial condition and the solution (right column). The

degree of similarity between these initial conditions and the corresponding equilibria is remarkable, indicating that, like in the simulation, the turbulent trajectory in the experiment passes close to the ECS. In all, 16 initial conditions from the experiment (about 7% of those tested) converged to 13 distinct equilibria. Five (distinct) equilibrium solutions computed from experimental initial conditions were also computed from numerical initial conditions, resulting in a total of 19 distinct solutions. That a smaller fraction of initial conditions in experiment converged cannot be attributed entirely to noise in the data or discrepancy between experiment and the 2D model. As mentioned earlier, the criteria for testing the initial conditions from simulation and experiment were different to account for the difference in the length of time-series available.

5.3 Quantifying the Closeness of Equilibria to Turbulent Trajectories

The vorticity contour plots in Fig. 5.5 and Fig. 5.6 suggest that turbulent trajectories come quite close to these ECS. However, the distance of closest approach can be quantified using,

$$D_0(t) = \frac{\|\mathbf{u}(t) - \mathbf{u}_0\|}{\|\mathbf{u}_0\|}, \tag{5.4}$$

where $\mathbf{u}(t)$ represents the turbulent velocity field at an instant t, $\mathbf{u}_0$ is an equilibrium solution, and $\|\cdots\|$ is the L2 norm. Fig. 5.7 shows the plot of $D_0(t)$ versus t over the interval which includes the instant of slowest evolution (cf. Fig. 5.4) in the simulation. Also plotted is the state space speed $s(t)$ of the turbulent trajectory. For convenience, $t = 0$ is locally reset to coincide with the instant of local minimum in s, at which the initial condition was used to compute $\mathbf{u}_0$. The instants of slowest evolution and closest approach are close to each other in time, but are not identical.

For the specific example plotted in Fig. 5.7, the distance between the initial condition $\mathbf{u}_{ic}^{sim}$ and the converged solution $\mathbf{u}_0$ is $D_0^{ic} = 0.20$. The closest point on the

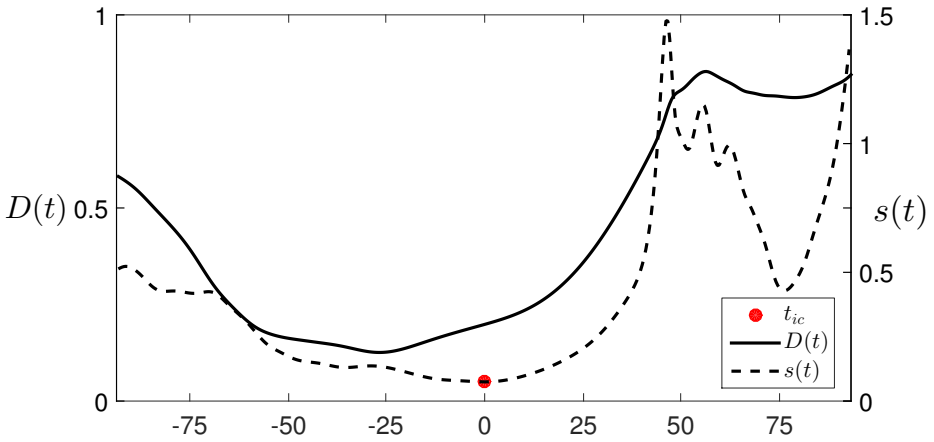

Figure 5.7: Comparing the state space speed $s(t)$ (solid line) in the vicinity of an equilibrium $\mathbf{u}_0$ and the distance of the turbulent trajectory $D_0(t)$ from it. While the instant of slowest evolution (indicated by red rot) is fairly close to the instant of closest approach to the equilibrium, they do not coincide. Time t in the above plot is given in non-dimensional units.

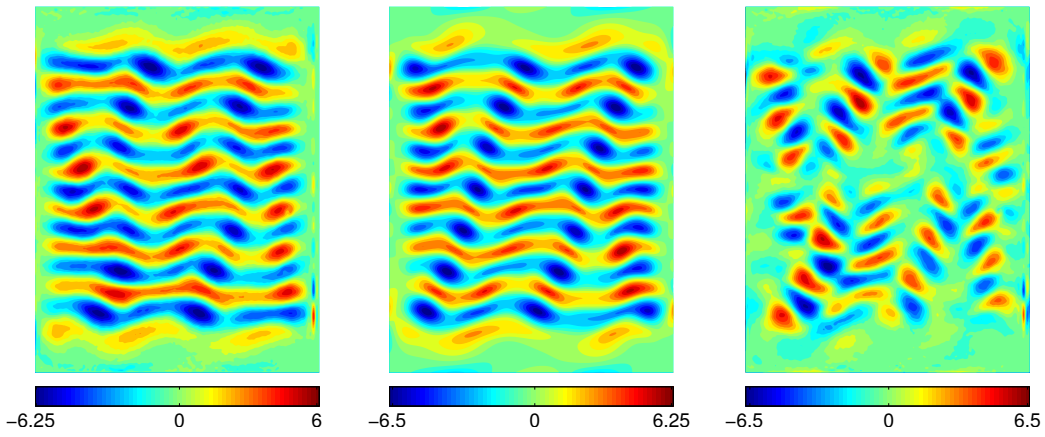

(a)

Figure 5.8: Example of a convergence to a solution far away from the initial condition. The flow field on the left is the initial condition from the experiment, the one in the middle is the solution computed using the 2D model, and the flow field on the right is the difference between the initial and converged states, the normalized difference between the two being 0.79, computed using equation (5.4).

turbulent trajectory within the interval analyzed, however, is $D_{0,min} = 0.13$ from the solution. Furthermore, the instant of closest approach is 25 time units (or about 50 seconds) before the minimum in state space speed is observed. For the solution shown

in Fig. 5.5(b), which is indicated using the red square in Fig. 5.4, the distance estimates are $D_0^{ic} = 0.61$ and $D_{0,min} = 0.58$. The closest approach to the solution within

Table 5.1: Summary of equilibrium solutions computed from initial conditions obtained from simulations (S), experiments (E), or both (B). The solutions are sorted in ascending order of their L2 norm $\|\mathbf{u}_0\|$. D_0^{ic} is the normalized difference between the initial condition and the converged solution, defined using equation (5.4). N_{us} is dimensionality of the unstable manifold, while N_{KY} is the Kaplan-Yorke dimension. λ_1^+ is the eigenvalue with the largest real part, while $\sum_k \lambda_k^+$ is the summation of unstable eigenvalues.

Sol	$\|\mathbf{u}_0\|$	D_0^{ic}	$D_{0,min}^{sim}$	$D_{0,min}^{exp}$	N_{us}	N_{KY}	λ_1^+	$\sum_{k=1}^{N_{us}} \lambda_k^+$
01/B	254.74	0.19	0.13	0.57	2	4.53	0.0273	0.0518
02/S	258.21	0.50	0.23	0.40	8	13.61	0.151	0.241
03/B	258.46	0.24	0.19	0.37	7	12.93	0.149	0.189
04/E	261.12	0.79	0.63	0.70	7	15.00	0.194	0.494
05/S	264.13	0.50	0.42	0.52	3	6.81	$0.035 \pm 0.071i$	0.083
06/S	267.02	0.60	0.46	0.55	6	17.53	$0.152 \pm 0.110i$	0.691
07/S	267.36	0.61	0.44	0.50	5	13.33	$0.108 \pm 0.025i$	0.401
08/B	267.37	0.42	0.41	0.49	5	12.25	0.090	0.223
09/S	267.68	0.46	0.41	0.45	5	10.11	$0.023 \pm 0.191i$	0.091
10/E	268.35	0.52	0.47	0.61	6	15.89	$0.192 \pm 0.074i$	0.596
11/E	268.65	0.61	0.50	0.50	5	10.95	$0.075 \pm 0.078i$	0.249
12/B	269.212	0.49	0.47	0.48	6	16.86	0.162	0.424
13/E	270.71	0.59	0.51	0.51	8	16.94	$0.110 \pm 0.127i$	0.407
14/B	272.37	0.39	0.40	0.40	4	15.22	$0.101 \pm 0.179i$	0.298
15/E	273.33	0.49	0.46	0.47	6	19.51	$0.179 \pm 0.086i$	0.553
16/E	274.00	0.72	0.54	0.56	9	20.35	0.245	0.762
17/S	278.07	0.55	0.44	0.50	6	17.41	$0.151 + 0.098i$	0.390
18/E	278.61	0.71	0.43	0.51	6	17.59	$0.104 \pm 0.033i$	0.448
19/E	278.83	0.55	0.44	0.46	5	14.58	$0.102 \pm 0.219i$	0.372

the interval analyzed occurs 7 time units (about 15 seconds) before the minimum in state space speed is observed. Note that the L2 norm was employed as the metric in the definitions of s and D_0 to measure differences in flow fields; whether it is the optimal metric to capture the most dynamically relevant information has not been tested. For example, in Fig. 5.5(b) the initial condition and the converged solution differ by $D_0^{ic} = 0.61$, which is significantly larger than $D_0^{ic} = 0.20$ for the pair shown in Fig. 5.5(a). However, the equilibria in both cases are strikingly similar to the initial conditions, visually. This suggests, one may need alternative techniques [139] to quantify flow features in a more efficient way. Finally, for the solution indicated in red diamond in Fig. 5.4, $D_0^{ic} = 0.60$ and $D_{0,min} = 0.60$, with the closest approach occurring 3 time units (7 seconds) after the minimum in state space speed was observed. This suggests that, while state space speed s serves as a valuable dynamical variable in identifying intervals when a turbulent trajectory is sufficiently close to an equilibrium, the instants of closest approach and slowest evolution do not coincide, in general.

Among the solutions that converged, the difference D_0^{ic} between initial condition and the converged solution varied between 0.13 and 0.79; convergence to the farthest solution is shown in Fig. 5.8. A summary of the properties of the solutions computed, indexed in ascending order[10] of $\|\mathbf{u}_0\|$, is provided in Table 5.1. For solutions where more than one initial condition converged, the closest initial condition to the solution is cataloged. Included in the table is the information whether a solution was computed using initial conditions from simulations (S), experiment (E), or both (B). Also included are the stability properties of the solutions, which will be discussed in the next section.

[10]The norm of the solutions turned out to be a very effective measure to cluster solutions and hence is used to sort them.

5.4 Geometry of State Space in the Vicinity of Unstable Equilibria

The dynamical role of ECS goes beyond the fact that turbulent flow fields look similar to nearby ECS and mimic their temporal behavior when in their vicinity. ECS shape their state space neighborhoods into a saddle; nearby turbulent trajectories approach the solutions along their stable manifolds, and subsequently depart following the unstable manifolds. While the full state space is very high dimensional (2×10^5 in the NPS), dissipation results in the asymptotic dynamics contracting on to a manifold of much lower dimensionality, often only a few tens in number [13, 25, 29]. Consequently, ECS that are frequently visited are conjectured to have only a few dynamically relevant stable and unstable directions, which can be used to construct low dimensional models to describe evolution of turbulent trajectories in their neighborhoods.

As can be seen from Table 5.1, the number of unstable eigendirections[11] N_{us} ranges from as low as 2 to as high as 9. While the number of stable directions is technically infinite ($\approx 2 \times 10^5$ in the NPS), the dynamically important ones are those which are not strongly contracting. Their number can be estimated by computing the local Kaplan-Yorke dimension (N_{KY}) of the chaotic attractor,

$$N_{KY} = k_0 + \frac{1}{\Re\{\lambda_{k_0+1}\}} \sum_{k=1}^{k_0} \Re\{\lambda_k\}. \tag{5.5}$$

Here, k_0 is the largest integer for which $\sum_{k=1}^{k_0} \Re\{\lambda_k\} \geq 0$ and $\Re$ indicates the real part of an eigenvalue. N_{KY}, in this case, provides an estimate of the dimensionality of a non-contracting state space volume in the vicinity of the ECS, spanned by all the unstable and the weakly-contracting (stable) eigendirections. For the solutions computed N_{KY} varies between 4.5 and 20.35 (cf. Table 5.1), resulting in dynamically important stable

[11] Unstable eigendirections have positive real parts for their eigenvalues, while the stable ones have negative real parts.

directions (N_{KY}-N_{us}) comparable in numbers to N_{us}, i.e, $O(10)$. Despite being low-dimensional, computing even the weakly contracting components of stable manifolds is quite complicated and subtle[12]. In contrast, low dimensional unstable manifolds are tractable under some not-so-uncommon scenarios, where they can be computed using simple numerical integration. The construction of such manifolds, their role in shaping the state space, and in guiding turbulent evolution will be discussed in the rest of this section.

5.4.1 Computing Unstable Manifolds: A Demonstration

From Table 5.1 is can be seen that the solution indexed "01/B" has just two unstable directions, both with real eigenvalues. The vorticity contour plots of the unstable eigenvectors $\hat{\mathbf{e}}_1$ and $\hat{\mathbf{e}}_2$ are shown in Fig. 5.9. This solution, shown in Fig. 5.5(a), was discussed in the context of both state space speed $s(t)$ (cf. Fig. 5.4) and the distance between solution and turbulent trajectory $D_0(t)$ (cf. Fig. 5.7). Having a low dimensional unstable manifold, besides being approached closely in the simulation $D_0 = 0.13$, it should serve as an ideal candidate to study the geometry of state space in its vicinity.

The 2D unstable manifold of this solution can be constructed by generating a circle of initial conditions around the solution, lying in the plane spanned by the eigenvectors $\hat{\mathbf{e}}_1$ and $\hat{\mathbf{e}}_2$, i.e., $\mathbf{u}_\theta^{ic} = \mathbf{u}_0 + \epsilon_1 \cos(\theta)\, \hat{\mathbf{e}}_1 + \epsilon_2 \sin(\theta)\, \hat{\mathbf{e}}_2$. Here, θ parametrizes the set of initial conditions. Since the unstable eigenvalues $\Re\{\lambda_1^+\} = 0.0273$ and

[12]To begin, eigenvectors are solutions of form $e^{\lambda t}\,\hat{\mathbf{e}}$ to the linearized governing equation. The contracting directions are ones with $\Re\{\lambda\} < 0$ while the expanding ones are those with $\Re\{\lambda\} > 0$. The transformations $t \to -t$, $\mathbf{u} \to -\mathbf{u}$, and $\lambda \to -\lambda$ leave the eigenvector equation unchanged, which implies that the stability of an eigenvector reverses with time-reversal. The eigendirections span a small neighborhood around the ECS where the linearized equation accurately describes the forward as well as backward temporal evolution of an initial condition. The nonlinear extension of an unstable manifold can be computed by evolving the nonlinear governing equation forward in time using initial conditions that lie within the linear neighborhood of the unstable manifold. However, since the nonlinear governing equation is not invariant under time-reversal (due to dissipation), numerical integration of trajectories backwards in time leads to components along most contracting (unimportant) directions under forward evolution amplifying exponentially under backward evolution. Consequently, tracking the dynamically relevant stable manifold components is challenging.

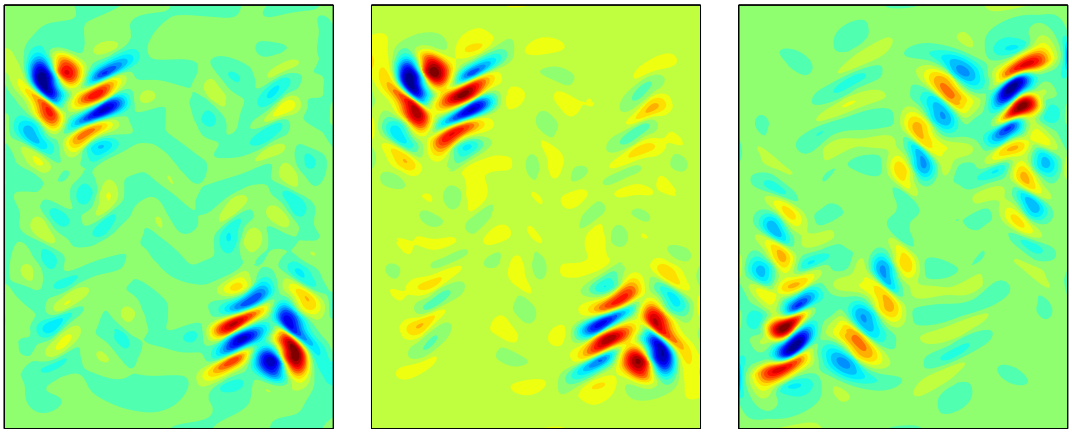

(a) (b) (c)

Figure 5.9: Eigenvectors of the solution indexed "01/B" (cf. table 5.1) which was approached the closest by a turbulent trajectory in the simulation. Panels (a) and (b) show the eigenvectors $\hat{\mathbf{e}}_1$ and $\hat{\mathbf{e}}_2$, respectively. The corresponding eigenvalues are $\lambda_1^+ = 0.0273$ and $\lambda_2^+ = 0.0245$. Panel (c) shows a stable eigenvector $\hat{\mathbf{e}}_3$ used to construct state space visualization.

$\Re\{\lambda_2^+\} = 0.0245$ are comparable in magnitude, one can set $\epsilon_1 = \epsilon_2 = \epsilon$ and numerically evolve them using the 2D model. The trajectories $\mathbf{u}_\theta(x, y, t)$, which are uniquely parametrized by θ, then generate a surface which corresponds to the 2D unstable manifold of the solution.

Fig. 5.10(a) shows a state space visualization of the unstable manifold (blue surface) around the equilibrium (red sphere) placed at the origin. The manifold was generated using 1440 initial conditions, each 1/4 degrees apart, lying on a circle with radius $\epsilon = 10^{-4} \times \|\mathbf{u}_0\|$. Sample manifold trajectories $\mathbf{u}_\theta(t')$ are depicted using red curves originating at the equilibrium. Starting from a smaller ϵ would necessitate integrating for a longer duration t' to generate the same manifold trajectory, making time t' arbitrary on the manifold. The visualization was constructed by projecting the manifold trajectories relative to the solution, $\mathbf{u}_\theta(t') - \mathbf{u}_0$, onto an orthonormal basis constructed using eigenvectors $\hat{\mathbf{e}}_1$, $\hat{\mathbf{e}}_2$, and $\hat{\mathbf{e}}_3$, where $\hat{\mathbf{e}}_3$ is a stable eigenvector[13]

[13]This eigenvector is not the least contracting one. It is a weakly-contracting eigendirection along which the turbulent trajectory has large components during approach as well as departure, which makes it an ideal candidate for constructing state space visualization.

shown in Fig. 5.9(c). One may notice that the manifold is planar only near the equilibrium; the nonlinearity of the governing equations results in significant curvature moving away from the solution.

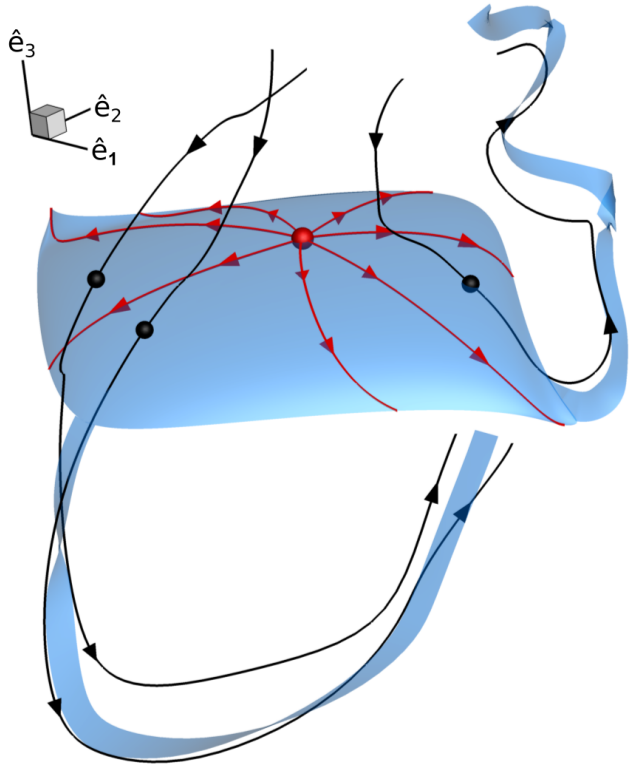

Figure 5.10: Turbulent trajectories (black curves) following the two-dimensional unstable manifold (blue surface) around an equilibrium (red sphere). The 2D manifold was constructed by integrating a circle of initial conditions around the solution, lying in the plane spanned by the unstable eigenvectors $\hat{\mathbf{e}}_1$ and $\hat{\mathbf{e}}_2$. The red curves with arrows indicate sample trajectories originating near the equilibrium that constitute the manifold. The black spheres on the trajectories indicate the instants at which the minimum in state space speed was observed.

Also plotted in Fig. 5.10 are projections of turbulent trajectories in the numerical simulation (black curves) $\mathbf{u}(t) - \mathbf{u}_0$, corresponding to three different intervals during which they were found to be close to the equilibrium. The instant at which the state space speed minimum was observed is marked using a black sphere on each trajectory. The (U-shaped) trajectory on the right includes the slowest evolving instant as well as closest pass to the solution observed across the entire (experiment and simulation) time series (cf. Fig. 5.4, Fig. 5.7). The turbulent trajectories are attracted towards

the unstable manifold, and subsequently follow specific "routes" (blue strips) into regions where the manifold becomes strongly nonlinear. Lastly, while the solution was converged from experimental initial condition, the closest pass was not close enough to unambiguously demonstrate that it tracks the manifold, and hence is not being analyzed here.

This state space picture provides some insight into why the instant of closest approach and state space speed need not coincide. The state space speed depends on the specific contracting as well as repelling directions a turbulent trajectory closely follows. Approach along a strongly contracting direction would result in a large state space speed which would eventually decrease to a minimum when the component along such contracting direction is minimum. During this contraction along a stable direction, however, the trajectory moves away from the solution along the unstable directions which results in an increase in $s(t)$. Since the combined rates of approach and departure determine the state space speed, a simple relation between $s(t)$ and distance from solution may not be feasible even for very simple cases like the 2D manifold shown here.

The specific route on the manifold that each turbulent trajectory follows the closest on average can be identified either by inspecting the projection figure, or more systematically using the measures

$$\langle D_1(\theta,t)\rangle_t = \frac{1}{T}\int_{t=0}^{T} D_1(\theta,t)dt \quad \text{where} \quad D_1(\theta,t) = \min_{\forall t'} \frac{\|\mathbf{u}(t)-\mathbf{u}_\theta(t')\|}{\|\mathbf{u}_\theta(t')\|}, \tag{5.6}$$

where $D_1(\theta,t)$ and $\langle D_1(\theta,t)\rangle_t$ yield the instantaneous and the average separations between the turbulent trajectory and a specific manifold route $\mathbf{u}_\theta(t')$, specified by θ. $T = 8\tau_c$ ($\approx$ 200s) was chosen as the time interval over which the average separation is computed, starting at the instant of slowest evolution $t = 0$. Fig. 5.11(a) shows the plot of $\langle D_1(\theta,t)\rangle_t$ versus θ for the three turbulent trajectories plotted in

Fig. 5.10; the closest pass is plotted in black, and the other two in gray. θ_c corresponding to minimum $\langle D_1(\theta_c,t)\rangle_t = \min_{\forall\theta}\langle D_1(\theta,t)\rangle_t$ yields the specific manifold trajectory each turbulent trajectory follows the closest, as well as the mean separation between them over the duration $T = 8\tau_c$. For the case of the most dramatic slowing down, $\langle D_1(\theta_c,t)\rangle_t = 0.13$, while for the other two $\langle D_1(\theta_c,t)\rangle_t = 0.19$ and 0.25, respectively.

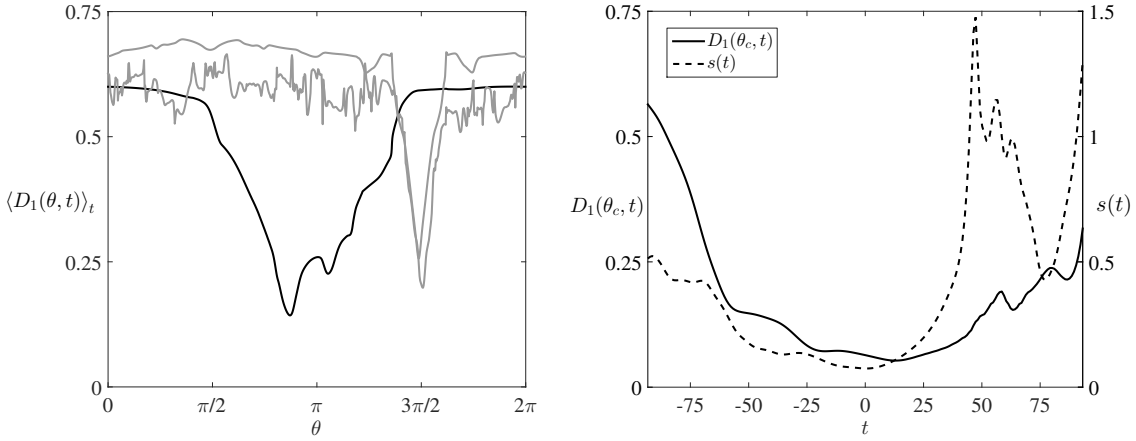

Figure 5.11: Separation between the turbulent trajectory and the 2D manifold of an equilibrium. Panel (a) shows the mean separation $\langle D_1(\theta_c,t)\rangle_t$ between the turbulent trajectory and $\mathbf{u}(t)$ and the manifold trajectories, which are parametrized using $\theta \in [0, 2\pi]$. The trajectory corresponding to the least average separation θ_c is identified using the minimum in $\langle D_1(\theta_c,t)\rangle_t$. Panel (b) shows the instantaneous separation between the turbulent trajectory and the manifold route θ_c it follows the closest on an average. Time t in plot (b) is given in non-dimensional units.

The instantaneous separation between a turbulent trajectory and the manifold route θ_c it follows, given by $D_1(\theta_c,t)$, is plotted in Fig. 5.11(b). As before, $t = 0$ is (locally) reset to be the instant at which the minimum in $s(t)$ is observed (black sphere in Fig. 5.10). The turbulent trajectory follows its manifold counterpart θ_c with a near constant separation ≈ 0.06 for about 4 correlation times (50 nondimensional time units), deviating gradually over the next $4\tau_c$. For the two other trajectories identified to be in the neighborhood of the solution, the instantaneous separation is nearly constant at 0.06 for $4\tau_c$ as well. However, they were found to deviate very rapidly,

resulting in larger mean separations[14] $\langle D_1(\theta_c,t)\rangle_t = 0.19$ and $\langle D_1(\theta_c,t)\rangle_t = 0.25$ computed over the interval $8\tau_c$.

Fig. 5.12 shows sample turbulent flow fields which are 3.4 correlation times apart, the corresponding closest points on the manifold trajectory $\mathbf{u}_{\theta_c}(t')$, and the difference between them. These flow fields correspond to instants t = 0, 45,90 on the turbulent trajectory, at which the separation from manifold trajectory $\mathbf{u}_{\theta_c}(t')$ were measured to be $D_1(\theta_c,t) = 0.06, 0.13, 0.21$, respectively. The snapshots on the manifold which are closest to the turbulent flow fields, however, are not separated by $3.4\tau_c$. It was found that the evolution along $\mathbf{u}_{\theta_c}(t')$ *on* the manifold is slower compared to the turbulent trajectory, such that t' and t are related (approximately) as $\Delta t' = 1.2\Delta t$. This disagreement is expected, since, while the turbulent trajectory follows the path shaped by the manifold in the state space, it need not evolve at the same rate as the nearest manifold trajectory.

While the dynamics near the equilibrium are slow, they become quite complicated as the turbulent trajectory moves away, while still being guided by the manifold. For instance, at $t \approx 43$ the state space speed is fairly large $s \approx 1.5$ (recall $\langle s\rangle_t = 1$), while it is still very close to the manifold, with $D_1(\theta_c, t = 43) \approx 0.1$. Hence, while the ECS have simple temporal dynamics, the low-dimensional unstable manifolds around them can capture dynamics that are fairly complicated. When the turbulent trajectory is found close to the solution, one can identify a manifold route it follows and forecast its evolution, which can be further improved by iteratively refining its position relative to the manifold.

Lastly, the solution and its 2D unstable manifold discussed above were found to be approached closely by the turbulent trajectory only in the numerics, but not in the experiment ($D^{exp}_{0,min} = 0.54$). This can possibly be due to the significantly shorter

[14] In some sense, time near an equilibrium is not the appropriate measure of tracking the manifold. The state space picture should be equivalently described in terms of lengths of curves. Such a task has not been pursued in this thesis, but seems rather correct path to pursue in future.

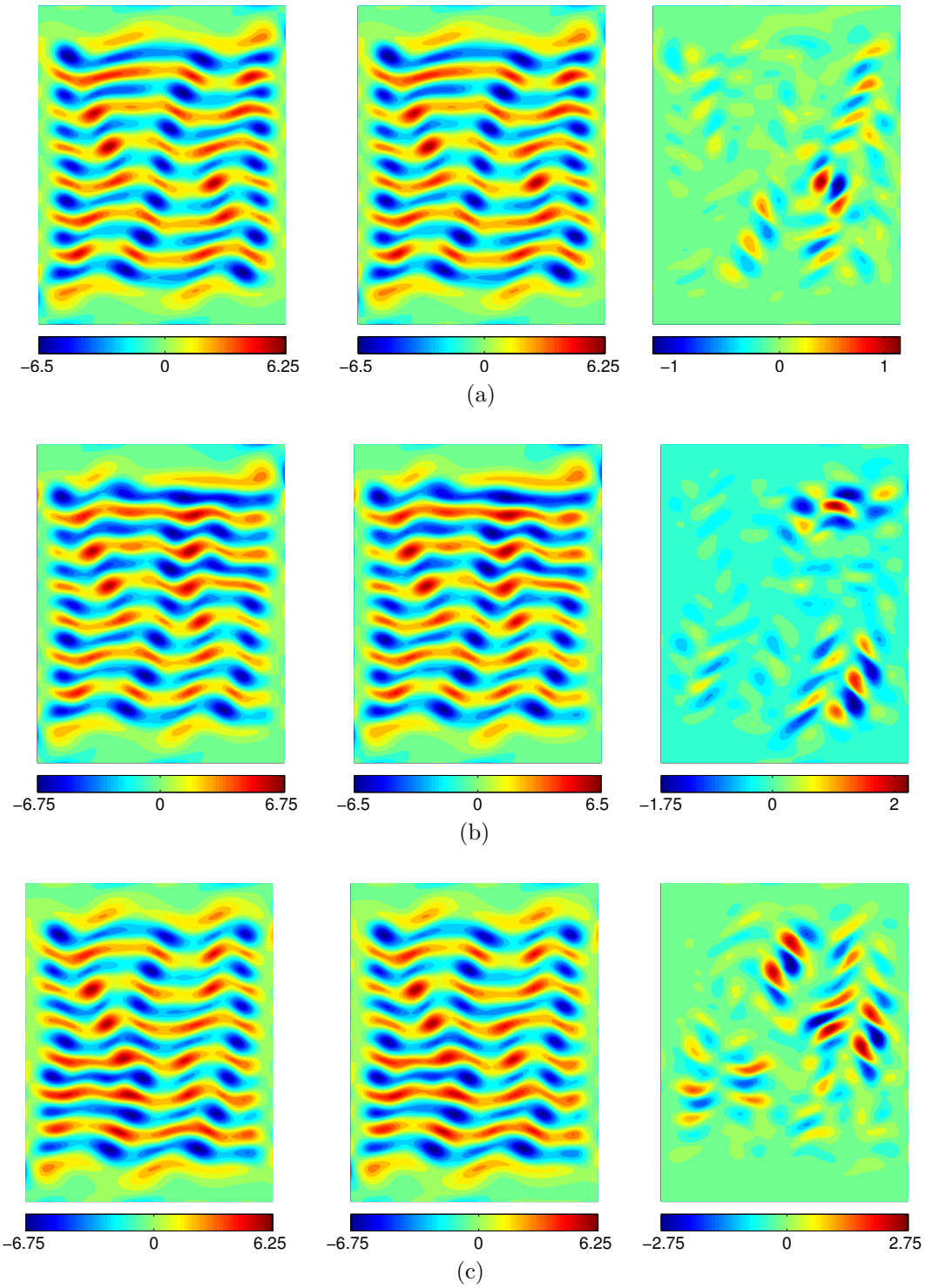

Figure 5.12: Contour plots of vorticity of turbulent flow fields and the manifold fields on the 2D surface closest to them. The flow fields are separated in time by $3.4\tau_c$, with the first set of figures corresponding to the instant of slowest evolution.

lengths of the time series available in the experiment. Alternatively, it may indeed be the case that the solution, being invariant under rotation $\mathcal{R}_y\mathcal{R}_x$ (cf. Fig. 5.5(a)), is never approached very closely by the turbulent trajectory in experiment, where the symmetry is only approximate due to inhomogeneity in the strength of the magnets.

5.4.2 Forecasting Fluid Flows Using the Geometry of Turbulence

The solution discussed in the previous section provided an excellent platform to explore the geometry of state space as shaped by an ECS and its unstable manifold. However, strictly 2D and 3D unstable manifolds are rare, as can be seen from Table 5.1. Constructing manifolds of dimensionality four or higher by evolving multiple initial conditions around the solution, while being embarrassingly parallel, is data intensive. However, significant simplification can be achieved in some cases, when the unstable eigenspectrum shows clear separation between the real parts of the eigenvalues. Consider for example the solution indexed "03/B", which was computed from both experimental and numerical initial conditions. The initial condition in the experiment resulting in convergence and the solution are shown in Fig. 5.13(a) and (b), respectively. For this solution, while the unstable manifold is seven dimensional, the real part of the leading eigenvalue ($\lambda_1^+ = 0.1492$) is more than ten times larger than the real parts of each of the remaining six eigenvalues, $0.0147 \pm 0.1680i$, $0.0045 \pm 0.1104i$, and $0.0009 \pm 0.4500i$. The eigenvectors associated with the unstable eigenvalues are shown in panels (c)-(i) in Fig. 5.13.

The clear separation in the real parts of the eigenvalues suggests that turbulent trajectories in the neighborhood of the equilibrium depart following either of the two trajectories, each originating near the equilibrium and evolving (initially) in opposite directions following $\pm\hat{\mathbf{e}}_1$, the leading unstable eigenvector. These two trajectories, indicated using the red curves in Fig. 5.14(a), constitute the 1D unstable submanifold of the equilibrium. The state space visualization in Fig. 5.14 was constructed by

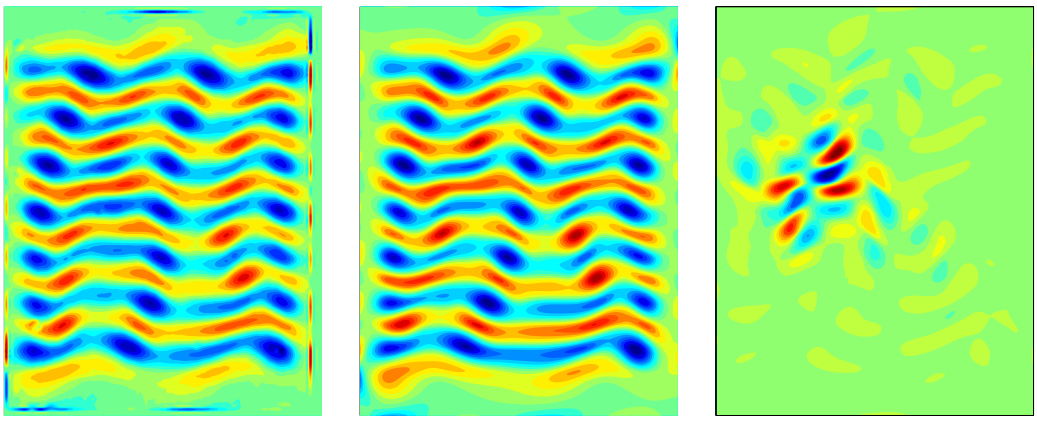

(a) (b) (c)

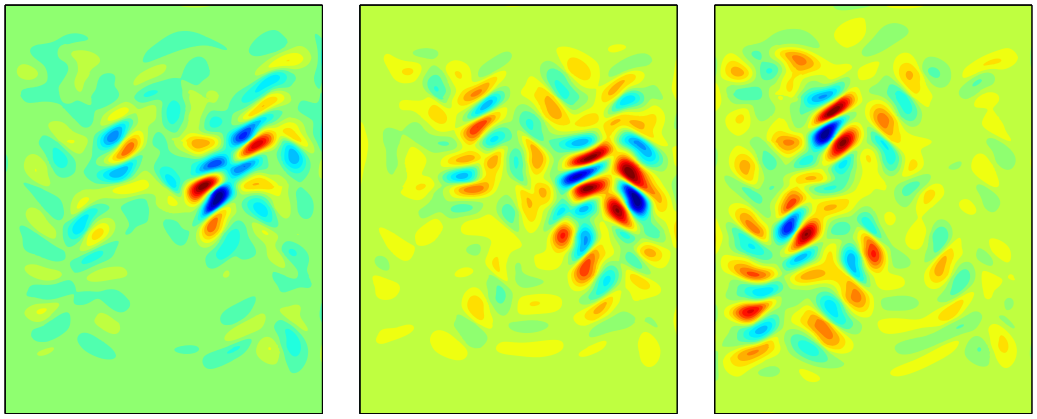

(d) (e) (f)

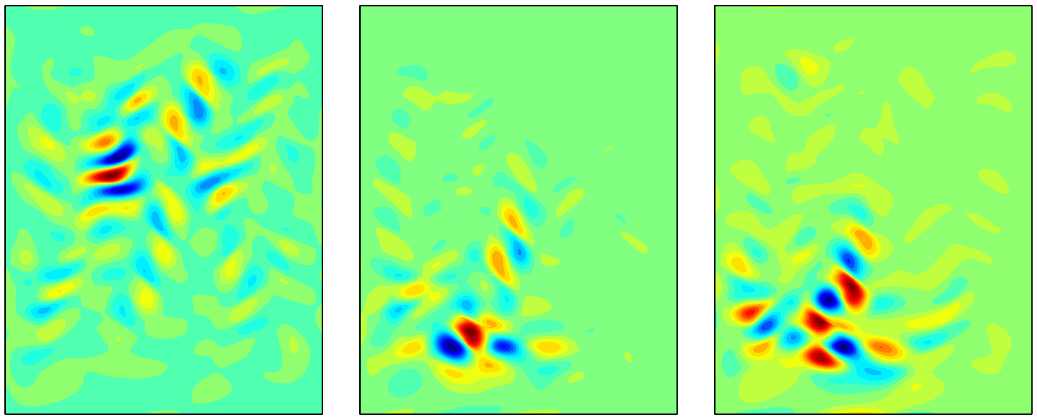

(g) (h) (i)

Figure 5.13: Solution indexed "03/B" computed from an initial condition in experiment (as well as simulation) and its unstable eigenvectors. Panels (a) and (b), respectively, show the initial condition from the experiment and the equilibrium solution computed. Panels (c)-(i) show the unstable eigenvectors, in descending order of the real parts of the eigenvalues. The 3D state space visualization is constructed using eigenvectors shown in (c),(h), and (i).

projecting the manifold and turbulent trajectories onto an orthogonal basis spanned by the leading eigenvector $\hat{\mathbf{e}}_1$ shown in Fig. 5.13(a), and those in panes (h) and (i). Like in the case of the 2D unstable manifold discussed in the previous section, the submanifold trajectories are generated by integrating $\mathbf{u}_0 \pm \epsilon\,\hat{\mathbf{e}}_1$, where $\epsilon > 0$ is the initial perturbation to the equilibrium along $\pm\,\hat{\mathbf{e}}_1$. The choice of the specific complex conjugate pair used to construct the projection is motivated by the shape of the submanifold in the full state space. As Fig. 5.14(a) illustrates, while the submanifold trajectories are linear in the vicinity of the solution, they exhibit significant curvature away from it due to the nonlinearity of the evolution equations. As a result, initial disturbances that initially have no components in the direction of either of the three

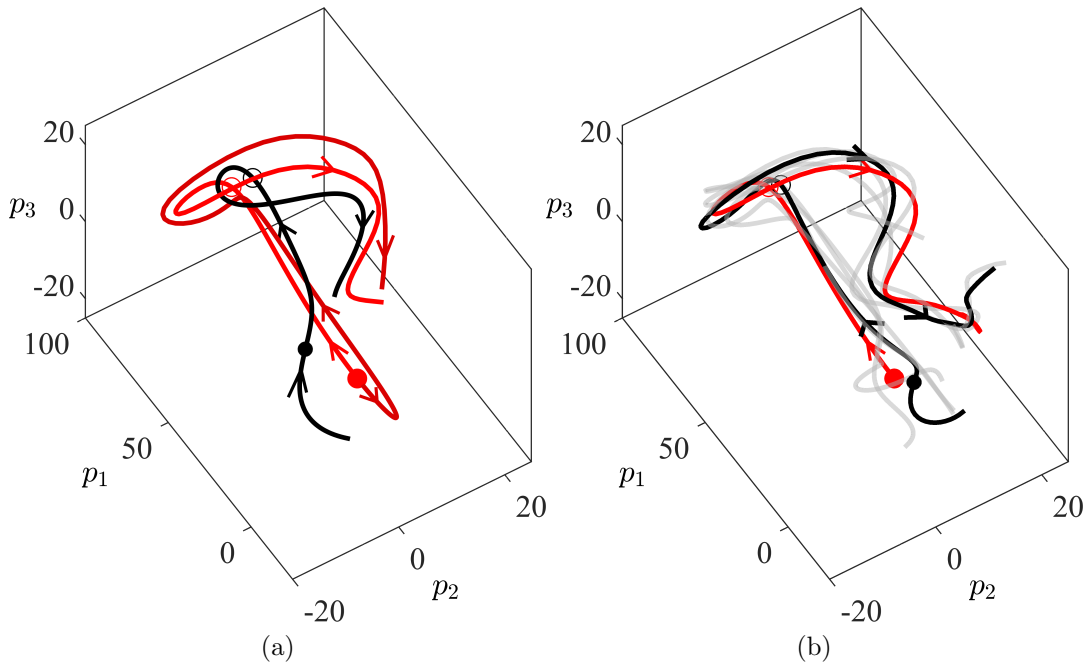

Figure 5.14: Turbulent trajectories (black curves) from the experiment (a) and simulation (b) following the 1D submanifold (red curves) of an equilibrium (red sphere). In panel (a) the two red curves correspond to submanifold trajectories originating at the equilibrium, evolving initially in opposite directions along $\pm\,\hat{\mathbf{e}}_1$. Away from the equilibrium, they follow each other, suggesting the submanifold associated with $+\,\hat{\mathbf{e}}_1$ should be sufficient to forecast the evolution of turbulence. The black spheres indicate the instants the initial condition was used to compute the solution. The gray curves in panel (b) correspond to several different occasions the turbulent trajectory was found following the 1D submanifold.

complex conjugate pairs, will eventually acquire nonvanishing components along each of these six directions. The components along the third complex conjugate pair happen to be the largest by far, which makes a case for choosing them to construct the state space visualization.

While the two submanifold trajectories evolve in opposite directions initially, the one directed along $-\hat{\mathbf{e}}_1$ eventually turns around and approximately aligns with the one along $+\hat{\mathbf{e}}_1$. This suggests, the submanifold along $+\hat{\mathbf{e}}_1$ shapes the state space and should prove sufficient to forecast the evolution of nearby turbulent trajectories. This hypothesis is validated in both the experiment and the simulations. Fig. 5.14(a) shows the state space projection of the turbulent trajectory in the experiment (black curve) approaching the equilibrium, and departing following the unstable 1D submanifold into the region well beyond the linear neighborhood. The black sphere indicates the instant where the minimum in the state space speed was observed. In the numerical simulation as well, the turbulent trajectory was found to depart the neighborhood of the solution following the 1D submanifold during several different close passes, as depicted using black and gray curves in Fig. 5.14(b).

The evolution of the turbulent trajectories in the physical space bears striking resemblance to that along the submanifold, as shown in Fig. 5.15. The first row of images is a comparison of flow fields at the end of the linear segment along the 1D submanifold, indicated by circles in Fig. 5.14(a),(b). The images in the second and third rows (b-c) compare evolution along the submanifold with that along turbulent trajectories, one and two correlation times from the start of the nonlinear extension of the submanifold. The choice of sampling using the manifold time is different from the 2D manifold example, where flow fields along the turbulent trajectories were sampled. This is necessary since the rates of evolution in the experiment and the simulation were slightly different from each other, and the submanifold serves as a common reference. The agreement between the nonlinear extension of the manifold and experiment stays

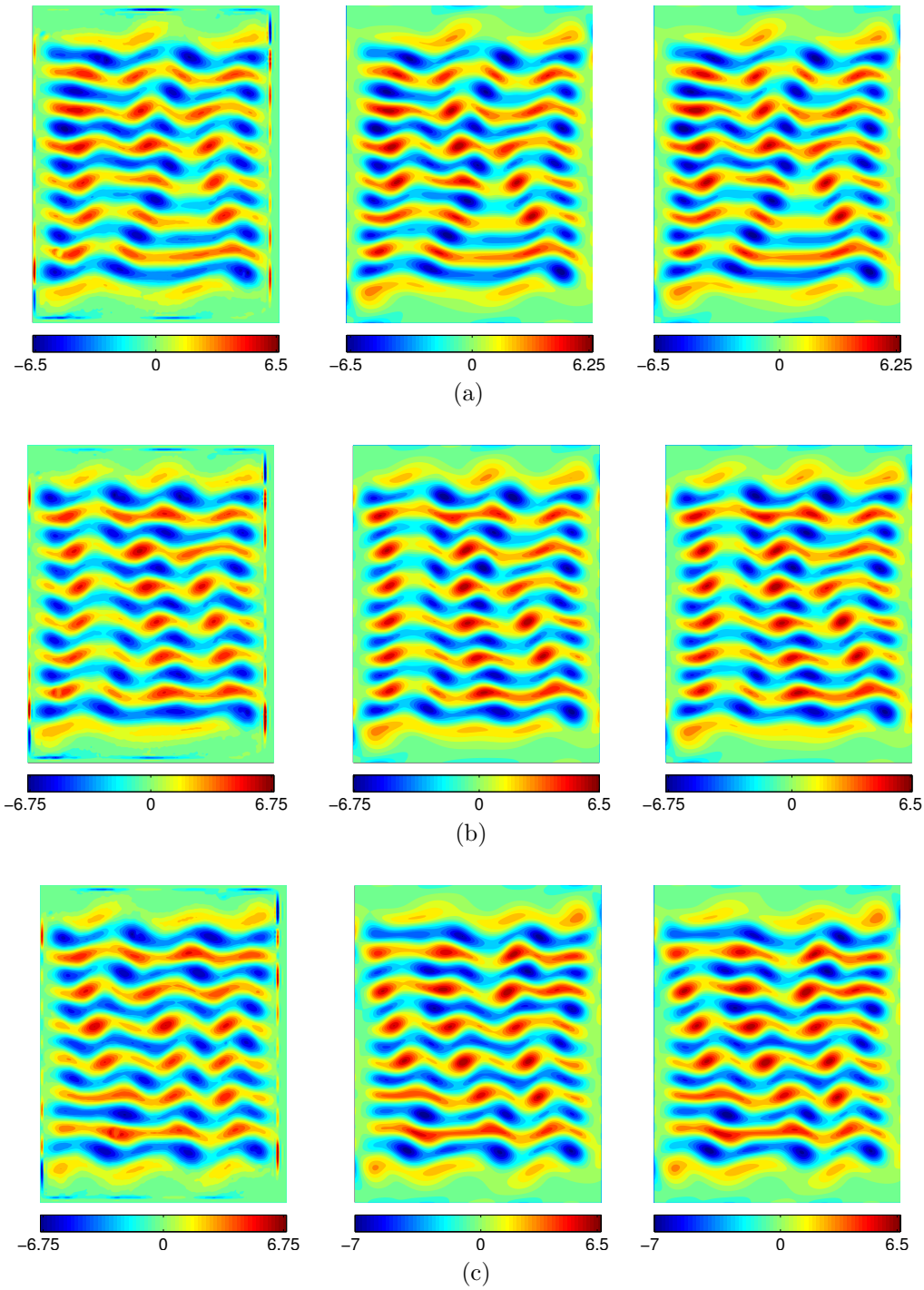

Figure 5.15: Contour plots of vorticity of turbulent flow fields and the manifold fields closest to them. The left panels show flow fields from the experiment, the center panels show the flow fields along the submanifold, while the panels on the right show flow fields from the NPS. The flow fields under row (a) correspond to the instant which marks the end of linear neighborhood. Rows (b) and (c) correspond to instants τ_c along the submanifold thereafter, and the nearest flow fields on the turbulent trajectories.

very good for at least one correlation time, with only qualitative similarity remaining at the end of the second. In contrast, the simulation follows the nonlinear extension of the submanifold submanifold for 3 correlation times. Lastly, while the comparison provided here is using the submanifold trajectory evolving (initially) along $\hat{\mathbf{e}}_1$, it was found that the agreement with the submanifold trajectory directed along $-\hat{\mathbf{e}}_1$ trajectory is comparable in both simulation and experiment for one correlation time into the nonlinear extension of the manifold.

5.4.3 Testing The Linear Approximation

For both the 2D manifold and the 1D submanifold cases discussed above, it was found that the turbulent trajectories evolve at slightly different rates compared to their manifold counterparts. This brings into question the applicability of a simple linear approximation in describing the temporal evolution of turbulent trajectories in the neighborhood of a solution. A manifold trajectory evolving entirely within the unstable manifold can be approximated in the linear neighborhood as $\mathbf{u}(t) = \mathbf{u}_0 + \sum_{k=1}^{N_{us}} p_k(t)\,\hat{\mathbf{e}}_k$, where $p_k(t) \sim e^{\lambda_k t}$ is the component along eigendirection $\hat{\mathbf{e}}_k$ at each instant t. If a turbulent trajectory enters the linear neighborhood of the solution, the components p_k along the eigendirections should grow exponentially as well, i.e., $\ln(p_k)$ should vary linearly in time t.

The validity of the linear approximation in describing evolution following the 2D unstable manifold can be tested by plotting the growth of projections $p_1 = \langle\, \hat{\mathbf{e}}_1 | \mathbf{u} - \mathbf{u}_0 \rangle$ and $p_2 = \langle\, \hat{\mathbf{e}}_2 | \mathbf{u} - \mathbf{u}_0 \rangle$ for the turbulent trajectory $\mathbf{u}(t)$ as well as its manifold counterpart $\mathbf{u}_{\theta_c}(t')$ (cf. section (5.4.1)). Fig. 5.16(a) shows the plots of $\ln(p_1)|_{sim}$, $\ln(p_2)|_{sim}$ (in black) for the turbulent trajectory in the numerical simulation and $\ln(p_1)|_{\theta_c}$, $\ln(p_2)|_{\theta_c}$ (in red) for the manifold trajectory θ_c. The zero of time t' is set to

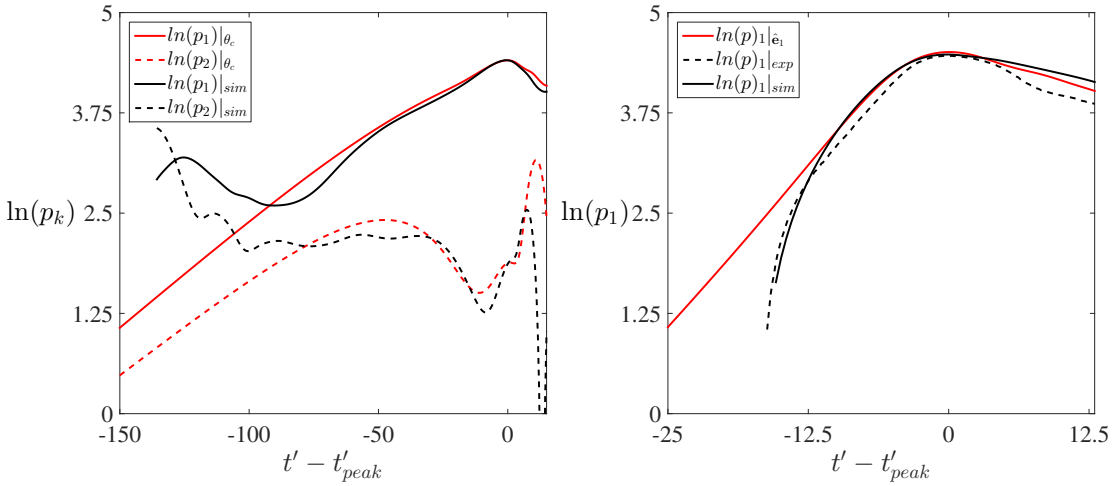

Figure 5.16: Testing linear approximation in describing dynamics in the vicinity of equilibrium solutions. Panel (a) shows the growth of components p_1 and p_2 along eigenvectors $\hat{\mathbf{e}}_1$ and $\hat{\mathbf{e}}_2$ for the solution with a 2D unstable manifold. Panel (b) shows the projections along the leading eigendirection for the 1D submanifold example. The red curves represent the components on the (sub)manifold, while the black curves indicate components of the turbulent trajectory.

match instant t'_{peak} when $p_1|_{\theta_c}$ is maximum[15]. The zero of time t along the turbulent trajectory is set by identifying the instant on it which is closest to the manifold flow field $\mathbf{u}_{\theta_c}(t'_{peak})$.

From the plots $\ln(p_1)|_{\theta_c}$, $\ln(p_2)|_{\theta_c}$, it can be concluded that the linear approximation of the manifold corresponds to the region $t' - t'_{peak} \leq -75$, where both $\ln(p_1)|_{\theta_c}$ and $\ln(p_2)|_{\theta_c}$ vary linearly in time. A linear fit in this region yields growth rates 0.0272 and 0.0247, which are in excellent agreement with the eigenvalues $\lambda_1 = 0.0273$ and $\lambda_2 = 0.0245$, respectively. However, beyond $t' - t'_{peak} \geq -75$, while the evolution along the $\hat{\mathbf{e}}_1$ can be considered approximately linear, one finds significant nonlinearity in the growth of components along $\hat{\mathbf{e}}_2$, showcasing the asymmetric geometry of state

[15]As per this convention $t' \to -\infty$ corresponds to the initial condition $\mathbf{u}_{ic}$ along θ_c near the equilibrium when $\epsilon_1, \epsilon_2 \to 0$ (cf. section (5.4.1)). While in panel (a) one can choose time on the turbulent trajectory as a reference, it is not feasible for panel (b), since the experiment and simulation are being plotted simultaneously, rendering the manifold as the only common reference. Lastly, choosing a different reference point may shift the curves within a plot relative to each other along t' axes, but will not change whether the growth is linear or not.

space. It is this nonlinear section of the 2D manifold that is tracked by the turbulent trajectory, as opposed to the strictly linear section $t' - t'_{peak} \leq -75$.

For the 1D submanifold as well linearization does not seem to provide an accurate description of temporal evolution, as can be seen from Fig. 5.16(b). As expected, $\ln(p_1)|_{\hat{\mathbf{e}}_1}$ for the submanifold trajectory along $\hat{\mathbf{e}}_1$ was found to grow linearly in time, at a rate 0.15 ± 0.001 which in close agreement with the leading eigenvalue $\lambda_1 = 0.149$. However, the turbulent trajectory in the simulation, despite approaching the solution and its submanifold very closely, does not show a clear linear growth of $\ln(p_1)|_{sim}$ with t. Nevertheless, in the region $-12.5 \leq t' - t'_{peak} \leq 0$, a linear fit of $\ln(p_1)_{sim}$ versus t yields a growth rate 0.175 ± 0.2 which is markedly different from that along the submanifold. In the experiment, despite a larger separation with the submanifold compared to the simulation trajectory, $\ln(p_1)$ was found to grow linearly at a rate 0.161 ± 0.001.

These results suggest that turbulent trajectories may not enter the strictly linear unstable neighborhood of an equilibrium. This implies that a simple linear model using the eigenvectors of the equilibrium as basis functions will prove inaccurate in forecasting the evolution of such trajectories. Consequently, construction of unstable manifolds – even if coarsely sampled – and their nonlinear extensions may be required to develop accurate forecasting models. While unstable manifolds are attracting close to equilibria they become repelling far away from them. This necessitates linearization about manifolds to capture the progressive deviation of turbulent trajectories from unstable manifolds (cf. Fig. 5.11(b)). Such linearization facilitates exploring the geometry of state space in the neighborhoods of manifolds and may help quantitatively understanding the differences in the rates of evolution of turbulent trajectories compared to the nearest manifold trajectories.

5.5 Heteroclinic Connections Between Unstable Equilibria

The discussion so far focused on understanding the dynamics of turbulent trajectories in the neighborhoods of equilibrium solutions, and using unstable manifolds to forecast their evolution for a few correlation times. Long term forecasting can be attempted if it turns out that there exist "special" pathways a turbulent trajectory follows which guide it from the neighborhood of one solution to that of another. In more formal terms, there can be dynamical connections between solutions – trajectories that originate on the unstable manifold of a solution and evolve in time, only to merge into the stable manifold of another or the same solution. The former are called heteroclinic connections [140–142], while the latter are homoclinic connections. The asymptotic dynamics on such connections are not chaotic, but they may play a crucial role in shaping the state space and guiding turbulent trajectories over longer durations. Computing heteroclinic and homoclinic connections requires sophisticated numerical techniques [55, 143, 144]. However, signatures of such connections which originate at ECS with very few unstable eigendirections can be identified using simple numerical integration, which will be demonstrated below using the 2D manifold.

With the motivation to search for dynamical connections, the state space speeds for all 1440 trajectories that were evolved to approximate the 2D manifold were computed. Recall that each trajectory originates from an initial condition lying on the circle of radius ϵ around the equilibrium, i.e., $\mathbf{u}_{ic}^{\theta} = \epsilon \cos\theta\, \hat{\mathbf{e}}_1 + \epsilon \sin\theta\, \hat{\mathbf{e}}_2$ (cf. section (5.4.1)). Fig. 5.17 shows the plot of $s(t)$ for two different trajectories on the 2D manifold at different angles θ. The behavior seen in Fig. 5.17(a) is representative of the vast majority of trajectories; in the neighborhood of the solution they evolve slowly ($s \approx 0$) but eventually become turbulent ($s \approx 1$). However, for the case of the initial perturbation along $+\hat{\mathbf{e}}_2$, the state space speed showed a deep minimum after displaying complicated dynamics, as can be seen in Fig. 5.17(b). This suggests there may be a dynamical connection between two equilibrium solutions, the "source"

being the solution "01/B" shown in Fig. 5.5(a).

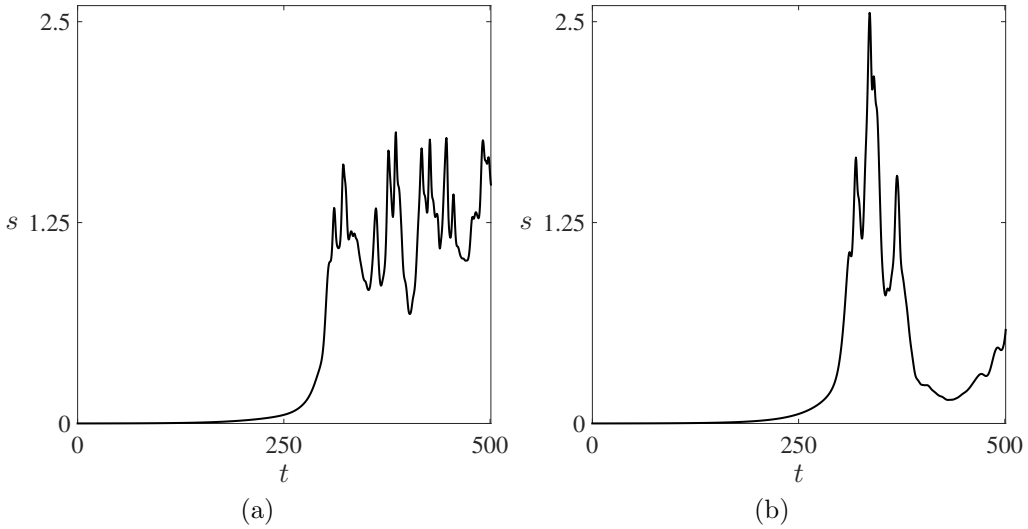

Figure 5.17: State space speed $s(t)$ of two sample trajectories on the 2D manifold. Panel (a) captures the behavior of $s(t)$ for most trajectories, which evolve slowly in the neighborhood of the equilibrium but eventually become turbulent. Panel (b) shows $s(t)$ for a "special" trajectory, where a very deep minimum in $s(t)$ was observed, suggesting a possible heteroclinic connection between two equilibrium solutions.

Since a deep minimum in the state space speed $s(t)$ indicates a close pass of the turbulent trajectory to a nearby equilibrium (cf. section (5.2)), the Newton-Krylov solver was initialized using the flow field from the instant of slowest evolution ($t \approx 450$ in Fig. 5.17(b)), which resulted in convergence to an equilibrium $D_0^{ic} = 0.13$ units away. The initial condition, the solution, and the difference between the two are shown in Fig. 5.18. This solution, shown in Fig. 5.18(b), was not found from either numerical or experimental initial conditions corresponding to state space speed minima of turbulent trajectories (cf. section (5.2)). Convergence to a solution so close to the manifold trajectory suggests that if a heteroclinic connection exists, it may be feasible to compute it by refining the initial condition on the circle around the source "01/B". Consequently, initial conditions within an arc ± 0.25 degrees wide, around the direction $\hat{\mathbf{e}}_2$ ($\theta = \pi/2$), were refined to about 0.005 degrees. The minimum in $s(t)$ of the resulting trajectories was tested after integrating for about 500 time units, in

hope of asymptotically approaching the "target" equilibrium, shown in Fig. 5.18(b). However, this method proved unsuccessful, with the minimum in $s(t)$ not decreasing sufficiently with refinement, and the trajectories eventually becoming turbulent.

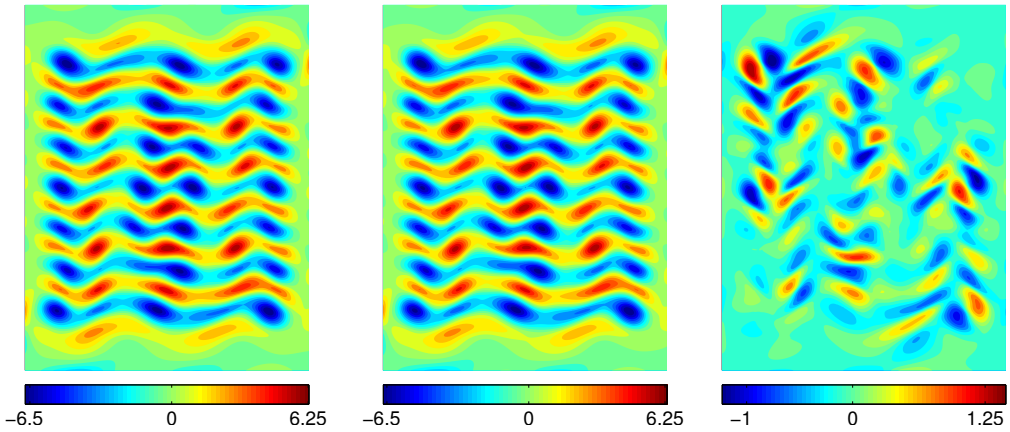

Figure 5.18: Flow field at an instant on a 2D manifold trajectory (left panel) when a dramatic slowing down was observed. The nearby equilibrium (middle panel) was computed using the Newton-Krylov solver. The difference between the two (right panel), computed using equation (5.4), is 13%.

The breakthrough in understanding the evolution of the heteroclinic-like trajectories initially evolving along $+\hat{\mathbf{e}}_2$ was achieved by associating the symmetries of the source and target solutions, with those of the eigendirections $\hat{\mathbf{e}}_1$ and $\hat{\mathbf{e}}_2$ of the 2D manifold at the source. To begin with, the governing equation in the NPS is equivariant under rotation $\mathcal{R}_y\mathcal{R}_x$. If $\mathbf{u}(t) = f^t(\mathbf{u}_{ic})$ represents the time evolution of an initial state, then $\mathcal{R}_y\mathcal{R}_x\mathbf{u}(t) = f^t(\mathcal{R}_y\mathcal{R}_x\mathbf{u}_{ic})$, since the time evolution operator commutes with the symmetries of the governing equation [143]. If the initial flow field is invariant under rotation, i.e., $\mathcal{R}_y\mathcal{R}_x\mathbf{u}_{ic} = \mathbf{u}_{ic}$, then one obtains $\mathcal{R}_x\mathcal{R}_y\mathbf{u}(t) = f^t(\mathbf{u}_{ic}) \implies \mathcal{R}_y\mathcal{R}_x\mathbf{u}(t) = \mathbf{u}(t)$. This means the evolution of a flow field which is invariant under rotation is always restricted to the rotationally symmetric subspace.

From Fig. 5.5(a) and Fig. 5.9, it can be seen that the source $\mathbf{u}_0$ (Index 01/B) and eigenvector $\hat{\mathbf{e}}_2$ are invariant under rotation, but $\hat{\mathbf{e}}_1$ is not. Hence, only those initial

conditions with zero component along $\hat{\mathbf{e}}_1$ on the circle $\mathbf{u}_{ic}^{\theta} = \mathbf{u}_0 + \epsilon\cos\theta\,\hat{\mathbf{e}}_1 + \epsilon\sin\theta\,\hat{\mathbf{e}}_2$ remain invariant under $\mathcal{R}_y\mathcal{R}_x$. Consequently, only two trajectories on the 2D manifold, which initially evolve along $\pm\,\hat{\mathbf{e}}_2$ ($\theta = \pi/2, 3\pi/2$), remain in the rotationally symmetric subspace. These constitute the rotationally symmetric 1D unstable submanifold of the solution. Since the target solution, shown in Fig. 5.18(b), is rotationally symmetric as well, the connection, if one exists, should be in the rotationally symmetric subspace. During integration, however, numerical noise at every iteration breaks the rotational symmetry infinitesimally, which eventually amplifies such that the desired rotationally symmetric trajectory cannot be traced in simulations. This was conjectured to be the possible reason behind the trajectory along $\hat{\mathbf{e}}_2$ not approaching the target equilibrium Fig. 5.18 asymptotically, even upon refining the initial conditions. For example, time integration of an initial condition invariant under $\mathcal{R}_y\mathcal{R}_x$, i.e., $\mathbf{u}_{ic} - \mathcal{R}_y\mathcal{R}_x\mathbf{u}_{ic} = 0$, for 500 units resulted in a deviation $\|\mathbf{u}(t) - \mathcal{R}_y\mathcal{R}_x\mathbf{u}(t)\| \approx 10^{-3}$ from rotational symmetry. Strict rotational symmetry, however, can be enforced by projecting-out the noise after each step of integration onto the rotationally symmetric subspace by replacing $\mathbf{u}(t)$ with $\mathbf{u}_{sym}(t) = (\mathbf{u}(t) + \mathcal{R}_y\mathcal{R}_x\mathbf{u}(t))/2$. The difference $\|\mathbf{u}_{sym}(t) - \mathbf{u}(t)\|/|\mathbf{u}(t)\|$ at each step was of the order 10^{-16}.

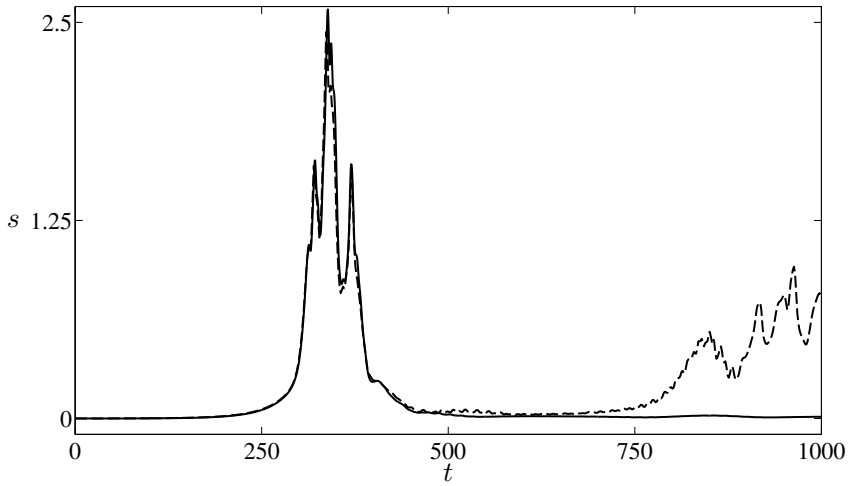

Figure 5.19: State space speeds $s(t)$ of (dashed curve) the heteroclinic-like trajectory with rotational symmetry enforced and (solid curve) of the exact connection computed by varying simulation parameters by 3%.

Fig. 5.19 shows the plot (dashed curve) of the state space speed along the heteroclinic-like trajectory, initially evolving along $\hat{\mathbf{e}}_2$, with rotational symmetry enforced at integration each step. The strict confinement to the rotationally-symmetric subspace brings the trajectory significantly closer to the target solution, than the one without the symmetry enforced (cf .Fig. 5.17(b)). However, the trajectory asymptotically does not merge into the target solution, as a true connection would, but instead deviates to become turbulent again. This behavior was understood using the symmetries of the eigenvectors of the target solution, which, in the full state space has 6 unstable eigendirections with associated eigenvalues $0.0522 \pm 0.0459i$, $0.008 \pm 0.427i$, and $0.002 \pm 0.186i$. The eigenvectors associated with the leading pair of eigenvalues were found to not be invariant under $\mathcal{R}_y\mathcal{R}_x$. Since the heteroclinic-like trajectory approaches the target from within the rotationally-symmetric subspace, numerical noise along the leading eigendirections near the target cannot amplify; it can, however, amplify along the weakly unstable directions associated with $0.008 \pm 0.427i$, and $0.002 \pm 0.018i$ which are invariant under $\mathcal{R}_y\mathcal{R}_x$. Since these eigendirections are close to being marginal (real parts ≈ 0), the trajectory remains in the neighborhood of the target for a duration comparable to $1/0.008 \approx 100$ time units, as can be seen from the speed plot Fig. 5.19, and eventually deviates.

As mentioned earlier, computing exact connections requires sophisticated numerical techniques. In contrast, the trick followed here, resembling the OGY-method [47], is to vary the simulation parameters by tiny amounts, such that the weakly unstable eigendirections become weakly stable. It was found that by increasing the friction coefficient α by 3%, and compensating it with a 3% increase in the driving strength, the leading eigenvalues of the target solution change to $0.0547 \pm 0.0472i$, $-0.0001 \pm 0.433i$, and $-0.0002 \pm 0.018i$. Any trajectory approaching the solution from within the rotationally-symmetric subspace will then be attracted towards it, and the connection can be computed by simple numerical integration. The speed plot

(solid curve) for the rotationally symmetric trajectory originating at the source, with simulation parameters changed by 3%, suggests that it asymptotically approaches the target solution. This was validated by integrating the trajectory for an additional 4×10^4 time units, which is comparable to the time scale of convergence to the solution 1/0.0001, determined by the slowest contracting mode.

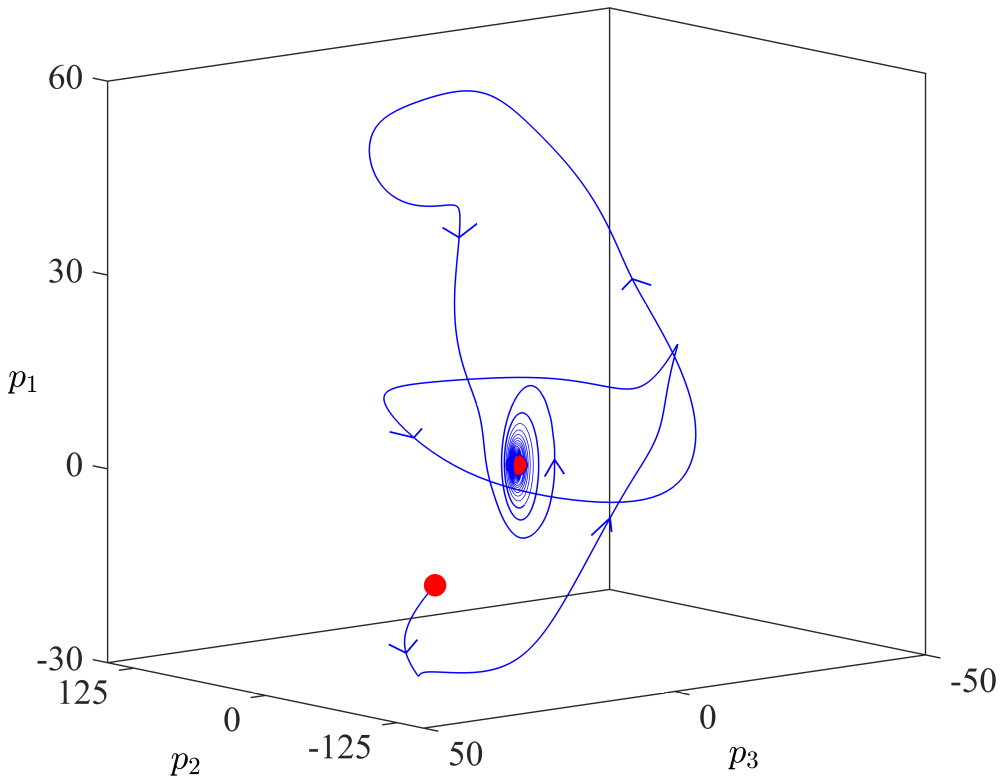

Figure 5.20: Heteroclinic connection (blue curve) between two equilibrium solutions (red spheres). The "source" solution has two unstable eigendirections, only one of them being invariant under rotational symmetry $\mathcal{R}_y\mathcal{R}_x$. The "target" solution, however, has no unstable eigendirection which is invariant under $\mathcal{R}_y\mathcal{R}_x$. Numerical integration was employed to compute the connection, which leaves the source along the eigenvector with rotational symmetry. The state space visualization was constructed by projecting the connection, and the solutions, along three eigenvectors of the "target" solution.

Fig. 5.20 shows a state space visualization of the heteroclinic connection between the two equilibria, constructed by projecting the connection $\mathbf{u}(t)$, as well as the source and target solutions onto a set of three eigenvectors associated with the target solution. Two of these were chosen to be the weakly contracting direction with eigenvalues

$-0.0001 \pm 0.433i$. The third was a stable eigendirection, which was identified to have a large component as the trajectory approaches the target.

The above exercise shows that there are dynamical connections between ECS which are far apart in state space. When a turbulent trajectory comes very close to a connection, it should follow it. While unstable manifolds and connections close to solutions are attracting, they become repelling far away from the solutions. This leaves the question regarding what fraction of a certain connection is followed, in general, by a turbulent trajectory. Hence, while it is speculative, it must be the case that the shorter a connection is, the more useful it should be in building forecasting models and controlling turbulence.

5.6 Summary

In this chapter a systematic study of the role of unstable equilibrium solutions in weakly turbulent quasi-two-dimensional flow was performed. It was found, in both the simulation and the experiment, that the evolution of a weakly turbulent flow is devoid of clear signatures of periodic orbits. In contrast, turbulent evolution was found to be punctuated by intervals of dramatic slowing down. This behavior was conjectured to be related to the turbulent trajectory visiting the neighborhoods of unstable equilibrium solutions. The flow fields at instants of deep local minima in the rate of evolution were tested for convergence to nearby unstable equilibria using a Newton solver. The converged equilibria in the physical space were found to bear striking resemblance with the turbulent flow fields used to compute them, suggesting close passes of the turbulent trajectory to these solutions. Identifying solutions with a few unstable directions, it was shown that turbulent trajectories in the neighborhood of these solutions depart following their unstable manifolds. Lastly, as a demonstration, a heteroclinic connection between two equilibrium solutions was computed using symmetry arguments. While the connection itself is restricted to the

rotationally symmetric subspace, and may never be followed for extended durations in the experiment, it serves to show that despite the apparent complexity displayed in turbulence, nonchaotic solutions indeed exist that may govern long term evolution.

CHAPTER VI

CONCLUSIONS

At the outset, the goal of the project leading to this dissertation was to provide unambiguous experimental evidence for the role of exact coherent structures in fluid turbulence at moderate Reynolds numbers. This was accomplished for the case of equilibrium solutions through a combined experimental and numerical study of a quasi-two-dimensional Kolmogorov-like flow. The flow in the experiment was generated by driving a shallow electrolyte layer, which floats on a heavier dielectric fluid, using electromagnetic forcing with a near-sinusoidal spatial profile. This Q2D flow was quantified using the 2D velocity field at the electrolyte-air interface, measured by tracking groups of tracer particles using 2D particle image velocimetry. The flow in the experiment was theoretically modeled using a strictly 2D equation, which was numerically simulated on a domain with boundary conditions and dimensions identical to the experimental one. That the flow in both experiment and simulations could be treated as 2D proved extremely useful in circumventing computational overhead associated with 3D flows as well as dramatically simplifying the analysis of experimental data.

6.1 Summary of Scientific Contribution

2D problems may appear simple, however, achieving quantitative agreement between an inherently 3D experiment and a 2D reduced model proved very challenging, requiring identification and resolution of several shortcomings of previous studies. The summary of specific scientific advances accomplished as a part of the research presented herein are summarized in the following sections.

6.1.1 Theoretical Modeling of Q2D Flows

Moderate Reynolds number flows in shallow electrolyte layers supported by a solid surface have previously been modeled by adding a linear friction term to the 2D Navier-Stokes equation; the coefficient of friction was treated as a fitting parameter to match theory and experiment. In contrast, the research presented herein provided the first systematic derivation of a 2D model, by depth-averaging the full 3D Navier-Stokes equation that describes the evolution of the flow in the experiment. The Rayleigh friction term in this 2D model appeared naturally as a consequence of the depth-averaging procedure employed. Furthermore, the 2D model accounted for the change in the effective inertia of the fluid layers due to the gradient in the magnitude of the horizontal velocity along the fluid layer depth. This modification, which enters the governing equation as a prefactor $\beta \neq 1$ to the nonlinear term, distinguishes the model from all previous empirical variations of 2D Navier-Stokes.

The vertical variation in the velocity magnitude for two-fluid-layer setups (miscible or immiscible) like the one employed in this study had not been previously studied. Consequently, 2D models for two-fluid-layer systems used dimensional and geometrical criteria to estimate model parameters. To address these shortcomings the velocity profile in the two-immiscible-layer configuration was analytically computed and validated by comparing the amplitude of the near-sinusoidal velocity in the experiment with analytical estimates. Additionally, analytical expressions for the 2D model parameters were derived in terms of experimentally measurable fluid layer properties; the parameters so computed account for both the inhomogeneity of the fluid properties as well as the vertical variation in velocity magnitude. Lastly, as a consequence of computing the vertical profile, it was identified that by increasing the viscosity of the electrolyte layer in comparison to that of the dielectric, one can create a nearly perfect 2D flow in the electrolyte layer, which is advantageous when comparing experiments with results from the 2D model.

6.1.2 Bifurcations in Kolmogorov-like flow

To test the accuracy of the 2D model, the bifurcation sequence in the Kolmogorov-like flow was studied both experimentally and theoretically. The primary instability of the near-sinusoidal straight flow resulting in a steady vortex pattern has been previously studied theoretically assuming spatial periodicity, infinite lateral extent, and a strict sinusoidal forcing. Analytical estimates using empirical models for critical Reynolds number characterizing the primary instability were found to be 30% smaller, than those measured in experiments. Employing the 2D model derived herein, the disagreement was found to decrease to 17% using a purely analytical approach. However, since assuming spatial periodicity constitutes unrealistic modeling of the flow in experiment, a non-periodic numerical simulation of the 2D model with the inclusion of realistic, no-slip velocity boundary conditions was developed, wherein spatiotemporal derivatives were approximated using finite differences. The magnetic field profile in the experiment over the entirety of the domain was accurately reproduced numerically using a 3D point dipole model of the magnet array. Also, the lateral dimensions of the non-periodic domain were chosen to be identical to that in the experiment to facilitate direct, quantitative comparison between the two.

Following this careful numerical modeling, it was shown that the flow fields measured in the pre-turbulent regimes in the experiment could be reproduced using the non-periodic simulation with remarkable accuracy. The critical Reynolds number Re_c and the wavenumber κ_c that characterize the primary bifurcation measured in experiment were reproduced in simulations to within 5% without requiring any fitting parameters. Furthermore, the secondary instability of the flow leading to an oscillatory vortex pattern was studied both using experiments and simulations. The numerical predictions of the critical Reynolds number Re_p and the critical period T_p using depth-averaged parameters agreed to within 15% of experimentally measured values. By modifying the simulation parameters by around 6%, the disagreement was

found to decrease to 8%. These results confirm that the 2D equation, with its realistic numerical model, indeed captures the dynamics in the experiment *significantly* more accurately than all previous studies.

Besides comparing the bifurcation sequence in the experiment with that from the non-periodic simulation, the effect of lateral confinement on the nature of the first bifurcation was explored using periodic simulations with varying degrees of confinement. It was shown that, on a domain periodic in both lateral directions, the transition from straight to modulated flow is a circle pitchfork bifurcation, which gets modified to a sequence of two pitchfork bifurcations when one confines the flow longitudinally, which is eventually reduced to an *imperfect* pitchfork in the non-periodic simulation and in the experiment. This is in stark contrast with results from previous studies, which have characterized the transition in the experiment as a pitchfork bifurcation, using analytical computations on an unbounded domain. The two unstable branches emerging from the imperfect pitchfork bifurcation, which describe flows that are not observed in either experiment or simulations under normal conditions, were computed using a Newton-Krylov solver.

The systematic study of pre-turbulent regimes has provided valuable insights into the strengths as well as the limitations of the 2D model in describing the flow in the experiment. The main source of discrepancy between the 2D simulation and the experiment was identified to be the deviation of the latter from being strictly Q2D; while viscous coupling ensures the velocity field is Q2D, the forcing that drives it was found to deviate from being Q2D. This is a limitation of possibly every 2D model describing an inherently 3D flow which is driven by a horizontal forcing. In favor of the 2D model, however, it was found that the depth-averaged parameters are fairly robust to changes in the local wavenumber of the flow pattern. This robustness is crucial to compare simulations with experiments in the turbulent regime, where the wavenumber can vary spatiotemporally in a complicated manner. Hence, while a

single set of parameters cannot accurately describe the flow across a wide range of Reynolds numbers, one should be able to get quantitative agreement with experiment for a select range of Re by modifying the simulation parameters from their depth-averaged values only by a few percent.

6.1.3 Unstable Equilibrium Solutions in Weak Turbulence

The agreement between the experiment and 2D model in the pre-turbulent regimes laid a strong foundation to explore the role of ECS in the turbulent regime. Studying long time series from both numerical simulations and experiment, it was identified that turbulent evolution was punctuated by intervals of dramatic slow evolution. This behavior was reasoned to be due to the turbulent trajectory fleetingly visiting the neighborhoods of unstable equilibrium solutions in the state space. Flow fields from instants of deep local minima in the rate of evolution were input into a Newton-Krylov solver to test convergence to a nearby equilibrium. Around 50 initial conditions successfully converged, to a total of 19 distinct solutions; 13 of these were computed using flow fields from experiments. Unlike previous studies of ECS in 3D flows, where invoking Taylor's frozen hypothesis was necessary to compare 3D velocity fields from simulations with 2D measurements in experiments, the "state" of the flow in the Q2D experiment is resolved both spatially and temporally in the entire flow domain. Hence, the striking similarity between the initial conditions and the solutions in physical space implied that turbulent trajectories in the full state space indeed approach the solutions rather closely.

This visual confirmation provided the impetus to explore the role of these equilibrium solutions in shaping the geometry of state space around them. Computing the eigenspectrum associated with each solution, it was found that the number of unstable directions across solutions varied between 2 and 9, with a comparable number of dynamically relevant stable directions. Since computing stable manifolds or unstable

manifolds of high effective dimensionality ($\geq$4) is challenging, the geometry of state space was explored around those solutions with only a few unstable directions. Using numerically generated time series it was shown that turbulent trajectories in the vicinity of a solution with only 2 unstable eigendirections depart following its 2D unstable manifold. Moreover, it was demonstrated that even when the unstable manifold is high-dimensional, a clear separation between the leading eigenvalues leads to dramatic simplification of state space geometry. For a solution with 7 unstable eigendirections, but with the leading real eigenvalue being 10 times larger than each of the remaining six, it was shown that turbulent trajectories in both experiment and simulation evolve following the 1D submanifold corresponding to the leading unstable eigendirection. This was the first experimental validation for the dynamical role of ECS in turbulence at moderate Reynolds numbers as well as the first demonstration of ECS-based forecasting in experiments. Finally, in the numerical simulations, the presence of dynamical connections between unstable ECS was demonstrated by computing a heteroclinic connection between two pairs of equilibria in the rotationally-symmetric subspace.

These findings demonstrate the potential power of this geometrical approach: Using direct numerical simulations one can pre-compute ECS and their dominant submanifolds, once and for all. Turbulent evolution can then be forecast moderately far into the future, based solely on the fact that the turbulent trajectory was found close to an ECS. By computing a sufficiently large set of ECS, including time-periodic ones, and their dominant submanifolds, and the dynamical connections between ECS, it should be possible to "tile" the entire region of state space inhabited by turbulence. Such tiling should also enable long-term predictions which requires that the chaotic trajectory be periodically refined by comparing predictions with measurements, as done currently in weather prediction.

6.2 Unaddressed and Open Questions

While the results presented herein provide unambiguous evidence, both experimental and numerical, for the role of ECS at moderate Reynolds numbers, there are a lot of questions that remain open to analysis even in the simple Q2D case. For example, the geometrical description and the forecasting calculations were tested only in the neighborhoods of equilibrium solutions with very few unstable eigendirections. Extending such an approach to forecast evolution, even for a few correlation times, in the neighborhoods of equilibria with several (4 or more) unstable directions is fairly challenging, since computing unstable manifolds becomes data intensive and intractable. Hence, methods to forecast the dynamics in a computationally efficient way in the neighborhoods of equilibria with many unstable directions, in some sense, should form the natural extension of the work presented herein. Such a study will also throw light on the strengths, limitations, and practical applicability of ECS based forecasting.

Additionally, the study presented in this dissertation focused only on the role of unstable equilibrium solutions. Which other types of ECS (periodic orbits, heteroclinic and homoclinic connections, etc.), and how many of each kind, are necessary to build a reliable deterministic model of turbulence remains unaddressed. At the very least, the role of unstable periodic orbits should be explored as a followup study. Recurrence analysis of the numerical (experimental) turbulent trajectory, generated for about 2000 (400) correlation times, suggests that a flow field at an instant rarely ever recurs within the subsequent 20 correlation times. If it is indeed the case that, at this Re, periodic orbits do not play a dynamically important role, then forecasting long term temporal evolution of a turbulent trajectory may require identifying and computing heteroclinic and homoclinic connections, a task significantly more difficult than computing equilibria or periodic orbits. Furthermore, cycle-expansions developed for low-dimensional dynamical systems include contributions only from periodic orbits to estimate the temporal average of a quantity. Since sufficiently close passes

to periodic orbits were not observed in the present study, the role of dynamical connections in governing turbulent statistics should be addressed in future studies.

While building forecasting models using ECS is of great practical utility, retrieving statistical measures of turbulent time series in experiments using ECS is equally important, but was not explored in previous studies. The 2D model, however, may pose some challenges in relating 2D quantities to their Q2D counterparts since the depth-averaging procedure employed in its derivation is lossy, eliminating the dependence on the coordinate in the confined direction completely. As a demonstration, the energy input into a Q2D flow is $I_{Q2D} = \langle \mathbf{F} \cdot \mathbf{V} \rangle_{xyz} = \langle P(z) D(z) \rangle_z \langle \mathbf{F}_0 \cdot \mathbf{u} \rangle_{xy}$, where the Q2D ansatz for both forcing and the velocity field were invoked. In contrast, the energy input into 2D flow is $I_{2D} = \langle \langle \mathbf{F} \rangle_z \cdot \mathbf{u} \rangle_{xy} = \langle D(z) \rangle_z \langle \mathbf{F}_0 \cdot \mathbf{u} \rangle_{xy}$ which is different from I_{Q2D}. Similar anomalies with respect to dissipation exist as well, which may have to be addressed in future studies comparing turbulent statistics in 2D models and Q2D flows.

Lastly, the ultimate challenge for the ECS-based forecasting approach pursued in this thesis will stem from its applicability to 3D flows, both in simulations and experiments. Even with recent advances in computational powers, numerical simulation of the 3D Navier-Stokes equation are notoriously slow. Consequently, computing solutions, manifolds, and connections is significantly more challenging. The technological limitations on the experimental front pose similar limitations with regard to measurement of spatiotemporally resolved velocity fields for extended durations. However, with rapid improvements to both imaging and computing speeds, an ECS based description of 3D flows may indeed be tested in the coming years, which would hopefully pave the way to solving the turbulence problem.

APPENDIX A

SOLVING POISSON'S EQUATION

In this appendix a brief discussion of solving the Poisson's equation $\nabla^2 p = g$ on a 2D rectangular domain, subject to homogeneous Neumann boundary conditions $\nabla p \cdot \hat{\mathbf{n}} = 0$ is presented (cf. sections 3.3.1 and 5.2.2). Here, $\hat{\mathbf{n}}$ is the unit vector normal to the boundary at each point. If $\mathbf{L}$ and $\mathbf{g}$, respectively, are the discretized 2D Laplacian matrix and source vectors, then the vector $\mathbf{p}$ is the solution to the discrete Poisson's equation $\mathbf{Lp} = \mathbf{g}$. As discussed in section (3.3.2) $\mathbf{L}$ for homogeneous Neumann boundary conditions is singular, since if f is a solution to the Poisson's equation, every function $\tilde{f} = f + c$ is also a solution, where c is a constant.

One procedure to regularize the discrete Laplacian $\mathbf{L}$ and make the solution $\mathbf{p}$ unique is to specify the value of p at a point on the boundary, say $\mathbf{p}(1) = c$. This modifies the first row of $\mathbf{L}$ to $[1, 0, 0, \cdots, 0]$ and sets the source vector element $\mathbf{g}(1) = c$. The resulting $\tilde{\mathbf{L}}$ is no longer singular, and one can use LU decomposition to solve the equation $\tilde{\mathbf{L}}\mathbf{p} = \tilde{\mathbf{g}}$. Alternatively, one can use the generalized inverse of $\mathbf{L}$ to solve the linear equation [132, 145], which is the method followed in this thesis. To begin, the null space of $\mathbf{L}$ is spanned by vector $\mathbf{e} = [1, 1, 1, \cdots, 1]^\intercal$, i.e., $\mathbf{Le} = \mathbf{0}$. Any specific solution $\mathbf{p}_0$ can be modified by adding the vector $c\,\mathbf{e}$ to it; the modified $\mathbf{p}$ still remains a solution to the Poisson's equation. Since $\mathbf{L}$ is symmetric, for any arbitrary vector $\mathbf{w}$, $\mathbf{e}^\intercal(\mathbf{Lw}) = (\mathbf{Le})^\intercal\mathbf{w} = 0$. This implies that the matrix $\mathbf{L}$ projects every arbitrary vector into a space normal to $\mathbf{e}$, i.e., $\mathbf{Lw} \perp \mathbf{e}$. The compatibility condition, then requires that $\mathbf{g}$ is normal to $\mathbf{e}$ as well, i.e., $\mathbf{e}^\intercal\mathbf{g} = 0$.

Consider the modified matrix[1] $\tilde{\mathbf{L}} = \mathbf{L} + \mathbf{v}\mathbf{v}^\intercal$, where $\mathbf{v} = [1, 0, 0, \cdots, 0]^\intercal$ is not orthogonal to $\mathbf{e}$. The product

$$\tilde{\mathbf{L}}\mathbf{w} = (\mathbf{L} + \mathbf{v}\mathbf{v}^\intercal)\mathbf{w} = \mathbf{L}\mathbf{w} + (\mathbf{v}\mathbf{v}^\intercal)\mathbf{w} = \underbrace{\mathbf{L}\mathbf{w}}_{\perp \mathbf{e}} + \underbrace{(\mathbf{v}^\intercal\mathbf{w})\mathbf{v}}_{\not\perp \mathbf{e}}, \tag{A.1}$$

can be zero only if $\mathbf{w} = 0$ since it is a sum of two non-parallel vectors; $\mathbf{L}\mathbf{e}$ is normal to $\mathbf{e}$ while $\mathbf{v}$ is not; note that $\mathbf{v}^\intercal\mathbf{w}$ is a scalar. Hence, $\tilde{\mathbf{L}}$ is not singular. Setting $\mathbf{w} = \mathbf{e}$ and $\mathbf{v}^\intercal\mathbf{e} = 1$ the above equation results in $\mathbf{e} = \tilde{\mathbf{L}}^{-1}\mathbf{v}$. That the solution to the regularized equation $\mathbf{p} = \tilde{\mathbf{L}}^{-1}\mathbf{g}$ is indeed a solution to the Poisson equation can be shown by pre-multiplying the modified equation with $\mathbf{L}$:

$$\begin{aligned}
\mathbf{L}\mathbf{p} &= \mathbf{L}\tilde{\mathbf{L}}^{-1}\mathbf{g} = (\tilde{\mathbf{L}} - \mathbf{v}\mathbf{v}^\intercal)\tilde{\mathbf{L}}^{-1}\mathbf{g} \\
&= (\mathbf{I} - \mathbf{v}\mathbf{v}^\intercal\tilde{\mathbf{L}}^{-1})\mathbf{g} = \mathbf{g} - \mathbf{v}(\mathbf{v}^\intercal\tilde{\mathbf{L}}^{-1})\mathbf{g} = \mathbf{g} - \mathbf{v}(\mathbf{e}^\intercal)\mathbf{g} = \mathbf{g} - \mathbf{v}(\mathbf{e}^\intercal\mathbf{g}) \\
&= \mathbf{g},
\end{aligned} \tag{A.2}$$

where we use $\mathbf{L} = \tilde{\mathbf{L}} - \mathbf{v}\mathbf{v}^\intercal$ and $\mathbf{e}^\intercal\mathbf{g} = 0$. Since $\tilde{\mathbf{L}}$ is invertible, as well as symmetric, one can use Cholesky decomposition to compute the solution to Poisson's equation efficiently using MATLAB's "A solve b" command.

Fig. A.1(a) shows the contour plot of pressure p for the modulated flow at $Re \approx 15$ computed using numerical integration. The Poisson's equation (cf. 3.26) at each projection step is solved using the generalized inverse procedure described above, using Cholesky decomposition. The solution computed is validated by replacing the incompressibility condition $\nabla \cdot \mathbf{u} = 0$ with artificial compressibility, $\partial_t p = -c^2 \nabla \cdot \mathbf{u}$, where c is a constant $O(1)$. The solutions and their stability for steady states computed using the projection and artificial compressibility methods should be identical, since $\partial_t p = 0 \implies \nabla \cdot \mathbf{u} = 0$. This is confirmed, from Fig. A.1(b), where the contour plot of difference in the pressure fields computed using both the methods is shown, which

[1] The solution to the Poisson's equation using this modified matrix is using the generalized inverse $\mathbf{G}$ of a singular matrix $\mathbf{A}$, to solve $\mathbf{A}\mathbf{x} = \mathbf{y}$. The matrix $\mathbf{G}$ satisfies $\mathbf{A}\mathbf{G}\mathbf{y} = \mathbf{y}$. Solutions of $\mathbf{x} = \mathbf{G}\mathbf{y}$ are also solution of the equation $\mathbf{A}\mathbf{x} = \mathbf{y}$. Wikipedia has a decent explanation of it.

differ by $\approx 10^{-11}$. The pressure computed using the generalized inverse Cholesky solver is also practically identical to the one computed using LU decomposition with the Dirichlet condition for a point on the boundary, say $\mathbf{p}(1) = 0$, as can been from Fig. A.1(c). Lastly, the comparison with an iterative successive-over-relaxation (SOR) method, which does not include any matrix inversions, is shown in Fig. A.1(d). While accurate, the SOR method proved computationally very slow and was used only as a validation technique. In summary, one can use either of the techniques described here to correctly solve the Poisson's equation with homogeneous Neumann boundary conditions.

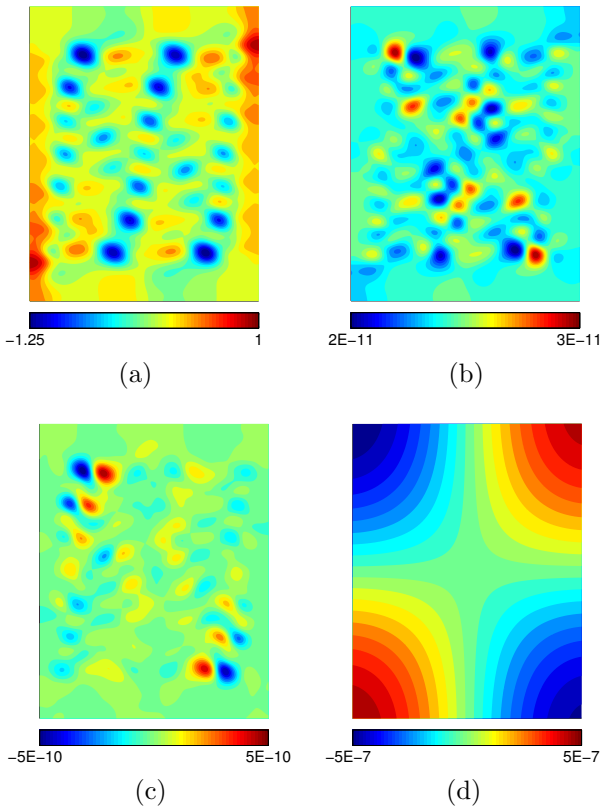

Figure A.1: Comparison of pressure fields associated with the modulated flow at $Re = 15.4$, computed using four different procedures. Panel (a) shows the pressure field computed using generalized inverse method, using Cholesky solver. Panel (b) shows the difference in pressure obtained using Cholesky solver and artificial compressibility. Panels (c) and (d) show differences between pressure using Cholesky solver, and those using LU-decomposition and iterative SOR solver, respectively. Note the differences in colorbar scales.

APPENDIX B

ROBUSTNESS OF RESULTS TO CHANGING SIMULATION PARAMETERS

In this appendix a brief discussion of the tests validating the choice of spatiotemporal resolution in the NPS is presented. To begin, a spatial resolution of 20 cells per magnet width was found adequate to describe the flow in the experiment accurately. This was tested for the runs in the pre-turbulent regimes (cf. chapter 4) by recomputing the modulated flow at $Re \approx 15.5$ by doubling the spatial resolution, i.e., using 40 cells per magnet width. This velocity field ($\mathbf{u}_{40}$) was compared with the one computed on the 20-cell grid ($\mathbf{u}_{20}$) by interpolating (required due to the staggered nature of the grid) $\mathbf{u}_{40}$ onto the 20-cell grid to obtain $\mathbf{u}_{\text{interp}}$. The difference between $\mathbf{u}_{\text{interp}}$ and $\mathbf{u}_{20}$, computed as $\|(\mathbf{u}_{\text{interp}} - \mathbf{u}_{20})\|/\|\mathbf{u}_{20}\| \times 100$, was 1.2%. Since interpolation introduces error, it can be concluded that the actual error is less than 1.2%. Global measures such as Re or $\langle u_y^2 \rangle$ (used to characterize the primary instability) computed directly using $\mathbf{u}_{40}$ and $\mathbf{u}_{20}$ differed by less than 0.2%.

The temporal discretization of the governing equation (cf. equation (3.22)) in the pre-turbulent regime was performed using a time-step $dt = 1/40\,\text{s}$ ($\approx 1/100$ nondimensional units), limiting the CFL number (cf. equation (3.37)) to less than 0.5. The adequacy in temporal resolution was tested by recomputing the evolution of the periodic orbit at $Re \approx 16.2$ using $dt = 1/80\,\text{s}$ and comparing the difference in the initial and final flow states after integrating for one time-period ($T \approx 130\,\text{s}$), i.e., $\|\mathbf{u}(t) - \mathbf{u}(t+T)\|/\|\mathbf{u}(t)\|$, which measured to be approximately 10^{-5}.

The 2D model with the depth-averaged parameters computed from first principles [114] underestimates the onset of turbulence observed in the experiment by $\Delta Re \approx$

1.5 (cf. chapter 4). While modifying the parameters, as discussed in section (4.4), improves the agreement between experiment and simulation to some extent, adding numerical diffusion through the discretization of the nonlinear term [126] was found to be more effective in achieving agreement. Consequently, the runs presented in chapter 5 were performed with the addition of numerical dissipation amounting to 6% of the combined dissipation due to viscosity and friction. The existence of the solutions with the 2D and the (effectively) 1D manifolds, as well as the robustness of their eigenspectra, has been tested by changing the numerical dissipation between 0% and 8%. Similar tests for robustness were performed by changing the values of α ($\pm 7.5\%$), ν ($\pm 5\%$), as well as the Reynolds number ($20 \leq Re \leq 23.6$).

The adequacy of the spatial resolution was tested by recomputing the solution with the dominant 1D submanifold on a grid with four times the resolution, i.e., 80 cells per magnet width. The refined solution $\mathbf{u}_{80}$ interpolated on to grid with 20 cells ($\mathbf{u}_{interp}$) differs from the solution $\mathbf{u}_{20}$ by 3.5%. However, the leading eigenvalue changes by less than 1% with change in the resolution. The evolution along the dominant 1D submanifold was also tested to remain robust to refinement in the spatial resolution. These spatial refinement tests were carried out for the case with no addition of numerical dissipation. A time-step of $dt = 1/50\,\mathrm{s}$ was used for the turbulent runs, which was tested to be adequate. Turbulent trajectories starting from identical initial conditions but computed using different time-steps, $dt = 1/50\,\mathrm{s}$ and $dt = 1/100\,\mathrm{s}$, were found to deviate (on average) by less than 0.5% after evolving for 10 temporal correlation times ($\approx 300\,\mathrm{s}$). The blending parameter, however, was scaled by a factor 2 when the time step is refined by a factor 2 to keep the numerical dissipation across the two runs identical. In summary, the resolution employed for the simulations is adequate to capture the dynamics observed in the experiment and the results were found to be robust to changes in numerical parameters.

APPENDIX C

LINEAR STABILITY ANALYSIS OF THE STRICTLY SINUSOIDAL FLOW

In this appendix, the linear stability calculation of the straight sinusoidal flow with respect to perturbations having longitudinal wavenumber k is discussed. To begin, any allowed perturbation $\tilde{\mathbf{u}}$ to the straight flow $\mathbf{u}_s$ should lie in the divergence-free subspace, i.e., $\nabla \cdot \tilde{\mathbf{u}} = 0$, if one attempts to analyze the stability using equation (3.3). Furthermore, for such analysis, the perturbation to the pressure should be computed, which is quite complicated. To circumvent this difficulty, it is convenient to perform the linear stability analysis in the vorticity-stream function formulation, which is given by equation (3.45), with implicit treatment of incompressibility. The straight flow and the associated vorticity field are given by:

$$\mathbf{u}_s = u_s\,\hat{\mathbf{x}} = u_0 \sin(\kappa y)\,\hat{\mathbf{x}} \quad \text{and} \quad \omega_s = \nabla \times \mathbf{u}_s \cdot \hat{\mathbf{z}} = -u_0 \kappa \cos(\kappa y). \tag{C.1}$$

The equation governing the evolution of a perturbation $\tilde{\omega} = (\nabla \times \tilde{\mathbf{u}}) \cdot \hat{\mathbf{z}}$ is given by substituting $\omega = \omega_s + \tilde{\omega}$ into equation (3.45), which yields

$$\underbrace{\left(\partial_t \omega_s + \beta \mathbf{u}_s \cdot \nabla \omega_s + \alpha \omega_s - \nu \nabla^2 \omega_s + W\right)}_{=0} \cdots$$
$$+ \left(\partial_t \tilde{\omega} + \beta \mathbf{u}_s \cdot \nabla \tilde{\omega} + \beta \tilde{\mathbf{u}} \cdot \nabla \omega_s + \underbrace{\beta \tilde{\mathbf{u}} \cdot \nabla \tilde{\omega}}_{\approx 0} + \alpha \tilde{\omega} - \nu \nabla^2 \tilde{\omega} \right) = 0, \tag{C.2}$$

wherein the terms highlighted using the under-braces are set to zero; the first term is identically zero since it corresponds to the equation employed to solve for $\mathbf{u}_\mathrm{s}$ with $W = \chi \kappa \cos(\kappa y)$, and in the second term $\tilde{\mathbf{u}} \cdot \nabla \tilde{\omega}$ is approximated to zero since it is a higher-order nonlinear correction.

Using $(\tilde{u}, \tilde{v}) = (\partial_y \tilde{\psi}, -\partial_x \tilde{\psi})$, and $\tilde{\omega} = -\nabla^2 \psi$, where $\tilde{\psi}$ is the stream function of the perturbation, the equation governing the evolution of the perturbation can be written as:

$$\partial_t \tilde{\omega} + \beta u_s \partial_x \tilde{\omega} - \beta \partial_x \tilde{\psi} \partial_y \omega_s + \alpha \tilde{\omega} - \nu \nabla^2 \tilde{\omega} = 0, \tag{C.3}$$

where, the substitutions $\mathbf{u}_\mathrm{s} \cdot \nabla \tilde{\omega} = u_s \partial_x \tilde{\omega}$ and $\tilde{\mathbf{u}} \cdot \nabla \omega_s = \tilde{v} \partial_y \omega_s = -\partial_x \tilde{\psi} \partial_y \omega_s$ were made, since $v_s = 0$, and $\partial_x \omega_s = 0$, following equation (C.1).

Since $\tilde{\omega} = -\nabla^2 \tilde{\psi}$, choosing perturbations of the form

$$\tilde{\omega}(x, y, t) = \sum_{k,l} \hat{\omega}(k, l) e^{ikx + ily} e^{\sigma t} \quad \text{and} \quad \tilde{\psi}(x, y, t) = \sum_{k,l} \frac{\hat{\omega}(k, l)}{k^2 + l^2} e^{ikx + ily} e^{\sigma t}, \tag{C.4}$$

with the choice $\tilde{\psi}(0, 0) = 0$, and substituting $u_s = u_0 \sin(\kappa y) = u_0 (e^{i\kappa y} - e^{-i\kappa y})/2i$, one can expand equation (C.3) as:

$$\begin{aligned} \sum_{k,l} \left(\sigma + \alpha + \nu(k^2 + l^2)\right) \hat{\omega}(k, l) e^{ikx + ily} \cdots \\ + \sum_{k,l} \frac{\beta u_0 k}{2} \left(1 - \frac{\kappa^2}{k^2 + l^2}\right) \hat{\omega}(k, l) e^{ikx + i(l+\kappa)y} \cdots \\ - \sum_{k,l} \frac{\beta u_0 k}{2} \left(1 - \frac{\kappa^2}{k^2 + l^2}\right) \hat{\omega}(k, l) e^{ikx + i(l-\kappa)y} = 0. \end{aligned} \tag{C.5}$$

Changing summation index in the second and third terms, $l + \kappa \to l$ and $l - \kappa \to l$, respectively, and subsequently setting the coefficient of each exponent to zero, one arrives at the following system of equations for eigenvalue σ,

$$\begin{aligned} \sigma \hat{\omega}(k, l) = -\frac{\beta u_0 k}{2} \left(1 - \frac{\kappa^2}{k^2 + (l - \kappa)^2}\right) \hat{\omega}(k, l - \kappa) - \left(\alpha + \nu(k^2 + l^2)\right) \hat{\omega}(k, l) \\ + \frac{\beta u_0 k}{2} \left(1 - \frac{\kappa^2}{k^2 + (l + \kappa)^2}\right) \hat{\omega}(k, l + \kappa). \end{aligned} \tag{C.6}$$

The solution of the above system of equations yields the growth rate σ for a given value u_0. The quantity one is interested in estimating, however, is u_0 such that σ becomes zero. Setting $\sigma = 0$ one arrives at the following system of equations,

$$\begin{aligned} \frac{1}{u_{0,n}} \hat{\omega}(k, l) = -\frac{\beta k}{2\left(\alpha + \nu(k^2 + l^2)\right)} \left(1 - \frac{\kappa^2}{k^2 + (l - \kappa)^2}\right) \hat{\omega}(k, l - \kappa) \cdots \\ + \frac{\beta k}{2\left(\alpha + \nu(k^2 + l^2)\right)} \left(1 - \frac{\kappa^2}{k^2 + (l + \kappa)^2}\right) \hat{\omega}(k, l + \kappa). \end{aligned} \tag{C.7}$$

The largest eigenvalue $1/u_{0,n}$ yields the inverse of the (smallest) critical velocity at which the perturbations are neutrally stable. For the three-mode truncation, with $l = \{-\kappa, 0, \kappa\}$, the right hand side of the above equation can be written in matrix form

$$\begin{bmatrix} 0 & \frac{\beta k}{2\alpha+2\nu(k^2+\kappa^2)}\left(1-\frac{\kappa^2}{k^2}\right) & 0 \\ -\frac{\beta k}{2\alpha+2\nu k^2}\left(1-\frac{\kappa^2}{k^2+\kappa^2}\right) & 0 & \frac{\beta k}{2\alpha+2\nu k^2}\left(1-\frac{\kappa^2}{k^2+\kappa^2}\right) \\ 0 & -\frac{\beta k}{2\alpha+2\nu(k^2+\kappa^2)}\left(1-\frac{\kappa^2}{k^2}\right) & 0 \end{bmatrix} \begin{bmatrix} \hat{\omega}(k,-\kappa) \\ \hat{\omega}(k,0) \\ \hat{\omega}(k,\kappa) \end{bmatrix}$$

The real eigenvalues of the above equation yield the critical peak velocity $u_{0,n}$ as a function of k, from which one can compute the expression in equation (4.1) for neutral stability,

$$Re_n(k) = \frac{u_{0,n}}{\sqrt{2}}\frac{\pi}{\kappa}\frac{1}{\bar{\nu}}, \tag{C.8}$$

where, the spatial root-mean-squared velocity U was computed using $U = u_{0,n}/\sqrt{2}$, since the straight flow is sinusoidal. The analytical estimate for Re_c obtained using the three-mode truncation discussed here lies within 0.5% of the asymptotic value of Re_c obtained by including higher harmonics 3κ, 5κ, $\cdots$, 15κ in the truncation.

APPENDIX D

LIMITATIONS OF THE 2D MODEL IN DESCRIBING A Q2D FLOW

In this appendix the mathematical accuracy of a 2D model (equation (1.8), equation (3.3)) in describing a flow in the experiment is discussed. This discussion is motivated by the observation that the magnetic field in the experiment has harmonics of the base frequency κ. Since all such frequencies decay at different rates above the magnet array, the forcing deviates from being Q2D. The sensitivity of the dynamics (only the primary instability) to the vertical variation in magnetic field is discussed, which offers a possible explanation for the observed discrepancies between the 2D model and the experiment. Furthermore, from a theoretical standpoint, Q2D models in shallow electrolyte layers have been derived almost exclusively in the studies of linear, sinusoidal, Kolmogorov-like flows. Only a few studies [81, 82] have previously discussed the validity of the Q2D approximation when multiple spatial frequencies emerge, which is revisited herein.

D.1 Inherent Three-Dimensionality of the Forcing in the Experiment

As discussed in section (3.2), the Lorentz force density due to the specific arrangement of magnets employed in the experiment is to a very good approximation given by $\mathbf{F} = JB_z\hat{\mathbf{x}}$, where J is the magnitude of current density and $B_z(x, y, z)$ is the z-component of the magnetic field at any given location within the electrolyte. In deriving equation (3.3) it was *implicitly* assumed (cf. section (3.1)) that B_z can be decomposed as the product of a 2D horizontal profile $B_{2D}(x, y)$, which depends

exclusively on the extended coordinates (x, y), and a 1D vertical profile $D(z)$, which captures the variation of the magnetic field above the magnet array, i.e., $B_z(x, y, z) = D(z)B_{2D}(x, y)$. This implies that, when normalized, the planar magnetic field profiles at various heights z within the electrolyte are identical. Such a magnetic field, which can be called "Q2D," facilitates the decomposition of the plane-parallel Q2D velocity field (2.1) which underpins the strictly 2D model (3.3).

A magnetic field that is truly Q2D, however, cannot be created using a magnet array with finite dimensions, i.e., the *shape* of the magnetic field profile generated by permanent magnets in the laboratory always changes with the vertical height z to some extent. Experimental measurements of magnetic field from previous studies have shown such changes in the shape of the field profile as a function of z [114, 146], which is very much the case for the setup detailed in section (2.1), as can be seen from the magnetic field profiles shown in Fig. 3.1 (a). For instance, if one rescales the transverse magnetic field profiles at heights $z = 0.438$ and $z = 0.265$ such that they match near the centre of the array, it can be seen that these profiles would *not* match near the end magnets. This is most apparent by comparing the relative heights of the peaks at $y = -6.5$ and $y = -4.5$ for the two profiles in Fig. 3.1 (a).

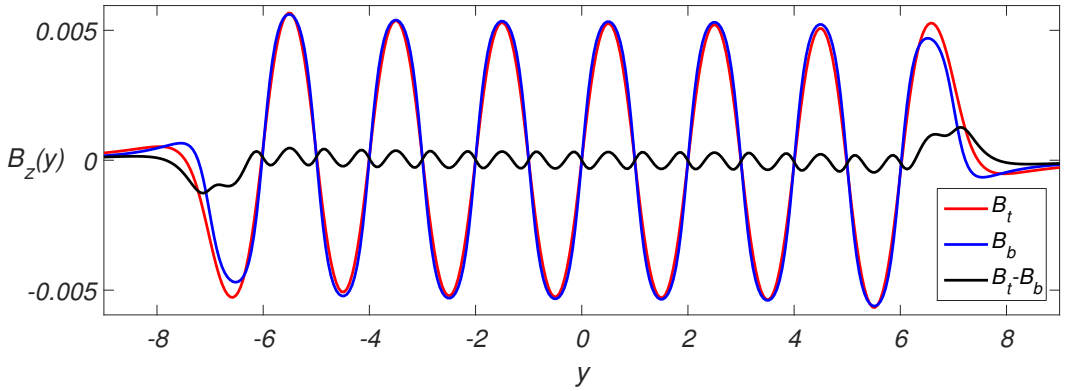

(a)

Figure D.1: Deviation of the magnetic field from being quasi-two-dimensional. The red and blue curves are the transverse cross sections, along $x = 0$, of the normalized magnetic field profiles at the electrolyte-air (B_t) and electrolyte-dielectric (B_b) interfaces, respectively. The black curve is the difference in the two profiles.

To further explore the nature of this deviation, it is useful to compare the magnetic field profiles computed using the dipole model described in section (3.2). Figure D.1 shows the transverse cross sections, along $x = 0$, of the rescaled magnetic fields at the dielectric-electrolyte and electrolyte-air interfaces, i.e., $B_t = B_z(x, y, z = 0.236)$ and $B_t = B_z(x, y, z = 0.472)$. The normalization criterion chosen is that the amplitude of the $\sin(\kappa y)$ mode is the same across the two profiles. Also shown in Fig. D.1(b) is the difference between the normalized profiles at $z = 0.236$ and $z = 0.472$. The average root-mean-squared difference between the two profiles is around 10%.

To demonstrate the impact of the z-dependence of the forcing profile on the flow, the straight and modulated flow fields in the NPS were recomputed using $B_{2D} = B_b$ and $B_{2D} = B_t$, in addition to the depth-averaged magnetic field B_{da}. The value of α was increased by 22% relative to the depth-averaged value to reduce the influence of the uncertainty in the model parameters on the flow pattern (cf. Fig. 4.8). This choice also yields the best agreement between the average wavelengths of the flow pattern in the simulation and experiment for $Re_c < R < Re_s$. As Fig. D.2 (a) shows, the forcing profile strongly affects both Re_c and the amplitude of the modulation of the flow for $Re > Re_c$. It also shows that B_{da} produces substantially better agreement with experiment that either B_b or B_t. Similarly, the forcing profile strongly influences the modulation wavelength. Similar results (not shown) are obtained if, instead of α, either β or ν is modified to match Re_c.

The above analysis shows that, although the NPS with the depth-averaged magnetic field profile captures the salient features of the dynamics fairly well, the flow pattern depends fairly sensitively on the details of the forcing. Hence, one should expect systematic deviations between the 2D model derived for a Q2D flow and the experiment where quasi-two-dimensionality is broken by the forcing. It should be mentioned that the wavelength of the modulated flow measured by either seeding the dielectric-electrolyte interface or the top surface of the electrolyte are virtually

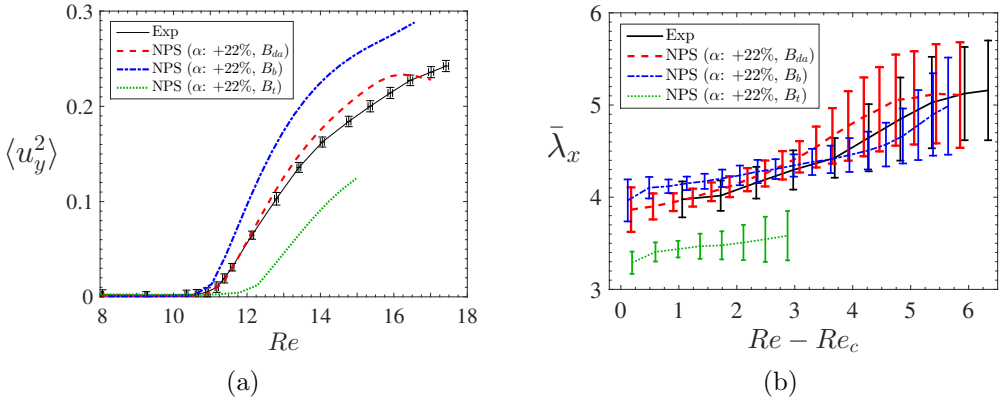

Figure D.2: Sensitivity to the magnetic field profile. (a) A bifurcation diagram for the primary instability and (b) the average wavelength of the pattern in the modulated regime. The simulations were performed with α increased by 22% relative to the depth-averaged value for the straight flow and used either B_{da}, B_b, or B_t.

identical. This implies that viscous coupling across the fluid layers produces a Q2D flow despite the fact that forcing profile driving the flow is not perfectly Q2D.

While the above analysis shows that the deviation of the forcing from being Q2D is, in all likelihood, the reason behind the disagreement between experiment and simulation, it does not show which specific features of the deviation affect the flow the most. For example, the deviation $B_t - B_b$ can be thought of as composed of two profiles: (1) the localized deviation from quasi-two-dimensionality close to the end magnets, and (2) the presence of a higher harmonic (of the sinusoidal profile) spread in the interior of the domain. The effects of the two deviations can be separately studied by swapping the normalized profile in the region $-6 \leq y \leq 6$, say in B_t (B_b) with that from B_b (B_t). Recomputing the straight and modulated flows, it was found that such a "mixed" magnetic field profile yields results similar to those obtained using B_t (B_b), instead of B_b (B_t). This suggests that the profile over the end magnets strongly affects the structure and the dynamics of the flow. The role of the higher-harmonics, nevertheless, is analyzed in the following section

D.2 Robustness of Vertical Profile to Changes in Spatial Length Scales

In the derivation of the depth-averaged 2D model, it was assumed that one can express the nearly 2D velocity field $V(x, y, z, t)$ as the product of a vertical profile $P(z)$ and a strictly 2D horizontal velocity $\mathbf{u}$, i.e., $\mathbf{V}(x, y, z, t) = P(z)\mathbf{u}(x, y, t)$. The profiles $P_\kappa(z)$ for the sinusoidal flow and $P_0(z)$ for the uniform flow were shown to be almost identical (cf. section (3.1.2)). However, due to the presence of the $\sin(3\kappa y)$ term in the forcing, the velocity profile in the vertical direction should be recomputed, with the inclusion of this harmonic. Modeling the magnetic field[1] as $\mathbf{B} = B_z\,\hat{\mathbf{z}} = (B_\kappa e^{-\kappa z}\sin(\kappa y) + B_{3\kappa}e^{-3\kappa z}\sin(3\kappa y))\,\hat{\mathbf{z}}$ necessitates modifying the solution for the straight flow to $\mathbf{u}_\mathrm{s} = P_\kappa(z)u_\kappa\sin(\kappa y)\,\hat{\mathbf{x}} + P_{3\kappa}(z)u_{3\kappa}\sin(3\kappa y)\,\hat{\mathbf{x}}$. In the above decomposition the normalization $P_\kappa(h) = P_{3\kappa}(h) = 1$ is imposed, which implies $u_\kappa + u_{3\kappa}$ is the peak velocity of straight flow at the free surface. If P_κ and $P_{3\kappa}$ are similar in shape, much like P_κ and P_0 shown in Fig. 2.6 and Fig. 2.7(a), one can approximate both using a common profile $P(z)$. Whether such an approximation is feasible for various wavenumbers is discussed below.

$P_k(z)$, with $k = \kappa$ or 3κ being the wavenumber of the Kolmogorov forcing, is computed as the solution to the following linear equations (cf. equation (2.7)), subject to the boundary conditions specified by equation (2.2):

$$\begin{aligned} P'' - k^2 P &= -\frac{JB_k}{u_k\mu_c}e^{-kz}, \quad h_d < z < h_d + h_c, \\ P'' - k^2 P &= 0. \qquad\qquad\qquad\quad 0 < z < h_d \end{aligned} \tag{D.1}$$

Figure D.3 shows the vertical profiles computed for $k = 0,\ \kappa,\ 3\kappa$. While the profile in the electrolyte is very robust, owing to the higher viscosity relative to the dielectric, the profile in the dielectric is fairly sensitive to changes in k. Using the profile $P_{3\kappa}$ the depth-averaged parameters (cf. equation (3.4)) turn out to be $\alpha = 0.0358\mathrm{s}^{-1}$,

[1]The linear decay presented in the chapter 2 can be obtained using a Taylor expansion of this form, retaining only the linear terms.

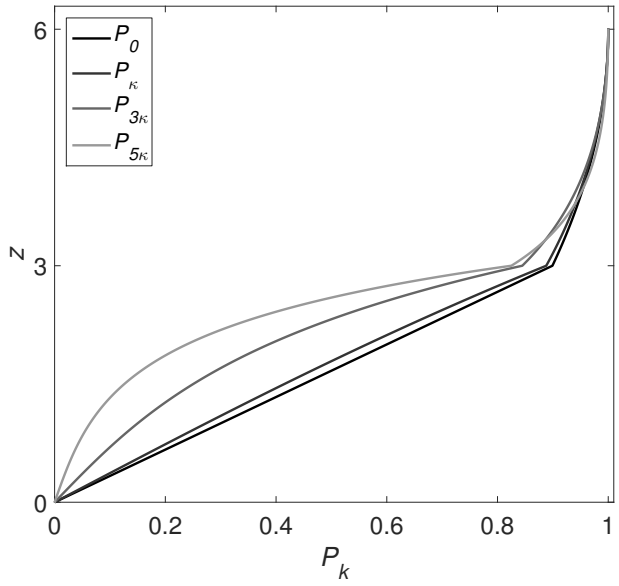

Figure D.3: Wavenumber dependence of the vertical profile assuming a strict sinusoidal horizontal profile. As the wavenumber of the driving is increased the vertical profile in the dielectric changes in a nontrivial manner, while the flow in the electrolyte remains fairly robust, being highly viscous.

$\beta = 0.805$, $\bar{\nu} = 3.59\times\ 10^{-6}\mathrm{m}^2/\mathrm{s}$, and $\bar{\rho} = 841\ \mathrm{kg/m}^3$. One can compare these with the parameters computed using P_κ, i.e., $\alpha = 0.0626\mathrm{s}^{-1}$, $\beta = 0.811$, $\bar{\nu} = 3.28\times 10^{-6}\mathrm{m}^2/\mathrm{s}$, and $\bar{\rho} = 951\ \mathrm{kg/m}^3$. As can be seen, β is very robust to changes in wavenumber, while $\bar{\nu}$ and $\bar{\rho}$ vary by about 10%. In contrast, α decreases significantly, by about 40%. This suggests that modeling the dissipation of the bottom boundary using a linear friction term is a good approximation only for flows where the spread in spatial frequencies is relatively narrow.

How much the sensitivity of the parameters to changes in wavenumber influences the comparison between the 2D model and the experiment is an open question. For example, when the flow transitions from the straight to modulated flow, the characteristic wavenumber of the pattern changes in a continuous manner. This implies that the parameters near the transition should be sufficiently close to the ones estimated using sinusoidal straight flow. Consequently, the magnitude of changes to the 2D

parameters (β by 6%, $\bar{\nu}$ by 7%, and α by 22%) necessary to reconcile the disagreement between the NPS and the experiment cannot be attributed to the changes in wavenumber associated with the transition. However, in the modulated and turbulent flow regimes, one should still recompute the profile $P_k(z)$ for a wavenumber which is estimated using the dominant wavenumber of the pattern. One option, suggested by Satijn *et al.* [82], is to study the decay of a monopolar vortex in the stratified setup. This *may* give some insight into the shape of $P_k(z)$ in the modulated flow regime and above, when vortices form the building blocks of the flow.

APPENDIX E

GUIDE TO THE MATLAB NEWTON-KRYLOV SOLVER

The Newton-Krylov solver employed for computing unstable equilibrium solutions was originally developed by Radford Mitchell [133], following the MATLAB function suites[1] supplementary to C.T.Kelley's SIAM books "Iterative Methods for Linear and Nonlinear Equations" [147] and "Solving Nonlinear Equations with Newton's Method" [138]. The solver code was modified, as a part of this dissertation work, to include computing equilibrium as well as time-periodic solutions in the non-periodic, finite-difference simulations. Furthermore, the solver suite was modified to be significantly more user friendly. This Appendix serves as a reference manual to run the solver in conjugation with the NPS code to compute (only) equilibria. The function names from Kelley's books [138, 147] have been included as footnotes to guide the reader to the relevant online sources. Lastly, the solver has been tested using MATLAB versions 2014a and 2014b.

- `Solver_FD_NP_FP(`*`ic_file,T,nlt_type,param_dir,save_tag`*`)`: This parent function requires as input the name of a file which contains velocity fields u and v as 2D matrices. The input argument T, typically 1 second, is the duration for which the initial state is integrated to compute the residual $r = \|\mathbf{u}(T) - \mathbf{u}\|$. The discretization method for the nonlinear term is specified as a string: 'cds' for central differencing, 'foh' for hybrid differencing, and 'fou' for upwinding. The path to the directory which contains the simulation parameters like forcing profile, finite difference matrices, etc., is also a required input argument. This

[1] The following are SIAM bookstore weblinks for downloading the MATLAB Newton-Krylov solver codes `http://www.siam.org/books/kelley/fr16/matlabcode.php` and `http://www.siam.org/books/fa01/?_ga=2.259016840.306407841.1500459970-1920949757.1498436165`

function calls `NewtonKrylov_FD_NP_FP` to iteratively modify $\mathbf{u}$ to converge it to an equilibrium. Finally, the state at the end of Newton iterations is saved as a MAT file which can be identified using the user defined save tag string, e.g., '20070810'.

- `NewtonKrylov_FD_NP_FP`[2]: The Newton iterations that modify the velocity field to minimize the residual $r = \|\mathbf{u}(T) - \mathbf{u}\|$ are computed within this function. The set of arguments is too numerous and specific to the NPS code to be listed here. However, they need modification only when the integrator is changed. The hard-coded variables within this function that may need tweaking are `maxit` and `maxitl`, which are the maximum number of Newton steps and the dimensionality of the Krylov subspace. Typical values for these variables are 80 and 120, respectively. Lastly, this function calls additional functions `NS2D_FD_NP`, `GMRES_FD_NP_FP`, and `Parab3p`.

- `NS2D_FD_NP`[3]: This function evolves a velocity field $\mathbf{u}$ for a duration T using the discrete form of governing equation (cf. equation (3.21)) and returns the final state $\mathbf{u}(T)$.

- `GMRES_FD_NP_FP`[4]: The direction in the state space which minimizes the residual is computed within this function by approximating the Jacobian in the Krylov subspace. Consequently, this function makes calls to `NS2D_FD_NP` as well as `DirDer_FD_NP_FP`.

- `DirDer_FD_NP_FP`[5]: Computes the finite difference approximation of the directional derivative necessary to construct the Jacobian in the Krylov subspace.

[2] nsoli.m and nsola.m

[3] feval.m

[4] fdgmres.m. Kelley's and Radford's versions included an intermediate function dkrylov.m that was removed in the current version.

[5] dirder.m

The code also includes a sub-function `Projection_DivFree_FD_NP` which projects the directional derivative onto a divergence free subspace.

- `Parab3p`[6]: A three-point parabolic line search in state space to identify the exact size of the Newton step in the direction of descent given by the GMRES code.

[6] parab3p.m

APPENDIX F

COMPUTING UNSTABLE BRANCHES OF PITCHFORK BIFURCATION

In this appendix details of computing the various branches that emerge at the pitchfork bifurcations in the SPS and the NPS (cf. section (4.5)) are presented. To begin, The schematic depicting the pitchfork bifurcation in Fig. 4.9 was constructed following the computation of all the stable and unstable states using the matrix-free Newton-Krylov solver [138]. Guesses for the stable states, to initialize the Newton solver, can be easily obtained using numerical integration. However, those for the unstable states should be constructed using continuation or by computing the marginal eigenvector at the bifurcation.

For example, initial guesses for the unstable straight flow branches in the SPS and NPS simulations were constructed by extrapolating the stable straight solutions in Reynolds number Re, i.e.,

$$\mathbf{u}_s^2(Re_c + \epsilon) \approx \mathbf{u}_s^1(Re_c) + \epsilon \left(\frac{\partial \mathbf{u}_s^1}{\partial Re} \right)_{Re_c}, \tag{F.1}$$

where the derivative $(\partial \mathbf{u}_s^1 / \partial Re)$ was approximated using finite differences,

$$\left(\frac{\partial \mathbf{u}_s^1}{\partial Re} \right)_{Re} \approx \frac{\mathbf{u}_s^1(Re) - \mathbf{u}_s^1(Re - \Delta Re)}{\Delta Re}. \tag{F.2}$$

This method proved useful in obtaining a good initial guess for the unstable straight flow $\mathbf{u}_s^2$ in the NPS, since it is disconnected from $\mathbf{u}_s^1$, as shown in Fig. 4.9 (c). In the NPS $Re_c \approx 10.5$ is not estimated by identifying the instability of $\mathbf{u}_s^1$, since there is none. Instead, it is computed[1] using the intercept of a linear fit to the amplitude $\langle v^2 \rangle$

[1] Computing Re_c in this manner facilitates direct comparison with experiment, where the unstable branches are not available.

versus Re, shown in Fig. 4.7, close to the onset of modulation. Hence the initial guess at $Re \approx 10.75$ was constructed by extrapolating $\mathbf{u}_s^1$ from a lower $Re \approx 10.25$. This can be done by deliberately choosing a coarse step $\epsilon = 0.5$ in Re in equation (F.1).

A good initial guess for the unstable modulated branches $\mathbf{u}_m^3$ ($\mathbf{u}_m^4$) emerging from the second pitchfork in the SPS is constructed using $\mathbf{u}_m^3 \approx \mathbf{u}_s^2 \pm p\,\hat{\mathbf{e}}_2$. Here $\hat{\mathbf{e}}_2$ is the second marginally unstable eigenvector of the straight flow which has the symmetry $\mathcal{R}_x\mathcal{T}_y^w$. The amplitude p is not known *a priori*, but, too small an amplitude p results in the initial guess converging back to $\mathbf{u}_s^2$. However, initial conditions constructed using sufficiently large p converge to $\mathbf{u}_m^3$ when input to the Newton-Krylov solver. In the NPS, the initial guess for the unstable branch $\mathbf{u}_m^2$ was similarly constructed, $\mathbf{u}_m^2 \approx \mathbf{u}_s^2 - p\,\hat{\mathbf{e}}_1$, using the eigenvector with the $\mathcal{R}_y\mathcal{R}_x$ symmetry. However, p in the NPS case can be estimated using $p = \langle\, \hat{\mathbf{e}}_1 | \mathbf{u}_m^1 - \mathbf{u}_s^2 \rangle$, since the stable modulated flow is known from numerical integration and $\mathbf{u}_s^2$ is computed from extrapolation.

Bibliography

[1] O. Reynolds, "An experimental investigation of the circumstances which determine whether the motion of water shall be direct or sinuous, and of the law of resistance in parallel channels," *P. R. Soc. London* **35**, 84 (1883).

[2] A. N. Kolmogorov, "The local structure of turbulence in incompressible viscous fluid for very large Reynolds numbers," in *Dokl. Akad. Nauk SSSR* volume 30 pp. 299–303 1941.

[3] G. I. Taylor, "Statistical theory of turbulence," in *Proceedings of the Royal Society of London A: Mathematical, Physical and Engineering Sciences* volume 151 pp. 421–444 The Royal Society 1935.

[4] T. Von Karman, "On the statistical theory of turbulence," *Proceedings of the National Academy of Sciences* **23**, 98 (1937).

[5] T. De Karman and L. Howarth, "On the statistical theory of isotropic turbulence," in *Proceedings of the Royal Society of London A: Mathematical, Physical and Engineering Sciences* volume 164 pp. 192–215 The Royal Society 1938.

[6] A. N. Kolmogorov, "Dissipation of energy in locally isotropic turbulence," in *Dokl. Akad. Nauk SSSR* volume 32 pp. 16–18 1941.

[7] G. Kawahara and S. Kida, "Periodic motion embedded in plane Couette turbulence: regeneration cycle and burst," *J. Fluid Mech.* **449**, 291 (2001).

[8] L. Van Veen, S. Kida, and G. Kawahara, "Periodic motion representing isotropic turbulence," *Fluid dynamics research* **38**, 19 (2006).

[9] D. Viswanath, "Recurrent motions within plane Couette turbulence," *J. Fluid Mech.* **580**, 339 (2007).

[10] P. Cvitanović and J. F. Gibson, "Geometry of the turbulence in wall-bounded shear flows: periodic orbits," *Phys. Scripta* **2010**, 014007 (2010).

[11] T. Kreilos and B. Eckhardt, "Periodic orbits near onset of chaos in plane Couette flow," *Chaos: An Interdisciplinary Journal of Nonlinear Science* **22**, 047505 (2012).

[12] A. P. Willis, K. Y. Short, N. B. Budanur, M. Farazmand, and P. Cvitanović, "Relative periodic orbits form the backbone of turbulent pipe flow," *arXiv preprint arXiv:1705.03720* (2017).

[13] E. Hopf, "A mathematical example displaying features of turbulence," *Commun. Pur. Appl. Math.* **1**, 303 (1948).

[14] L. D. Landau and E. M. Lifshitz, "Fluid mechanics," (1987).

[15] V. I. Arnold and L. D. Meshalkin, "Seminar led by A. N. Kolmogorov on selected problems of analysis (1958-1959)," *Usp. Mat. Nauk* **15**, 20 (1960).

[16] V. I. Arnold, "Instability of dynamical systems with several degrees of freedom," *Collected Works: Representations of Functions, Celestial Mechanics and KAM Theory, 1957–1965* , 423 (2009).

[17] P. Sekar and S. Narayanan, "Chaos in mechanical systems — A review," *Sadhana* **20**, 529 (1995).

[18] S. H. Strogatz, *Nonlinear dynamics and chaos: with applications to physics, biology, chemistry, and engineering* (Westview press, 2014).

[19] T. Matsumoto, "A chaotic attractor from Chua's circuit," *IEEE Transactions on Circuits and Systems* **31**, 1055 (1984).

[20] O. Rssler, "An equation for continuous chaos," *Physics Letters A* **57**, 397 (1976).

[21] J. Lindsay, R. J. Field, and M. Burger, *Oscillations and traveling waves in chemical systems* (Wiley, 1985).

[22] R. M. May, "Biological populations with nonoverlapping generations: stable points, stable cycles, and chaos," *Science* **186**, 645 (1974).

[23] A. Kelley, "The stable, center-stable, center, center-unstable, unstable manifolds," *Journal of Differential Equations* **3**, 546 (1967).

[24] S. Smale, "Differentiable dynamical systems," *Bulletin of the American mathematical Society* **73**, 747 (1967).

[25] D. Ruelle and F. Takens, "On the nature of turbulence," *Commun. Math. Phys* **20**, 167 (1971).

[26] S. Newhouse, D. Ruelle, and F. Takens, "Occurrence of strange AxiomA attractors near quasi periodic flows onT m, m? 3," *Communications in Mathematical Physics* **64**, 35 (1978).

[27] J. P. Gollub and H. L. Swinney, "Onset of turbulence in a rotating fluid," *Phys. Rev. Lett.* **35**, 927 (1975).

[28] G. Ahlers, "Low-Temperature Studies of the Rayieigh-Bénard Instability and Turbulence," *Phys. Rev. Lett.* **33**, 1185 (1974).

[29] A. Brandstäter, J. Swift, H. L. Swinney, A. Wolf, J. D. Farmer, E. Jen, and P. J. Crutchfield, "Low-Dimensional Chaos in a Hydrodynamic System," *Phys. Rev. Lett.* **51**, 1442 (1983).

[30] T. Bohr, M. H. Jensen, G. Paladin, and A. Vulpiani, *Dynamical systems approach to turbulence* (Cambridge University Press, 2005).

[31] F. Heslot, B. Castaing, and A. Libchaber, "Transitions to turbulence in helium gas," *Phys. Rev. A* **36**, 5870 (1987).

[32] L. A. Smith, "Intrinsic limits on dimension calculations," *Physics Letters A* **133**, 283 (1988).

[33] B. Castaing, G. Gunaratne, F. Heslot, L. Kadanoff, A. Libchaber, S. Thomae, X.-Z. Wu, S. Zaleski, and G. Zanetti, "Scaling of hard thermal turbulence in Rayleigh-Bnard convection," *Journal of Fluid Mechanics* **204** (1989).

[34] J.-P. Eckmann and D. Ruelle, "Fundamental limitations for estimating dimensions and Lyapunov exponents in dynamical systems," *Physica D: Nonlinear Phenomena* **56**, 185 (1992).

[35] P. Holmes, J. L. Lumley, and G. Berkooz, *Turbulence, coherent structures, dynamical systems and symmetry* (Cambridge, 1998).

[36] R. Narasimha, "Order and chaos in fluid flows," (1986).

[37] J. P. Gollub, "Order and disorder in fluid motion," *Proceedings of the National Academy of Sciences* **92**, 6705 (1995).

[38] T. Shinbrot, C. Grebogi, J. Wisdom, and J. A. Yorke, "Chaos in a double pendulum," *American Journal of Physics* **60**, 491 (1992).

[39] M. C. Gutzwiller, "Periodic orbits and classical quantization conditions," *Journal of Mathematical Physics* **12**, 343 (1971).

[40] R. Bowen and J.-R. Chazottes, *Equilibrium states and the ergodic theory of Anosov diffeomorphisms*volume 470 (Springer, 1975).

[41] D. Ruelle, "Generalized zeta-functions for Axiom A basic sets," *Bull. Am. Math. Soc.* **82** (1976).

[42] D. Ruelle, "Zeta-functions for expanding maps and Anosov flows," *Inventiones mathematicae* **34**, 231 (1976).

[43] D. Auerbach, P. Cvitanović, J. P. Eckmann, G. Gunaratne, and I. Procaccia, "Exploring chaotic motion through periodic orbits," *Phys. Rev. Lett.* **58**, 23 (1987).

[44] P. Cvitanović, "Invariant Measurement of Strange Sets in Terms of Cycles," *Phys. Rev. Lett.* **61**, 2729 (1988).

[45] R. Artuso, E. Aurell, and P. Cvitanovic, "Recycling of strange sets: I. Cycle expansions," *Nonlinearity* **3**, 325 (1990).

[46] R. Artuso, E. Aurell, and P. Cvitanovic, "Recycling of strange sets: II. Applications," *Nonlinearity* **3**, 361 (1990).

[47] E. Ott, C. Grebogi, and J. A. Yorke, "Controlling chaos," *Phys. Rev. Lett.* **64**, 1196 (1990).

[48] W. L. Ditto, S. N. Rauseo, and M. L. Spano, "Experimental control of chaos," *Phys. Rev. Lett.* **65**, 3211 (1990).

[49] Z. Gills, C. Iwata, R. Roy, I. B. Schwartz, and I. Triandaf, "Tracking unstable steady states: Extending the stability regime of a multimode laser system," *Phys. Rev. Lett.* **69**, 3169 (1992).

[50] R. Roy, T. W. Murphy Jr., T. D. Maier, Z. Gills, and E. R. Hunt, "Dynamical control of a chaotic laser: Experimental stabilization of a globally coupled system," *Phys. Rev. Lett.* **68**, 1259 (1992).

[51] A. Garfinkel, "Controlling cardiac chaos," *Science* (1992).

[52] V. Petrov, V. Gaspar, J. Masere, and K. Showalter, "Controlling chaos in the Belousov–Zhabotinsky reaction," *Nature* **361**, 240 (1993).

[53] Y. Saad and M. H. Schultz, "GMRES: A Generalized Minimal Residual Algorithm for Solving Nonsymmetric Linear Systems," *SIAM Journal on Scientific and Statistical Computing* **7**, 856 (1986) http://dx.doi.org/10.1137/0907058.

[54] D. A. Knoll and D. E. Keyes, "Jacobian-free Newton-Krylov methods: a survey of approaches and applications," *J. Comput. Phys.* **193**, 357 (2004).

[55] Y. Lan and P. Cvitanović, "Variational method for finding periodic orbits in a general flow," *Physical Review E* **69**, 016217 (2004).

[56] A. A. Townsend, "Measurements in the Turbulent Wake of a Cylinder," *Proceedings of the Royal Society of London A: Mathematical, Physical and Engineering Sciences* **190**, 551 (1947) http://rspa.royalsocietypublishing.org/content/190/1023/551.full.pdf.

[57] A. A. Townsend, *The structure of turbulent shear flow* (Cambridge university press, 1980).

[58] A. Roshko, "Structure of turbulent shear flows: a new look," *AIAA journal* **14**, 1349 (1976).

[59] J. L. L. Henry P. Bakewell Jr., "Viscous Sublayer and Adjacent Wall Region in Turbulent Pipe Flow," *The Physics of Fluids* **10**, 1880 (1967) http://aip.scitation.org/doi/pdf/10.1063/1.1762382.

[60] S. Kline, W. Reynolds, F. Schraub, and P. Runstadler, "The structure of turbulent boundary layers," *Journal of Fluid Mechanics* **30**, 741 (1967).

[61] H. Kim, S. Kline, and W. Reynolds, "The production of turbulence near a smooth wall in a turbulent boundary layer," *Journal of Fluid Mechanics* **50**, 133 (1971).

[62] F. Waleffe, J. Kim, and J. M. Hamilton, "On the origin of streaks in turbulent shear flows,", in *Turbulent Shear Flows 8* pp. 37–49 Springer 1993.

[63] J. M. Hamilton, J. Kim, and F. Waleffe, "Regeneration mechanisms of near-wall turbulence structures," *Journal of Fluid Mechanics* **287** (1995).

[64] F. Waleffe, "Three-dimensional coherent states in plane shear flows," *Phys. Rev. Lett.* **81**, 4140 (1998).

[65] M. Nagata, "Three-dimensional finite-amplitude solutions in plane Couette flow: bifurcation from infinity," *J. Fluid Mech.* **217**, 519 (1990).

[66] M. Nagata, "Three-dimensional traveling-wave solutions in plane Couette flow," *Phys. Rev. E* **55**, 2023 (1997).

[67] F. Waleffe, "Exact coherent structures in channel flow," *J. Fluid Mech.* **435**, 93 (2001).

[68] H. Faisst and B. Eckhardt, "Traveling waves in pipe flow," *Phys. Rev. Lett.* **91**, 224502 (2003).

[69] F. Christiansen, P. Cvitanović, and V. Putkaradze, "Spatio-temporal chaos in terms of unstable recurrent patterns," *Nonlinearity* **10**, 55 (1997).

[70] S. M. Zoldi and H. S. Greenside, "Spatially localized unstable periodic orbits of a high-dimensional chaotic system," *Phys. Rev. E* **57**, R2511 (1998).

[71] P. Manneville, "Macroscopic Modeling of Turbulent Flows," *Lecture Notes in Physics* **230**, 319 (1984).

[72] G. J. Chandler and R. R. Kerswell, "Invariant recurrent solutions embedded in a turbulent two-dimensional Kolmogorov flow," *J. Fluid Mech.* **722**, 554 (2013).

[73] N. B. Budanur, *Exact coherent structures in spatiotemporal chaos: from qualitative description to quantitative predictions*, PhD thesis Georgia Institute of Technology 2015.

[74] B. Hof, C. W. H. van Doorne, J. Westerweel, F. T. M. Nieuwstadt, H. Faisst, B. Eckhardt, H. Wedin, R. R. Kerswell, and F. Waleffe, "Experimental Observation of Nonlinear Traveling Waves in Turbulent Pipe Flow," *Science* **305**, 1594 (2004).

[75] A. de Lozar, F. Mellibovsky, M. Avila, and B. Hof, "Edge State in Pipe Flow Experiments," *Phys. Rev. Lett.* **108**, 214502 (2012).

[76] D. J. C. Dennis and F. M. Sogaro, "Distinct Organizational States of Fully Developed Turbulent Pipe Flow," *Phys. Rev. Lett.* **113**, 234501 (2014).

[77] G. Lemoult, K. Gumowski, J.-L. Aider, and J. E. Wesfreid, "Turbulent spots in channel flow: An experimental study," *The European Physical Journal E* **37**, 1 (2014).

[78] B. Suri, J. Tithof, R. O. Grigoriev, and M. F. Schatz, "Forecasting Fluid Flows Using the Geometry of Turbulence," *Phys. Rev. Lett.* **118**, 114501 (2017).

[79] G. I. Taylor, "The Spectrum of Turbulence," *Proceedings of the Royal Society of London A: Mathematical, Physical and Engineering Sciences* **164**, 476 (1938) http://rspa.royalsocietypublishing.org/content/164/919/476.full.pdf.

[80] N. F. Bondarenko, M. Z. Gak, and F. V. Dolzhanskiy, "Laboratory and theoretical models of plane periodic flows," *Izv. Akad. Nauk SSSR, Fiz. Atmos. Okeana* **15**, 711 (1979).

[81] B. Jüttner, D. Marteau, P. Tabeling, and A. Thess, "Numerical simulations

of experiments on quasi-two-dimensional turbulence," *Phys. Rev. E* **55**, 5479 (1997).

[82] M. P. Satijn, A. W. Cense, R. Verzicco, H. J. H. Clercx, and G. J. F. van Heijst, "Three-dimensional structure and decay properties of vortices in shallow fluid layers," *Phys. Fluids* **13**, 1932 (2001).

[83] F. V. Dolzhanskii, V. A. Krymov, and D. Y. Manin, "An advanced experimental investigation of quasi-two-dimensional shear flows," *J. Fluid Mech.* **241**, 705 (1992).

[84] D. Lucas and R. R. Kerswell, "Spatiotemporal dynamics in two-dimensional Kolmogorov flow over large domains," *J. Fluid Mech.* **750**, 518 (2014).

[85] P. Cvitanović, "Recurrent flows: the clockwork behind turbulence," *J. Fluid Mech.* **726**, 1 (2013).

[86] Y. Couder, "Two-dimensional grid turbulence in a thin liquid film," *J. Phys. Lett.* **45**, 353 (1984).

[87] J. Sommeria and R. Moreau, "Why, how, and when, MHD turbulence becomes two-dimensional," *J. Fluid Mech.* **118**, 507 (1982).

[88] F. V. Dolzhansky, *Fundamentals of Geophysical Hydrodynamics*volume 103 of *Encyclopaedia of Mathematical Sciences* (Springer, 2013), Translated by B. A. Khesin.

[89] G. Boffetta and R. E. Ecke, "Two-dimensional turbulence," *Annu. Rev. Fluid Mech.* **44**, 427 (2012).

[90] J. Sommeria, S. D. Meyers, and H. L. Swinney, "Laboratory simulation of Jupiter's great red spot," *Nature* **331**, 689 (1988).

[91] P. Tabeling, S. Burkhart, O. Cardoso, and H. Willaime, "Experimental study of freely decaying two-dimensional turbulence," *Phys. Rev. Lett.* **67**, 3772 (1991).

[92] G. Haller and G. Yuan, "Lagrangian coherent structures and mixing in two-dimensional turbulence," *Physica D* **147**, 352 (2000).

[93] A. M. Obukhov, "Kolmogorov flow and laboratory simulation of it," *Russ. Math. Surv.* **38**, 113 (1983).

[94] E. B. Gledzer, F. V. Dolzhanskii, and A. M. Obukhov, "Hydrodynamic-Type Systems and Their Applications," 1981.

[95] A. M. Batchaev and V. A. Dowzhenko, "Experimental modeling of stability loss in periodic zonal flows," in *Dokl. Akad. Nauk* volume 273 p. 582 1983.

[96] Y. Kolesnikov, "Investigation of flat shear flow instability in a magnetic field," *Magn. Gidrodin.* **1**, 60 (1985).

[97] Y. B. Kolesnikov, *Instabilities and turbulence in liquid metal magnetohydrodynamics*, PhD thesis University of Riga 1985.

[98] A. M. Batchaev and V. M. Ponomarev, "Experimental and theoretical investigation of Kolmogorov flow on a cylindrical surface," *Fluid Dyn.* **24**, 675 (1989).

[99] O. Cardoso, D. Marteau, and P. Tabeling, "Quantitative experimental study of the free decay of quasi-two-dimensional turbulence," *Phys. Rev. E* **49**, 454 (1994).

[100] H. J. H. Clercx, G. J. F. Van Heijst, and M. L. Zoeteweij, "Quasi-two-dimensional turbulence in shallow fluid layers: the role of bottom friction and fluid layer depth," *Phys. Rev. E* **67**, 066303 (2003).

[101] D. Marteau, O. Cardoso, and P. Tabeling, "Equilibrium states of two-dimensional turbulence: An experimental study," *Phys. Rev. E* **51**, 5124 (1995).

[102] G. Boffetta, A. Cenedese, S. Espa, and S. Musacchio, "Effects of friction on 2D turbulence: An experimental study of the direct cascade," *Europhys. Lett.* **71**, 590 (2005).

[103] D. H. Kelley and N. T. Ouellette, "Onset of three-dimensionality in electromagnetically driven thin-layer flows," *Phys. Fluids* **23**, 045103 (2011).

[104] M. K. Rivera and R. E. Ecke, "Pair Dispersion and Doubling Time Statistics in Two-Dimensional Turbulence," *Phys. Rev. Lett.* **95**, 194503 (2005).

[105] R. A. D. Akkermans, L. P. J. Kamp, H. J. H. Clercx, and G. J. F. van Heijst, "Three-dimensional flow in electromagnetically driven shallow two-layer fluids," *Phys. Rev. E* **82**, 026314 (2010).

[106] M. Shats, D. Byrne, and H. Xia, "Turbulence decay rate as a measure of flow dimensionality," *Phys. Rev. Lett.* **105**, 264501 (2010).

[107] J. Tithof, *Novel methods of dimensionality reduction applied to a two-dimensional fluid flow*, PhD thesis Georgia Institute of Technology 2016.

[108] R. J. Adrian and J. Westerweel, *Particle image velocimetry* (Cambridge, 2011).

[109] A. Eckstein and P. P. Vlachos, "Digital particle image velocimetry (DPIV) robust phase correlation," *Meas. Sci. Technol.* **20**, 055401 (2009).

[110] B. Drew, J. Charonko, and P. P. Vlachos, "QI – Quantitative Imaging (PIV and more)," 2013.

[111] V. A. Dovzhenko, A. M. Obukhov, and V. M. Ponomarev, "Generation of vortices in an axisymmetric shear flow," *Fluid Dyn.* **16**, 510 (1981).

[112] A. Figueroa, F. Demiaux, S. Cuevas, and E. Ramos, "Electrically driven vortices in a weak dipolar magnetic field in a shallow electrolytic layer," *J. Fluid Mech.* **641**, 245 (2009).

[113] R. A. D. Akkermans, L. P. J. Kamp, H. J. H. Clercx, and G. J. F. Van Heijst, "Intrinsic three-dimensionality in electromagnetically driven shallow flows," *Europhys. Lett.* **83**, 24001 (2008).

[114] B. Suri, J. Tithof, R. Mitchell, R. O. Grigoriev, and M. F. Schatz, "Velocity profile in a two-layer Kolmogorov-like flow," *Phys. Fluids* **26**, 053601 (2014).

[115] F. V. Dolzhanskii, V. A. Krymov, and D. Y. Manin, "Stability and vortex structures of quasi-two-dimensional shear flows," *Sov. Phys. Usp.* **33**, 495 (1990).

[116] A. J. Chorin, "Numerical solution of the Navier-Stokes equations," *Mathematics of computation* **22**, 745 (1968).

[117] R. Témam, "Sur l'approximation de la solution des équations de Navier-Stokes par la méthode des pas fractionnaires (I)," *Archive for Rational Mechanics and Analysis* **32**, 135 (1969).

[118] J. Kim, P. Moin, and R. Moser, "Turbulence statistics in fully developed channel flow at low Reynolds number," *Journal of Fluid Mechanics* **177**, 133 (1987).

[119] J. van Kan, "A Second-Order Accurate Pressure-Correction Scheme for Viscous Incompressible Flow," *SIAM J. Sci. Stat. Comp.* **7**, 870 (1986) http://dx.doi.org/10.1137/0907059.

[120] P. M. Gresho and R. L. Sani, "On pressure boundary conditions for the incompressible Navier-Stokes equations," *International Journal for Numerical Methods in Fluids* **7**, 1111 (1987).

[121] S. Armfield and R. Street, "The Fractional-Step Method for the Navier-Stokes Equations on Staggered Grids: The Accuracy of Three Variations," *J. Comput. Phys.* **153**, 660 (1999).

[122] S. Armfield and R. Street, "An analysis and comparison of the time accuracy of fractional-step methods for the Navier?Stokes equations on staggered grids," *International Journal for Numerical Methods in Fluids* **38**, 255 (2002).

[123] R. J. LeVeque and R. J. Leveque, *Numerical methods for conservation laws*volume 132 (Springer, 1992).

[124] R. Temam, "Remark on the pressure boundary condition for the projection method," *Theoretical and Computational Fluid Dynamics* **3**, 181 (1991).

[125] F. H. Harlow and J. E. Welch, "Numerical Calculation of Time Dependent Viscous Incompressible Flow of Fluid with Free Surface," *Phys. Fluids* **8**, 2182 (1965).

[126] C. W. Hirt, B. D. Nichols, and N. C. Romero, "SOLA – A numerical solution algorithm for transient fluid flows," *Los Alamos Sci. Lab. Rep.* (1975).

[127] B. Leonard, "A stable and accurate convective modelling procedure based on quadratic upstream interpolation," *Computer Methods in Applied Mechanics and Engineering* **19**, 59 (1979).

[128] C. Hirt, "Heuristic stability theory for finite-difference equations," *Journal of Computational Physics* **2**, 339 (1968).

[129] D. B. Spalding, "A novel finite difference formulation for differential expressions involving both first and second derivatives," *International Journal for Numerical Methods in Engineering* **4**, 551 (1972).

[130] G. Strang, *Computational science and engineering*volume 1 (Wellesley-Cambridge Press, 2007).

[131] M. Griebel, T. Dornseifer, and T. Neunhoeffer, *Numerical Simulation in Fluid Dynamics* (SIAM, 1998).

[132] C. Pozrikidis, "A Note on the Regularization of the Discrete Poisson?Neumann Problem," *Journal of Computational Physics* **172**, 917 (2001).

[133] R. Mitchell, *Transition to turbulence and mixing in a quasi-two-dimensional Lorentz force-driven Kolmogorov flow*, PhD thesis Georgia Institute of Technology 2013.

[134] U. M. Ascher, S. J. Ruuth, and B. T. R. Wetton, "Implicit-explicit methods for time-dependent partial differential equations," *SIAM J. Numer. Anal.* **32**, 797 (1995).

[135] A. Thess, "Instabilities in two-dimensional spatially periodic flows. Part I: Kolmogorov flow," *Phys. Fluids A* **4**, 1385 (1992).

[136] D. Armbruster, B. Nicolaenko, N. Smaoui, and P. Chossat, "Symmetries and dynamics for 2-D Navier-Stokes flow," *Physica D: Nonlinear Phenomena* **95**, 81 (1996).

[137] J.-P. Eckmann, S. O. Kamphorst, and D. Ruelle, "Recurrence plots of dynamical systems," *EPL (Europhysics Letters)* **4**, 973 (1987).

[138] C. Kelley, *Solving Nonlinear Equations with Newton's Method* (SIAM, 2003).

[139] M. Kramár, R. Levanger, J. Tithof, B. Suri, M. Xu, M. Paul, M. F. Schatz, and K. Mischaikow, "Analysis of Kolmogorov flow and Rayleigh-Bénard convection using persistent homology," *Physica D* (2016).

[140] J. F. Gibson, J. Halcrow, and P. Cvitanović, "Visualizing the geometry of state space in plane Couette flow," *J. Fluid Mech.* **611**, 107 (2008).

[141] Y. Duguet, A. P. Willis, and R. R. Kerswell, "Transition in pipe flow: the saddle structure on the boundary of turbulence," *J. Fluid Mech.* **613**, 255 (2008).

[142] J. Halcrow, J. F. Gibson, P. Cvitanović, and D. Viswanath, "Heteroclinic connections in plane Couette flow," *J. Fluid Mech.* **621**, 365 (2009).

[143] P. Cvitanović, R. Artuso, R. Mainieri, G. Tanner, and G. Vattay, *Chaos: Classical and Quantum* (Niels Bohr Institute, Copenhagen, 2012), `http://ChaosBook.org`.

[144] C. Dong and Y. Lan, "A variational approach to connecting orbits in nonlinear dynamical systems," *Physics Letters A* **378**, 705 (2014).

[145] B. Seibold, "A compact and fast Matlab code solving the incompressible Navier-Stokes equations on rectangular domains.," (2008).

[146] V. A. Dovzhenko, V. A. Krymov, and V. M. Ponomarev, "Experimental and theoretical investigation of the shear flow generated by an axially symmetric force," *Izv. Akad. Nauk SSSR, Fiz. Atmos. Okeana* **20**, 693 (1984).

[147] C. Kelley, *Iterative Methods for Linear and Nonlinear Equations* (Society for Industrial and Applied Mathematics, 1995) http://epubs.siam.org/doi/pdf/10.1137/1.9781611970944.